

Kingdom of Saudi Arabia
Ministry of Education
Umm Al-Qura University
Faculty of Applied Science
Physics Department



Synthesis, Characterization and Optical Properties Studies of Core/Shell Nanoparticles and their Applications in Solar Cells

**A Thesis Submitted to Physics Department, Faculty of Applied
Science, Umm Al-Qura University**

**In partial Fulfillment of the Requirements for the Degree of Master
of Physics**

By

Samiyah Abdulrahman Othman Al-Ghamdi

(B.Sc In Physics)

No.43880212

Under Supervision

Prof. Dr. Roshdi Seoudi Mohamed Awed

Prof. of Spectroscopy and Nanotechnology, Physics Department,

Faculty of Applied Science, Umm Al-Qura University

Assistant Supervision

Prof. Dr. Saud Hamed Allehyani

Prof. of Medical Physics, Physics Department,

Faculty of Applied Science, Umm Al-Qura University

(1441-2020)

بِسْمِ اللَّهِ الرَّحْمَنِ الرَّحِيمِ

This thesis dedicated to my parents,

ABDULRAHMAN AL-GHAMDI and SALIHAH AL-ABDULLAH

For their endless love, support, and encouragement

Kingdom of Saudi Arabia
Ministry of Education
Umm Al-Qura University
Faculty of Applied Science
Physics Department



Synthesis, Characterization and Optical Properties Studies of Core/Shell Nanoparticles and their Applications in Solar Cells

By


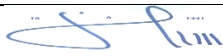
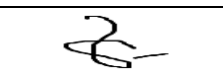
Samiyah Abdulrahman Othman Al-Ghamdi

(B.Sc In Physics)

No.43880212

**This Thesis was Discussed and Approved in 11/5/2020 A.D.,
18/9/1441 A.H.**

Committee of Examiners

Name	Committee of Examiners	Signature
Prof. Dr. Roshdi Seoudi	Advisor	
Prof. Dr. Yosry Mostafa	Examiner	
Prof. Dr. Adel Al-Madani	Examiner	

Contents

Contents

Acknowledgments	ii
Abstract	iv
Summary	vii
List of Abbreviations	xv
List of Figures	xviii
List of Tables	xxv

CHAPTER I

GENERAL INTRODUCTION AND LITERATURE REVIEW

1.1 History of Nanomaterials	2
1.2 Introduction of Nanomaterials	3
1.3 Important Definition	5
1.3.1 Nanomaterials	5
1.3.2 Nanotechnology	5
1.3.3 Nanoscience	6
1.4 Classification of Nanomaterials	6
1.4.1 Based on Origin	6
1.4.2 Based on Dimensionality	6
1.4.2.1 Zero-Dimensional (0-D).....	6
1.4.2.2 One-Dimensional (1-D).....	7
1.4.2.3 Two-Dimensional (2-D).....	7
1.4.2.4 Three-Dimensional (3-D).....	7

1.4.3 Based on Morphology	8
1.4.4 Based on Composition	9
1.5 Factors Affecting of the Nanomaterials	9
1.5.1 Confinement Effect	9
1.5.2 Surface Effects	10
1.5.3 Effect of Surface to Volume Ratio	11
1.5.4 Size Effects on Structure and Morphology of Free or Supported Nanoparticles	12
1.5.5 Composition and Surface Composition of Nanomaterials	12
1.6 Fabrication of Nanomaterials	13
1.6.1 Preparation of Nanoparticle-Based on Built Structures... 13	
1.6.1.1 Top-Down Route	14
1.6.1.2 Bottom-Up Route	14
1.7 Preparation of Nanoparticle-Based on The Starting State of Material	14
1.7.1 Physical Vapor Deposition (PVD)	15
1.7.2 Chemical Vapor Deposition (CVD)	18
1.7.3 Sol-Gel Processing Route for Synthesis of Nanomaterials	19
1.8 Properties of Nanomaterials	20
1.8.1 Optical Properties of Nanomaterials.....	20
1.8.2 Magnetic Properties of Nanomaterials	21
1.8.3 Thermal Properties of Nanomaterials	23
1.8.4 Catalytic/Photocatalytic Activity.....	24
1.9 The Importance of Nanomaterials	24

1.10 Application of Nanomaterials	25
1.11 Literature Review	30
1.12 Aim of the Present Work	32

CHAPTER II

THEORETICAL PRINCIPLES OF THE INSTRUMENTS

2.1 Theoretical Principle of UV-Visible Spectroscopy	37
2.1.1 Quantitative Aspects of Ultraviolet Spectroscopy	38
2.1.2 Classification of UV Absorption Bands	39
2.2 Theoretical Principle of Transmission Electron Microscopy (TEM).....	41
2.2.1 The Electron Gun.....	44
2.2.2 Thermionic Emission	44
2.3 Theoretical Principle of Light Scattering Techniques	48
2.3.1 Dynamic Light Scattering	48
2.3.1.1 Brownian Motion	48
2.3.1.2 The Hydrodynamic Diameter	48
2.4 Theoretical Principle of X-Ray Diffraction (XRD)	50
2.4.1 Introduction to Diffraction	50
2.4.2 Bragg's Law	51
2.4.3 The Powder Diffraction File	54
2.5 Theoretical Principle of Fourier Transform Infrared Spectroscopy (FTIR)	55
2.5.1 The number of Mode Vibration in The Infrared Spectra	57
2.5.2 The Origin of IR Absorption Spectra	58

2.6 Theoretical Principle of Solar Cell	63
2.6.1 Solar Cell	63
2.6.1.1 Generations of Solar Cells	65
2.6.1.2 Factors Affecting the Efficiency of Solar Cells	65
2.6.2 Solar Radiation	65
2.6.3 Ideal Conversion Efficiency	66

CHAPTER III

EXPERIMENTAL METHODS AND INSTRUMENTATIONS

3.1 Chemicals	72
3.1.1 Gold (III) Chloride Trihydrate $\text{HAuCl}_4 \cdot 3\text{H}_2\text{O}$	72
3.1.2 Silver Nitrate (AgNO_3)	72
3.1.3 Sodium Borohydride (NaBH_4)	72
3.1.4 Cetyltrimethylammonium Bromide (CTAB)	73
3.1.5 Sodium Sulfide (Na_2S)	73
3.1.6 Zinc Acetate Dihydrate ($\text{Zn}(\text{CH}_3\text{COO})_2 \cdot 2\text{H}_2\text{O}$)	73
3.1.7 Polyvinylpyrrolidone (PVP)	74
3.1.8 Chloroform	74
3.1.9 Ascorbic Acid	74
3.1.10 Sodium Hydroxide (NaOH)	75
3.1.11 Ammonium Nitrate (NH_4NO_3)	75
3.1.12 Solar Cell	75
3.2 Preparation of Gold Nanoparticles (AuNPs)	76
3.2.1 Preparation of Gold Nanoparticles (AuNPs) at Different Concentrations of Sodium Borohydride (NaBH_4)	76

3.2.2	Preparation of AuNPs at Different Concentrations of CTAB ..	78
3.3	Preparation of Silver Nanoparticles (AgNPs)	80
3.3.1	Preparation of Silver Nanoparticles (AgNPs) Using a Reverse Micelle Method at Different Concentrations of Silver Nitrate ..	80
3.4	Preparation of Zinc Sulfide Nanoparticles (ZnSNPs)	82
3.4.1	Preparation of Zinc Sulfide Nanoparticles (ZnSNPs) at Different Zinc Cetate Dihydrate Molar Ratio	82
3.4.2	Preparation of ZnSNPs at Different Temperatures	84
3.5	Preparation of Silver Nanoparticles (AgNPs) Capped by Polyvinylpyrrolidone (PVP)	86
3.6	Preparation of (Ag/ZnS) Core-Shell Nanoparticles	87
3.7	Deposition of Nanoparticles on Silicon Solar Cell	88
3.8	Samples Characterization	88
3.8.1	Experimental Aspect of UV-Vis Spectroscopy	89
3.8.2	Experimental Aspect of Transmission Electron Microscopy	90
3.8.3	Experimental Aspect of Dynamic Light Scattering	98
3.8.3.1	Dynamic Light Scattering Optical Configuration	101
3.8.3.2	Variable Measurement Position for Sizing	103
3.8.4	Experimental Aspect of X-Ray Diffraction	104
3.8.5	Experimental Aspects of Fourier Transform Infrared Spectroscopy (FTIR)	106
3.9	Measurements of the Current-Voltage	111

CHAPTER IV

RESULTS AND DISCUSSION

4.1 Results of Ultraviolet-Visible Spectroscopy	113
4.1.1 UV-Vis for Gold Nanoparticle Prepared at Different Concentrations of Sodium Borohydride	113
4.1.2 UV-Vis for Gold Nanoparticle Prepared at Different CTAB Concentrations	115
4.1.3 UV-Vis for Silver Nanoparticle Prepared at Different Concentrations of Silver Nitrate	116
4.1.4 UV-Vis for Zinc Sulfide Nanoparticle Prepared at Different Concentrations of Zinc Acetate Dihydrate.....	118
4.1.5 UV-Vis for Zinc Sulfide Nanoparticle Prepared at Different Temperatures	122
4.1.6 UV-Vis for Silver \ Zinc Sulfide Core-Shell Nanoparticles	125
4.2 Results of Transmission Electron Microscopy (TEM)	127
4.2.1 Transmission Electron Microscopy (TEM) Images of Gold Nanoparticle Synthesized at Different Concentrations of NaBH ₄	127
4.2.2 Transmission Electron Microscopy (TEM) Image of Gold Nanoparticle Synthesized Using CTAB as a Surfactant.	128
4.2.3 Transmission Electron Microscopy (TEM) Images of Silver Nanoparticle Synthesized at Different Concentrations of AgNO ₃	129

4.2.4	Transmission Electron Microscopy (TEM) Images of Zinc Sulfide Nanoparticle Synthesized at Different Concentrations of Zinc Acetate Dihydrate	131
4.2.5	Transmission Electron Microscopy (TEM) Images of Zinc Sulfide Nanoparticle Synthesized at Different Temperatures.	132
4.2.6	Transmission Electron Microscopy (TEM) Images of Silver/Zinc Sulfide Core-Shell Nanoparticle Synthesized at Different Quantities of Ag Nanoparticles.	132
4.3	Results of Dynamic Light Scattering (DLS)	134
4.4	Results of X-Ray Diffraction (XRD).....	141
4.4.1	X-Ray Diffraction (XRD) for Gold Nanoparticle Prepared at Different Concentrations of Sodium Borohydride	141
4.4.2	X-Ray Diffraction (XRD) for Gold Nanoparticle Prepared at Different CTAB Concentrations.....	143
4.4.3	X-Ray Diffraction (XRD) for Silver Nanoparticle Prepared at Different Concentrations of Silver Nitrate.....	144
4.4.4	X-Ray Diffraction (XRD) for Zinc Sulfide Nanoparticle Prepared at Different Concentrations of Zinc Acetate Dihydrate	146
4.4.5	X-Ray Diffraction (XRD) for Zinc Sulfide Nanoparticle Prepared at Different Temperatures	147
4.5	Results of Fourier Transform Infrared Spectroscopy (FT-IR)	149
4.5.1	Fourier Transform Infrared Spectroscopy (FT-IR) for Gold Nanoparticle Prepared at Different Concentrations of Sodium Borohydride or Different Concentrations of CTAB.....	149

4.5.2 Fourier Transform Infrared Spectroscopy (FT-IR) for Silver Nanoparticle Prepared at Different Concentrations of Silver Nitrate	153
4.5.3 Fourier Transform Infrared Spectroscopy (FT-IR) of Zinc Sulfide Nanoparticle Prepared at Different Concentrations of Zinc Acetate Dihydrate	156
4.5.4 Fourier Transform Infrared Spectroscopy (FT-IR) For Zinc Sulfide Nanoparticle Prepared at Different Temperatures	159
4.5.5 Fourier Transform Infrared Spectroscopy (FT-IR) Silver \ Zinc Sulfide Core-Shell Nanoparticles	160
4.6 Application of Nanoparticles in Solar Cells	162
4.6.1 I-V Characteristic Curve of Polycrystalline Silicon Solar Cell Coated by Gold Nanoparticles.....	162
4.6.2 I-V Characteristic Curve of Polycrystalline Silicon Solar Cell Coated by Zinc Sulfide Nanoparticles	165
4.6.3 I-V Characteristic Curve of Polycrystalline Solar Cell Deposited by Silver/Zinc Sulfide Core-Shell Nanoparticles.....	167
4.6.4 Photocurrent Measurements	169
Conclusion	172
References	176
Arabic Summary	192

Acknowledgments

Acknowledgments

All praises to ALLAH ALMIGHTY for sound health and his blessing in successfully performing this thesis, and without the help of ALLAH, this work would never see the light.

I would like sincerely to thank my supervisor, **Prof. Dr. Roshdi Seoudi Mohamed Awed**, Professor of Spectroscopy and Nanotechnology, Physics Department, Faculty of Applied Science, Umm Al-Qura University, for his valuable comments and suggestion and expertly guided me throughout this work. His enthusiasm, patience, the endless pursuit of excellence, and dedication to research have given me the motivation to work hard and seek perfection and made my master's experience productive and stimulated.

I would also thank my assistant supervisor, **Prof. Dr. Saud Hamed Allehyani**, Professor of Medical Physics, Faculty of Applied Science, Umm Al-Qura University, for his participation in this work.

My appreciation also extended to all the faculty members in the physics department and research lab.

Last but not least, my sincere gratitude goes to my ever-loving parents, my mother, **Salihah Al-Abdullah**, and my father, **Abdulrahman AL-Ghamdi**, who nurtured my learning and supported me emotionally and financially, without their prayer, encouraged, and confidence in me I would have never succeeded. I would also to thank my brothers and sisters, who deserve my wholehearted thanks as well.

I am thankful for everyone who has indirectly helped me to bring out this thesis.

Samiyah Abdulrahman Othman Al-Ghamdi

(1441-2020)

Abstract

Abstract

This thesis focused on the preparation of gold, silver, zinc sulfide, and silver/zinc sulfide core-shell nanoparticles using chemical methods and their application in the solar cell. Gold nanoparticles were prepared at different sodium borohydride and cetyltrimethylammonium bromide concentrations. Silver nanoparticles were prepared using a reverse micelle method at different silver nitrate concentrations. Zinc sulfide nanoparticles were prepared at various molar ratios of zinc acetate dihydrate and at different temperatures. Silver/zinc sulfide core-shell nanoparticles were prepared using different quantity of our prepared silver nanoparticles. UV-visible spectra of all samples were explaining the effect of particle size on surface plasmon band position, which increase when the position shift toward higher wavelength (red-shift) and decrease when it shifted toward a lower wavelength (blue-shift). Transmission electron microscopy images confirmed the formation of the nanoparticles with spherical shape and some triangle and hexagon shapes in different sizes. Moreover, these results indicated that the zinc sulfide nanoparticles were surrounded by the silver nanoparticles by showing a color contrast implying the particle composed of different materials confirming the formation of silver/zinc sulfide core-shell. Average particle sizes were measured using dynamic light scattering. X-ray diffraction illustrates the crystallization nature of the nanoparticles, and crystal sizes were estimated using Scherrer's equation, which was changed with change conditions. The results of Fourier transform spectroscopy confirmed the chemical coordination between the nanoparticles obtained with the suitable functional groups of the capping materials molecules. Current-voltage measurements under illumination for polycrystalline silicon solar cells deposited by gold, silver, zinc sulfide, and silver/zinc sulfide core-shell nanoparticles were studied. Cells

deposited by the nanoparticles were found to provide enhanced photocurrent because the samples were investigated after a long time, and the samples were dried.

Summary

Summary

This thesis focused on two main purposes: (1) preparation of gold, silver, zinc sulfide, silver/zinc sulfide core-shell nanoparticles (2) investigation of the effects of incorporating the prepared samples with the solar cells

This Thesis contains Four Main Chapters as Follows:

Chapter I

This chapter contains two main sections: an exhaustive introduction to nanomaterials and a literature review. It has started with a brief history of nanomaterials. Then, it presented the introduction of nanomaterials. Some important definition of nanomaterials has been mentioned. In addition, the classification of nanomaterials according to origin, dimensionality, morphology, and composition was reviewed. Also, the two main factors that affect the properties of nanoparticles, such as quantum confinement effect and surface effect, were explained. Preparation methods of nanomaterials based on the built structure and starting state of materials were presented. Properties, importance, and some applications of nanomaterials were highlighted. Outline several previous studies related to preparing gold, silver, zinc sulfide, silver/zinc sulfide core-shell nanoparticles, and their application in the solar cell were reviewed. Aim and plan of the work are written at the end of this chapter.

Chapter II:

This chapter contains some of the underlying theoretical principles required to understand the mathematical basis of the instruments used in the characterization of our prepared nanoparticle samples. It has initiated with a short introduction to electromagnetic radiation. Then, introduce the mathematical basis of UV-Vis spectroscopy, transmission electron

microscopy, dynamic light scattering, x-ray diffraction, Fourier transform infrared spectroscopy. Moreover, solar cell generations, parameters, factors affecting their efficiency were described in detail.

Chapter III:

In this chapter, the chemicals and experimental methods used to prepare the gold, silver, zinc sulfide, and silver/zinc sulfide core-shell nanoparticles were mentioned.

Gold nanoparticles were prepared in two different methods: First method, a fixed concentration of gold chloride hydrate ($\text{HAuCl}_4 \cdot 3\text{H}_2\text{O}$) and cetyltrimethylammonium bromide (CTAB) with a change in the ratio of sodium borohydride (NaBH_4). Second method: fixed concentration of gold chloride hydrate ($\text{HAuCl}_4 \cdot 3\text{H}_2\text{O}$) and sodium borohydride (NaBH_4) with a change in the ratio of cetyltrimethylammonium bromide (CTAB).

Silver nanoparticles were prepared using a fixed concentration of cetyltrimethylammonium bromide (CTAB) (in chloroform), sodium borohydride (NaBH_4), and polyvinylpyrrolidone (PVP) with different ratios of silver nitrate (AgNO_3).

Zinc sulfide nanoparticles were prepared in two different ways (i) constant sodium sulfide (Na_2S) molar ratio and temperature with different zinc acetate dihydrate ($\text{Zn}(\text{CH}_3\text{COO})_2 \cdot 2\text{H}_2\text{O}$) molar ratios. (ii) fixed sodium sulfide (Na_2S) and zinc acetate dihydrate ($\text{Zn}(\text{CH}_3\text{COO})_2 \cdot 2\text{H}_2\text{O}$) molar ratio with different temperatures [50°-100°].

Two steps were used to prepare silver/zinc sulfide core-shell nanoparticles: first, preparation of silver nanoparticles using ascorbic acid ($\text{C}_6\text{H}_8\text{O}_6$), polyvinylpyrrolidone (PVP), sodium hydroxide (NaOH), and silver nitrate (AgNO_3). Second step: using a fixed amount of zinc acetate

dihydrate ($\text{Zn}(\text{CH}_3\text{COO})_2 \cdot 2\text{H}_2\text{O}$), ammonium nitrate (NH_4NO_3), polyvinylpyrrolidone (PVP), sodium sulfide (Na_2S), and ascorbic acid ($\text{C}_6\text{H}_8\text{O}_6$) at a different quantity of as-prepared silver nanoparticles (first step).

In addition to the above, components of the characterization technique such as UV-Visible spectroscopy, transmission electron microscopy, dynamic light scattering, x-ray diffraction, Fourier transform spectroscopy, solar cell deposition, and current-voltage equipment was also reviewed.

Chapter IV:

During this chapter, the result obtained from our present prepared samples were presented and explained, where the ultraviolet-visible spectra of gold nanoparticles were measured and discussed. The distinctive band of the surface plasmonic resonance (SPR) appeared at wavelengths 527nm, 526nm, 526nm, and 526nm for [AuNPs(S1)-AuNPs(S4)] samples, respectively. The SPR band appeared at 528 nm for all samples [AuNPs (S5)- AuNPs(S8)]. We concluded from these results that the particle sizes of AuNPs do not affect by the change of concentrations for both sodium borohydride (NaBH_4) and ammonium bromide (CTAB). However, it has an apparent effect on the full width at half maximum (FWHM) of SPR bands. Surface plasmonic resonance (SPR) bands of silver nanoparticles (AgNPs) samples was appeared at (414nm, 413nm, 415nm, 417nm, and 425nm) for the samples [AgNPs(S9)- AgNPs(S13)], respectively. These results indicated that the SPR band's position was shifted to a higher wavelength by increasing the silver nitrate concentration, which means the particle size increased. Also, FWHM was increased by increasing the silver nitrate concentration. Maybe attributed to the increase of the particle sizes by the increasing of silver ions, which leads to a decrease the number of

silver nanoparticles, but it increases the particle sizes. Absorption bands of zinc sulfide has appeared at (305 nm, 289 nm, 287 nm, 284 nm, and 283 nm) for the samples [ZnSNPs(S14)- ZnSNPs(S18)], and at (308 nm, 307 nm, 304 nm, 303 nm, and 300 nm) for the samples [ZnSNPs(S19)- ZnSNPs(S24)], respectively. The optical band gaps were calculated via Tauc's plot at (4.66 eV, 4.78 eV, 4.92 eV, and 4.93 eV for the samples [ZnSNPs(S14)- ZnSNPs(S18)], and at (4.77 eV, 4.74 eV, 4.75 eV, 4.74 eV, 4.73 eV, and 4.66 eV) for samples [ZnSNPs(S19)- ZnSNPs(S24)], respectively. Based on the quantum size effect, as the wavelength decrease, the particle size also decreases, and the band gap increased. The plasmon band position of the as-prepared silver nanoparticles AgNPs(S25) that used in core-shell preparation has appeared at 408 nm. Absorption bands of the silver/zinc sulfide core-shell nanoparticles were observed at 450 nm, 469 nm, and 498 nm for the samples [Ag/ZnS(S26)-Ag/ZnS(S28)], respectively. The broadening that occurred in the bands implying to the formation of the core-shell.

TEM images of gold nanoparticles visualize the nanoparticles spherical form with a narrow size polydispersity, except for some triangle and hexagon form that has appeared in AuNPs(S7). The particle sizes were calculated for the TEM image using ImageJ software, then the average sizes were obtained by Gaussian distribution at 7 nm, 7 nm, and 10 nm for the samples AuNPs(S3), AuNPs(S4), and AuNPs(S7), respectively. TEM images of the sample AgNPs(S10) showed that the particles were formed as a dark point with a spherical shape with an average size of 2 nm, whereas most of the silver nanoparticles of AgNPs(S11) were spherical with a random distribution with average size 4 nm. Zinc sulfide images have confirmed the preparation of ZnSNPs with a nearly spherical shape; also, it shows that TEM images have two regions, one is low distribution, and

the other is high. The average particle sizes were estimated at 5 nm, 3 nm, 3 nm, and 3 nm for ZnSNPs(S14) and ZnSNPs(S18), ZnSNPs(S19), and ZnSNPs(S22), respectively. Silver/zinc sulfide core-shell nanoparticle images reveal a different image contrast implying that a zinc sulfide shell successfully coated the surface of the silver nanoparticles. The average particle sizes were estimated at 27 nm, 81 nm, and 177 nm for Ag/ZnS(S26), Ag/ZnS(S27), and Ag/ZnS(S28), respectively.

Dynamic light scattering has also been used to estimate the average particle size of the samples. The average particle sizes were obtained at 33.03 nm, 23.46 nm, and 30.26 nm for gold nanoparticles AuNPs(S3), AuNPs(S4), and AuNPs(S7), respectively, at 87 nm and 77.68 nm for silver nanoparticles AgNPs(S10) and AgNPs(S11), at 11.74 nm, 132.9 nm, and 315.9 nm for zinc sulfide nanoparticles ZnSNPs(S14), ZnSNPs(S19), and ZnSNPs(S22), respectively, and at 39.04 nm, 127.8 nm, and 48.39 nm for silver/zinc sulfide core-shell nanoparticles Ag/ZnS(S26), Ag/ZnS(S27), and Ag/ZnS(S28), respectively. The large variation in particle size obtained by dynamic light scattering and transmission electron microscopy is logical because dynamic light scattering measures the average particle size of huge quantity comparable with the transmission electron microscopy. Besides that, TEM measure only the inorganic core of the particle, since the organic shell is less electron-dense in comparison to the inorganic core and thus transparent in TEM.

The crystalline nature of gold, silver, and zinc sulfide nanoparticles were studied using x-ray diffraction. The particle sizes were calculated using Scherrer's equation from the mean peak at 2θ around (38.45°) is 21.48 nm, 33.57 nm, and 30.74 nm for the samples [AuNPs(S1)-AuNPs(S3)], and it was at 9.94 nm, 8.25 nm, and 8.59 nm for the samples [AuNPs(S5)-

AuNPs(S7)], respectively. The mean peak of silver nanoparticles was seen at 2θ around (37.7°), and the crystal sizes calculated at 8.08 nm, 7.89 nm, 8.12 nm, 12.42 nm, and 8.23 nm for the samples [AgNPs(S9)-AgNPs(S13)], respectively. The particles size of zinc sulfide were measured at 2θ (28°) is 2.83 nm, 2.18 nm, 2.19 nm, 2.15 nm, and 2.14 nm for the samples [ZnSNPs(S14)-ZnSNPs(S18)], and the particle size is 2.83 nm, 4.04 nm, 3.97 nm, 3.92 nm, 3.76 nm, and 4.17 nm for the samples [ZnSNPs(S19)-ZnSNPs(S24)], respectively.

Fourier transform infrared results studies the chemical coordination between our nanoparticles prepared samples and the functional groups of capping materials. Gold nanoparticles obtained a band at about 1481 cm^{-1} indicating the coordination of gold nanoparticles with $C - N^+$ group in the CTAB molecule. In addition, the absorption bands appeared in the silver nanoparticles spectra at around 1346 cm^{-1} resulted from the involvement of nitrogen atom in pyrrolidine in silver nanoparticles formation. Also, the band position shift that occurs in silver nanoparticles occurred at 530 cm^{-1} , and 452 cm^{-1} indicates to the coordination between silver atom and oxygen or nitrogen atom. Furthermore, the zinc sulfide nanoparticles spectra reveal a band at about 1004 cm^{-1} and 925 cm^{-1} due to the asymmetric and symmetric $Zn - S$ vibration. Moreover, silver/zinc sulfide core-shell nanoparticles show a variation in the band position from the capping materials due to the surrounding of silver nanoparticles by zinc sulfide nanoparticles, which proved the formation of the core-shell.

The current-voltage characteristics of the polycrystalline silicon solar cell deposited by gold, silver, zinc sulfide, silver/zinc sulfide core-shell nanoparticles under illumination were investigated. The effect of the nanoparticles on the parameter of the solar cell, such as open-circuit

voltage (V_{OC}), short circuit current (I_{SC}), maximum circuit voltage (I_m), and the maximum circuit current (I_m) were measured, fill factor (FF), and power conversion efficiency (η) were calculated. Compared with the power conversion efficiency achieved for polycrystalline silicon solar cell ($\eta = 14.29\%$), cell deposited by gold nanoparticles exhibit efficiency at ($\eta = 13.65\%$ and 13.14%) for AuNPs(7 nm) and AuNPs(10 nm) , zinc sulfide at ($\eta = 12.57\%$ and 11.74%) for ZnSNPs(2.15 nm) and ZnSNPs(3.97 nm), silver/zinc sulfide core-shell nanoparticles at ($\eta = 13.02\%$) for Ag/ZnS(177 nm). From these findings, we can conclude that the nanoparticles sample does not affect the efficiencies of the solar cells, which may be attributed to the low surface coverage of the silicon solar cells by the nanoparticles leading to reduce light scattering. Moreover, the samples may require annealing at high temperatures before measurements to evaporate the water from the surface of the samples. What assured our hypothesis, photocurrent measurements show a remarkable enhancement that has examined after a long time of I-V measurements, which caused the sample to dry. The photocurrent values were estimated at 58.5, 72, 75.7, 78.4, 76.3, 76.5, and 79.4 for the samples blank (silicon solar cell), Si/AuNPs(S7), Si/AgNPs(S11), Si/ZnSNPs(S17), Si/ZnSNPs(S21), Si/[Ag/ZnS(S26)], and Si/[Ag/ZnS(S28)], respectively.

Appendices

List of Abbreviations

No.	Definition	Abbreviations
1	Langmuir-Blodgett	LB
2	Atomic Force Microscope	AFM
3	Physical Vapor Deposition	PVD
4	Chemical Vapor Deposition	CVD
5	Carbon Nanotubes	CNTs
6	Dye-Sensitized Solar Cell	DSSCs
7	Power Conversion Efficiency	PCE
8	Dimethylformamide	DMF
9	Ultraviolet-Visible	UV-Vis
10	Transmission Electron Microscope	TEM
11	High-Resolution Transmission Electron Microscope	HRTEM
12	multi-crystalline Silicon	mc-Si
13	Copper-Indium-Gallium-Diselenide	CIGS
14	Textured Silicon	T-Si
15	Nanoparticles	NPs
16	Indium Tin Oxide	ITO
17	Surface Plasmon Resonance	SPR
18	Gold Nanoparticles	AuNPs

19	Dynamic Light Scattering	DLS
20	Fourier Transform Infrared Spectroscopy	FTIR
21	X-Ray Diffraction	XRD
22	Electromagnetic	EM
23	Charge-Coupled Device	CCD
24	Highest Occupied Molecular Orbital	HOMO
25	Lowest Unoccupied Molecular Orbital	LUMO
26	Direct Current	dc
27	Air Mass	AM
28	Energy Gap	E_g
29	Gold Tri-chloride	HAuCl_3
30	Silver Nitrate	AgNO_3
31	Sodium Borohydride	NaBH_4
32	Cetyltrimethylammonium Bromide	CTAB
33	Sodium Sulfide	Na_2S
34	Zinc Acetate Dihydrate	$\text{Zn}(\text{CH}_3\text{COO})_2 \cdot 2\text{H}_2\text{O}$
35	Polyvinylpyrrolidone	PVP
36	Ascorbic Acid	$(\text{CH}(\text{OH}))_2 \cdot \text{CH}_2\text{OH}$
37	Sodium Hydroxide	NaOH
38	Ammonium Nitrate	NH_4NO_3
39	Silver Nanoparticles	AgNPs

40	Zinc Sulfide Nanoparticles	ZnSNPs
41	Silver/Zinc Sulfide Core-Shell	Ag/ZnS
42	Core-Shell Nanoparticles	CSNPs
43	Full Width at Half Maximum	FWHM
44	Zinc Oxide	ZnO
45	Titanium Dioxide	TiO ₂

List of Figures

Figure 1. 1: Eighteenth-century Damascus steel sword.	3
Figure 1. 2: Lycurgus Cup dates from the Roman empire (British Museum) (a) light reflection, (b) light transmitted	4
Figure 1. 3: A size comparison of nanoparticle with other larger-sized materials	5
Figure 1. 4: Dimensionality-based classification of nanomaterials	8
Figure 1. 5: Classification of nanostructured materials according to their morphology	9
Figure 1. 6: The schematic representation of the bottom-up and top-down approaches for the fabrication of metal oxide nanostructures.	15
Figure 1. 7: Representation of a type of thermal evaporation system. ...	17
Figure 1. 8: Schematic representation of an experimental apparatus for the growth of oxide nanostructures.	18
Figure 1. 9: CVD process.....	19
Figure 1. 10: Material synthesis by sol-gel method (a) different forms of synthesized materials; (b) sol-gel methods to synthesize different forms of materials	20
Figure 1. 11: Application of Nanoparticles	29
Figure 2. 1: sine wave representation of electromagnetic radiation.	35
Figure 2. 2: Electromagnetic spectrum regions in terms of both frequency (ν) and wavelength (λ).....	36
Figure 2. 3: Definition of Absorbance (A)	38
Figure 2. 4: The electronic transition levels.	40
Figure 2. 5: Molecular orbitals and the energy gap needed to excite the electron energy state.....	41
Figure 2. 6: Schematic of the electron gun of TEM.....	44
Figure 2. 7: An illustration of a DLS experiment.	49
Figure 2. 8: Geometry for the interface of a wave scattered from two planes separated by a spacing, d . The dashed lines are parallel to the crest or troughs of the incident and diffracted wavefronts. The total length difference for the two rays is the sum of the two dark segments.	52
Figure 2. 9: Infrared spectroscopy regions.	56

Figure 2. 10: Possible physical processes following the absorption of a photon.	56
Figure 2. 11: Six different ways in which molecular bonds can vibrate.	57
Figure 2. 12: Relationship between molecular energy level and absorption band.	59
Figure 2. 13: Potential energy diagrams (a) harmonic oscillator or energy curve for a vibrating spring (b) and energy-constrained to quantum mechanical model curve 1 harmonic oscillator, curve 2 anharmonic motion.	62
Figure 2. 14: (a) Solar spectrum at different air-mass conditions. (b) Solar spectrum in photon flux density per photon energy for AM0 and AM1.5 conditions.	66
Figure 2. 15: Idealized equivalent circuit of the solar cell under illumination.	66
Figure 2. 16: I-V characteristics of the solar cell under dark and illumination.	68
Figure 2. 17: I–V characteristics of an illuminated solar cell.	69
Figure 3. 1: Chemical structure of Gold (III) chloride trihydrate $\text{HAuCl}_4 \cdot 3\text{H}_2\text{O}$	72
Figure 3. 2: Chemical structure of silver nitrate (AgNO_3).	72
Figure 3. 3: Chemical structure of sodium borohydride (NaBH_4).	73
Figure 3. 4: Chemical structure of cetyltrimethylammonium bromide (CTAB).	73
Figure 3. 5: Chemical structure of sodium sulfide Na_2S	73
Figure 3. 6: Chemical structure of zinc acetate.	74
Figure 3. 7: Chemical structure of polyvinylpyrrolidone (PVP).	74
Figure 3. 8: Chemical structure of chloroform.	74
Figure 3. 9: Chemical structure of ascorbic acid.	75
Figure 3. 10: Chemical structure of sodium hydroxide NaOH	75
Figure 3. 11: Chemical structure of ammonium nitrate.	75
Figure 3. 12: Schematic representation of gold nanoparticles preparation [AuNPs(S1)-AuNPs(S4)].	77
Figure 3. 13: Schematic representation of gold nanoparticles preparation [AuNPs(S5)-AuNPs(S8)].	79
Figure 3. 14: Schematic representation of silver nanoparticles preparation [AgNPs(S9)-AgNPs(S13)].	81

Figure 3. 15: Schematic representation of zinc sulfide nanoparticles preparation [ZnSNPs(S14)-ZnSNPs(S18)].	83
Figure 3. 16: Schematic representation of zinc sulfide nanoparticles preparation [ZnSNPs(S19)-ZnSNPs(S20)].	85
Figure 3. 17: Schematic representation of silver nanoparticles preparation capped by polyvinylpyrrolidone AgNPs(S25).	86
Figure 3. 18: Schematic representation of silver/zinc sulfide core-shell nanoparticles preparation [Ag/ZnS(S26)-Ag/ZnS(S28)].	87
Figure 3. 19: Vacuum spin coater.	88
Figure 3. 20: UV-Vis spectrometer instrument model (Evolution 220).	89
Figure 3. 21: Schematic representation of a UV spectrometer for liquid samples.	90
Figure 3. 22: JEOL Transmission Electron Microscope model (JEM – 1400) with LaB ₆ cathode, the maximum voltage is 120 kV, the resolution is 0.2 nm, and the maximum magnification is 1200000X.	91
Figure 3. 23: Basic component of TEM.	92
Figure 3. 24: Cathode and anode of TEM.	94
Figure 3. 25: Schematic diagrams of (a) a side-entry and (b) a top-entry specimen holder .	95
Figure 3. 26: Copper grid.	98
Figure 3. 27: Dynamic light scattering (DLS) instrument.	99
Figure 3. 28: Schematic representation of a speckle pattern.	99
Figure 3. 29: The observed signal depends on the phase addition of the scattered light falling on the detector. (A) two beams interfere and cancel each other out, resulting in a decreased intensity detected. (B) two beams interfere and enhance each other resulting in an increased intensity detected..	100
Figure 3. 30: Intensity fluctuations for large and small particles.	101
Figure 3. 31: Optical configuration of the Zetasizer Nano series for dynamic light scattering measurements	102
Figure 3. 32: Schematic diagram showing the measurement position for (a) small, weakly scattering samples and for (b) large, concentrated, and opaque samples. The change in measurement position achieved by moving the focusing lens accordingly .	103
Figure 3. 33: SmarLab SEX-Ray diffraction instrument.	104
Figure 3. 34: FT-IR instrument.	106
Figure 3. 35: Principle of the Fourier transform spectrometer.	106

Figure 3. 36: Basic component of an FT-IR spectrometer, including the light source, the detector, and a Michelson interferometer consisting of a beam splitter, a fixed mirror, and a moving mirror.	108
Figure 3. 37: The main spectroscopic methods used to characterize the molecular composition and stress response by FT-IR spectroscopy: (a) transmittance FT-IR; (b) diffuse reflectance FT-IR; (c) attenuated total reflectance (ATR) FT-IR . IR measurement samples can be prepared in several ways. For liquids, a drop of sample sandwiched between two salt plates, Such as NaCl and stove-dried before being measured	110
Figure 3. 38: The preparation of a KBr for IR spectroscopy.....	110
Figure 3. 39: I-V curve instrument.	111
Figure 4. 1: UV-Vis absorbance spectra of AuNPs using CTAB as a stabilizing agent and at different concentration of NaBH ₄ as a reducing agent.	114
Figure 4. 2: Surface plasmon resonance of metal nanoparticle.	115
Figure 4. 3: UV-Vis absorption spectrums of gold nanoparticles synthesized by reduction HAuCl ₄ .3H ₂ O using NaBH ₄ and stabilize it by different concentrations of CTAB [AuNPs(S5) 0.2gm, AuNPs(S6) 0.3gm, AuNPs(S7) 0.4gm, AuNPs(S8) 0.5gm].	116
Figure 4. 4: UV-Vis spectra of the silver nanoparticle samples prepared by diluted a different silver nitrate AgNO ₃ (1M) concentrations [AgNP(S9):1.5ml, AgNP(S10):2ml, AgNP(S11):2.5ml, AgNP(S12):3ml, AgNP(S13):3.5ml] in (0.1M) chloroform (first solution), and diluted a 0.8ml of (1M) NaBH ₄ in (0.1M) chloroform (second solution). Mixed these two solutions and add 0.4 ml of (0.5%) PVP during the ultrasonication.	117
Figure 4. 5: Change of surface plasmon band position with silver nitrate concentrations.	118
Figure 4. 6: UV-Vis absorbance spectra of the zinc sulfide nanoparticle prepared by adding 50 ml of sodium sulfide (0.2M) and 50 ml of zinc acetate dihydrate at different concentrations	

	[ZnSNPs(S14) 0.1M, ZnSNPs(S15) 0.2M, ZnSNPs(S16) 0.3M, ZnSNPs(S17) 0.4M, ZnSNPs(S18) 0.5M].....	120
Figure 4. 7:	Plasmon band position of ZnSNPs as a function of zinc acetate dihydrate molar ratio.	120
Figure 4. 8:	Tauc's Plot of ZnSNPs prepared at a different molar ratio of zinc acetate dihydrate [(ZnSNPs(S14)-ZnSNPs(S18))].	121
Figure 4. 9:	UV-Vis absorbance spectra of the zinc sulfide nanoparticle prepared by adding an equivalent quantity of sodium sulfide (0.2M) and zinc acetate dihydrate (0.1M) at different temperatures [ZnSNPs(S19) 50°C, ZnSNPs(S20) 60°C, ZnSNPs(S21) 70°C, ZnSNPs(S22) 80°C, ZnSNPs(S23) 90°C, ZnSNPs(S24) 100°C].....	122
Figure 4. 10:	Band position of ZnSNPs as a function of temperature. .	123
Figure 4. 11:	Tauc's Plot of ZnSNPs prepared at different temperatures [ZnSNPs(S19)-ZnSNPs(S24)].	124
Figure 4. 12:	UV-Vis absorbance spectra of Ag/ZnS (CSNPs) prepared at a different molar ratio of AgNPs(S25). Ag/ZnS(S26) [70 ml], Ag/ZnS(S27) [80 ml], and Ag/ZnS(S28) [90 ml]. .	126
Figure 4. 13:	Plasmon band position of Ag/ZnS (CSNPs) as a function of the Ag colloid ratio.....	126
Figure 4. 14:	(a,c) TEM images of AuNPs(S3) and AuNPs(S4) that prepared at different concentrations of NaBH ₄ and (b,d) histogram of the Gaussian size distribution.	128
Figure 4. 15:	(a) TEM image of AuNPs(S7) synthesized using CTAB and (b) the count of particles as a function of different particle sizes.	129
Figure 4. 16:	(a,c) TEM images of AgNPs(S10), and AgNPs(S11) prepared by reverse micelle method at different concentrations of AgNO ₃ and (b,d) the Gaussian size distribution.	130
Figure 4. 17:	(a,c) TEM images of Zinc Sulfide Nanoparticle ZnSNPs(S14), ZnSNPs(S18), and (b,d) their gaussian distribution.	131
Figure 4. 18:	(a,c) TEM images of zinc sulfide nanoparticle synthesized at different temperature ZnSNPs(S19) at (T=50°) and ZnSNPs(S22) at (T= 80°), and (b,d) Gaussian distribution of each sample.....	132
Figure 4. 19:	TEM images of silver/zinc sulfide core-shell nanoparticle ZnSNPs(S26), ZnSNPs(S27), and ZnSNPs(S28)	

	synthesized at a different quantity of AgNPs, and their Gaussian distribution.....	134
Figure 4. 20:	Hydrodynamic size distributions of AuNPs(S3) and AuNPs(S4) that synthesized at different concentrations of NaBH ₄	136
Figure 4. 21:	Hydrodynamic size distributions of AuNPs(S7) synthesized using CTAB as a surfactant.	137
Figure 4. 22:	Hydrodynamic size distributions of AgNPs(S10) and AgNPs(S11) that synthesized at different concentrations of AgNO ₃	138
Figure 4. 23:	Hydrodynamic size distributions of ZnSNPs(S14) that synthesized at (0.1M) of zinc acetate dihydrate.	138
Figure 4. 24:	Hydrodynamic size distributions of ZnSNPs(S19) and ZnSNPs(S22) that synthesized at different temperatures.	139
Figure 4. 25:	Hydrodynamic size distributions of Ag/ZnS(S26), Ag/ZnS(S27), and Ag/ZnS(S28) that synthesized at different quantities of AgNPs(S25).	140
Figure 4. 26:	XRD pattern of gold nanoparticle prepared at different concentrations of sodium borohydride AuNPs(S1): 0.1 ml NaBH ₄ , AuNPs(S2): 0.5 ml NaBH ₄ , and AuNPs(S3): 0.75 ml NaBH ₄	142
Figure 4. 27:	XRD pattern gold nanoparticle prepared at different CTAB concentrations.	143
Figure 4. 28:	XRD pattern of silver nanoparticles prepared at different concentrations of silver nitrate.....	145
Figure 4. 29:	XRD pattern of zinc sulfide nanoparticle prepared at different concentrations of zinc acetate dihydrate.	146
Figure 4. 30:	XRD pattern of zinc sulfide nanoparticle prepared at different temperatures.....	148
Figure 4. 31:	FT-IR spectra of (a) gold nanoparticle prepared at different concentrations of sodium borohydride and (b) gold nanoparticle prepared at different CTAB concentrations.	151
Figure 4. 32:	AgNPs coordinated with nitrogen and oxygen atom.	154
Figure 4. 33:	FT-IR spectra of silver nanoparticle prepared at different concentrations of silver nitrate.....	155
Figure 4. 34:	FT-IR spectra of zinc sulfide nanoparticle prepared at different concentrations of zinc acetate dihydrate.	158

Figure 4. 35: FT-IR spectra of zinc sulfide nanoparticle prepared at different temperatures.....	159
Figure 4. 36: FT-IR spectra of silver nanoparticle \ zinc sulfide core-shell nanoparticles.	161
Figure 4. 37: I-V of characteristics curves of the polycrystalline silicon solar cell and polycrystalline silicon solar cell deposited by AuNPs(7 nm) and AuNPs(10 nm) under illumination. .	164
Figure 4. 38: I-V of characteristics curves of the polycrystalline silicon solar cell, and it is covered by ZnSNPs(2.15 nm) and ZnSNPs(3.97 nm) under illumination.....	166
Figure 4. 39: I-V of characteristics curves of the polycrystalline silicon solar cell and polycrystalline silicon solar cell deposited by Ag/ZnS(177 nm) under illumination.	168

List of Tables

Table 3. 1	Preparation of gold nanoparticle samples [AuNPs(S1)-AuNPs(S4)] at different concentrations of sodium borohydride under heating continuously at 70°C.	77
Table 3. 2	Preparation of gold nanoparticle samples [AuNPs(S5)-AuNPs(S8)] at different concentrations of CTAB under heating at 70°C.....	79
Table 3. 3	Preparation of silver nanoparticle samples [AgNPs(S9)-AgNPs(S13)] at different AgNO ₃ concentration.....	81
Table 3. 4	Preparation of ZnS NPs at different concentrations of zinc acetate dihydrate.	83
Table 3. 5	Preparation of ZnS NPs at different temperatures	85
Table 3. 6	Preparation of AgNPs/ZnS CSNPs	88
Table 4. 1	Peaks position, full width at half maximum (FWHM), and crystallite size of gold nanoparticle prepared at different concentrations of sodium borohydride.....	142
Table 4. 2	Peaks position, full width at half maximum (FWHM), and crystallite size of gold nanoparticle prepared at different CTAB concentrations.....	144
Table 4. 3	Peaks position, full width at half maximum (FWHM), and crystallite size of silver nanoparticle prepared at different concentrations of silver nitrate.	145
Table 4. 4	Peaks position, full width at half maximum (FWHM), and crystallite size of zinc sulfide nanoparticle prepared at different concentrations of zinc acetate dihydrate.....	147
Table 4. 5	Peaks position, full width at half maximum (FWHM), and crystallite size of zinc sulfide nanoparticle prepared at different temperatures.	148
Table 4. 6	FT-IR bands and their assignments of AuNPs prepared at different concentrations of NaBH ₄	152
Table 4. 7	FT-IR band positions of AuNPs capped by different concentrations of CTAB.....	152
Table 4. 8	FT-IR band positions of AgNPs prepared at different concentrations of AgNO ₃	156
Table 4. 9	FT-IR band positions of ZnSNPs prepared at different concentrations of zinc acetate dihydrate.	158

Table 4. 10	FT-IR band positions of ZnSNPs prepared at different temperatures and their assignments.	160
Table 4. 11	FT-IR bands and their assignments of PVP and Ag/ZnS capped by PVP.	162
Table 4. 12	Performance parameters of polycrystalline silicon solar cell and polycrystalline silicon solar cell deposited by AuNPs(7 nm) and AuNPs(10 nm).	165
Table 4. 13	Performance parameters of polycrystalline silicon solar cell and polycrystalline silicon solar cell deposited by ZnSNPs(2.15 nm) and ZnSNPs(3.97 nm).	167
Table 4. 14	Performance parameters of polycrystalline silicon solar cell and polycrystalline silicon solar cell deposited by Ag/ZnS(177 nm).	169
Table 4. 15	Photocurrent Values.	170

CHAPTER I

General Introduction and Literature Review

CHAPTER I

GENERAL INTRODUCTION AND LITERATURE REVIEW

1.1 History of Nanomaterials

Civilizations are defined by the Stone Age, Bronze Age, Iron Age, and silicon Age due to the materials used in that period of Age. From past decades, materials have been of great interest to humans [1]. Now, Civilizations named the nanoworld and nanotechnology Age. We now live in the era of nanotechnology, and the words with prefix “nano-” have been used every day [2]. The nanoworld is not new because the human body includes protein such as hemoglobin, which carries oxygen through the bloodstream, is 5 nm in diameter [3]. However, it is interesting to know that nanotechnology was being used at least 400 years before it became the scientific buzzword of the twenty-first century. Damascus blades, as shown in Figure 1.1, were first manufactured in the Near East by using ingots of wootz steel. These ‘Damascus blades’ were strong but flexible enough to bend from hilt to tip. The secret was revealed after they dissolved part of the weapon in hydrochloric acid and studied it under an electron microscope. Interestingly, they observed that the sword contained carbon nanotubes; each one is half a nanometer larger than the other. These carbon nanotubes were cylindrical and hexagonally arranged. It was among the strongest materials with high elasticity and tensile strength. This structure helped blacksmiths to create the strongest weapon [4]. In 1990, the researcher noted that the light transmitted from the famous Lycurgus Cup, which placed in Rome, has a dichroism property, as shown in Figure 1.2. After analyzing the Cup by SEM, it was found that silver, gold, and copper impeded the Cup in nanosized range. The dichroism was affected by particle size. The light transmitted from the Cup appears as a red, and light

reflection appears as a green [5]. Also, lustered pottery shows shining surfaces with unique optical properties after doped by nanomaterials. The beautiful iridescent reflections of various colors obtained as the studies say from a thin metallic film containing silver, copper, iron oxide in nanoscales [6].



Figure 1. 1: Eighteenth-century Damascus steel sword.

1.2 Introduction of Nanomaterials

At the annual meeting of the American Physical Society On 29 December 1959, Nobel laureate Richard P Feynman opened up a whole new field, known as 'nanotechnology,' begin with his classic lecture titled "There is plenty of room at the bottom" not just "There is Room at the Bottom." He mentions controlling and manipulating things on a small scale. However, the research community took approximately three decades to apply his vision to reality. What Feynman realized was that "at the atomic level, we have new kinds of forces, new kinds of possibilities, and new kinds of effects [7-9]. Nanoworld was defined from the last century, and scientists consider nanotechnology as the revolutionary technology of the twenty-first century [3]. Unique properties of nanomaterials recognize due to ultrafine particle sizes [4]. In the 1960s and 1970s, Irving Langmuir and Katherine Blodgett made Langmuir-Blodgett (LB) films with extremely high periodicity in nanometer-scale [2]. The atomic force microscope (AFM) was invented by Calvin Quate and Christoph Gerber in 1982 [10].

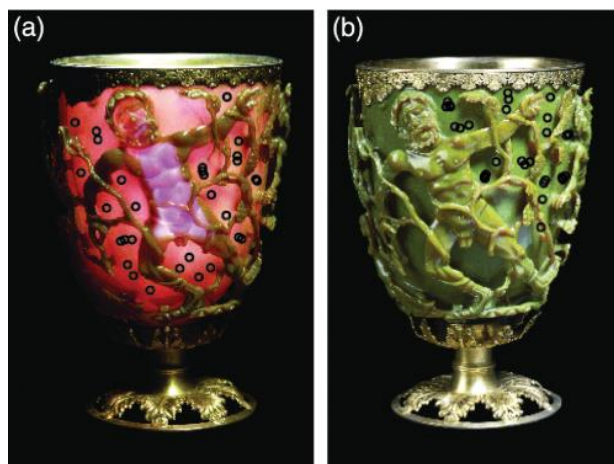


Figure 1. 2: *Lycurgus Cup* dates from the Roman empire (British Museum) (a) light reflection, (b) light transmitted [5].

In 1985, fullerene, shaped like a ball and just 1 nm in diameter, was discovered by Kroto et al. [11]. Nano revolution started when scanning tunneling microscopy was invented by Binnig and Rohrer (They received the Nobel Prize in Physics in 1986) in the mid-1980s [12]. Layered structure with the thickness of each layer in the nanometer range can be produced using molecular beam epitaxy [2]. In 1986, Eric Drexler built molecular machines and predicted the tremendous impact that would happen in nanotechnologies [13]. In 1991, Sumio Iijima discovered carbon nanotubes, which are tube-shaped materials whose diameter measures on the nanometer scale [14]. In 1995, SY. Chou and coworkers proposed the nanoimprint lithography [15]. In 1996, Sasaki discovered nanosheets and the investigation of nanosheets in photocatalytic activity [3]. Nanotechnology, with tools to create functional and intelligent nanomaterials, devices, and systems by controlling materials in the nanoscale, provides new physical, chemical, and biological properties of these nanomaterials [7]. Figure 1.3 compared a nanoparticle size with larger sized materials.

1.3 Important Definition

1.3.1 Nanomaterials

Nanomaterials can define as:

- (1) Nanomaterials are chemical substances or materials that are produced or used at a nanomaterials scale [3].
- (2) Material with any external dimension in the nanoscale (size range from approximately 1 to 100 nm) or having internal or surface structure in the nanoscale [16].
- (3) Natural, incidental or manufactured material containing particles, in an unbound state or as an aggregate or as an agglomerate and where for 50 % or more of the particles in the number size distribution have one or more external dimensions is in size range 1–100 nm [17].

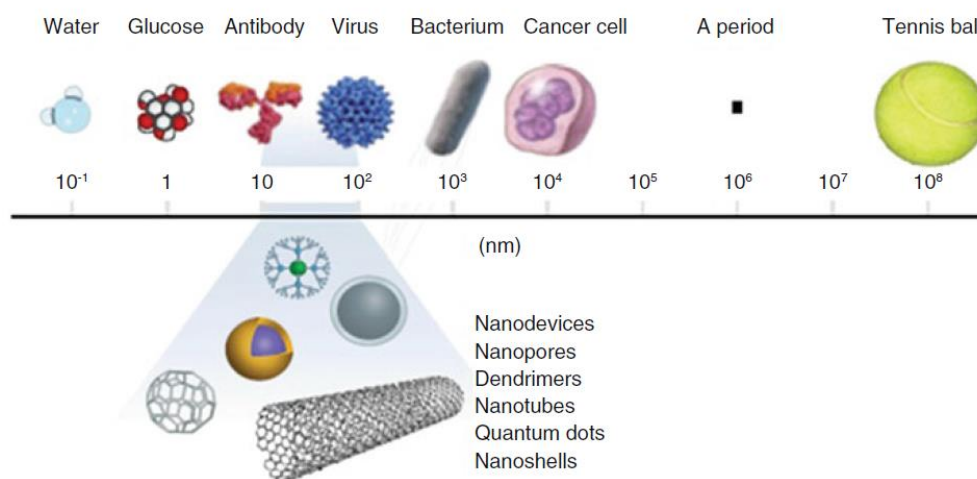


Figure 1. 3: A size comparison of nanoparticle with other larger-sized materials [3].

1.3.2 Nanotechnology

Nanotechnology means the understanding and control of matter at dimensions of roughly 1 to 100 nm, where phenomena enable novel applications [7]. Also, Nanotechnology can be defined as the systematic study and application of materials that have properties critically dependent on length scales on the order of nanometers [3].

1.3.3 Nanoscience

Nanoscience can be defined as:

- Study of nanoscale materials and the study of the remarkable properties and phenomena associated with nanoscale materials.
- Study the properties and phenomena of materials that are a function of size and size alone.
- Study the nanoscale materials that exhibit remarkable properties, functionality, and phenomena due to the influence of small dimensions and shapes [18].

1.4 Classification of Nanomaterials

Nanomaterials can be classified according to their origin (natural and synthetic). Also, It can be classified by it is dimensionality, morphology, composition, uniformity, and agglomeration state [3, 19]

1.4.1 Based on Origin: Classification of nanomaterials, according to their origin, can be divided into two types

1. Naturally (Non-intentionally made nanomaterials), which refers to nano-sized particles or nanomaterials that belong naturally in the environment (e.g., proteins, viruses, nanoparticles produced during volcanic eruptions, . . .etc.) or that are produced by human activity without intention (e.g., nanoparticles produced from diesel combustion).
2. Synthetic nanomaterials, which refer to nanomaterials produced deliberately through a defined fabrication process [20].

1.4.2 Based on Dimensionality

Nanomaterials with structural features at the nanoscale can be found in different forms [3]. From the point of view, the dimensionality of nanomaterials can be classified into four categories as shown in Figure 1.4 within the nanoscale as follows: [19]

1.4.2.1 Zero-Dimensional (0-D)

Nanomaterials with all external dimensions at the nanoscale between 1 and 100 nm. This includes quantum dots [21] atom clusters [22]. They are crystalline clusters that have a few hundred to a few thousand atoms, and their three dimensions in the range of 2 to 100 nm [3].

1.4.2.2 One-Dimensional (1-D)

The second class of nanoscale materials, referred to as 1-D nanostructures, is reserved for those materials that have two external dimensions at the nanoscale, the third one being usually at the microscale. It includes nanowires, nanorods, nanofibers, and nanotubes [21]. This class of nanomaterials used in laser, nanoelectronics, solar cells, resonators, and high sensitivity sensors [3].

1.4.2.3 Two-Dimensional (2-D)

Materials with one dimension in the nanoscale and the other two-dimension in the microscale like thin films or surface coatings [19]. They are mostly used in physics and electronics, for example, to manufacture electronic components with insulating or conductive surface properties or to change the optical reflectivity of surfaces [21].

1.4.2.4 Three-Dimensional (3-D)

The last dimensional category of nanomaterials 3-D nanomaterials it displays internal nanoscale features but no external dimension at the nanoscale [21]. However, these materials possess a nanocrystalline structure or involve the presence of features at the nanoscale (e.g., magnetic tunnel junctions, heterostructures, . . .etc.). They can be composed of multiple arrangements of nanosize crystals, most typically in different orientations [3]. For example, nanocomposites and nanostructured materials [21].

Classification of nanoparticles based on dimension

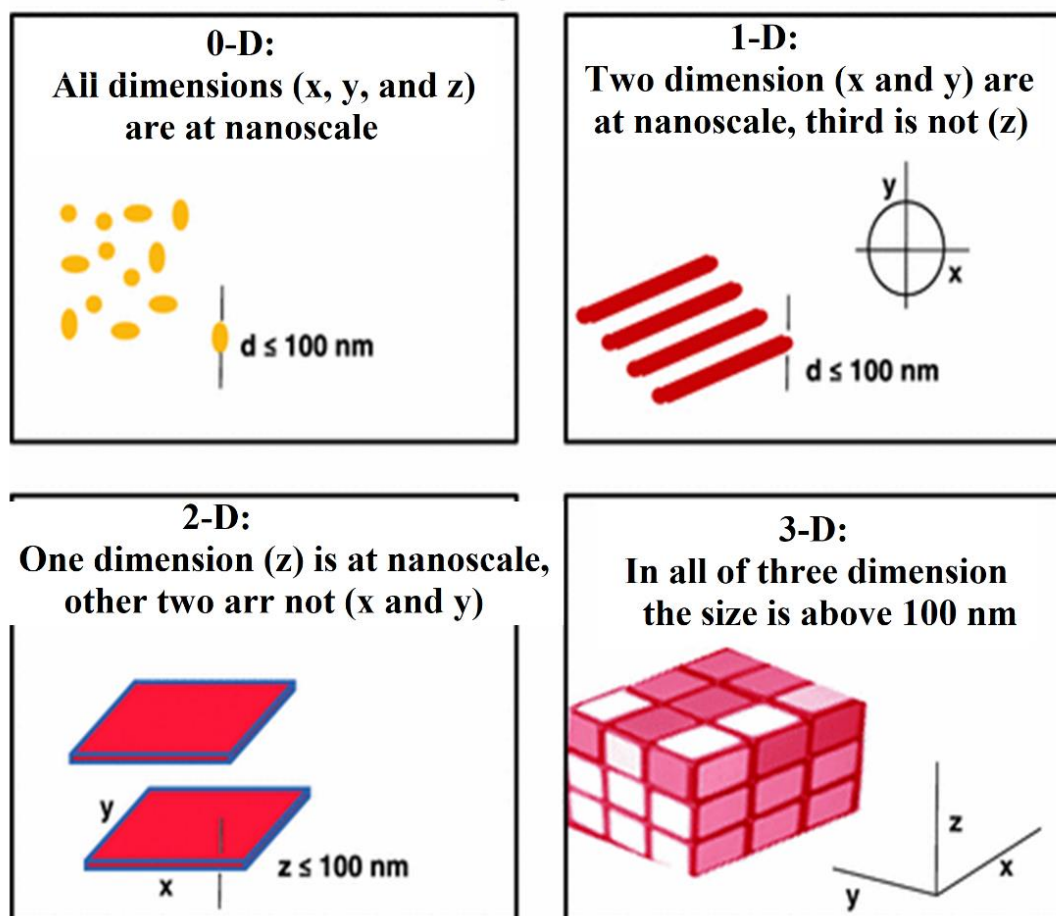


Figure 1. 4: Dimensionality-based classification of nanomaterials [21].

1.4.3 Based on Morphology

Nanomaterials that can be classified according to their morphology had divided into high and low aspect ratio particles, as shown in Figure 1.5. The high aspect ratio nanoparticles can have different shapes, such as nanowires, nanozigzags, nanohelices, nanopillars, nanotubes, or nanobelts. The low aspect ratio nanoparticles can have many shapes as well, such as helical, spherical, pillar-like, cubes, pyramidal, among others [19].

1.4.4 Based on Composition

Based on their chemical composition, nanoparticles can be classified into various categories, Metal-based materials are mainly composed of metals (e.g., gold, silver, and copper nanoparticles). Metal oxide nanomaterials are made of metal and oxygen, such as silica, Titania, and alumina... etc. [18]. Also, the nanomaterials can be classified according to shape, uniformity, distribution, and agglomeration state [19].

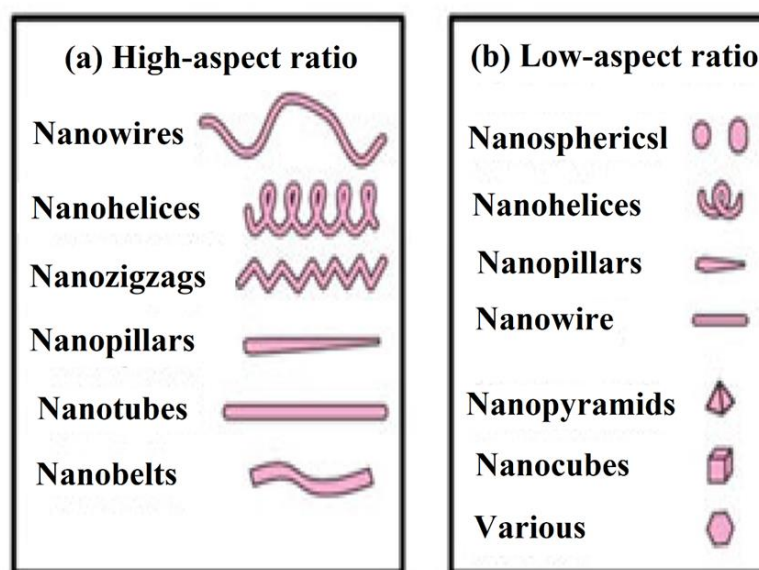


Figure 1. 5: Classification of nanostructured materials according to their morphology [19].

1.5 Factors Affecting the Nanomaterials

The physical and chemical properties of matter changed at the nanoscale. It can be quite different from those of larger particles of the same substance [23]. Quantum mechanics can be used to explain the behavior of the movement of the electron in nanoscale [24].

1.5.1 Confinement Effect

Quantum size effects play a crucial role in determining the physical and chemical properties in nanomaterials and related to the "dimensionality" of a system. This effect occurs in the case where the size of the system is

commensurable with the de-Broglie wavelength of the electron, phonons, or excitons propagating in them [25]. The nanograin behaves like a kind of box, within which a specific property may or may not exist. Confinement effect appears at one particular critical size, characteristics of the property directly, and strictly depends on the grain size [26].

1.5.2 Surface Effects

The Fraction of Atoms at The Surface: The surface area is an important parameter and plays a significant role in the interaction of nanomaterials with the exterior [27]. Atoms at surfaces have less than neighbors' atoms in bulk [28]. The smaller a particle, the more substantial the fraction of atoms at the surface, and the higher the average binding energy per atom. The surface-to-volume ratio scales with the inverse size. Numerous properties obey the same scaling law. Corner and edge atoms have even lower coordination and bind foreign atoms and molecules more tightly [29]. Decreasing the size of the nanoparticle leads to an exponential increase in surface area relative to volume, resulting in an enhanced reactivity [19].

Surface Structure Changes: The effect of size reduction is not without consequences for the atomic arrangement and the physical properties of materials. If the structure of the outer region of a particle is affected by the range of the particle size, a surface layer cannot be defined accurately. It is known that the composition or the crystal structure is modified at the free surface of the material. The volume of this surface layer becomes significant in nanoscale materials. The surface layer of nanoparticles, in that case, can be defined as the outer region where the composition or the crystal structure is different from those of the particle core. The clean surface of crystalline materials relaxes and reconstructs in order to minimize the total Gibbs energy, given the new chemical environment of the semi-infinite crystal [30].

1.5.3 Effect of Surface to Volume Ratio on The Physical Properties

Let us now consider the effects of the increase in the surface-to-volume ratio as the object size decreases. The increase of the surface to volume ratio of particles causes lower melting temperatures, lower magnetization, changes in catalytic activity, etc... A large number of atoms on the surface significantly increase “surface activity” that is very favorable for chemical reactions. However, due to increased activity, nanoparticles tend to form aggregates and agglomerates that could cause loss of preferred characteristics. Therefore, it is necessary to stabilize particles with some additional treatment. For example, it is possible to put particles in an adequate matrix or to coat them with a different material even though their characteristics change with this kind of surface modification. The coordination number of atoms on the surface is lower than the one for the atoms inside the particle, which would cause an increase in the surface energy. Therefore, the diffusion of atoms can take place at lower temperatures. For instance, the melting point of gold is 1063 °C, while nanoparticles of gold with particle diameters under 5 nm have the melting point of ≈ 300 °C. Decreasing the particle size has a significant influence on firmness and hardness of materials. The firmness of copper crystallite with different sizes have been increasing as the crystallite size decreases. The firmness of the copper samples with 50 nm size crystallites is 2 times higher, while in the copper samples with 10 nm size crystallites, it is 6 times higher than for the bulk. The elasticity limit of copper increases 2 times when crystallites decrease in size from 100 μm to 10 μm . One of the characteristics specific to nanomaterials is super elasticity. As opposed to bulk materials, nanomaterials can withstand the tension beyond the point of fracture. Super elasticity is explained by diffusion of atoms, i.e., moving of dislocations and sliding of the boundaries between particles [31].

1.5.4 Size Effects on Structure and Morphology of Free or Supported Nanoparticles

In the bulk properties of the material, the surface atoms comprise a negligible proportion of the total number of atoms and will, therefore, play a negligible role of the material. When the size of the object is reduced to the nanometric range, i.e., < 10 nm, the proportion of surface atoms is no longer negligible. Hence, at 5 nm (around 8,000 atoms), this proportion is about 20%, whilst at 2 nm (around 500 atoms), it stands at 50%. This proportion can be estimated for the transition metals by the relation

$$\frac{N_s}{N_v} \approx \frac{1}{2R} \quad (1.1)$$

Where R is the radius in nm, N_s is the number of the surface atom, and N_v is the volume atom, this empirical law gives a proportion of surface atoms of 100% for a size of 1 nm. Of course, Eq. (1.1) is no longer valid for smaller dimensions. We shall see the fact that a large fraction of the atoms are located at the surface of the object will modify its properties. To tackle this question, we shall need to review certain physical quantities associated with surfaces, namely the specific surface energy and surface stress [32].

1.5.5 Composition and Surface Composition of Nanomaterials

Nanoparticles can be made of a single material or composite materials. Many nanoparticles will oxidize in the presence of air and form a thin film at their surface. Nowadays, nanoparticles comprising different composite materials are easily fabricated using a physical vapor deposition process at grazing incidence over a nanoseeded pattern, involving the manipulation of substrate motion and temperature. This technique of deposition at a glancing angle incidence can be used to manipulate the morphology of single materials as well. They are often called encapsulated or core-shell nanoparticles. One can notice core-shells composite nanoparticles. Nanocomposites can be fabricated in the most unusual shapes, such as core-shell nanocubes. Crystalline structure is of paramount importance in

determining a nanoparticle's mechanical, chemical, and physical properties. The same material in a different crystalline form can have very different properties and applications. Nanoparticles can now be fabricated in almost any shape and containing various combinations of composites materials. Demonstrate nanoparticles with complex three-dimensional morphologies comprising a variety of different functional materials. Nanoparticles with different morphologies have been demonstrated, such as nanorods, nanohooks, nanozigzags, nanostars, nanohelices, nanocubes, and nanoplates. Nanoparticles can be insoluble or repelling water. Many of the engineered nanoparticles are hydrophobic and do not form stable suspensions in aqueous media. They are nanoparticles made of metals and their compounds. In order to improve their dispersibility via electrostatic repulsion, nanoparticles can be coated with different substances. For example, gold nanoparticles can be functionalized with citrate groups, while multi-walled carbon nanotubes are usually functionalized via a selective breaking of C = C bonds achieved through oxidation [33, 34].

1.6 Fabrication of Nanomaterials

The nanomaterial is an interdisciplinary field covering physics, biology, chemistry, materials science, and engineering [35]. The fabrication is a formidable challenge and the subject of many studies. Many techniques have been developed for the fabrication of nanoparticles [36]. The synthesis of nanomaterials and nanodevices can accommodate solid, liquid, and/or gaseous precursor materials [37].

1.6.1 Preparation of Nanoparticle-Based on Built Structures

The most popular way of classifying the synthesis routes and such an approach leads to two routes; top-down and bottom-up, as shown in Figure (1.6) [1]:

1.6.1.1 Top-Down Route

The Top-Down method, as shown in Figure 1.6, is suitable for large scale (bulk material), and it is reduced to nanoscale objects by mechanical, chemical, or physical methods [21]. This technique begins with a suitable starting material and then sculpts the functionality from the material [37]. The top-down approach starts with microsystems and miniaturizes them through carving, crushing, or grinding methods [3].

1.6.1.2 Bottom-Up Route

The bottom-up process consists of nucleation and growth of atoms from a stable dispersion into nanoparticles by changing external parameters [21]. Alternatively, individual atoms and molecules are brought together or self-assembled to form nanostructured materials in at least one dimension. These techniques start with liquid and gas as the starting material falls into this category [1]. Bottom-up methods mimic nature by starting at the atomic or molecular level and building up through nucleation and/or growth from liquid or gas precursors by chemical reactions or physical processes. More typically, large numbers of atoms, molecules, or particles are used or created by chemical synthesis, and then arranged through naturally occurring processes into the desired structure [3]. This technique has been used extensively in the formation of structural composite materials [37]. Furthermore, it is currently the most common synthesis route for the industrial production of nanomaterials [38].

1.7 Preparation of Nanoparticle-Based on The Starting State of Material

Physical vapor deposition (PVD) and chemical vapor deposition (CVD) and variants of these techniques (vapor condensation) use the gaseous state of matter as the starting material for synthesizing nanoparticles. Techniques such as sol-gel, chemical, and electrochemical (electrolytic) deposition and rapid solidification processing use liquids as the starting

material. Severe plastic deformation processes such as high-energy ball milling, nano-lithography, start with solids for synthesizing nanocrystalline materials [1].

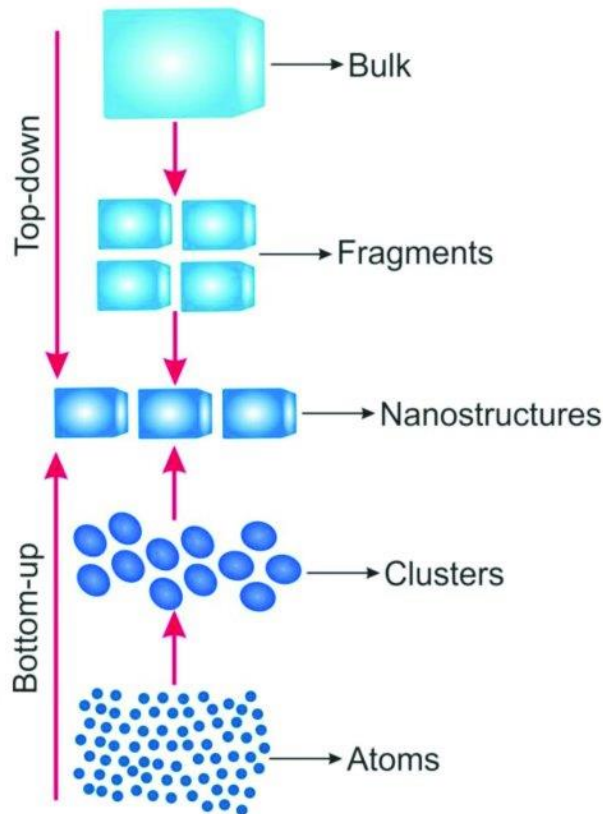


Figure 1. 6: The schematic representation of the bottom-up and top-down approaches for the fabrication of metal oxide nanostructures.

1.7.1 Physical Vapor Deposition (PVD)

PVD is a versatile synthesis method and can prepare thin-film materials with control at the nanometer scale by monitoring of the processing conditions [39]. It involves the generation of vapor phase either via sputtering, evaporation, Pulsed laser deposition (laser ablation), or by using an ion beam [40]. In a PVD process, the material to be deposited placed in an energetic environment. This environment evaporates the source material in the forms of particles such as molecules and ions. The escaping particles directed towards the surface of a substrate. This substrate surface draws

energy from these particles as they arrive, allowing them to form nucleation sites or thin layers. The whole system kept in a vacuum chamber, which allows the particles to travel as freely as possible, arriving on the surface with high energy promoting adhesion. The vacuum also helps a thin film deposition free from contaminant's interferences [7].

Evaporation is one of the most common methods of thin film deposition. Although it is one of the oldest physical techniques, it is still widely used in the laboratory and industry. As shown in Figure (1.7), in this process, a vapor is generated by evaporating or subliming a source material, which is subsequently condensed as a solid film on a substrate. A broad range of materials, with different reactivity and vapor pressures, can be used in this technique. Also, a broad diversity of source components such as resistance-heated filaments, electron beams, crucibles heated by conduction, radiation, RF-induction, arcs, exploding wires, and lasers can be employed. The following details of some of the most commonly used evaporation techniques [7].

Thermal evaporation in thermal evaporation, the target material is melted and evaporated or sublimed using an electric resistance heater. In this process, the vapor pressure in the chamber (Fig.1.7) is raised from the initially slight pressure to one that allows the material to be deposited on the substrate.

This initial high vacuum is necessary because it allows the vapor to reach the substrate without reacting with or scattering by other atoms in the chamber. In addition, the initial low-pressure pumps out unwanted residual gas that is in the room. By doing this, it reduces the chance of incorporating impurities in the deposited film. It is essential that we avoid melting or subliming the target holder and heater. Naturally, only materials with a much higher vapor pressure than the materials of the heating element and sample holder can be evaporated to obtain a highly pure thin film.

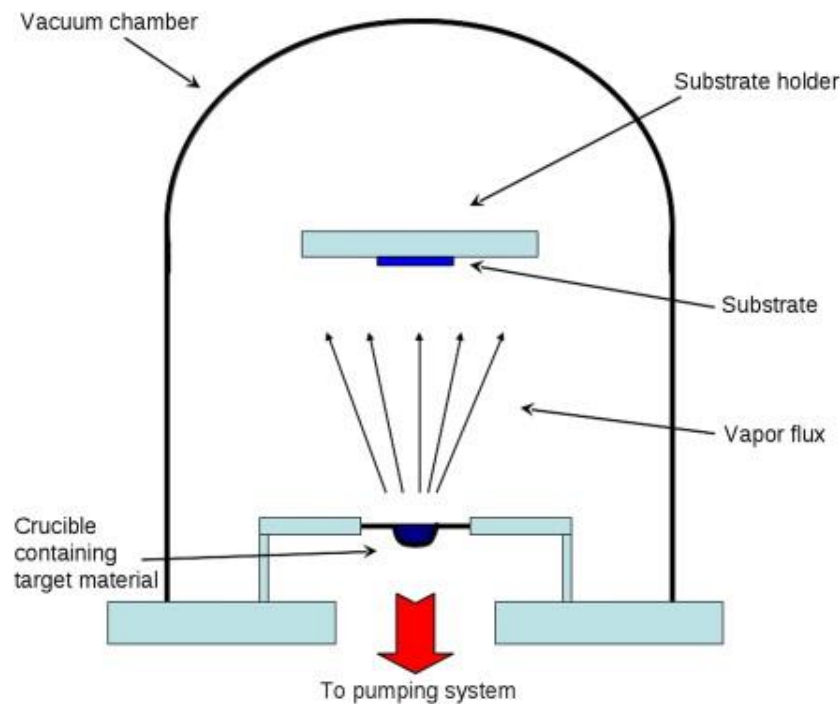


Figure 1. 7: Representation of a type of thermal evaporation system.

Typical metals used as heating elements include tantalum (Ta), molybdenum (Mo), and tungsten (W). The evaporation temperature is typically in a range of 1000-2000°C. This technique is straightforward and suitable for depositing metals and compounds that have low fusion temperatures such as Al, Ag, Au, and AgCl. Nanostructured thin films can be synthesized by a solid-vapor process. In this case, a powder source material is vaporized at elevated temperatures and is usually conducted in a horizontal tube furnace, as shown in Fig 1.8. Such systems are comprised of alumina or fused quartz tube, a rotary pump system, a gas supply, and control systems [7].

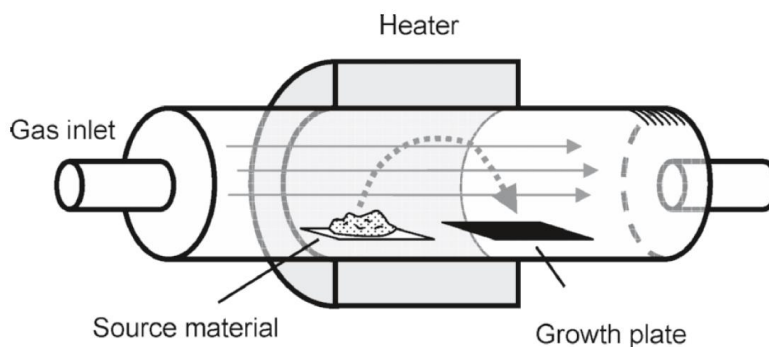


Figure 1. 8: Schematic representation of an experimental apparatus for the growth of oxide nanostructures.

1.7.2 Chemical Vapor Deposition (CVD)

Chemical vapor deposition (CVD) is a process where one or more gaseous adsorption species react or decompose on a hot surface to form stable solid products. As shown in Figure (1.9). The main steps that occur in the CVD process can be summarized as follows:

- ✓ Transport of reacting gaseous species to the surface
 - ✓ Adsorption of the species on the surface
 - ✓ The heterogeneous surface reaction catalyzed by the surface
 - ✓ Surface diffusion of the species to growth sites
 - ✓ Nucleation and growth of the film
 - ✓ Desorption of gaseous reaction products and transportation of reaction products away from the surface
- using CVD is a more complicated method than PVD for the formation of thin films and coatings. However, the CVD exhibits several distinct advantages, such as the capability to produce highly pure dense films or fine particles at reasonably high deposition rates, the ability of coating complex-shaped components uniformly due to its non-line of sight nature. CVD used a variety of metallic, ceramic, and semiconducting nanofilms. Depending on the activation sources for the chemical reactions, the deposition

process can be categorized into thermally activated, laser-assisted, and plasma-assisted CVD [1].

1.7.3 Sol-Gel Processing Route for Synthesis of Nanomaterials

Sol-Gel processing is a wet chemical synthesis approach that can be used to prepare nanoparticles by gelation, precipitation, and hydrothermal treatment. Either dopant can manipulate the size distribution of semiconductor, metal, and metal oxide nanoparticles [1, 2]. The sol-gel route offers a degree of control of composition and structure at the molecular level. The process involves the generation of a colloidal suspension ('sol'), which is subsequently converted to viscous gel and solid material.

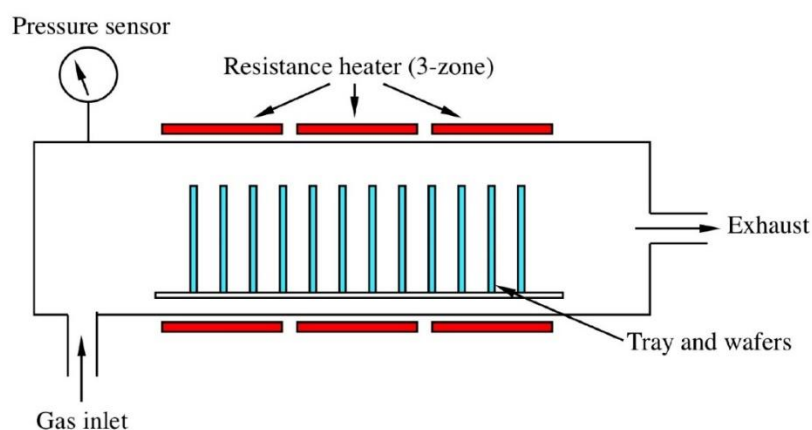


Figure 1. 9: CVD process.

All processes of the nanomaterials by this method, as shown in Figure (1.10). The factors that influence the hydrolysis reaction are nature of the alkyl group, nature of the solvent, the concentration of each species in the solvent, temperature, water to alkoxide molar ratio, and presence of acid or base catalysts [41].

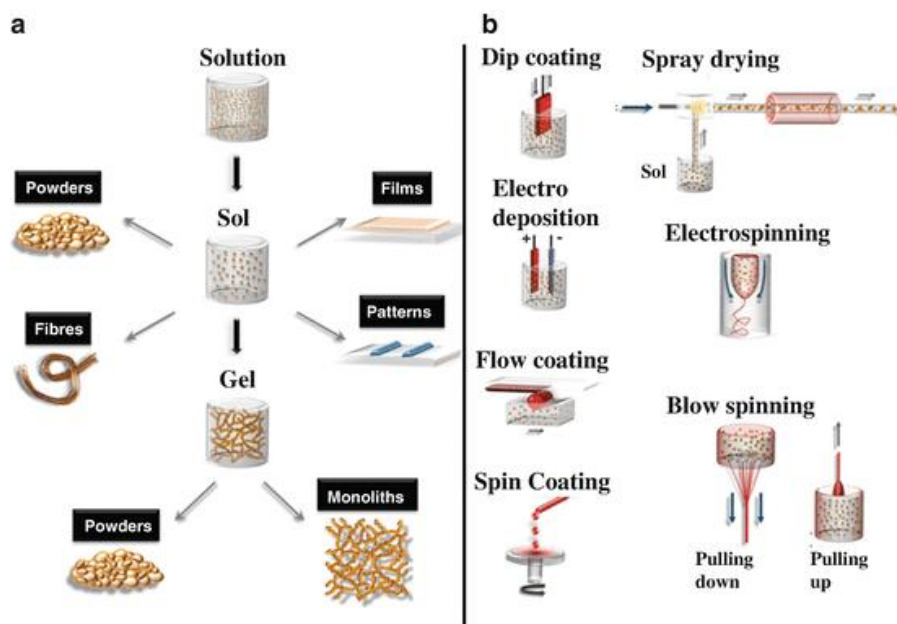


Figure 1. 10: Material synthesis by sol-gel method (a) different forms of synthesized materials; (b) sol-gel methods to synthesize different forms of materials [41].

1.8 Properties of Nanomaterials

1.8.1 Optical Properties of Nanomaterials

The optical properties of nanoparticles vary with their composition, morphology, and size. The optical properties of nanoparticles concern the way that they interact with light. If one exposes matter to light, several processes can occur:

- ✓ Absorption of light
- ✓ Scattering of light at the same frequency as the incoming light (Mie or Rayleigh scattering)
- ✓ Reemission of the absorbed light at other wavelengths (fluorescence)
- ✓ Enhancing of the local electromagnetic field of the incoming light, thus, enhancing spectroscopic signals from molecules at the material surface.

The optical properties of nanoparticles can also be modified as a result of their chirality or hardness [42].

The optical properties relate to electronic structure, a change in zone structure leads to a change in absorption and luminescence spectra. Their characteristics such as spectral width and position, and sensitivity to light polarization, depend not only on the intrinsic properties of the nano-objects (e.g., composition, structure, size, shape) but also on their environment [26]. The appearance of color is caused by the partial absorption of light by electrons in that material; the unabsorbed part of light remains visible. On smooth metals surfaces, the surfaces of slabs of metals have mirror-like appearance because the light is entirely reflected by the very high density of electrons. In contrast, small particles absorb some light, leading to the appearance of the color. As an example, bulk gold appears yellow in color; however, nanosized gold appears red in color. The particles are so small that electrons are not free to move about as in bulk gold because this movement is restricted, the particles react differently with light [43]. Au nanoparticles exhibit an enhancement of all the above-mentioned processes due to a unique interaction of the nanoparticle free electrons and light. When a gold nanoparticle is exposed to an external optical field, the electrical component of the light acts upon the conduction-band electrons and displaces them, creating uncompensated charges at the nanoparticle surface. Because the polarization occurs at the nanoparticle surface, these oscillations are called surface plasmons. The light scattering from Au nanoparticles can be 10^5 stronger than the light scattering from a fluorescein molecule, widely used as a fluorescent tracer [42].

1.8.2 Magnetic Properties of Nanomaterials

Nanomagnetism is a highly interesting topic of modern solid-state magnetism and nanotechnology [44]. The coercivity (measure the ability of ferromagnetic to stand without becoming diamagnetic) of magnetic

materials has a striking dependence on their size. It increases with the reduction of particle size in the nanometer range going through a maximum at the single domain size, and then decreases again for small particles because of thermal effects and becomes zero at the superparamagnetic particle size [45]. It can control the magnetic properties of nanoparticles by more precise controlling of the size and shape of nanoparticles. Namely, below a specific size, nanoparticles become mono-domain particles because that is energetically preferable, and they show super-magnetic behavior that takes place above certain temperatures, so-called blocking temperatures (TB). Above blocking temperatures, magnetic moments of particles fluctuate in all directions with the help of thermal activation [31]. Materials that change their magnetic behavior as a result of an external magnetic field are called magnetic materials. There are five main types of magnetic materials: ferromagnetic, paramagnetic, diamagnetic, antiferromagnetic, and ferrimagnetic. In *Ferromagnetic materials* (such as Fe, Ni, Co), the magnetism arises due to atomic net magnetic moments as a result of unpaired electrons. In *Paramagnetic materials* (Gd, Mg, Li, Ta), magnetic domains are absent even though atoms have net magnetic moment due to unpaired electrons. *Diamagnetic materials* (bulk Cu, Ag, Au, and most of the rest of the elements) have atoms with no unpaired electrons and show a zero net magnetic moment. *Antiferromagnetic materials* (MnO, CoO, NiO) have two different atom types occupying different lattice positions. The two types of atoms have opposite magnetic moments, resulting in zero net magnetic moments. *Ferrimagnetic materials* (magnetite-Fe₃O₄) also have different atoms types occupying different lattice sites with antiparallel magnetic moments, but different magnitudes. Hence the magnetic moments do not cancel out, which results in a net spontaneous magnetic moment. In an external magnetic field, both antiferromagnetic and ferrimagnetic materials behave similarly to

ferromagnetic materials. Some nanoparticles of materials which are not magnetic in the bulk form exhibit a magnetic behavior in nanoform, for nanoparticle size smaller than a few nanometers: as Au, Pt, Pd, and HfO₂. Magnetism has also been observed not only in Au nanoparticles but in thin films of Au with 27 nm thickness deposited on Pyrex glass. Magnetic behavior can be tuned by surface coatings or ligands [19].

1.8.3 Thermal Properties of Nanomaterials

Nanomaterials have an increase in the surface energy, in the amplitude of atomic vibrations, then tend to additional surface growth of thermal vibration energy. Also, specific heat increased with the decrease in particle size, whereas the melting entropy and enthalpy decreased as the particle size decreases [3]. The melting temperature decrease with decreasing particle size is a thermodynamic consequence of the change in the surface-to-volume ratio that is confirmed experimentally. Lowering further the particle size, in the cluster-size regime (tens to several hundreds of atoms), the simple addition or removal of a single atom can drastically change the physical properties of the cluster. While the decrease of melting temperature with the size is correct for large particles, when lowering the particle size below a certain threshold, the melting temperature starts showing size-dependent fluctuations. One can notice large fluctuations (several 100°) can occur just by simply adding or removing a single atom. Three leading causes can lead to a second feature in the heat capacity versus cluster size: partial melting when a part of the cluster melts at a lower temperature than the rest, the existence of two structural isomers with different melting temperatures, and a solid-to-solid transition followed by melting. In this size regime, it is possible that the melting temperature of very small clusters to be higher than the melting temperature of bulk, due to the fact that the structure of the clusters is different from the structure of the bulk [19].

1.8.4 Catalytic/Photocatalytic Activity

catalytic properties of nanoparticles have significant surface facets like those of their bulk counterparts with crystalline surfaces. The catalytic activity starts to deviate from its bulk behavior due to the increasing contribution of the corner and edge atoms of the nanoparticle with decreasing size, usually smaller than 3 nm. Spherical nanoparticles with a size around 3 nm have half of their atoms on the surface. In the case of nanoparticles with sizes between ~1 and 2 nm, even slight changes in its structure, the addition or deletion of a few atoms can have a significant impact on its catalytic properties. Furthermore, for a given crystalline structure, the different crystalline surface may show a different reactivity toward the same reaction [19].

1.9 The Importance of Nanomaterials

Nanoparticles are present in trace quantities in the atmosphere. The atmosphere is composed of chemical compounds in gaseous and solid forms [46]. Nanoparticles could be carried into aquatic environments from different sources, including “atmospheric outfalls, solid surface leaching, hot-spot industrial and urban emissions from municipal wastewater treatment, and electrothermal plants [46]. Molecular interactions in the aquatic medium are essential for the evaluation of mobility, transport behavior, bioavailability, (eco)toxicity, reactivity, and technological applicability of prepared nanoparticles. The source of nanomaterials in the water medium has resulted in several factors such as

- ✓ The medical and pharmaceutical industry
- ✓ Household and farms
- ✓ Industry and business
- ✓ Landfills,

Also, due to their unique physicochemical properties, nanoparticles are capable of accumulating solid elements of the aquatic environment.

Formation and transformation processes of nanoparticles in soil may result through an “abiotic (a non-living substance involved) or biotic (a living substance involved) pathways, or a combination of both. For example, the clay minerals formed via an abiotic pathway. Humic substances formed by biogenic routes based on the decomposition of plant materials (biopolymers). The formation of nanosized iron and manganese minerals in the soil is affected via a combination of abiotic and biological pathways” [46].

1.10 Application of Nanomaterials

Science and technology of nanomaterials are feeding a revolution in manufacturing and production, creating new materials with specific properties and novel applications [47]. This miniaturization of devices and systems to sizes of the elementary units below one μm has revolutionized our daily life. Therefore, nanomaterials with such unique properties investigated in a wide range, and it is expected to undergo explosive developments [48]. There are many applications in a number of areas such as:

In Energy: The world energy demand is continuously growing, and it is expected to rise by approx. 50% until 2030. Currently, over 80% of the primary energy demand is covered by fossil fuels. Therefore, there is an urgent need for energy resources alternative to fossil fuels [49]. Such challenges have resulted in increased attention being paid by policymakers, researchers, and corporations to new technologies, and the application of technologies in new ways [50]. Of these, renewable energy from (solar, wind, geothermal, . . .etc.) are an important source. However, tremendous technology breakthroughs will need to occur in the next years to make the conversion of these energy resources efficiently and economically viable options. Recognizing the rapid progress in nanoscience and technology, it is timely to touch the nano energy theme. Nanotechnology will offer huge

opportunities for applications in the energy field and for the development of clean energy systems, which will be very important in the light of the enormous challenges ahead with climate change and energy [51]. The most advanced nanotechnology working related to energy are storage, conversion, manufacturing improvements by reducing materials and process rates, energy-saving, and enhanced renewable energy sources [52]. While it is critical to developing new renewable energy generation technologies such as solar, it will remain important to make the best use of the limited resources currently available [53]. Solar energy production is rapidly becoming a vital source of renewable energy being developed as an alternative to traditional fossil fuel-based sources of power [54]. Photovoltaics involve the engineering expertise to generate electricity from light, and recently, it is developing into an important industrial product of the future. The low efficiency of solar cells and the expensive capital investments for large-scale electricity generation makes it a less popular option today. Possible avenues for nanotechnology are quantum dot structures providing an improvement of the conversion yield by shaping the solar spectrum, the improved use of high-tech light, optimized absorption properties [55]. Moreover, nanostructured (hybrid) materials will make it possible to use very cheap materials by minimizing the transport distances in the cell and through improved light housekeeping.... etc. Also, it has been reported that nanostructured materials are used to improve the efficiency of solar cells. The utilization of nanostructures could allow for solar cell efficiencies of 10% in the medium term and over 60% in the long run [49]. This utility is due to the fact that their optical band can be tuned by both material selection and quantum confinement and because advances in synthesis allow control over nanocrystal size and shape to optimize performance [54]. In addition to challenges in creating highly efficient energy-production systems, another hurdle facing the

scientific community is energy storage. Types of electrical power storage devices include the flywheel, supercapacitor, and battery. Supercapacitors and batteries are two crucial electrochemical energy storage devices that have been extensively developed for many applications. Improved energy storage capability, power delivery capability, and cycle life are highly desired for these devices to satisfy the increasing performance demands better.

In Solar Cell: The solar cell is considered a significant candidate for obtaining energy from the sun since it can convert sunlight directly to electricity with high conversion efficiency. It can provide nearly permanent power at low operating costs and is virtually free of pollution. To date, solar cells have been made from silicon, and in many other semiconductors, DSSC, organic semiconductors depend on metal and semiconductor nanoparticles using various device configurations and employing single crystal, polycrystal, and amorphous thin-film structures. Solar cells are useful for both space and terrestrial applications [56]. A solar cell is a self-generating arrangement which employs semiconductor contacts against metals. The current generated depends on the illuminated area. As an illustration, the current generated is about 10–100 mA from a junction of about 1 cm² area [57].

In Agriculture: Nanomaterials are playing a significant role in agriculture, by inclusion into fertilizer compounds and supplying the necessary nutrition for the growing plants [46].

In Food Science: Nanotechnology has the potential to impact many aspects of food systems, such as “food security, new tools for molecular and cellular biology, new materials for pathogen detection, and protection of the environment [46].

In Health care and Cosmetics: Solid lipid nanoparticles (SLN) exhibit advantages and properties making them applicable as carriers in the

cosmetology as (1) protection of labile compounds against chemical degradation, (2) controlled release of the active ingredients, (3) SLN acts as occlusive and can be used to increase the water content of the skin, and (4) SLN shows a UV-blocking potential, i.e., act as physical sunscreens by providing photoprotection [46].

In Medicine: Nanomedicine is an emerging field of life science, also related to the future medicine encompassing the application of nanotechnologies to drug delivery, diagnostics, treatment, and management of human health which spans nanoscience, physics, materials science, molecular biology, clinical translation, and pharmaceuticals [58].

In Cleaning and Washing: Nanomaterials based on the “liquid spray containing TiO₂, silver nanoparticles and polymer micelles are available recently. Nanopowders contain zeolites able to absorb heavy metals and bad-smelling compounds from the washing mixture” [46].

In Clothing and Textile Products: Nanotechnology was used for “producing of lightweight and comfortable protective clothing for various purposes including new developments such as sensor, antibacterial, energy storage, stain-resistant, conductivity, and decontaminant fabrics.” Carbon nanotubes (CNTs) can improve “tensile strength and thermal and electrical properties of textiles, and nano-sized clay materials can improve the hardness, abrasion, thermal, electrical and gas barrier, flame retardant and chemical resistance of textiles” [20, 46]

In Environment: Nanotechnology presents new opportunities to improve how contaminants in the environment are measured, monitored, managed, and minimized [58].

In Consumer Products: Nanotechnology is a growing global enterprise that will have enormous economic and social impacts, as can be observed with the ever-emerging products that utilize some form of nanotechnological application, whether it is a coating on cars to self-

cleaning windows [58]. The presence of metallic nanomaterials in consumer goods can be grouped into three categories based on the location where they are placed: (1) dispersed in bulk of products; (2) coated on the surface; (3) bound in products [59]. Figure 1.11 shows more applications of nanomaterials.

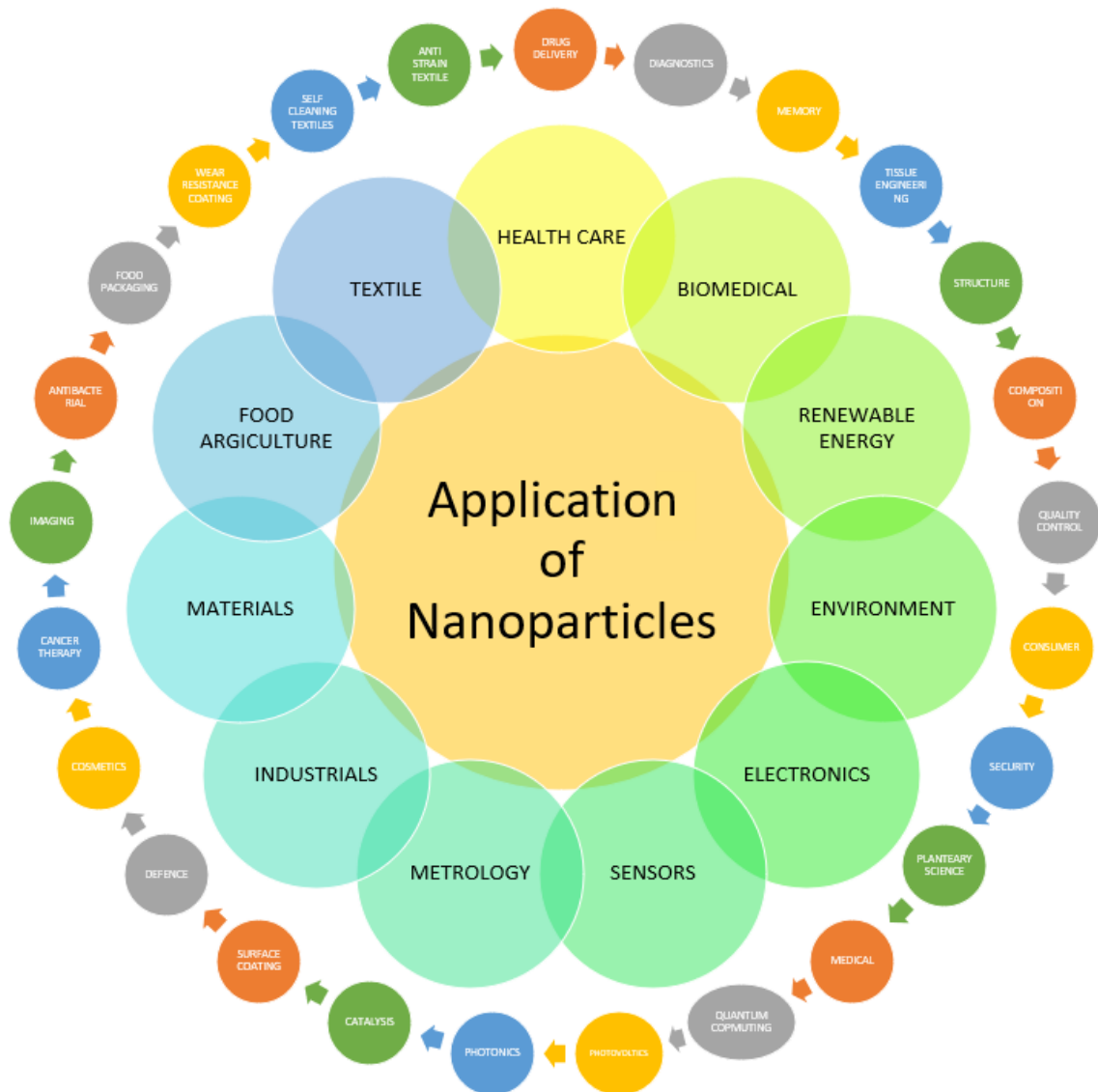


Figure 1. 11: Application of Nanoparticles [60, 61].

1.11 Literature Review

Jun et al., (2017) prepared AuNPs and AgNPs and embedded these samples on P4VP. They made a thin film from PVP doped by the nanoparticles and N719 dye as a photoactive layer of (DSSCs). They confirm that the photoactive layer is enhancing power conversion efficiency (PCE). The PCE increased by 8.05% and 5.78%, respectively (plasmonic Au nanoparticles: from 8.82% to 9.53%; plasmonic Ag nanoparticles: from 8.82% to 9.33%). These results could be explained by a broader range of light absorption resulting from the presence of the plasmonic layer [62].

Tapia et al., (2016) prepared silver nanoparticles in epoxy resin using N, N-dimethylformamide (DMF) as a reducing agent of silver ions at room temperature. Their prepared samples were characterized by UV–Vis, AFM, TEM, and HRTEM techniques. The results obtained that; silver nanoparticles viewed broadband absorption spectra due to high order plasmonic resonances. The authors deposited the silver nanoparticles on crystalline silicon by a spin coating process at room temperature. According to their observed results from measuring the antireflective properties, they inferred that the films of coalesced silver nanoparticles decrease the reflectance of crystalline silicon better than particles separated by large distances. These results are discussed in terms of forwarding scattering of large metallic nanoparticles where higher-order multipolar modes are dominant, and the retardation effects are significant [63].

Misra et al., (2015) proposed a facile route for the synthesis of Au@ZnS core-shell nanocomposite with single or multiple cores. They noticed photoluminescence quenched with an increase in Au core size. Moreover, it exhibits 21-fold increases in photocurrent with a four-time Au core concentration [64].

Jeng et al., (2015) deposited gold and silver nanoparticles on multi-crystalline silicon (mc-Si) and copper-indium-gallium-diselenide (CIGS)

solar cells by spin-coating method. The author discusses the enhancement of solar efficiency according to the light scattering by both nanoparticles, which changed with the nanoparticle concentration. The broadens of the plasmon band of Au and Ag are due to the random distribution for them by spin coater. They showed that the broadens is excellent for solar cell application [65].

Santos et al., (2015) study the incorporated of plasmon of AuNPs and TiO₂ and Dye in the dye-sensitized solar cell (DSSCs). They found that the presence of plasmonic nanoparticles enhanced photocurrent and energy conversion. The enhancement in photocurrent has induced a combination of strong plasmon-induced electric fields and light scattering, which overcome the loss in electrical properties. The scattered light increases the generation of the exciton, and the induced field increases the breakdown (separated of electron and hole) in exciton [66].

Vamsi et al., (2014) reported an average reflectance reduction of $\approx 8\%$ in the wavelength range of 300–1100 nm after coupling surface plasmon resonances of silver nanoparticles to textured silicon (T-Si) surface. The enhancement of photocurrent from T-Si solar cells in the off-resonant SPR region observed due to better radiative efficiency of NPs, leading to an outflow of scattered far-field into silicon maximized power generating electrons. Improvement in series resistance, fill factor, and open-circuit voltage is also observed with NPs along with photocurrent enhancement, which resulted in cell efficiency enhancement [67].

Nayfeh et al., (2014) investigated the effect of gold nanoparticles on the performance of a-Si: H solar cells experimentally. Their solar cell consists of 20 nm heavily doped p-type a-Si, 500 nm undoped a-Si, 20 nm heavily doped n-type a-Si, and finally 80 nm indium tin oxide (ITO) on the top. Au nanoparticles with different sizes are spin-coated on top of the ITO before metallization. The plasmonic effect of the Au nanoparticles allows for

additional scattering at the surface, thus reducing the overall reflectivity. The larger the nanoparticle size, the more scattering is obtained, and the median reflectivity decrease. The results show an increase in the short-circuit current density and efficiency with increasing nanoparticle size [68].

Meen et al., (2013) prepared a gold nanoparticle by seed-mediated growth method in different shapes like spherical, short nanorods, and long nanorods. Their prepared samples used as photoelectrodes of dye-sensitized solar cells (DSSCs). They study the surface plasma resonant (SPR) of the nanoparticles from the UV-Vis spectra. From the solar cell parameters, they found that the conversion efficiency of the dye-sensitized solar cells with spherical gold nanoparticles and short and long gold nanorods added in is 6.77%, 7.08%, and 7.29%, respectively. The increase in these results attributed to the surface plasmon resonance (SPR) [69].

Motta et al., (2013) reviewed different methods to synthesized gold nanoparticles and their application in organic solar cells. They confirmed that the particle size and shapes of AuNPs are an essential factor that affects the efficiency of the solar cell due to the improvement in the absorption light of the devices. The AuNPs were used as a thin film on a transparent electrode to enhance the organic layer. Due to the plasmonic effect, efficiency increased by up to 10% [70].

1.12 Aim of the present work

1. Preparation of gold, silver, zinc sulfide nanoparticles.
2. Synthesis of silver/zinc sulfide core-shell nanoparticles Ag/ZnS CSNPs.
3. Study the optical properties of the samples using the ultraviolet spectroscopy (UV-Vis).
4. Determines the bandgap of ZnS nanoparticles.

5. Characterization and study the morphology of the prepared samples using the transmission electron microscope (TEM).
6. Calculate the particle sizes and the thick of the shells using the ImageJ program and Dynamic Light Scattering (DLS) technique.
7. Explain the vibrational mode for the samples using Fourier transform infrared spectroscopy (FTIR).
8. Study the crystal structure of the prepared samples using X-ray diffraction (XRD) and calculate the crystal size.
9. Study the application of the prepared samples in the solar cells.
10. Estimate the efficiency of the solar cells.

CHAPTER II

Theoretical Principles of the Instruments

CHAPTER II

THEORETICAL PRINCIPLES OF THE
INSTRUMENTS

This chapter presents some of the underlying theoretical principles required to understand the mathematical basis of using the instrument. Many techniques depend on the electromagnetic wave. So, from our general point of view, we first consider the behavior of electromagnetic (EM) waves. In 1864, James Clerk Maxwell determined that the speed of propagation of an electromagnetic field is approximately the same as the light speed. He proposed that light is an electromagnetic phenomenon. Thus, light and other forms of electromagnetic radiation are transmitted by simultaneous oscillations of electrical and magnetic fields, as shown in Figure 2.1 [71].

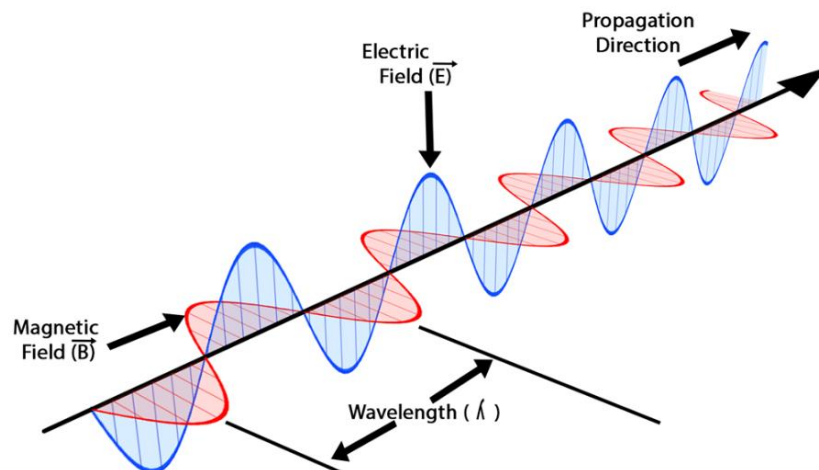


Figure 2. 1: sine wave representation of electromagnetic radiation.

It consists of two in-phase waves, with oscillation of the electric field in the xy plane, and the magnetic field perpendicular to it, in the xz plane. The relationship between the speed of travel of light (or any

electromagnetic radiation) through a vacuum c , the frequency of the radiation (ν) and its wavelength (λ) is given by:

$$\nu = \frac{c}{\lambda} = c\bar{\nu} \tag{2.1}$$

where $\bar{\nu}$ is known as the wavenumber. The speed of light in a vacuum is $c = 3 \times 10^8 \text{ m s}^{-1}$.

The electromagnetic spectrum covers a wide range of wavelengths (from 10^{-12} m to 10^3 m), as shown in Figure 2.2, it is classified into a large number of spectral regions. The way these regions deal with the matter varies widely. Usually, they are commonly thought of as unconnected entities. However, these differences arise solely as a result of the wide range of wavelengths involved (and hence energy, as shown below), not because of any fundamental differences in properties.

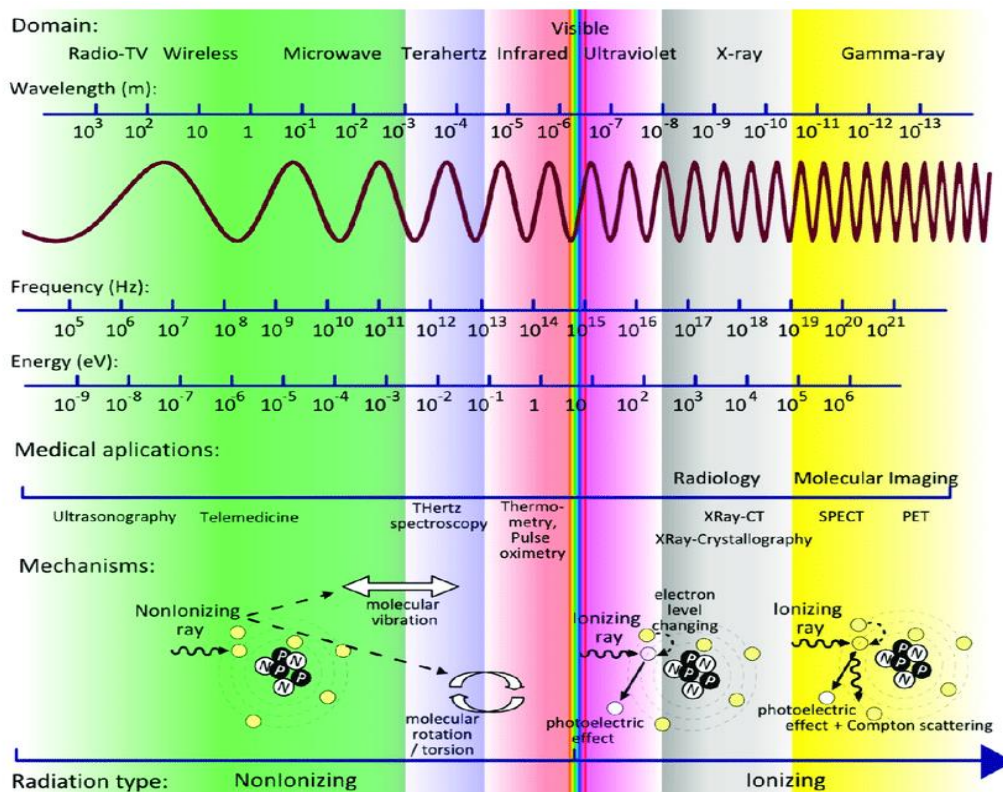


Figure 2. 2: Electromagnetic spectrum regions in terms of both frequency (s^{-1}) and wavelength (m).

In 1905, when Albert Einstein, gave the correct explanation for this effect by suggesting that light could be thought of not only as a continuous wave but also as discrete bundles or quanta, called photons, with an energy E given by:

$$E = \frac{hc}{\lambda} \quad (2.2)$$

where λ is the wavelength of the light, h is Planck's constant, and c is the speed of light in a vacuum [72].

2.1 Theoretical Principle of UV-Visible Spectroscopy

Ultraviolet-visible spectroscopy (UV-Vis) is commonly used for quantitative characterization of organic and inorganic nanosized molecules. Electromagnetic waves range in the ultraviolet is (200 nm -380 nm), and the visible range approximately is (380 nm - 800 nm). This irradiate spectra interact with the sample to analyze the absorbed light through the resulting spectrum [7, 73]. This spectrum is a graphical representation of the amount of light absorbed or transmitted by matter as a function of the wavelength [74]. UV-vis can be employed to identify the constituents of a substance, determine their concentrations, and to identify functional groups in molecules. The samples may exist in gaseous, liquid, or solid form. UV-vis spectroscopy can characterize different sized materials, ranging from small molecular weight organic molecules and transition metal ions, whose diameters can be several Ångstroms, polymers, supramolecular assemblies, nanoparticles and bulk materials. Size-dependent properties such as peak broadening and shifts in the absorption wavelength can also be observed in a UV-visible spectrum, particularly in the nano and atomic scales. Also, electronic properties, such as the bandgap of a material, can be determined by this technique. For instance, the absorption spectrum of semiconductor nanocrystals broadened owing to quantum confinement

effects. There is no longer a distinct peak as their size decreases; rather, there is a band. Besides, the absorption peaks of semiconductor nanoparticles shift to smaller wavelengths (higher energies) as their crystal size decreases. An essential consequence of using the UV-vis spectroscopy is that the bandgap of nanosized materials can be determined. The bandgap is size-dependent, and it increases as the particle dimensions decrease due to quantum confinement effects. The energies associated with UV-visible ranges are enough to excite molecular electrons to higher energy orbitals. The photons wavelength in the visible range is between 800 nm - 400 nm, which corresponds to energies between 36 kcal/mol and 72 kcal/mol. The near-UV range includes wavelengths down to 200 nm and has energies as high as 143 kcal/mol [7].

2.1.1 Quantitative Aspects of Ultraviolet Spectroscopy

Beer-Lambert Law: Absorbance is proportional to concentration and path length. The intensity of absorption is usually expressed in terms of molar absorbance or the molar extinction coefficient (ϵ) given by:

$$A = \epsilon \cdot C \cdot l \quad (2.3)$$

where C the concentration (in grams per liter) and l is the path length through the sample in centimeters [73]. Figure 2.3 illustrates the relationship between the wavelength and the intensity of light.

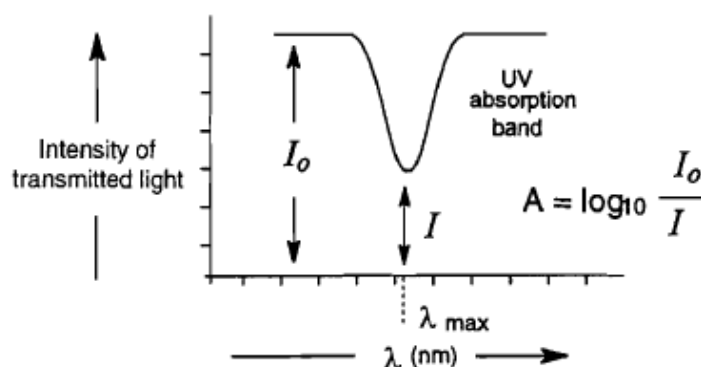


Figure 2. 3: Definition of Absorbance (A) [73].

Lambert-Beer law forms the mathematical-physical basis of light-absorption measurements on gases and solutions in the UV-Vis.

$$\log \left(\frac{I_0}{I} \right) = \log \left(\frac{100}{T(\%)} \right) = A = \epsilon \cdot c \cdot l \quad (2.4)$$

Where

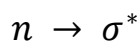
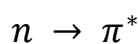
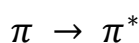
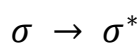
$$A = \log \left(\frac{I_0}{I} \right) \quad \text{is the absorbance (2.5)}$$

$$T = \frac{I}{I_0} \cdot 100 \text{ in } \% \quad \text{is the transmittance (2.6)}$$

I_0 is the intensity of the light that emerging from the sample [75].

2.1.2 Classification of UV Absorption Bands

UV absorption bands have fine structure due to the presence of vibrational sub-levels, but this is rarely observed in solution due to collisional broadening. As the transitions are associated with changes of electron orbitals, they are often described in terms of the orbitals involved, e.g.



Where n denotes a non-bonding orbital, the asterisk denotes an antibonding orbital, and σ and π have the usual significance [73].

A molecular electronic transition induced by photon absorption consists of the moving of the molecule from a lower electronic state, typically the lowest in energy (ground state), to a state of higher energy (excited state).

There are various types of molecular orbitals.

A σ orbital may be formed either from two s atomic orbitals, or from one and one p atomic orbital, or from two p atomic orbitals having a collinear axis of symmetry. The formed bond in this way is called a σ bond.

A π orbital is formed from two p atomic orbitals laterally overlapping. The resulting bond is called a π bond.

Absorption of a photon of suitable energy can promote one of the π electrons to an antibonding orbital denoted by π^* . The transition is then called $\pi \rightarrow \pi^*$.

The promotion of a σ electron requires much higher energy. A molecule may also possess nonbonding electrons located on heteroatoms such as nitrogen or oxygen. The corresponding molecular orbitals are called n orbitals.

The promotion of a nonbonding electron to an antibonding orbital is possible, and the associated transition is denoted by $n \rightarrow \pi^*$. Upon excitation, an electron is removed from the oxygen atom and goes into the π^* localized orbital half on the carbon atom and half on the oxygen atom.

These electronic transitions energy is generally in the following order:

$$n \rightarrow \pi^* < \pi \rightarrow \pi^* < n \rightarrow \sigma^* < \sigma \rightarrow \pi^* < \sigma \rightarrow \sigma^*$$

These energy levels illustrated in Figure 2.4 [76].

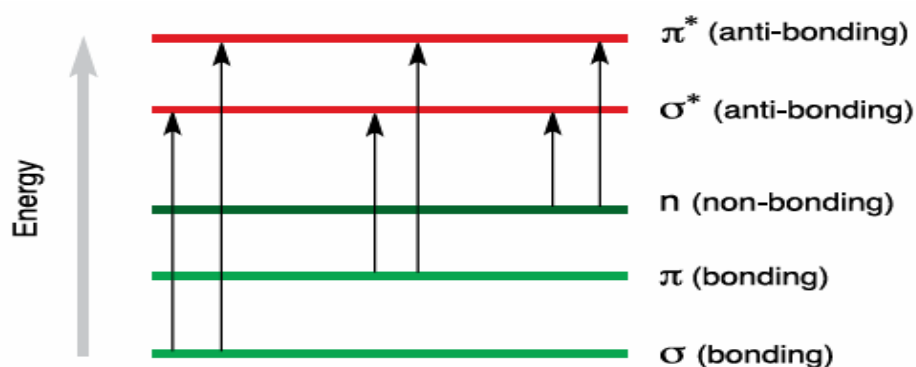


Figure 2. 4: The electronic transition levels.

UV-Visible spectroscopy is based on electronic transitions of organic molecules absorbing light that excite electrons from a lower energy orbital (HOMO highest occupied molecular orbital) to a higher energy unoccupied orbital (LUMO lowest unoccupied molecular orbital).

As shown in Figure 2.5, the energy of the light wavelength absorbed must be equal to ΔE of the HOMO-LUMO energy gap [77].

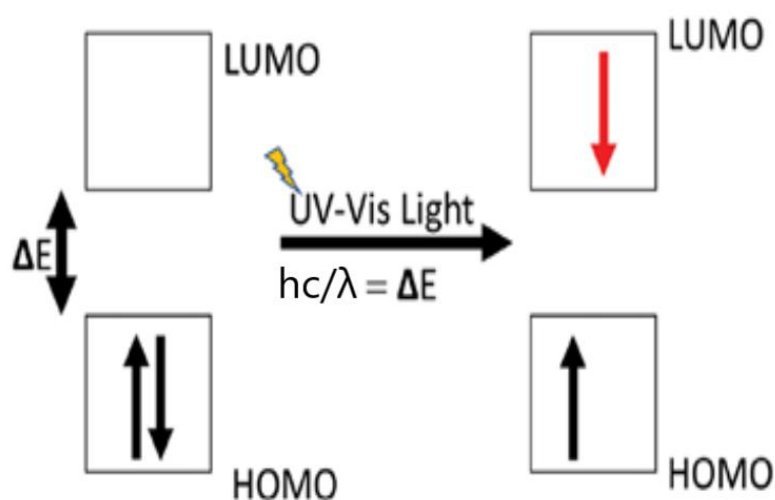


Figure 2. 5: Molecular orbitals and the energy gap needed to excite the electron energy state.

2.2 Theoretical Principle of Transmission Electron Microscopy (TEM)

Transmission electron microscope (TEM) is a microscopic tool that has become the premier tool for the microstructural characterization of materials [77, 78]. It can provide nanostructural, crystal structure, as well as micro-chemical information with high spatial resolution from each of the microscopic phases individually [1]. The TEM can display magnified images of a thin specimen, typically with a magnification in the range 10^3 to 10^6 . In addition, the instrument can be used to produce electron-diffraction patterns [79]. TEM can appear in several forms, such as high-resolution transmission electron microscopy (HRTEM), scanning

transmission electron microscopy (ESEM), and analytical electron microscope (AEM) [78]. In a TEM, a thin specimen is irradiated with a beam of focused high energy electrons and transmitted through it to reveal information about its morphology, crystallography, particle size distribution, and its elemental composition. Also, it can provide atomic-resolution lattice images, as well as giving chemical information at a spatial resolution of 1 nm or better [7, 80]. The sample must be thin enough for transmission to occur, and so a good deal of specimen preparation is typically necessary [39]. The acceleration voltage of routine instruments is 100 kV – 200 kV. Medium-voltage instruments work at 200 kV – 500 kV to provide better transmission and resolution, and in high-voltage electron microscopy (HVEM), the acceleration voltage reaches 500 kV–3 MV [80]. Because the special physical and chemical properties of nanomaterials not only depend on their composition but also their structures, TEM provides a method for characterizing and understanding such structures. TEM is unique because it can be used to focus on a single nanoparticle, then identify and quantify its chemical and electronic structure directly [7]. Since the beam goes through the sample, the interaction of the beam with the sample is much more complex, and this can be used to advantage in generating various imaging modes. Some of these modes include the ability to examine the diffraction of the beam through the crystal lattice and to select specific diffraction spots for imaging purposes. This, combined with the ability to tilt the sample in the beam, makes it possible to identify individual crystal structures, to see and identify the character of dislocations in the crystals, and to examine twin structures [39]. The pattern of diffraction measured by x-ray methods are more quantitative than electron diffraction patterns of TEM, but electrons have a remarkable advantage over x-rays; electrons can be focused easily. By focusing the electron beam, diffraction patterns can be measured from

microscopic regions, and it is frequently possible to choose a single microcrystal for a diffraction measurement. Electron microscope optics can be used to create images of the electron intensity emerging from the sample. For instance, intensity variations of electron diffraction across a thin specimen, called “diffraction contrast,” is useful for creating images of defects such as interfaces, dislocations, and second phase particles beyond diffraction contrast microscopy, which measures the diffracted waves intensity [77]. The TEM is without question the definitive instrument for use with nanomaterials since it can examine the interior of materials with the appropriate resolution. The difficulty with the use of the TEM is twofold: first, specimen preparation due to it can change the structure being observed if not done properly, and second, the use of the TEM and interpretation of the TEM images requires a very high degree of expertise. As instruments go, TEMs are expensive to maintain and operate (much more so than SEMs) [39]. TEM offers special resolution down to an Angstrom, high magnifications up to $10^6\times$ and it can work as a microscope and a diffractometer [1]. The resolution limit of TEM with the uncorrected conventional magnetic lens was reported as 0.17 nm, 0.15nm, and 0.14 nm at 200 kV, 300 kV, and 400 kV, respectively [78]. The resolution depends on the thickness of the specimen. high-resolution TEM (HRTEM) demands specimen thickness in the nanometer region. The functioning of a TEM is like a slide projector in some respects. As the electron beam passes through the sample. This causes only some part of the electron beam to be transmitted through some part of the slide. This transmitted beam is then projected on the viewing screen, forming an enlarged image of the slide [1]. The image crosses through a magnifying lens and is then projected onto a charge-coupled device (CCD), or a phosphor screen which enables for quantitative data processing. Information can also be obtained from backscattered and secondary

electrons, as well as emitted photons [7]. TEM is equipped with an “electron gun which can produce a beam of electrons able to pass via the thin areas of the observed sample [78].

2.2.1 The Electron Gun

The electron gun generates an electron beam whose kinetic energy is high enough to allow them to pass through thin areas of the specimen. The gun consists of an electron source known as the cathode because it is at a high negative potential and an electron-accelerating chamber [79]. The schematic of the electron gun in TEM is shown in Figure 2.6.

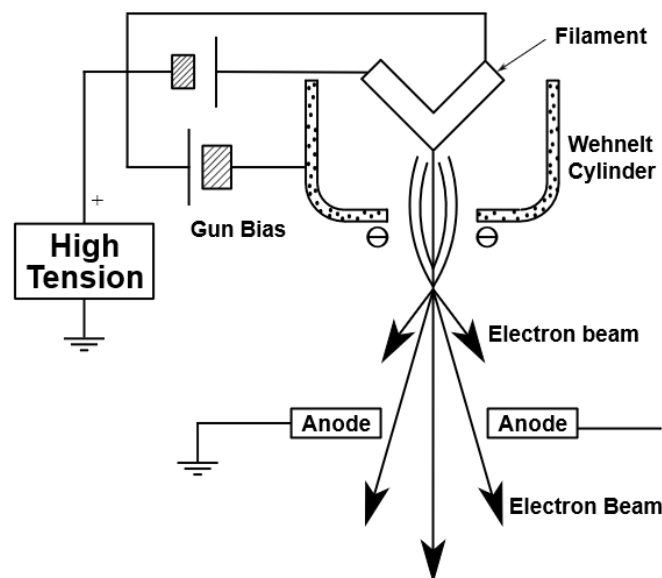


Figure 2. 6: Schematic of the electron gun of TEM.

2.2.2 Thermionic Emission

A direct current (dc) heats the filament to about 2700 K, at which temperature tungsten releases electrons into the surrounding vacuum by the process known as thermionic emission [79].

The electron emission rate can be represented as a current density J_e

(in A/m^2) at the cathode surface, which is given by the Richardson law:

$$J_e = AT^2 \exp(-\phi/kT) \quad (2.7)$$

In Equation 2.7, T is the absolute temperature (in K) of the cathode, and A is the Richardson constant ($\approx 10^6 \text{ Am}^{-2} \text{ K}^{-2}$), which depends to some degree on the cathode material but not on its temperature; k is the Boltzmann constant ($1.38 \times 10^{-23} \text{ J/K}$), and kT is approximately the mean thermal energy of an atom [79].

It is necessary to consider the interaction of electron waves with a variable refractive index medium for which the deviation from unity depends on the applied potential. For electrons accelerated by a voltage E, the electron wavelength is given approximately $(1.5/E)^{1/2}$ (ignoring relativistic effects). Electron diffraction experiments are usually done with a forward scattering geometry, and the scattering theory may often be simplified by the use of small-angle approximations. Scalar waves (electron or electromagnetic), the nonrelativistic, time-independent wave equation can be written as

$$\nabla^2 \Psi(r) + k^2 \Psi(r) = 0 \quad (2.8)$$

where k is the wavenumber, or the wave vector magnitude ($1/\lambda$), and $\Psi(r)$ is the wave function. The Schrödinger wave equation for electron waves is obtained by putting

$$k^2 = \left(\frac{2me}{h} \right) \{E_0 + \Psi(r)\} \quad (2.9)$$

The wave equation solution for an electron in the electrostatic potential field will be known, $\psi(r)$, but for the moment it can be noted only that the refractive index of the medium can be written as

$$n = \frac{k}{k_0} = \left\{ 1 + \frac{\Psi(r)}{E_0} \right\}^{\frac{1}{2}} \approx 1 + \left\{ \frac{\Psi(r)}{2E_0} \right\} \quad (2.10)$$

where the approximation of the last expression for solids and the potential $\Psi(r)$ has values on the order of 10 V, whereas the accelerating voltage E_0 is 10^5 V or more. For an electron wave passing through a solid in the z -direction, the change in the phase relative to the vacuum is then proportional to the integral of $(1 - n)$ over z , which gives $\Psi(x, y) = \int \Psi(x, y, z) dz$, so that an object may be considered to have a transmission function, which multiplies an incoming wave by:

$$q(x, y) = \exp\{-i \sigma(x, y)\} \quad (2.11)$$

$$\text{where } \sigma = \frac{\pi}{\lambda E} = \frac{2\pi m e \lambda}{h^2} \quad (2.12)$$

is the interaction constant in the expression (2.11). The phase object approximation (POA) consists two approximation. First, it assumes that the only effect of the object on the electron wave is to change its phase, i.e., changes of amplitude due to the absorption effects of inelastic scattering are ignored.

For the thin objects, this is a reasonable assumption. Second, the integration over the potential is made along a straight line, and the z -axis is the incident beam direction. No allowance is made for any change of direction due to scattering, refraction effects. Because, for high voltage electrons, such changes of direction are small (on the order of 10^{-2} radians), this approximation is reasonable for a thick object of no more than 10^2 times the width of an atom, or about 2 nm. Which is the weak phase object approximation (WPOA). This approximation can be made for light atoms only. Even for single heavy atoms.

$$q(x, y) \approx 1 - \{i \sigma \Psi(x, y)\} \quad (2.13)$$

If the phase change, $\sigma \Psi$, in (2.13) is small, it is convenient to make the further approximation of expanding the exponential to the first-order term only.

In 1924, Louis De Broglie proposed that all materials (including electrons) behave as waves and have their specific wavelengths.

$$\lambda = \frac{h}{p} \quad (2.14)$$

where λ is the wavelength, and h is the Planck constant. P is the momentum.

The momentum is given to the electron by accelerating it can result in a potential drop V in the TEM set. The kinetic energy eV must be equal to the potential energy so:

$$eV = \frac{m_0 v^2}{2} \quad (2.15)$$

$$p = m_0 v = (2m_0 eV)^{1/2} \quad (2.16)$$

All this leads to a relation between the electron microscope's accelerating voltage and the wavelength of an electron in the form.

$$\lambda = \frac{h}{(2m_0 eV)^{1/2}} \quad (2.17)$$

This association between λ and the accelerating voltage V gives rise to a very important concept: The wavelength of the electrons will decrease when the accelerating voltage is increased. Thus, make the velocity of electrons (as a particle) greater than half the velocity of light, the relativistic effects can not be ignored at 100 keV and above energies. Accordingly, the equation must be adjusted to be

$$\lambda = \frac{h}{\left(2m_0 ev \left(1 + \frac{ev}{2m_0 c^2}\right)\right)^{1/2}} \quad (2.18)$$

2.3 Theoretical Principle of Light Scattering Techniques

These techniques involve the analysis of light that is scattered from materials. The types of light scattering include elastic and inelastic. Elastic where the scattered light's wavelength remains unchanged from the incident light, and inelastic, where the scattered light's wavelength is different from that of the incident light. These techniques can provide information regarding the size, structure, and chemical composition of nanomaterials, depending on the frequency of light and the type of scattering. With such techniques, changes in these material properties can be monitored. Rayleigh scattering is an example of elastic scattering that happens when the particles are much smaller than the wavelength of the impinging light. Raman scattering, on the other side, is inelastic, where the scattering of a photon creates or annihilates a phonon, and the scattered light has a different wavelength than the incident light. Dynamic Light Scattering is one of the most relevant light scattering characterization techniques for nanotechnologies [7].

2.3.1 Dynamic Light Scattering

Dynamic light scattering (DLS) is a method of measuring submicron particle size in suspensions and emulsions by measuring their thermal motion (diffusion) [81]. DLS has become a powerful light-scattering technique for studying the properties of suspensions and solutions of colloids, macromolecules, and polymers [82]. In DLS, a light beam is directed onto a sample that scatters the light elastically. This light is scattered for a while and then analyzed statistically. DLS uses non-ionizing lower energy light sources and operates at room temperature.

A typical arrangement is shown in Figure 2.7. [7]

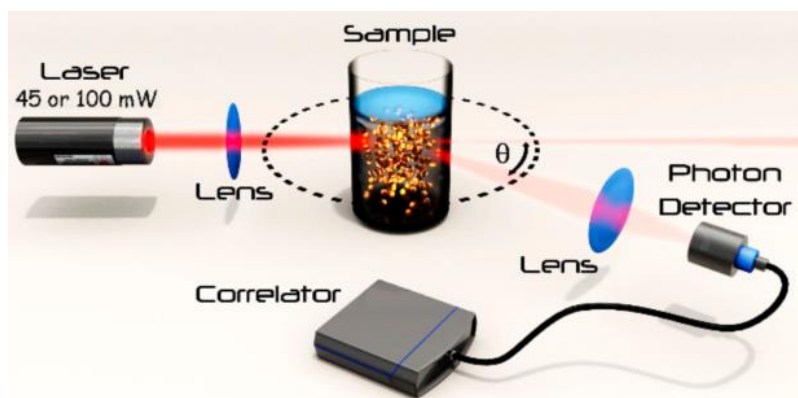


Figure 2. 7: An illustration of a DLS experiment.

2.3.1.1 Brownian Motion

DLS measures Brownian motion that is related to the size of the particles. Brownian motion is known as the random movement of particles due to the bombardment by the solvent molecules that surround them. Usually, DLS is concerned with the measurement of particles suspended within a liquid.

The larger the particle, the slower will be the Brownian motion. The solvent molecules further "hit" smaller particles and move faster. DLS needs an accurately known temperature and knowledge of this viscosity (because a liquid's viscosity is related to its temperature). Also, the temperature needs to be stable. Otherwise, the sample's convection current will cause nonrandom movements that ruin the correct size interpretation.

2.3.1.2 The Hydrodynamic Diameter

The diameter of nanoparticles measured in DLS is a value that refers to the diffusion of a particle within a fluid and is referred to as a hydrodynamic diameter.

The size of a particle is determined using the translational diffusion coefficient by using the Stokes-Einstein formula:

$$dH = \frac{kT}{3\pi\eta D} \quad (2.19)$$

where:

d_H = hydrodynamic diameter

k = Boltzmann's constant

T = absolute temperature

η = viscosity

D = The velocity of the Brownian motion that is known as the translational diffusion coefficient.

The obtained diameter by this method is the sphere diameter, which has the same translational diffusion coefficient as the particle. The translational diffusion coefficient not only depends on the size of the particle, but also on concentration, as well as any surface structure, and type of ions in the medium. Many factors, such as ionic strength of medium and surface structure, can be affected by the particle diffusion velocity [83].

2.4 Theoretical Principle of X-Ray Diffraction (XRD)

2.4.1 Introduction to Diffraction

As we know, materials are consisting of atoms or molecules. The knowledge of how atoms arranged into crystal structures and microstructures is the principle of understanding the structure, synthesis, and properties of materials. X-ray diffraction is the most powerful method for studying the crystal structure of materials. There is a profound geometrical relationship between the wave direction that interfere constructively, comprising the "diffraction pattern," and the material's crystal structure. The pattern of the diffraction is a spectrum of real space periodicities in a material. Atomic periodicities with short repeat distances cause diffraction at high angles, while with long repeat distances cause

diffraction at small angles. Crystals with precise periodicities over long distances have clear and sharp diffraction peaks. Crystals with defects such as impurities, planar faults, internal strains, dislocations, or small precipitates are less precisely periodic in their atomic arrangements, but they still have distinct diffraction peaks. Their diffraction peaks are broadened, distorted, and weakened.

Moreover, diffraction experiments are also used to study amorphous material structure, despite the lack of sharp diffraction peaks in their diffraction patterns [77]. X-Ray is an electromagnetic wave with a short wavelength (0.07 to 0.2 nm) that offers the possibility of better spatial resolution. Focusing on X-Ray relies device that use diffraction instead of refraction [79]. In XRD, the idea is to compare the intensities and the positions of the peaks in the observed pattern of the diffraction to a known pattern of peaks from a standard sample or from a calculation. There should be a one-to-one correspondence between the observed peaks and the indexed peaks in the candidate diffraction pattern [77]. Bragg law is employed here to discuss the theory of the X-Ray.

2.4.2 Bragg's Law

The incidence angle of the two parallel rays is θ , as shown in Figure 2.8. By showing that the triangles ACD and ABC are similar, we can prove that the small angle in the little triangle is equal to θ . (Hint: look at the shared angle of $\phi = \frac{\pi}{2} - \theta$) [77].

planes, we changed (even though this new d may not correspond to a real interatomic distance). For example, when our diffracting planes are (100) cube faces, and

$$2d_{100} \sin\theta = 2\lambda \quad (2.21)$$

then a (200) diffraction from planes separated by $d_{200} = (d_{100})/2$. A diffraction pattern from material typically contains many distinct peaks, each corresponding to a different interplanar spacing, d . For cubic crystals with lattice parameter a_0 , the interplanar spacings, d_{hkl} , of planes labeled by Miller indices (hkl) are:

$$d_{hkl} = \frac{a_0}{\sqrt{h^2+k^2+l^2}} \quad (2.22)$$

(as can be proved by the definition of Miller indices and the 3-D Pythagorean theorem). From Bragg's law (2.20) we find that the (hkl) diffraction peak occurs at the measured angle $2\theta_{hkl}$:

$$2\theta_{hkl} = 2\arcsin\left(\frac{\lambda\sqrt{h^2+k^2+l^2}}{2a_0}\right) \quad (2.23)$$

There are often many individual crystals of random orientation in the sample, so all possible Bragg diffractions can be observed in the "powder pattern." There is a convention for labeling, or "indexing," the different Bragg peaks in a powder diffraction pattern using the numbers (hkl) [77].

The diffracted beam intensity is calculated as a function of the angle of diffraction (2θ) and the specimen's orientation. The pattern of diffraction can be used to specify the crystalline phases and they are structural characteristics. XRD does not require detailed sample preparation. It is possible to measure homogeneous and inhomogeneous strains in materials as X-ray intensity, which depending on the Bragg angle.

Homogeneous or uniform elastic strain without changing the peak profile, changes the diffraction peak positions. A shift in the X-ray peak positions indicates a change in d-spacing caused by a change in lattice constants.

Inhomogeneous strain varies between crystallite and crystallite or even within a single crystallite. Since XRD provides average information from all such volumes of crystallite, it leads to the broadening of diffraction peaks, which increases as $\sin \theta$ increases. Fine crystallite size, which is independent of $\sin \theta$, can also cause a peak broadening. The contribution of crystallite size and lattice strain to peak broadening can be independently determined by peak profile analysis.

The crystallite size, D , In the absence of inhomogeneous strains, can be estimated from the peak broadening using Scherrer's formula:

$$D = \frac{k\lambda}{\beta \cos \theta} \quad (2.24)$$

where λ is the X-ray wavelength, β is the full width at half maximum (FWHM) height of a diffraction peak, θ is the diffraction angle, and k is Scherrer's constant, which is of the order of unity for a spherical crystal. However, nanoparticles often form twinned structures since that Scherrer's formula may not always give exact particle sizes. It is also important to note that diffraction by X-ray only provides an average crystallite size [1].

2.4.3 The Powder Diffraction File

The International Centre for Diffraction Data (ICDD) produces the Powder Diffraction File (PDF). In 1938 was the first publication appeared; the importance of the diffraction information was central to the formation of the Joint Committee for Chemical Analysis by Powder Diffraction Methods (JCPDS). In 1978 the ICDD was formed; the ICDD also began to support development activities, including programs for the

improvement of the quality of the diffraction data. The PDF is a collection of single-phase X-ray powder diffraction patterns in the form of tables of the interplanar spacings (d) and relative peak intensities $I(\text{rel})$ characteristic of the compound. The PDF has been used for almost five decades, and the ICDD maintains the PDF by continually adding new and updated diffraction patterns to the collection [84].

2.5 Theoretical Principle of Fourier Transform Infrared Spectroscopy (FTIR)

Infrared (IR) spectroscopy is a popular characterization technique that measures a sample in the path of an IR radiation source and its absorption of different IR frequencies. This technique characterized samples in solid, liquid, and gaseous form [7].

In general, spectroscopy studies how a wave interacts with matter, mainly through excitation and de-excitation phenomena, as a function of its frequency or its energy. Molecular vibrations information of matter can be obtained by studying the absorption of electromagnetic waves in the infrared frequency range. The range of wavelength is $4000\text{--}400\text{ cm}^{-1}$ ($2.5\text{--}25\text{ }\mu\text{m}$), referred to as the mid-infrared, is particularly interesting because it contains all the vibrational bands of organic compounds. Besides, Infrared spectroscopy is an efficient tool for identifying the chemical composition of matter [85]. Three well-defined infrared regions have the potential to provide different information (Figure 2.9):

- Near-Infrared ($12820\text{--}4000\text{ cm}^{-1}$): overtones; very useful for quantitative analysis
- Mid-Infrared ($4000\text{--}400\text{ cm}^{-1}$): useful for organic analysis
- Far-Infrared ($400\text{--}33\text{ cm}^{-1}$): vibrations of molecules containing heavy atoms, molecular skeleton vibrations, and crystal lattice vibrations [86]

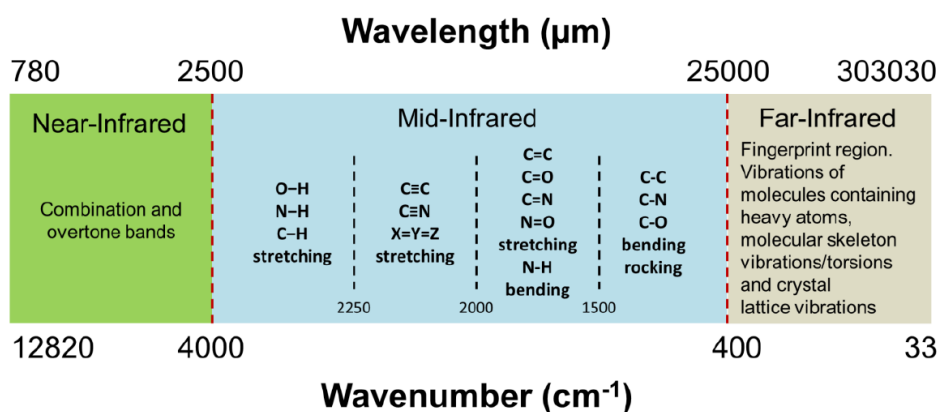


Figure 2. 9: Infrared spectroscopy regions.

IR photons energies ranging from 1 kcal/mol to 15 kcal/mol, are insufficient to excite electrons to higher electronic energy states, only transitions in vibrational energy states will occur (Figure 2.10).

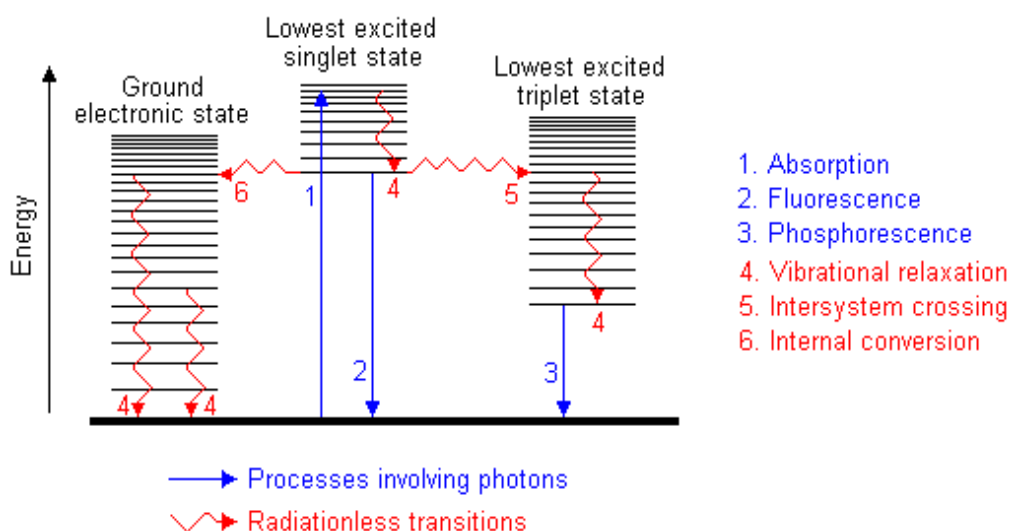


Figure 2. 10: Possible physical processes following the absorption of a photon.

These states are associated with a bond of the molecule, and consequently, each molecule has its unique signatures. Therefore, IR spectroscopy may be applied to identify the type of bond between two or more atoms and consequently recognize functional groups. It is possible to determine the number of bond types since IR spectroscopy is quantitative. The covalent bonds holding molecules together are neither stiff nor rigid, but they

vibrate at specific frequencies that correspond to their vibrational energy levels. Several factors can affect the vibrational frequencies such as bond strength and the atomic mass.

In a similar way to spring, the bonds can be modified in different ways. As shown in Figure 2.11, six different ways for contorting chemical bonds: stretching (both symmetrical and asymmetrical), rocking, scissoring, twisting, and wagging. Absorption of the IR radiation causes the bond to move from the lowest vibrational state to the next higher vibrational state, converting the energy associated with absorbed IR radiation into these types of motions.

Many complex molecules contain dozens or even hundreds of different possible bonds stretch and bending motion, which may lead to dozens or hundreds of absorption lines in the spectrum. This means that the spectrum of IR absorption can be the unique fingerprint for molecule identification. The wavenumbers in the fingerprint are between 400 cm^{-1} and 1500 cm^{-1} .

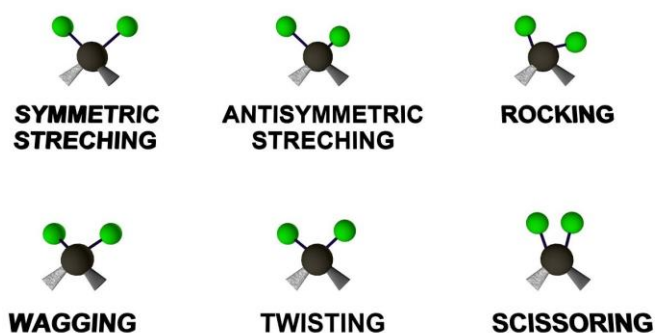


Figure 2. 11: Six different ways in which molecular bonds can vibrate.

2.5.1 The number of Mode Vibration in The Infrared Spectra

A diatomic molecule that has only one bond will vibrate in one direction.

For a linear molecule (e.g., hydrocarbons) with n atoms, there are $3n-5$

vibrational modes.

If the molecule is non-linear (such as methane, aromatics, etc.), then there will be $3n-6$ modes [7].

2.5.2 The Origin of IR Absorption Spectra

Infrared absorption spectra are presented as either wavenumber (ν) or wavelengths (λ). Wavelengths expressed in micrometers: $1\mu m = 10^{-6}m$. The use of wavenumber is currently preferred, although IR spectra are sometimes reported in micrometers. Wavenumbers and wavelengths can be interconverted using the following equation: [73, 87]

$$\text{wavenumber } \bar{\nu} (cm^{-1}) = \frac{1 \times 10^4}{\text{wavelength (in } \mu m)} \quad (2.25)$$

The energy radiation can be calculated from the equation:

$$\Delta E = hc\bar{\nu} = \left(\frac{hc}{\lambda}\right) \quad (2.26)$$

where E is the gain energy at the expense of the incident radiation energy of a frequency ν and λ wavelength, c is the velocity of light, and h is the Planck's constant. Figure (2.12) shows the change of the molecular energy level with infrared radiation.

The molecular energy consists of three energy levels, which were:

- 1- The electronic energy term $E_{el,n}$ (where n is a quantum number characterizing the energy level).
- 2- The vibrational energy $E_{vib,v}$ of the molecule associated with the vibrations of the nuclei with respect to one another (where v is the vibrational quantum number).

3- The rotational energy $E_{\text{rot},k}$ of the molecule (where k is the rotational quantum number).

Thus, the total energy of the molecule is a sum of its electronic, vibrational and rotational energies.

$$E_T = E_{\text{el},n} + E_{\text{vib},v} + E_{\text{rot},k} \quad (2.27)$$

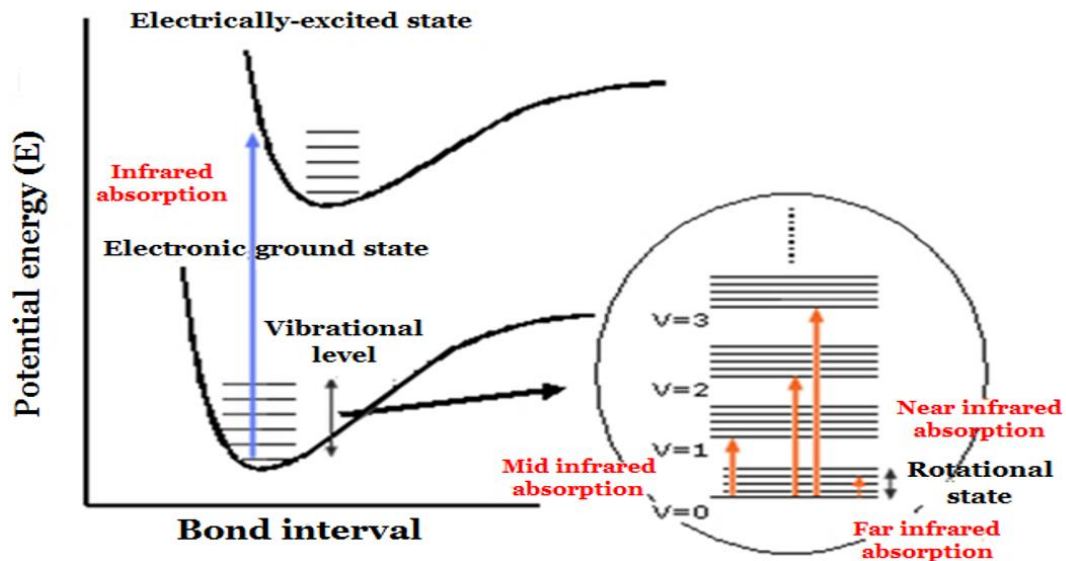


Figure 2. 12: Relationship between molecular energy level and absorption band.

Following equation represent the change of the molecular energy of the molecule due to absorption of radiation:

$$\Delta E = E_{n',v',k'} - E_{n,v,k} \quad (2.28)$$

Note that vibrational energy is lower than the electronic energy transfer and higher than the rotational energy.

The vibrational transfer occurs as a result of the infrared absorption radiation.

From Eq.(2.26) and Eq.(2.28):

$$h\nu = E_{n',v',k'} - E_{n,v,k} \quad (2.29)$$

where $E_{n,v,k}$ is the total energy of the molecule in the initial state and $E_{n',v',k'}$ its energy in the excited state.

1- If $n=n'$ and $v=v'$: The rotational energy of the molecule will change only, and a pure rotation spectrum is observed, where its frequency (ν) occurs in the microwave or far-infrared region.

2- If $n=n'$ but $v \neq v'$: Both the vibrational and rotational energies of the molecule will change. So, a vibrational, rotational spectrum will be obtained, and its frequency (ν) will fall in the medium infrared region.

3- If $n \neq n'$ and $v \neq v'$: There will be a change in the electronic, vibrational, and rotational energies of the molecule. "The electronic spectrum corresponds to the change in the electronic energy levels of the molecule". Hence the frequency of the radiation (ν) is much higher and will be found in the ultraviolet region of the spectrum

Hook's law known as the restoring force in the harmonic oscillator model, which is proportional to the first power of displacement. The curve of the energy for a simple harmonic oscillator is illustrated in Figure 2.13. The function of potential energy is proportional to the square of the displacement. This model can calculate for the fundamental vibrations occurring among the non-vibrating state and the next vibrationally excited state. In the typical diatomic molecule X-Y, the stretching of periodic along the X-Y distance is the only vibration, which can happen. This vibration considered identical to the oscillation of two mass X and Y connected via a spring and applicable Hook's law to a first approximation. The level of the vibrational energy of a diatomic molecule is therefore written by:

$$E_{Vib} = \frac{h}{2\pi} \sqrt{\frac{K}{\mu}} \left(v + \frac{1}{2} \right) \quad v = 0, 1, 2, \dots \quad (2.30)$$

where v is the vibrational quantum number, h is the Plank's constant, K is the force constant of the bond, and μ is the reduced mass of the molecule which is written by:

$$\mu = \frac{m_x m_y}{m_x + m_y} \quad (2.31)$$

where m_x and m_y are the atomic masses of x and y molecules in grams unit.

The change in vibrational energy E_{vib} for the transition, $v = 0 \rightarrow 1$.

$$E_{Vib} = \frac{h}{2\pi} \sqrt{\frac{K}{\mu}} \quad (2.32)$$

When putting Bohr relation, one finds that:

$$hv = hc \bar{\nu} = \frac{h}{2\pi} \sqrt{\frac{K}{\mu}} \quad (2.33)$$

where ν is the frequency of vibrational in (sec^{-1}), $\bar{\nu}$ is the frequency in wavenumber (cm^{-1}), and c is the velocity of light. Thus, the vibrational frequency in cm^{-1} will be writing by:

$$\bar{\nu} = \frac{1}{2\pi c} \sqrt{\frac{K}{\mu}} \text{ cm}^{-1} \quad (2.34)$$

The treatment of quantum mechanics for the linear harmonic oscillator produce the next equation for the vibrational energy level:

$$E_{Vib} = \left(v + \frac{1}{2} \right) ch \bar{\nu}_0 \quad (2.35)$$

where v is the vibrational quantum number ($n = 0, 1, 2, 3, \dots$) and $\bar{\nu}_0$ is the frequency of fundamental vibrational in wavenumber (cm^{-1}).

If the molecule vibrations accurately harmonics, the vibrational energy will only convert one step at a time, which is $\Delta v = \pm 1$.

From Eq (2.35).

$$\text{for } \nu = 0 \quad E_{Vib} = \left(\frac{1}{2}\right) ch \bar{\nu}_o \quad (2.36)$$

$$\text{and } \nu = 1 \quad E_{Vib} = \left(\frac{3}{2}\right) ch \bar{\nu}_o \quad (2.37)$$

The vibrational energy difference among these states it can writ as:

$$E_{Vib} = h c \bar{\nu}_o \quad (2.38)$$

This amount is equal to the energy of an infrared photon whose frequency in cm^{-1} is $\bar{\nu}_o$. This photon is totally absorbed when the molecule moves from the ground state $\nu=0$ into the first excited vibrational state $\nu = 1$. Other $\Delta\nu = 1$ changes such as $\nu = 1 \rightarrow \nu = 2$ return to the same result as Eq. (2.38).

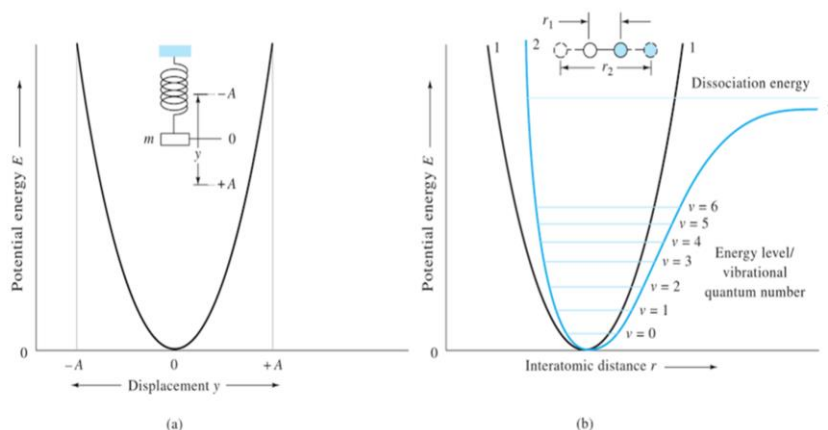


Figure 2. 13: Potential energy diagrams (a) harmonic oscillator or energy curve for a vibrating spring (b) and energy-constrained to quantum mechanical model curve 1 harmonic oscillator, curve 2 anharmonic motion.

2.6 Theoretical Principle of Solar Cell

2.6.1 Solar Cell

A solar cell is an electronic device for the direct conversion of solar energy into electrical energy using the photovoltaic effect [88].

2.6.1.1 Generations of Solar Cells

First generation silicon wafers made in high volume and, therefore, the little potential for cost reduction. This trend is expected to continue as the photovoltaic industry continues to mature.

Second generation thin-film solar cell offers prospects for a large reduction in material costs by eliminating the costs of the silicon wafer. It is also offering other advantages, such as the increased size of the unit of manufacturing.

Third generation such as the dye-sensitized solar cells based on simple manufacturing processes, roll-to-roll mass production, and cheap, easily available materials would offer one potential solution [90]. Also, Quantum dot (QD) solar cells have the potential to increase the maximum attainable thermodynamic conversion efficiency of solar photons [91].

2.6.1.2 Factors Affecting the Efficiency of Solar Cells

There are three main factors that influence the efficiency of solar cells, as:

- Energy gap E_g of the emitter/absorber material.
- Absorption coefficient α of the absorber.
- Diffusion length of the minority carrier [57].

Effect of Energy Gaps

The energy gap determines the threshold frequency f_0 and the maximum current that can be generated, the maximum Electromotive force generated by the solar cell. Consequently, the energy gap will effectively control the

maximum efficiency that can be achieved with a given absorbing material [57].

Effect of Absorber

The degree of solar flux absorption by the absorber depends on the thickness of the specimen and the absorption coefficient α of the material. The minimum thickness required to absorb almost all the useful photon flux is having energy greater than E_g which depends on the nature of the material. The absorption of direct band materials is higher than the indirect band materials because of reduced transition, since silicon is an indirect band semiconductor, optical absorption requires a minimum thickness of 300 μm . It was found that the high efficiency absorbing material must have high α values over most of the high-density area of the solar spectrum [57].

Effect of Diffusion Length

The third factor that controls solar cell efficiency is the diffusion length of minority carriers. After absorption of light quanta from the solar flux produces the electron-hole pairs, the carrier must be diffused to the junction in order to be separated. Therefore, the diffusion length must be greater than the thickness of the absorption layer. Since this thickness is already a fixed value from the maximum absorption consideration, the diffusion length must optimize by regulating the physical parameters of the material. The diffusion length L_{diff} is proportional to $\sqrt{\mu\tau}$ Where μ is mobility, and τ is the lifetime of the charge carrier. The value of μ depends on temperature; τ depends on the cross-section for recombination and the density of defects, density, and types of defects. All these factors have to be taken into account while choosing an appropriate material for the solar cell [57].

2.6.2 Solar Radiation

The solar constant is the intensity of solar radiation outside the atmosphere of the earth, at the average distance of its orbit around the sun, and it has a value of 1367 W/m^2 . The “air mass” is defined as $1/\cos \phi$, where ϕ is the angle between the vertical and the sun’s position [80]. Air mass (AM) number is the secant of the angle between the sun and the zenith ($\sec \theta$), and it measures the atmospheric path length relative to the minimum path length when the sun is directly overhead. Thus, the AM_0 represents the solar spectrum outside the atmosphere of the earth. The AM_1 spectrum represents the sunlight at the surface of the earth when the sun is at the zenith, and the incident power is about 925 W/m^2 . The AM1.5 conditions (with the sun at 45° above the horizon) represent a satisfactory energy-weighted average for terrestrial applications. The AM_2 spectrum is for $\theta = 60$ and has an incident power of about 691 W/m^2 , and so on.

The photon flux density per unit energy for AM1.5 is shown in Figure 2.14 together with wavelength to photon energy, and we use the relationship

$$\lambda = \frac{c}{\nu} = \frac{1.24}{h\nu(\text{eV})} \quad \mu\text{m} \quad (2.39)$$

The total incident power for AM 1.5 is 844 W/m^2 [56].

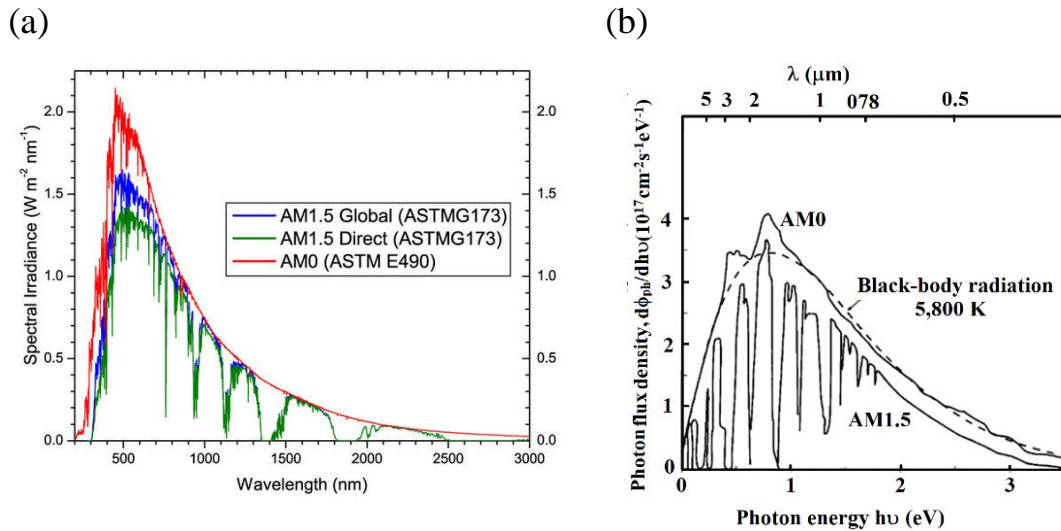


Figure 2. 14: (a) Solar spectrum at different air-mass conditions. (b) Solar spectrum in photon flux density per photon energy for AM0 and AM1.5 conditions.

2.6.3 Ideal Conversion Efficiency

The conventional solar cell, typically a p-n junction, has a single bandgap E_g . When the cell is exposed to the solar spectrum, a photon with energy less than E_g makes no contribution to the cell output. A photon with energy greater than E_g contributes an electric charge to the cell output, and the excess energy over E_g is wasted as heat. To derive the ideal conversion efficiency, we shall consider the energy band of the semiconductor used. The solar cell is assumed to have ideal diode I-V characteristics. The equivalent circuit is shown in Figure 2.15, where a constant-current source of photocurrent is in parallel with the junction.

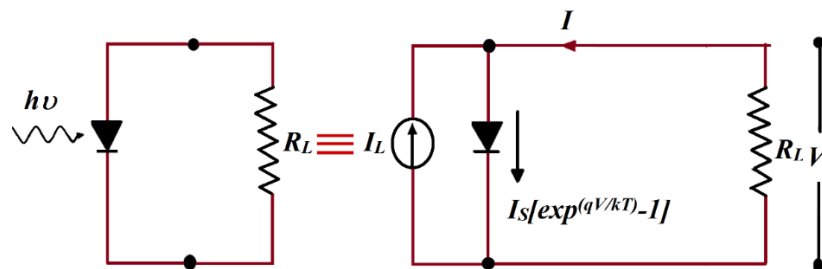


Figure 2. 15: Idealized equivalent circuit of the solar cell under illumination.

The source I_L results from the excitation of excess carriers by solar radiation; I_s , is the diode saturation current, and R_L is the load resistance. To obtain the photocurrent I_L , we need to integrate the total area under the graph shown in Figure 2.16, that is,

$$I_L(E_g) = Aq \int_{hv=E_g}^{\infty} \frac{d\phi_{ph}}{dh} d(hv) \quad (2.40)$$

For the photocurrent consideration, the smaller bandgap, the better because more photons are collected. The total I-V characteristics of such a device under illumination is simply a summation of the dark current and the photocurrent, given as

$$I = I_s \left[\exp\left(\frac{qV}{kT}\right) - 1 \right] - I_L \quad (2.41)$$

From eq. (2.41) the open-circuit voltage is obtained by setting $I = 0$:

$$V_{OC} = \frac{kT}{q} \ln\left(\frac{I_L}{I_s} + 1\right) \approx \frac{kT}{q} \ln\left(\frac{I_L}{I_s}\right) \quad (2.42)$$

Hence for a given I_L , the open-circuit voltage increases logarithmically with decreasing saturation current I_s . The ideal saturation current for a regular p-n junction is given by

$$I_s = AqN_CN_V \left(\frac{1}{N_A} \sqrt{\frac{D_n}{\tau_n}} + \frac{1}{N_D} \sqrt{\frac{D_p}{\tau_p}} \right) \exp\left(\frac{-E_g}{kT}\right) \quad (2.43)$$

As seen, I_s decreases exponentially with E_g . So, a large E_g is required to obtain a large V_{OC} . Qualitatively, we know the maximum V_{OC} , is the built-in potential of the junction, and the maximum built-in potential is close to the energy gap.

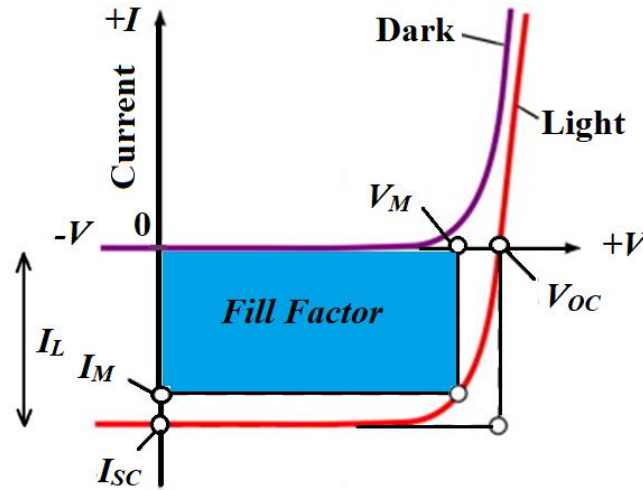


Figure 2. 16: *I-V characteristics of the solar cell under dark and illumination.*

The shaded area is the maximum power output.

We also define in Figure 2.17 the quantities I_m and V_m that correspond to the current and voltage for the maximum power output $P_m (= I_m V_m)$. To derive the maximum power operating point, the output power is given by

$$P = IV = I_s V \left[\exp\left(\frac{qV}{kT}\right) - 1 \right] - I_L V \quad (2.44)$$

The condition for maximum power can be obtained when $dP/dV = 0$, or

$$I_m = I_s \beta V_m \exp(\beta V_m) \approx I_L \left(1 - \frac{1}{\beta V_m} \right) \quad (2.45)$$

$$V_m = \frac{1}{\beta} \ln \left[\frac{\left(\frac{I_L}{I_s}\right) + 1}{1 + \beta V_m} \right] \approx V_{oc} - \frac{1}{\beta} \ln(1 + \beta V_m) \quad (2.46)$$

where $\beta = q/kT$ The maximum power output P_m is then

$$P_m = I_m V_m = F_F I_{sc} V_{oc} \approx I_L \left[V_{oc} - \frac{1}{\beta} \ln(1 + \beta V_m) - \frac{1}{\beta} \right] \quad (2.47) [56]$$

The short-circuit current I_{sc} , and open-circuit voltage V_{oc} for a given light level is plotted therein. Theoretically, a solar cell will reach maximum power to a load when the product VI is a maximum. Practically, the

maximum delivered power by a solar cell for a given light level is equal to the hatched area, as shown in Fig. 2.17. This area is less than the product of $V_{oc}I_{sc}$ [87].

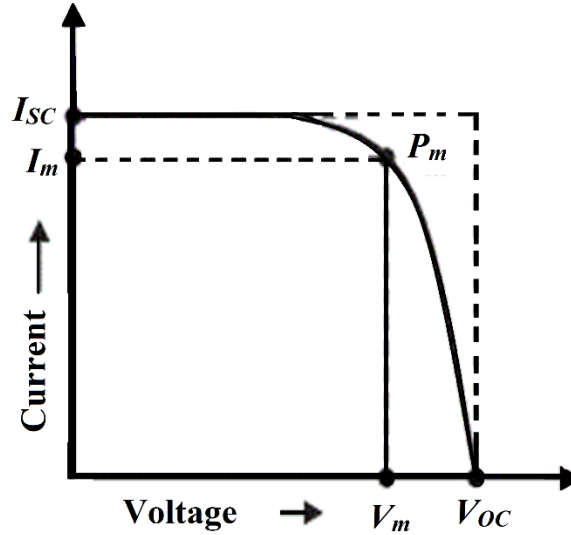


Figure 2. 17: *I–V characteristics of an illuminated solar cell.*

where the fill factor F_F measures the sharpness of the curve and is defined as

$$F_F = \frac{I_m V_m}{I_{sc} V_{oc}} \quad (2.48)$$

Its value is less than 1. In practice, a good fill factor is around 0.8. This is an important parameter for solar cell design. The ideal conversion efficiency is the ratio of the maximum power output to the incident power P_{in} ,

$$\eta = \frac{P_m}{P_{in}} = \frac{I_m V_m}{P_{in}} = \frac{V_m^2 I_s (q/kT) \exp(qV_m/kT)}{P_{in}} \quad (2.49)$$

Theoretically, the ideal efficiency can be calculated. We have shown that the photocurrent increases with decreasing in E_g . On the other hand, the voltage increases with E_g by having a small saturation current. So, there is an optimum value for the bandgap E_g to maximize the power. Furthermore, the theoretical maximum conversion efficiency can be calculated by using

the ideal saturation current of Eq. (2.44) in relation to E_g . Many factors degrade the ideal efficiency [56].

CHAPTER III

Experimental Methods and Instrumentations

CHAPTER III

EXPERIMENTAL METHODS AND INSTRUMENTATIONS

3.1 Chemicals

3.1.1 Gold (III) Chloride Trihydrate $\text{HAuCl}_4 \cdot 3\text{H}_2\text{O}$

Gold (III) chloride trihydrate $\text{HAuCl}_4 \cdot 3\text{H}_2\text{O}$, with molecular weight 393.83 g/mol and 99.99% purity, was purchased from Sigma-Aldrich, and their chemical structure is shown in Figure 3.1.

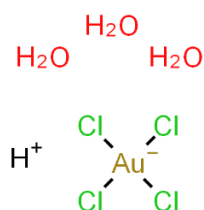


Figure 3. 1: Chemical structure of Gold (III) chloride trihydrate $\text{HAuCl}_4 \cdot 3\text{H}_2\text{O}$.

3.1.2 Silver Nitrate (AgNO_3)

Silver nitrate (AgNO_3) with molecular weight 169.87 g/mol has a white color and purchased from BDH. Their structure is shown in Figure 3.2.

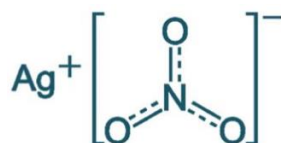


Figure 3. 2: Chemical structure of silver nitrate (AgNO_3).

3.1.3 Sodium Borohydride (NaBH_4)

Sodium borohydride (NaBH_4) with molecular weight 37.832g/mol was purchased from Sigma-Aldrich. Their chemical structure is shown in Figure 3.3.

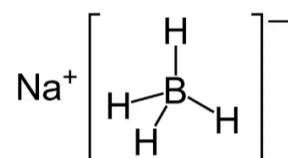


Figure 3. 3: Chemical structure of sodium borohydride (NaBH_4).

3.1.4 Cetyltrimethylammonium Bromide (CTAB)

Cetyltrimethylammonium Bromide (CTAB) $\text{CH}_3(\text{CH}_2)_{15}\text{N}(\text{Br})(\text{CH}_3)_3$ with a molecular weight 364.45 g/mol was purchased from Sigma-Aldrich, and their structure is shown in Figure 3.4.

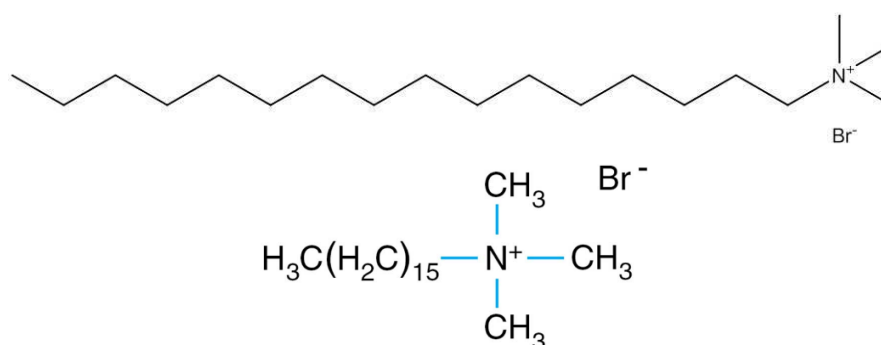


Figure 3. 4: Chemical structure of cetyltrimethylammonium bromide (CTAB).

3.1.5 Sodium Sulfide (Na_2S)

Sodium sulfide Na_2S with a molecular weight of 78.04 g/mol was purchased from Merck and had a structure is shown in Figure 3.5.

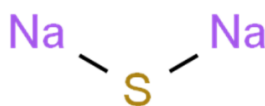


Figure 3. 5: Chemical structure of sodium sulfide Na_2S .

3.1.6 Zinc Acetate Dihydrate ($\text{Zn}(\text{CH}_3\text{COO})_2 \cdot 2\text{H}_2\text{O}$)

Zinc acetate dihydrate ($\text{Zn}(\text{CH}_3\text{COO})_2 \cdot 2\text{H}_2\text{O}$) with a molecular weight of 219.51 g/mol was purchased from Sigma-Aldrich, and their chemical structure is shown in Figure 3.6.

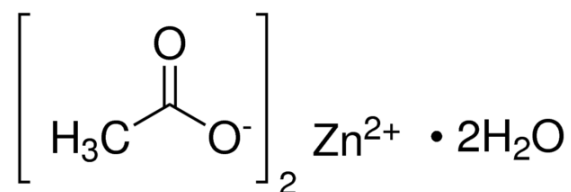


Figure 3. 6: Chemical structure of zinc acetate.

3.1.7 Polyvinylpyrrolidone (PVP)

Polyvinylpyrrolidone (PVP) $(\text{C}_6\text{H}_9\text{NO})_n$ with a molecular weight of 58,000 g/mol was purchased from ACROS ORGANIC and had a chemical structure is shown in Figure 3.7.

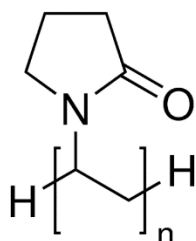


Figure 3. 7: Chemical structure of polyvinylpyrrolidone (PVP).

3.1.8 Chloroform

Chloroform with a purity 99.0-99.4% was purchased from SIGMA-ALDRICH and had a chemical composition shown in Figure 3.8.

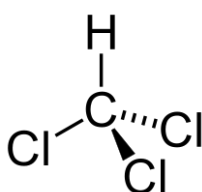


Figure 3. 8: Chemical structure of chloroform.

3.1.9 Ascorbic Acid

Ascorbic acid $(\text{CH}(\text{OH})\cdot\text{CH}_2\text{OH})$, with a molecular weight 176.13 g/mol, was purchased from BDH Chemical Ltd Poole England, has a chemical structure that shown in Figure 3.9.

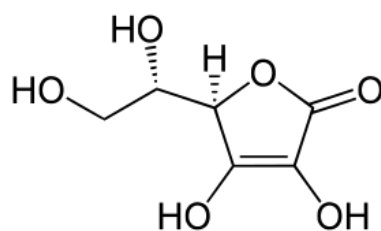


Figure 3. 9: Chemical structure of ascorbic acid.

3.1.10 Sodium Hydroxide (NaOH)

Sodium hydroxide (NaOH) with a molecular weight 40 g/mol was purchased from SIGMA-ALDRICH, has a chemical structure shown in Figure 3.10.

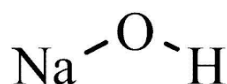


Figure 3. 10: Chemical structure of sodium hydroxide NaOH.

3.1.11 Ammonium Nitrate (NH₄NO₃)

Ammonium nitrate (NH₄NO₃) With a molecular weight of 80.04 g/mol was purchased from AVONCHEM, has a chemical structure shown in Figure 3.11.

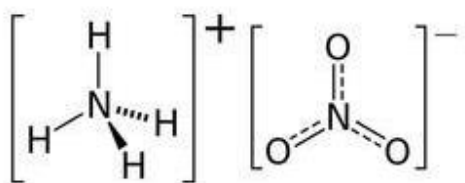


Figure 3. 11: Chemical structure of ammonium nitrate.

3.1.12 Solar Cell

Polycrystalline solar cells 52 mm x 52 mm with an efficiency 17%, Volt=0.5V, Power=0.45W.

3.2 Preparation of Gold Nanoparticles (AuNPs)

3.2.1 Preparation of Gold Nanoparticles (AuNPs) at Different Concentrations of Sodium Borohydride (NaBH₄)

AuNPs were synthesized using Cetyltrimethylammonium Bromide (CTAB) as a surfactant stabilizing agent and sodium borohydride (NaBH₄) as a reducing agent. To prepare H₂AuCl₄·3H₂O with concentration (25mM) as a stock (0.1698925 gm) was dissolved in 20 ml distilled water and stored in a conical flask at dark. From the stock of H₂AuCl₄·3H₂O with a concentration of (25mM), 2 ml were added to 50 ml of distilled water and heated at (70 °C) under vigorous stirring (1000 rpm) then after two minutes 0.1 ml of freshly prepared ice-cold NaBH₄ with a concentration (0.35M) was added immediately. The color change from yellow to ruby-red directly from NaBH₄ added, which indicates the formation of AuNPs. After two minutes (0.25038gm) of (CTAB) was added to the colloidal solution of AuNPs. About 10 ml of the solution was stored to characterize it using a transmission electron microscope (TEM), Ultraviolet-Visible spectroscopy, and zetasizer. The residual solution of AuNPs was centrifugation at (15500 rpm) to remove the excess of CTAB. The precipitation was separated and clean by water and ethanol. After cleaning, the precipitate was dried in the oven at (40°C) for 95 hours and named AuNPs(S1). This precipitated powder was used to measure the X-Ray diffractometer (XRD), and Fourier transforms infrared spectrometer (FT-IR). The samples [AuNPs(S2)-AuNPs(S4)] were prepared by the same method as AuNPs(S1) except that the concentration of NaBH₄ was changed according to Table 3.1. The schematic diagram of gold nanoparticle prepared at different concentrations of sodium borohydride has been depicted in Figure 3.12.

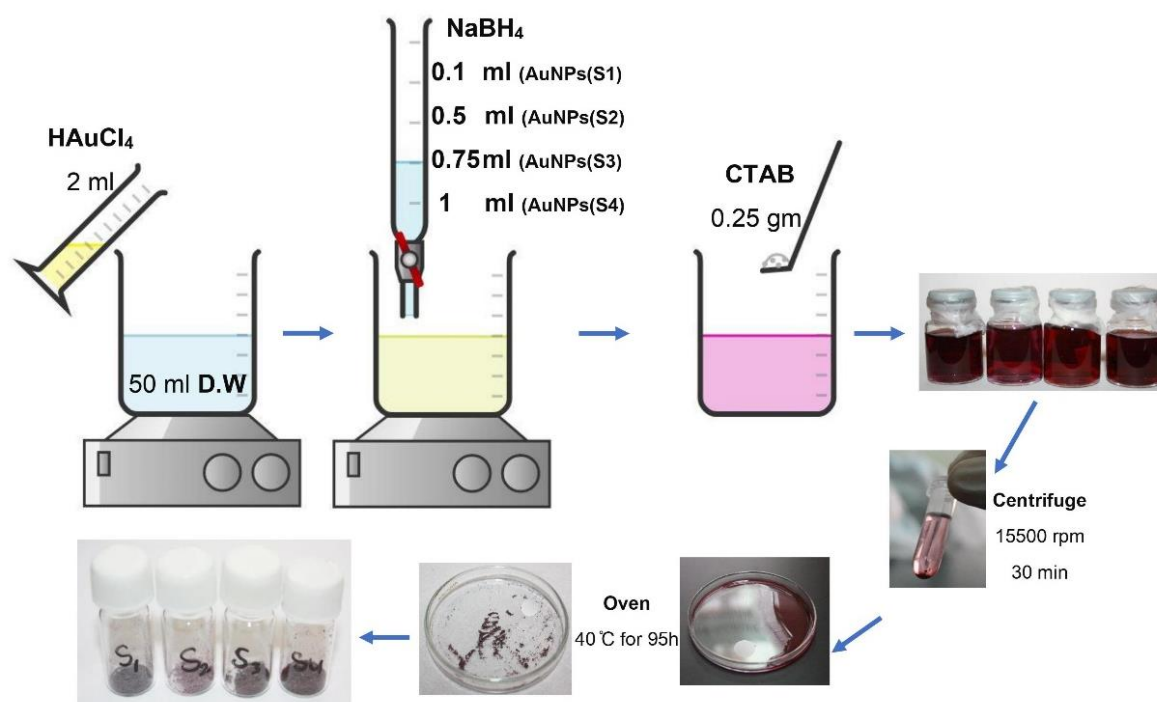


Figure 3. 12: Schematic representation of gold nanoparticles preparation [AuNPs(S1)-AuNPs(S4)].

Table 3. 1 Preparation of gold nanoparticle samples [AuNPs(S1)-AuNPs(S4)] at different concentrations of sodium borohydride under heating continuously at 70°C.

Samples	HAuCl ₄ .3H ₂ O (25mM)	NaBH ₄ (0.35M)	CTAB
AuNPs(S1)	2ml	0.1ml	0.25038gm
AuNPs(S2)	2ml	0.5ml	0.25030gm
AuNPs(S3)	2ml	0.75ml	0.25065gm
AuNPs(S4)	2ml	1ml	0.25088gm

3.2.2 Preparation of AuNPs at Different Concentrations of CTAB

AuNPs sample (S5) was synthesized using chloroauric acid as a gold source, sodium borohydride as a reducing agent, and cetyltrimethylammonium Bromide (CTAB) as a capping agent as described before. (25mM) concentration of $\text{HAuCl}_4 \cdot 3\text{H}_2\text{O}$ stock was prepared by adding (0.08494375gm) to 10 ml distilled water. From the gold stock, 2 ml of $\text{HAuCl}_4 \cdot 3\text{H}_2\text{O}$ was added to 50 ml distilled water then add 0.5 ml of (0.35M) NaBH_4 under vigorously stirring (1000 rpm) at (70°C) for two minutes, then add (0.20571 gm) of CTAB. The same processes of the samples AuNPs(S1) was repeated such that, 10 ml of the solution was stored to characterize the samples by transmission electron microscope (TEM), ultraviolet-Visible spectroscopy, and zetasizer. The residual solution was centrifuged at (15500 rpm), then wash it with water and ethanol and dried in the oven at (40°C) for 95 hours, then this powder had been used to measure the X-Ray diffraction (XRD) and Fourier transform infrared spectrometer (FT-IR). The samples [AuNPS(S6)-AuNPs(S8)] were prepared by the same method with different concentrations of CTAB, according to Table 3.2. The schematic diagram of gold nanoparticle prepared at different concentrations of cetyltrimethylammonium bromide has been illustrated in Figure 3.13.

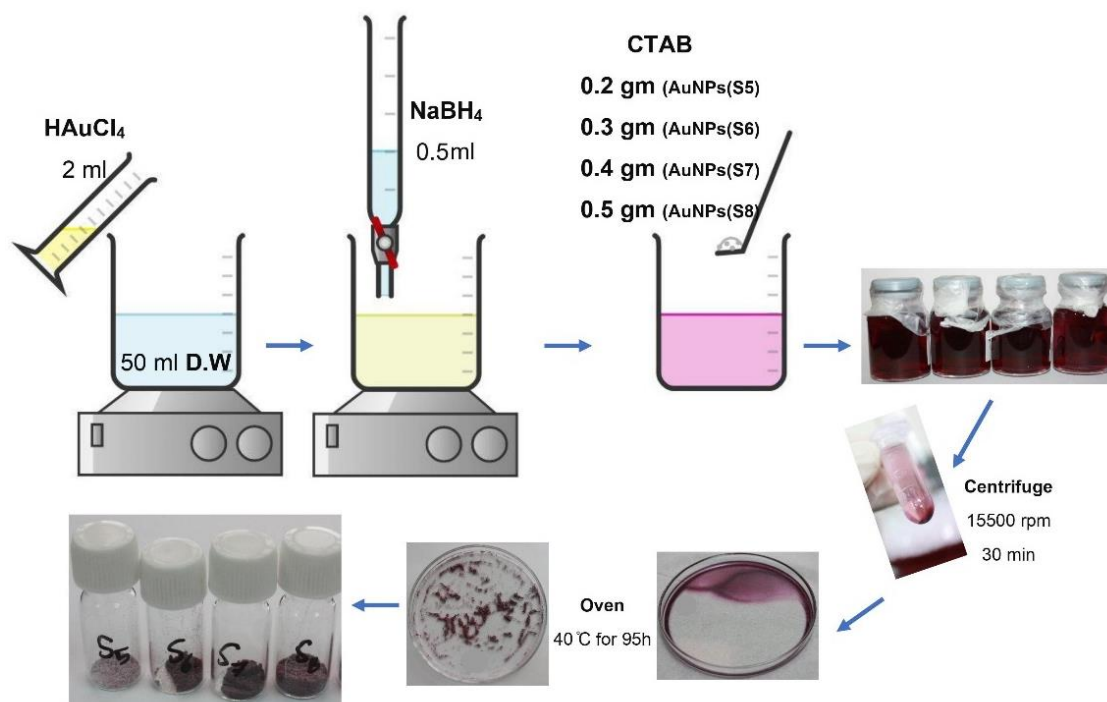


Figure 3. 13: Schematic representation of gold nanoparticles preparation [AuNPs(S5)-AuNPs(S8)].

Table 3. 2 Preparation of gold nanoparticle samples [AuNPs(S5)-AuNPs(S8)] at different concentrations of CTAB under heating at 70 °C.

Samples	HAuCl_4 (25mM)	NaBH_4 (0.35M)	CTAB
AuNPs(S5)	2ml	0.5 ml	0.20571gm
AuNPs(S6)	2ml	0.5 ml	0.30088gm
AuNPs(S7)	2ml	0.5 ml	0.40119gm
AuNPs(S8)	2ml	0.5 ml	0.501gm

3.3 Preparation of Silver Nanoparticles (AgNPs)

3.3.1 Preparation of Silver Nanoparticles (AgNPs) Using a Reverse Micelle Method at Different Concentrations of Silver Nitrate

Silver nanoparticle was synthesized using a reverse micelle method. To prepare our sample AgNPs(S9); 1.5 ml of silver nitrate with a concentration (1M) was added to 60 ml of (0.1M) CTAB solution in chloroform under magnetic stirring at (1000 rpm) for 1 hour as a first solution. In addition, sodium borohydride was prepared with (1M) and 0.8 ml was added to 60 ml of (0.1M) CTAB solution in chloroform under magnetic stirring at (1000 rpm) for 1 hour as a second solution. Then, the first and second solution was mixed under vigorously stirred and ultrasonicate (50%) for two hours to form reverse micelle emulsions, and during this time (0.4 ml) of 0.5% polyvinylpyrrolidone (PVP) was added in order to stabilize silver nanoparticles sample AgNPs(S9). Ultraviolet-Visible spectroscopy, transmission electron microscope (TEM), and zetasizer were measured of this sample as a colloid solution at that time. The last quantity of this sample was dried in air to get a powder nanoparticle, and then it used to measure X-ray diffractometer (XRD) and Fourier transform infrared spectrometer (FT-IR). The samples [AgNPs(S10)-AgNPs(S13)] were synthesized by the same previous method except that silver nitrate concentration was changed according to Table 3.3. The schematic diagram of silver nanoparticles prepared at different concentrations of silver nitrate has been presented in Figure 3.14.

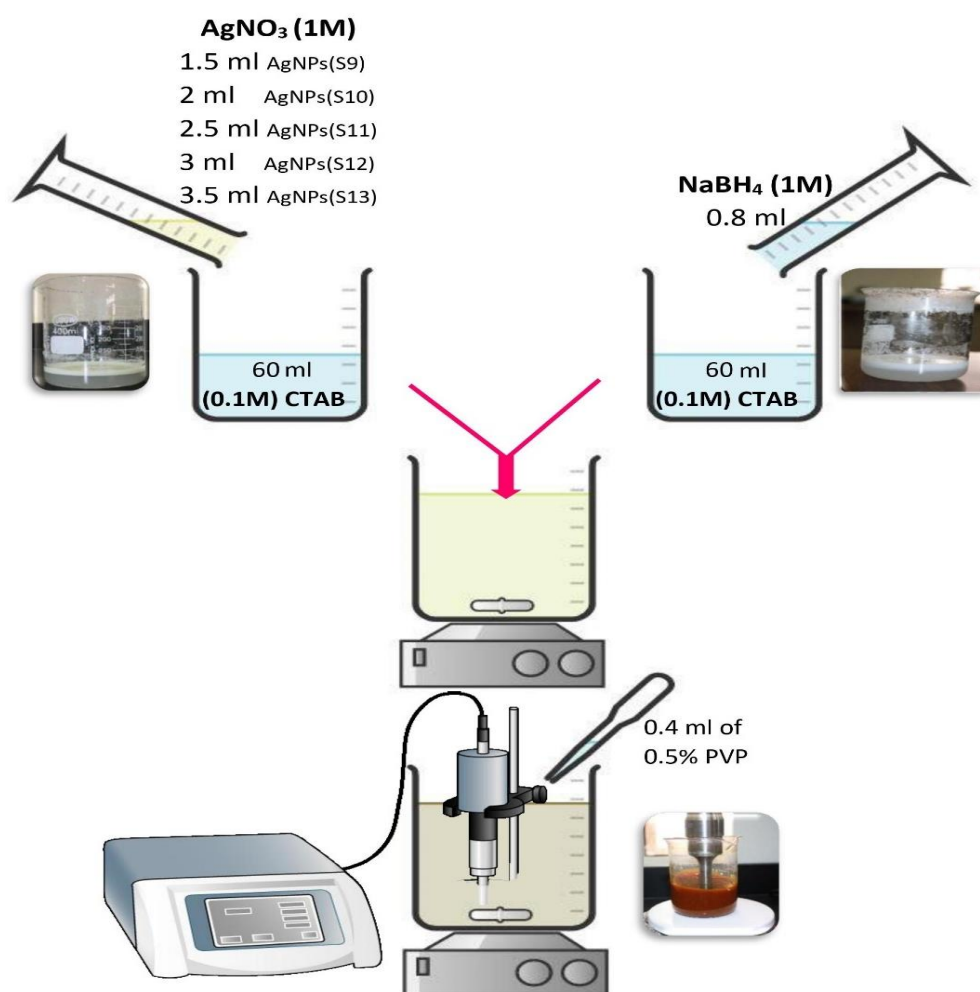


Figure 3. 14: Schematic representation of silver nanoparticles preparation [AgNPs(S9)-AgNPs(S13)].

Table 3. 3 Preparation of silver nanoparticle samples [AgNPs(S9)-AgNPs(S13)] at different AgNO₃ concentration.

Samples	CTAB	NaBH ₄ (1M)	AgNO ₃ (1M)	PVP 0.5%
AgNPs(S9)	0.1M	0.8 ml	1.5 ml	0.4 ml
AgNPs(S10)	0.1M	0.8 ml	2.5 ml	0.4 ml
AgNPs(S11)	0.1M	0.8 ml	2 ml	0.4 ml
AgNPs(S12)	0.1M	0.8 ml	3 ml	0.4 ml
AgNPs(S13)	0.1M	0.8 ml	3.5 ml	0.4 ml

3.4 Preparation of Zinc Sulfide Nanoparticles (ZnSNPs)

3.4.1 Preparation of Zinc Sulfide Nanoparticles (ZnSNPs) at Different Concentrations of Zinc Acetate Dihydrate

For the synthesis of ZnSNPs sample ZnS(S14), sodium sulfide (0.2M) was prepared as a stock solution by adding (9.60595gm) to 500 ml distilled water. Briefly, (0.1M) of zinc acetate dihydrate was prepared by adding (1.09776gm) to 50 ml of distilled water then mixed with 50 ml of sodium sulfide stock under vigorous magnetic stirring (1000 rpm), while the temperature of the mixture was maintained at (70°C) for about 20 minutes. Up to white colloidal solution was formed; this solution was used to measure the ultraviolet-visible spectroscopy, transmission electron microscope (TEM), and zetasizer. The residual sample was filtered and dried in the oven at temperature 70°C for four hours. The powder of the samples was used to measure the X-Ray diffraction (XRD), and Fourier transforms infrared spectrometer (FT-IR). The samples [ZnS(S14)-ZnS(S18)] were synthesized by the same above discussed method with a different molar ratio of zinc acetate dihydrate, according to Table 3.4. The schematic diagram of zinc sulfide nanoparticle prepared at different concentrations of zinc acetate dihydrate has been delineated in Figure 3.15.

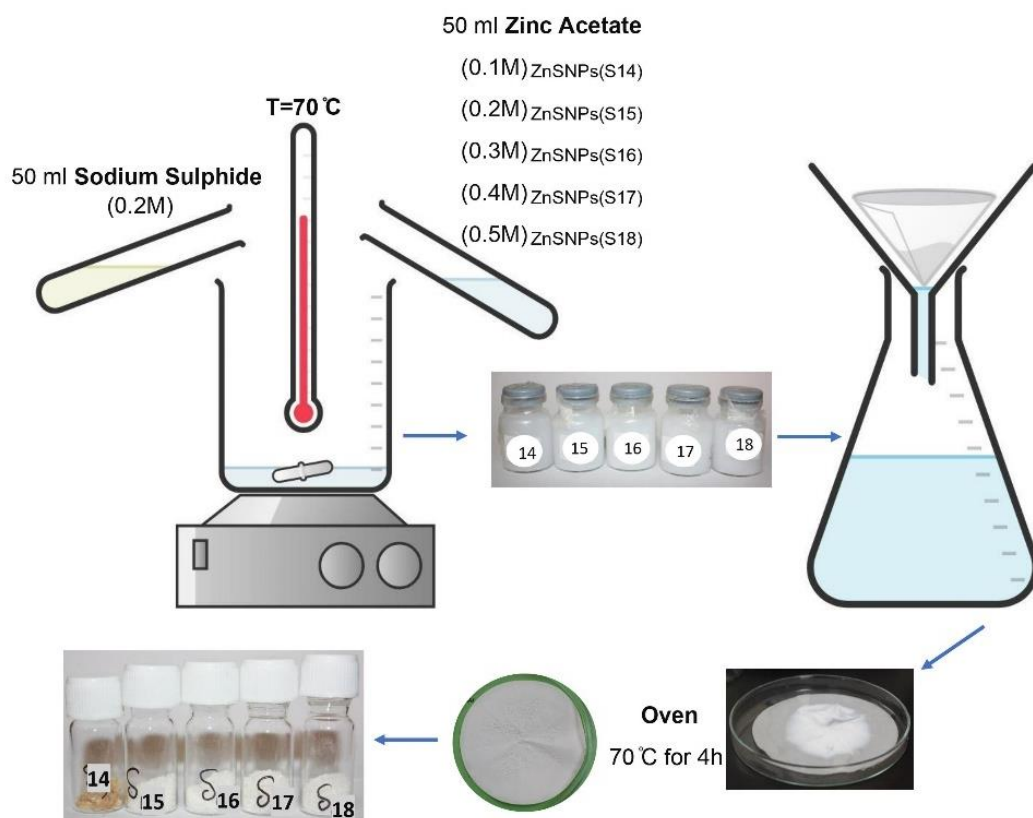


Figure 3. 15: Schematic representation of zinc sulfide nanoparticles preparation [ZnSNPs(S14)-ZnSNPs(S18)].

Table 3. 4 Preparation of ZnS NPs at different concentrations of zinc acetate dihydrate.

Samples	Na ₂ S	Zn(CH ₃ COO) ₂ .2H ₂ O
ZnSNPs(S14)	0.2M	0.1M
ZnSNPs(S15)	0.2M	0.2M
ZnSNPs(S16)	0.2M	0.3M
ZnSNPs(S17)	0.2M	0.4M
ZnSNPs(S18)	0.2M	0.5M

3.4.2 Preparation of ZnSNPs at Different Temperatures

To synthesis, ZnSNPs sample ZnS(S19) and, as discussed in the last section for the preparation of samples ZnSNPs(S14), (9.60595gm) sodium sulfide was added to 500 ml distilled water to make a (0.2M) sodium sulfide as a stock solution. In addition, (10.97536gm) zinc acetate dihydrate was added to 500 ml distilled water to prepare a (0.1M) zinc acetate dihydrate as a stock. From these two stocks, 50 ml of sodium sulfide was mixed with 50 ml of zinc acetate dihydrate under vigorous stirring (1000 rpm) at temperature (70°C) for about 20 minutes. A white colloidal solution was formed and used to analyze our sample using ultraviolet-visible spectroscopy, transmission electron microscope (TEM), and zetasizer. The residual solution was filtered and dried in the oven at temperature 70°C for four hours. The dried powder was used to characterizes the sample by X-ray diffractometer (XRD) and Fourier transform infrared spectrometer (FT-IR). The samples [ZnSNPs(S20)-ZnS(S24)] were synthesized by the same method at different temperatures, according to Table 3.5. The schematic diagram of zinc sulfide nanoparticle prepared at different temperatures has been depicted in Figure 3.16.

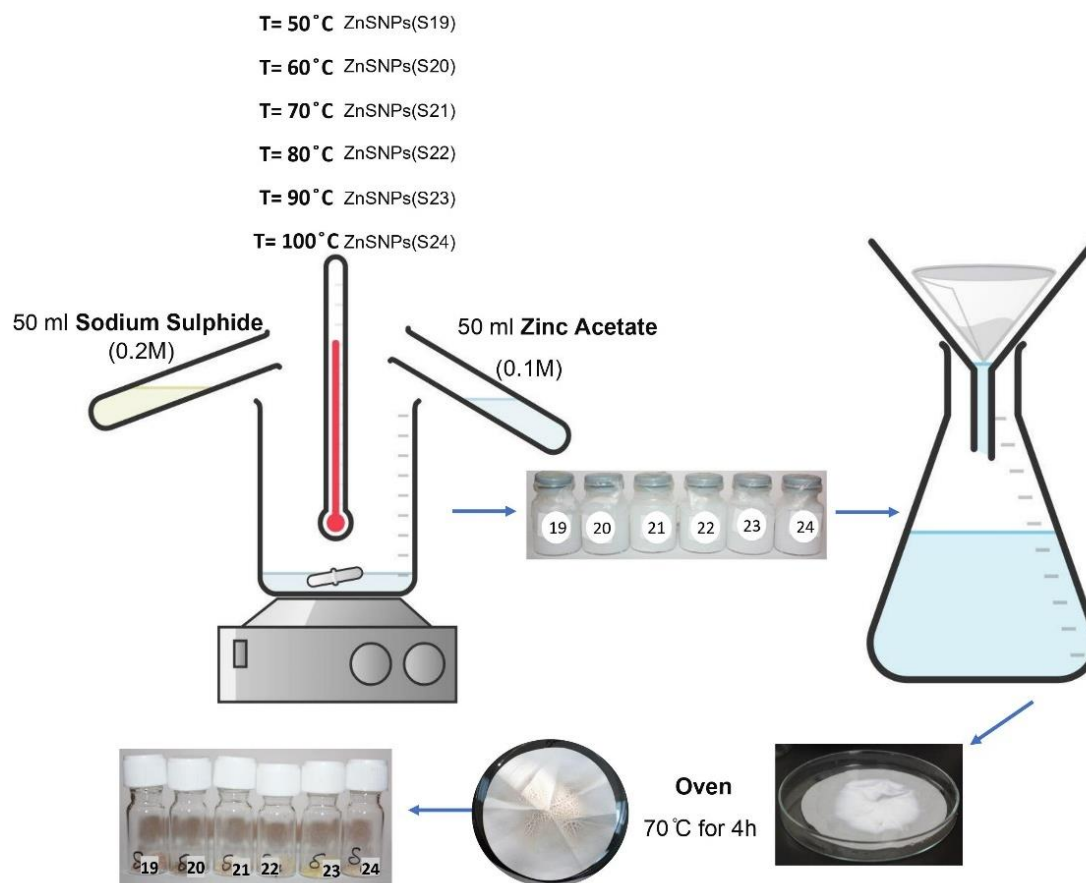


Figure 3. 16: Schematic representation of zinc sulfide nanoparticles preparation [ZnSNPs(S19)-ZnSNPs(S20)].

Table 3. 5 Preparation of ZnS NPs at different temperatures

Samples	Na ₂ S	Zn(CH ₃ COO) ₂ ·2H ₂ O	Temperature
ZnSNPs(S19)	50 ml (0.2M)	50 ml (0.1M)	50°C
ZnSNPs(S20)	50 ml (0.2M)	50 ml (0.1M)	60°C
ZnSNPs(S21)	50 ml (0.2M)	50 ml (0.1M)	70°C
ZnSNPs(S22)	50 ml (0.2M)	50 ml (0.1M)	80°C
ZnSNPs(S23)	50 ml (0.2M)	50 ml (0.1M)	90°C
ZnSNPs(S24)	50 ml (0.2M)	50 ml (0.1M)	100°C

3.5 Preparation of Silver Nanoparticles (AgNPs) Capped by Polyvinylpyrrolidone (PVP)

Silver Nanoparticles were prepared using ascorbic acid as a reducer and polyvinylpyrrolidone as a stabilizer. First, 2.41254 gm of PVP was added to 240 ml of (5×10^{-4} mol/L) ascorbic acid aqueous that prepared by dissolving 0.01956 gm in 240 ml distilled water and stirred for 15 minutes. Then 4.2 ml of (0.1M) sodium hydroxide NaOH was added and stirred for 5 minutes. Afterward, 2.4 ml of (0.1M) silver nitrate AgNO_3 was added to the solution under vigorous stirring for 15 minutes at 30°C water bath then stirring for 30 minutes at 80°C . This sample is marked by AgNPs(S25). The obtained solution was used to measure in ultraviolet-visible spectroscopy and transmission electron microscope (TEM) and to form AgNPs/ZnS core/shell. The schematic diagram of the silver nanoparticles capped by polyvinylpyrrolidone has been represented in Figure 3.17.

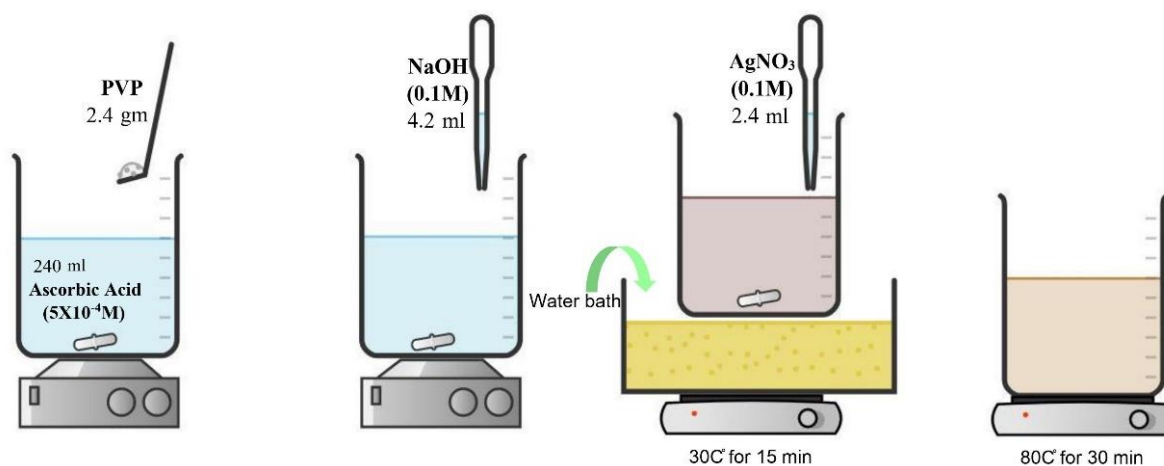


Figure 3. 17: Schematic representation of silver nanoparticles preparation capped by polyvinylpyrrolidone AgNPs(S25).

3.6 Preparation of (Ag/ZnS) Core-Shell Nanoparticles

In order to synthesis the AgNPs/ZnS core-shell (CSNPs) Ag/ZnS(S26), 0.04558 gm of zinc acetate dihydrate were dispersed in 50 ml distilled water. Subsequently, (0.11295 gm) of ammonium nitrate NH_4NO_3 was added to the solution under constant stirring. Next, add (0.19217 gm) of polyvinylpyrrolidone PVP and stirred then add 70 ml of as-prepared AgNPs colloid sample AgNPs(S25). After that, 1.8 ml of (0.2M) sodium sulfide Na_2S was dropwise added at 1 drop/s speed under stirring for 5 minutes. Finally, 3.8 ml of (0.1M) ascorbic acid was dropped wisely added at 1 drop/3s speed and keep it about 10 ml to characterize this sample using ultraviolet-Visible spectroscopy and transmission electron microscope (TEM). The AgNPs/ZnS (core-shell) nanoparticles were centrifuged for 30 minutes at (15500 rpm) and dried in the oven at 40 °C for 50 hours. Samples AgNPs/ZnS (core-shell) (27) and (28) were synthesized by the same method, according to Table 3.6. The schematic diagram of silver/zinc sulfide core-shell nanoparticles has been represented in Figure 3.18.

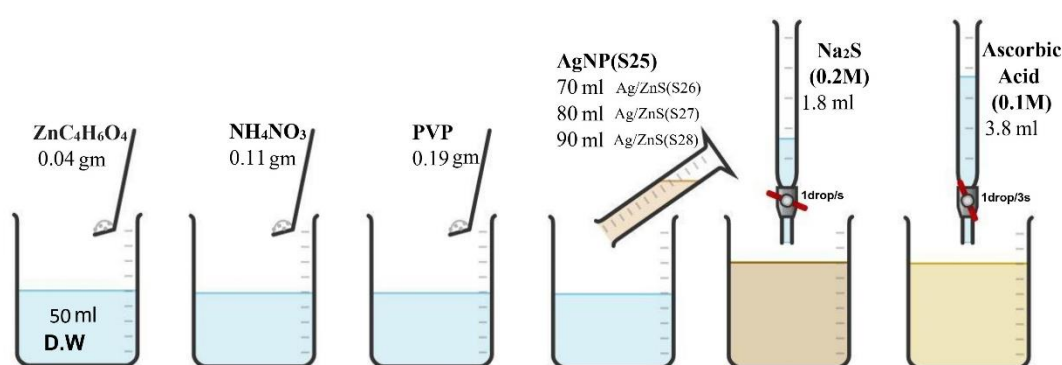


Figure 3. 18: Schematic representation of silver/zinc sulfide core-shell nanoparticles preparation [Ag/ZnS(S26)-Ag/ZnS(S28)].

Table 3. 6 Preparation of AgNPs/ZnS CSNPs

Samples	Zn(CH ₃ COO) ₂ . 2H ₂ O	NH ₄ NO ₃	PVP	AgNPs(S25)	Na ₂ S	CH(OH) CH ₂ O
AgNPs/ZnS(S26)	0.046 m	0.113 gm	0.192 gm	70 ml	1.8 ml	3.8 ml
AgNPs/ZnS(S27)	0.046 gm	0.115 gm	0.194 gm	80 ml	1.8 ml	3.8 ml
AgNPs/ZnS(S28)	0.045 gm	0.115gm	0.194gm	90 ml	1.8 ml	3.8 ml

3.7 Deposition of Nanoparticles on Silicon Solar Cell

Gold, silver, zinc sulfide, and silver/zinc sulfide nanoparticles were deposited on silicon solar cells by using vacuum spin coater (VTC-100) as shown in Figure 3. 19

**Figure 3. 19: Vacuum spin coater.**

3.8 Samples Characterization

Various techniques are used to characterize our prepared samples. These techniques included Ultraviolet-visible spectrometer (UV), Transmission electron microscopy (TEM), Dynamic Light Scattering (DLS), X-ray diffraction (XRD), and Fourier transform infrared spectroscopy (FTIR).

The results obtained from these techniques are used to study the electronic transition (UV-Vis), morphology and particle size (TEM, DLS), crystallinity and crystalline size (XRD), and vibration mode (FTIR).

3.8.1 Experimental Aspect of UV-Vis Spectroscopy

Thermo UV-Vis spectrometer model (Evolution 220) Figure 3.20 is used for measuring the spectra of our synthesized samples in the range (200 - 1100 nm)



Figure 3. 20: UV-Vis spectrometer instrument model (Evolution 220).

Basic instrumentation for UV spectroscopy comprises an energy source, a sample cell, a dispersing device (prism or grating), and a detector, arranged as schematically shown in Figure 3.21 [73]. A mirror splits the beam of monochromatic light into two beams, one of them is passed through the sample, and the other passes a reference. The measuring light splits up (dispersed) into its constituent wavelengths by a prism or a grating monochromator. With a deuterium lamp for the Ultra-Violet region and a tungsten (tungsten-halogen) lamp for the Visible region, these two lamps cover the range of 190 nm to 900 nm. The primary light beam is split and directed along two paths which traverse alternately the reference and measurement cuvette, which are approximately 10-15 cm apart.

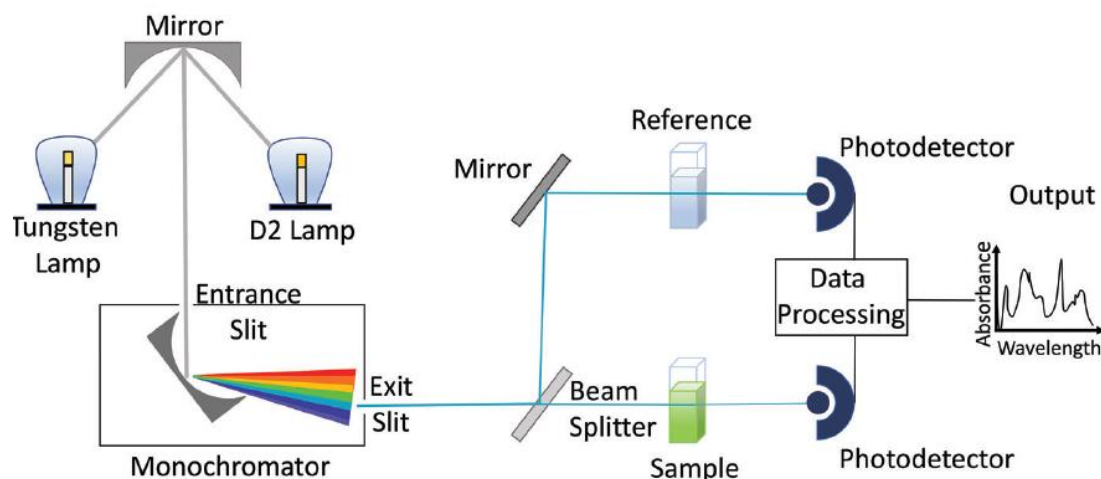


Figure 3. 21: Schematic representation of a UV spectrometer for liquid samples.

Thus, after transmission through the sample and reference both beams have been refocused, the light of varying intensity falls onto the detector where they are compared. The difference between the signals is the basis of the measurement and generates an alternating-voltage signal. Liquid samples are usually contained in a cell which is called a cuvette that has flat, fused quartz faces. Quartz is commonly used because it is transparent to both UV and visible lights. This principle forms the basis of recording spectrophotometers [7, 75]. In the present work, all the sample were measured as colloidal, and so, we use the chloroform as a reference in silver samples and water for the rest of samples.

3.8.2 Experimental Aspect of Transmission Electron Microscopy

JEOL Transmission Electron Microscope model (JEM –1400) is used to study the distribution, morphology, shapes and to calculate the particle sizes of our prepared materials. The instrument is shown in Figure 3.22



Figure 3. 22: JEOL Transmission Electron Microscope model (JEM – 1400) with LaB₆ cathode, the maximum voltage is 120 kV, the resolution is 0.2 nm, and the maximum magnification is 1200000X.

It is convenient to divide the instrument component into three sections:

The **illumination system** usually located near the top of the microscope column. Comprises the electron gun, together with two or more condenser lenses that focus the electrons onto the specimen. Its design and operation determine the diameter of the electron beam at the specimen and the intensity level in the final TEM image.

The **specimen stage** allows specimens to either be held stationary or else

intentionally moved and inserted or withdrawn from the TEM. The mechanical stability of the specimen stage is an essential factor that determines the spatial resolution of the TEM image.

The **imaging system** contains at least three lenses that together produce a magnified image (or a diffraction pattern) of the specimen on a fluorescent screen, on photographic film, or the monitor screen of an electronic camera system [79]. The TEM construction is shown in Figure 3.23

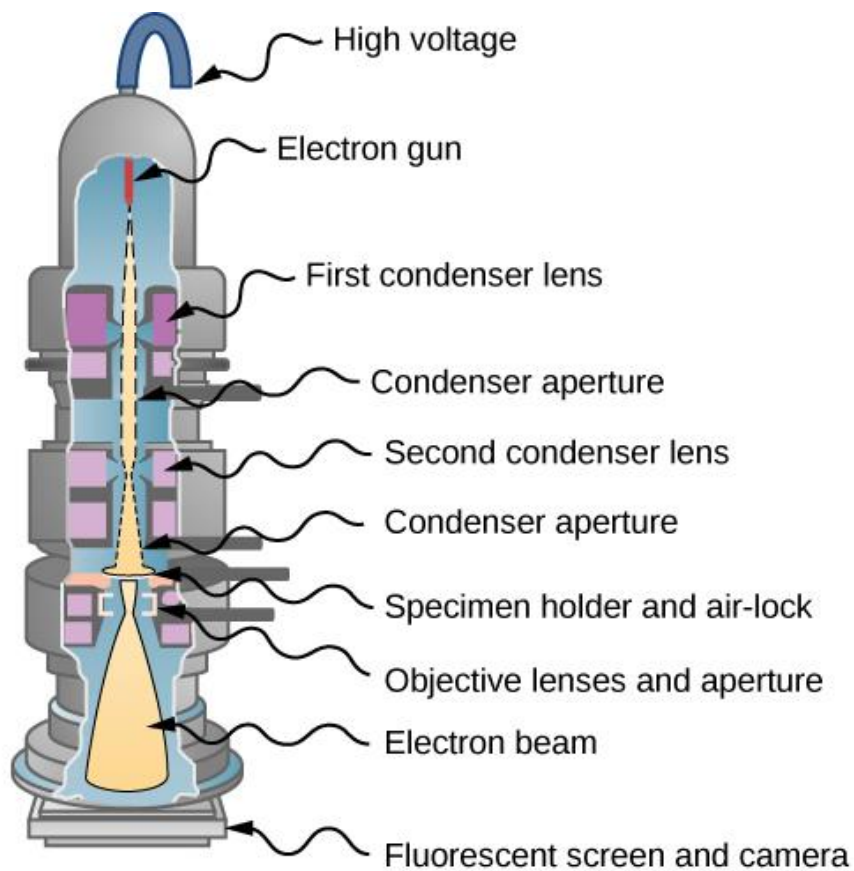


Figure 3. 23: Basic component of TEM.

Electron Guns

The electron source is electrically biased at a large negative potential concerning the microscope column and repels the electrons that leave its surface. For many years the electron source was a sharply bent tungsten wire. When heated electrically, this tungsten filament gets hottest at its

sharp tip, owing to a reduced area and higher resistivity. At high temperatures, some electrons receive enough thermal energy to surmount the work function of the tungsten/vacuum interface and leave the metal. This is the process of thermionic emission, Increasing the temperature of the filament will increase the electron emission sharply, but unfortunately leads to evaporation of the filament material and a decrease in the filament lifetime [77]. The gun consists of an electron source, also known as the **cathode** because it is at a high negative potential and an electron-accelerating chamber [79].

Electron Acceleration

After emission from the cathode, electrons are accelerated to their final kinetic energy E_0 by means of an electric field parallel to the optic axis. This field is generated by applying a potential difference V_0 between the cathode and an **anode**, a round metal plate that placed vertically below the cathode containing a central hole through which the beam of accelerated electrons emerges. Many of the accelerated electrons are absorbed in the anode plate, and only around 1% pass through the hole, so the beam current in a TEM is typically 1% of the emission current from the cathode. To produce electron acceleration, it is only necessary that the anode be positive relative to the cathode. This situation is most conveniently arranged by having the anode and the rest of the microscope column at ground potential and the electron source at a high negative potential. Therefore, the cathode and its control electrode are mounted below a high-voltage insulator (Figure 3.24) made of a ceramic (metal-oxide) material, with a smooth surface to deter electrical breakdown and long enough to withstand the applied high voltage, which is usually at least 100 kV [79].

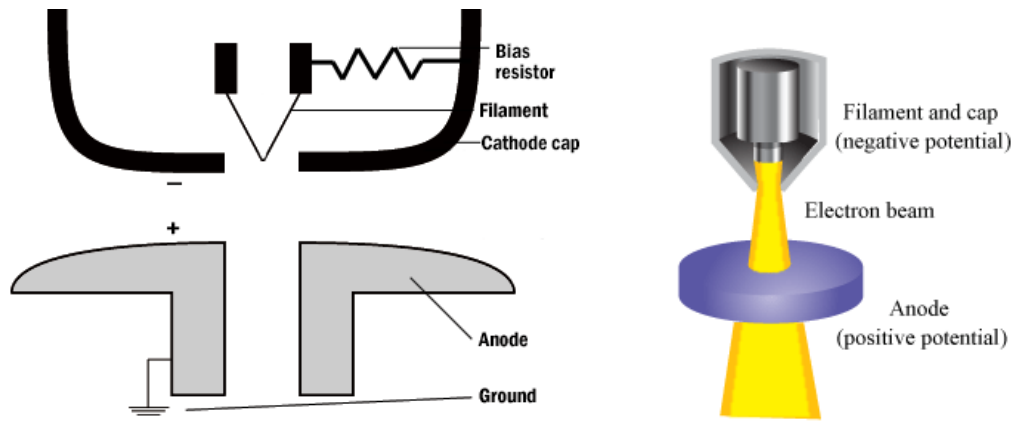


Figure 3. 24: Cathode and anode of TEM.

Condenser-Lens System

The condenser-lens system of a TEM performs the following tasks:

- Focusing of the electron beam on the specimen. So, even at high magnification, sufficient image intensity is obtained.
- Irradiation of a specimen area that corresponds as closely as possible to the viewing screen with a uniform current density. Thereby reducing specimen drift by heating and limiting the radiation damage and contamination in nonirradiated areas.
- Variation of the illumination aperture α_i .
- Production of a small electron probe (0.2–100 nm in diameter) for x-ray microanalysis, electron-energy-loss spectroscopy, microbeam electron-diffraction methods, and the scanning mode, and simple switching from the probe mode to area illumination.

Transmission electron microscopes are equipped with at least two condenser lenses to satisfy these requirements; the morefield of a strongly excited objective lens can act as an additional condenser lens [80].

Specimen Stage

TEM specimens are always made circular with a diameter of 3 mm. Perpendicular to this disk, the specimen must be thin enough (at least in

some regions) to allow electrons to be transmitted to form the magnified image [79]. The specimen stage is designed to hold the specimen as stationary as possible, as any drift or vibration would be magnified in the final image, impairing its spatial resolution. But in order to view all possible regions of the specimen, it is also necessary to move the specimen horizontally over a distance of up to 3 mm if necessary [79]. The design of the stage must also allow the specimen to be inserted into the vacuum of the TEM column without introducing air. This is achieved by inserting the specimen through an airlock, a small chamber into which the specimen is placed initially, and which can be evacuated before the specimen enters the TEM column. Not surprisingly, the specimen stage and airlock are the most mechanically complex and precision-machined parts of the TEM [79]. There are two basic designs of the specimen stage: top-entry stage and side-entry stage, as shown in Figure 3.25. Now they are nearly all side-entry [92].

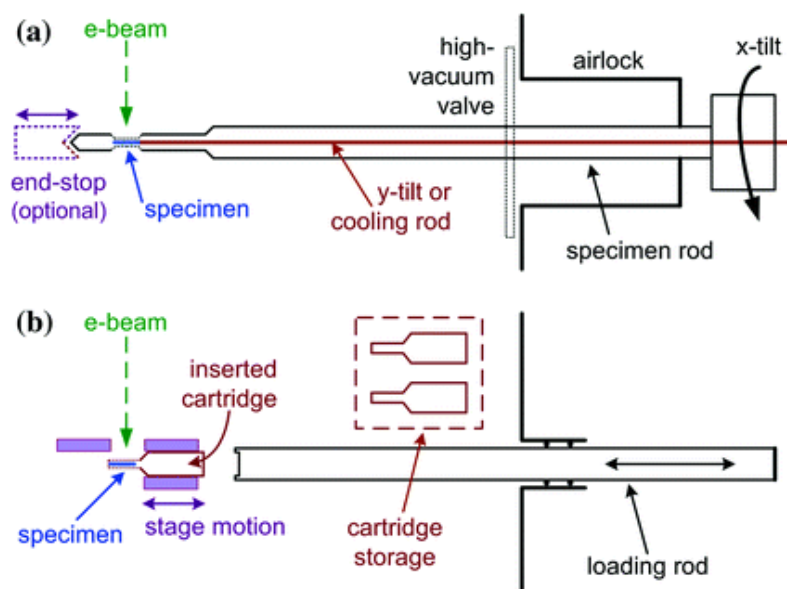


Figure 3. 25: Schematic diagrams of (a) a side-entry and (b) a top-entry specimen holder [79].

In a side-entry stage, the specimen is clamped close to the end of a rod-shaped specimen holder and is inserted horizontally through the airlock. The airlock-evacuation valve and a high-vacuum valve are activated by rotation of the specimen holder about its long axis. In a top-entry stage, the specimen is clamped to the bottom end of a cylindrical holder that is equipped with a conical collar [79].

Imaging Modes of a TEM

The imaging system of a TEM consists of at least three lenses: the objective lens, the intermediate lens (or lenses), and the projector lens. The intermediate lens can magnify the first intermediate image, which is formed just in front of this lens, or the first diffraction pattern, which is formed in the focal plane of the objective lens, by reducing the excitation. In many microscopes, an additional diffraction lens is inserted between the objective and intermediate lenses to image the diffraction pattern and to enable the magnification to be varied in the range 10^2 to 10^6 [80].

TEM Imaging System

The imaging lenses of a TEM produce a magnified image or an electron diffraction pattern of the specimen on a viewing screen or a camera system. The spatial resolution of the image is largely dependent on the quality and design of these lenses, especially on the first imaging lens: the objective.

Objective lens

An objective lens is the lens closest to the specimen. It is a strong lens with a small focal length. Because focusing power depends on lens excitation, the current for the objective lens must be highly stabilized, using negative feedback within its dc power supply.

Objective aperture

Although in practice, the objective behaves like a thick lens. Accordingly, an electron that leaves the specimen parallel to the optic axis is deflected at the principal plane and crosses the axis at the BFP, a distance f below the principal plane.

Projector lens

The purpose of the projector lens is to produce an image or a diffraction pattern across the entire TEM screen, with an overall diameter of several centimeters. As in the case of light optics, the final image magnification is the algebraic product of the magnification factors of each of the imaging lenses.

TEM screen and camera

A phosphor screen is used to convert the electron image to a visible form. It consists of a metal plate coated with a thin layer of powder that fluoresces under electron bombardment. The traditional phosphor material is zinc sulfide (ZnS) with small amounts of metallic impurity added. The phosphor is chosen so that light is emitted in the middle of the spectrum (yellow-green region), to which the human eye is most sensitive. Nowadays, photographic film has been largely replaced by electronic image-recording devices based on charge-coupled diode (CCD) sensors [79].

Vacuum System

It is essential to remove most of the air from the inside of a TEM column so that the accelerated electrons can follow the principles of electron optics, rather than being scattered by gas molecules. In addition, the electron gun requires a sufficiently good vacuum in order to prevent a high-voltage

discharge and to avoid oxidation of the electron-emitting surface. There are several types of vacuum that can be used in TEM, such as A mechanical rotary pump (RP), a diffusion pump (DP), a turbomolecular pump (TMP), and an ion pump [79].

Sample Preparation

The procedure involves several steps, each of which is very strict, in order to produce an electron-transparent thin vitrified film in a reproducible manner. Preparing to deposit the suspension on the TEM support grid A 4–5 μl drop of an aqueous suspension of previously dispersed particles is spread on a copper grid (300 or 400 mesh), 3 mm in diameter, coated with a holey carbon film (Figure 3.26). The film is usually thinner in the center of the holes. The average size of the holes must be 1–3 μm [93].

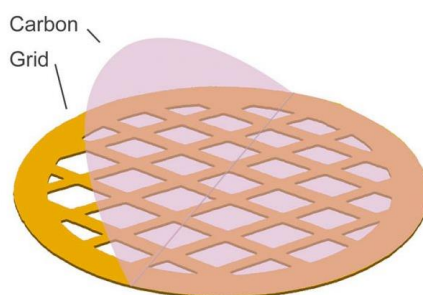


Figure 3. 26: Copper grid.

In our work, all samples were measured as colloidal, and we drop a sample on the copper grid, then dried it and measured it through TEM.

3.8.3 Experimental Aspect of Dynamic Light Scattering

Malvern Zetasizer Nano S model was used to measure the size of the nanoparticles; its instrument is shown in Figure 3.27



Figure 3. 27: Dynamic light scattering (DLS) instrument.

Dynamic light scattering measures the speed at which the particles are diffusing due to Brownian motion. This is achieved by measuring the rate at which the intensity of the scattered light fluctuates when detected using a suitable optical arrangement. The intensity fluctuations of scattered light arise when a cuvette, containing particles which are stationary illuminated by a laser and view the sample cell through a frosted glass screen. Figure 3.28 shows a classical speckle pattern that would appear.

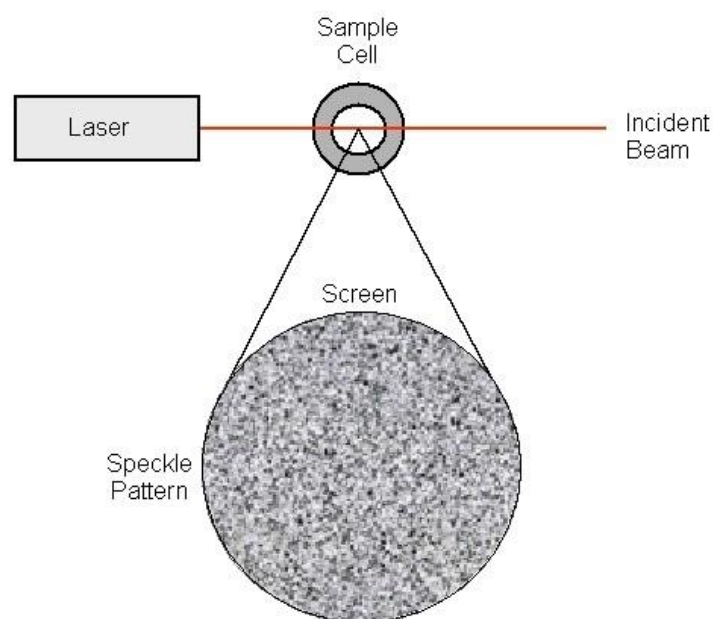


Figure 3. 28: Schematic representation of a speckle pattern.

The speckle pattern will be constant both in size and position because the entire system is stationary. This is because of the moving particles phase addition is continuously evolving and making new patterns. The rate at which these fluctuations in intensity occur depends on the particle size. Figure (3.29 A) shows the dark spaces where the scattered light phase additions are mutually destructive and cancel each other out. Figure (3.29 B) shows the bright blobs of light in the speckle pattern where the particle-scattered light reaches the same phase and constructively interferes with forming a bright patch.

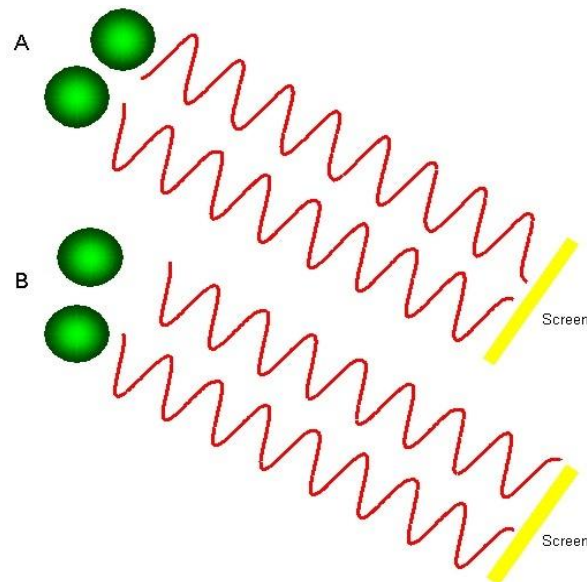


Figure 3. 29: *The observed signal depends on the phase addition of the scattered light falling on the detector. (A) two beams interfere and cancel each other out, resulting in a decreased intensity detected. (B) two beams interfere and enhance each other resulting in an increased intensity detected.*

Figure 3.30 shows schematically common variations in intensity resulting from large particle dispersion and small particle dispersion. The large particles cause the intensity to fluctuate less rapidly than the small ones.

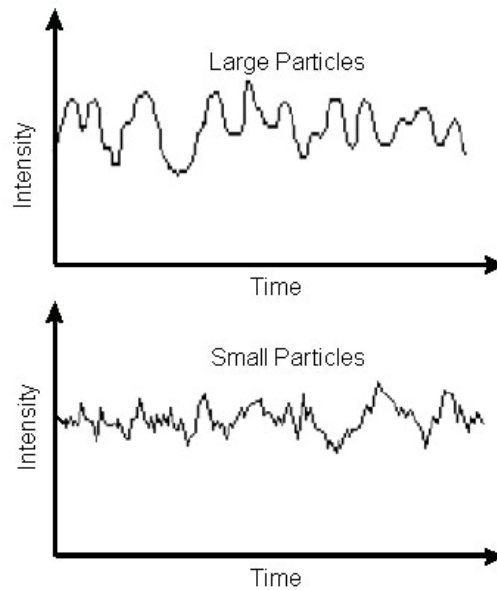


Figure 3. 30: *Intensity fluctuations for large and small particles.*

It is possible to calculate the direct spectrum of frequencies in the intensity fluctuations resulting from the particles Brownian motion, but it is inefficient to do so. Using a device called a digital autocorrelator is the best way to do this.

3.8.3.1 Dynamic Light Scattering Optical Configuration

There are six main components in a typical dynamic light scattering system. Firstly, a laser (1) Provides a source of monochromatic light to illuminate the sample in a cell (2). Most of the laser beam passes through the sample for diluted concentrations, but some scattered through the particles within the sample at all angles. The scattered light intensity is uniform in all directions with the amount of Rayleigh scattering depending on the particle size and the incident light wavelength. Detector (3) measures the scattered light. The position of the detector will be at either 173° or 90° , depending upon the particular model. The scattered light intensity must be within a specific range for the detector to measure it successfully. The detector will become saturated if too much light is

detected. To overcome this, an attenuator (4) is used to reduce the laser source intensity and hence reduce the intensity of scattering. For samples that do not scatter much light, such as very small particles or low concentration samples, it is necessary to increase the amount of scattered light. And by using the attenuator to control the laser light, the scattered light for large samples or samples with higher concentration decreased. Nano software automatically determines the appropriate attenuator position and covers a transmission range of 100% to 0.0003%. The scattering intensity signal from the detector is passed to a digital processing board called a correlator (5). The correlator compares the scattering intensity to derive the rate at which the intensity varies at successive time intervals. This information is then passed on to a computer (6), where the Nano software will analyze the data and derive size information [7, 83]. Measurements that had taken months to set up and hours to make were now reduced to minutes [82].

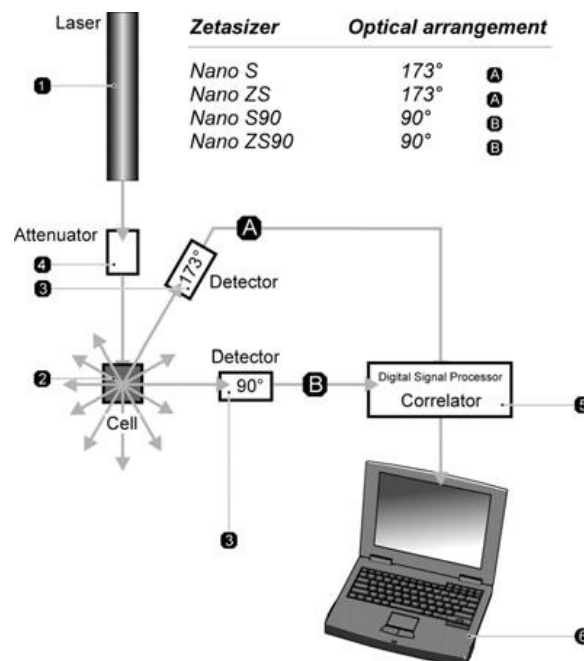


Figure 3. 31: Optical configuration of the Zetasizer Nano series for dynamic light scattering measurements

3.8.3.2 Variable Measurement Position for Sizing

The measurement position is changed by moving the focusing lens, which is determined automatically by the Nano software. This allows a much broader range of sample concentrations to be measured. The measurement position is automatically determined through a combination of the intensity of the light scattered and the intercept of the correlation function. It is desirable to maximize the amount of scattering from the sample for small particles or samples at low concentrations. The laser will cause flare as it passes through the cuvette wall and into the dispersant, this flare may swamp the signal from the scattering particles. As shown in (Figure 3.32 a) moving the measurement point away from the cuvette wall towards the center of the cuvette will remove this effect. Large particles or samples at high concentrations scatter much lighter. In this condition, measuring closer to the cuvette wall will reduce the effect of multiple scattering by minimizing the scattered light path length (Figure 3.32 b).

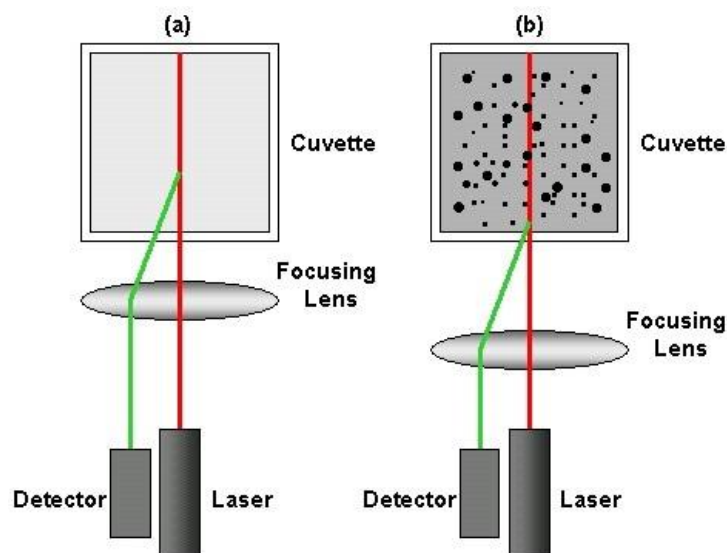


Figure 3. 32: Schematic diagram showing the measurement position for (a) small, weakly scattering samples and for (b) large, concentrated, and opaque samples. The change in measurement position achieved by moving the focusing lens accordingly [83, 94].

In our work, all the samples were measured as a colloidal. The ZnS samples were filtered before the measurements.

3.8.4 Experimental Aspect of X-Ray Diffraction

The SmartLab SE is a highly versatile multipurpose X-ray diffractometer with built-in intelligent guidance, which is shown in Figure 3.33. X-ray diffraction technique studies the crystal structures and atomic spacing. X-ray diffractometers consist of three essential elements: an X-ray tube, a sample holder, and an X-ray detector [95].

Sources The most common radiation source in the lab is the X-ray tube, which, operating at a typical power of 2 kW, can provide photon fluxes at the sample close to 10^8 ph/s.

Detectors Disregarding the physical nature of the X-ray detection event and its conversion into a machine-readable electrical current.



Figure 3. 33: SmarLab SEX-Ray diffraction instrument.

Samples Usually consisting of incoherent particles of sizes below $10\ \mu\text{m}$ to a few nm for very small specimens of nanoparticles, powder samples

need to be confined in suitable sample holders, which must not affect or disturb, the collected data, ideally giving no contribution at all [96].

Bragg's law relates electromagnetic radiation's wavelength to the angle of diffraction and the lattice spacing in a crystalline sample. Then, the diffracted X-rays detected, processed, and counted. By scanning the specimen through a range of 2θ angles, all possible diffraction directions of the lattice should be achieved due to the random orientation of the powdered material. As it is known, each compound has a set of unique d-spacings, conversion of the diffraction peaks to d-spacings allows identification of the compound. This identification usually accomplished by comparison of d-spacings with standard reference patterns [95]. X-rays are generated by heating a filament to produce electrons in a cathode ray tube, accelerating the electrons to a target by applying a voltage, and bombarding the target material with electrons. Characteristic X-ray spectra are produced when electrons have enough energy to dislodge electrons in the inner shell of the target material. These X-rays are collimated and directed onto the specimen. As the specimen and detector are rotated, the reflected X-rays intensity is recorded. When the geometry of the incident X-rays impinging the specimen satisfies Bragg's law, constructive interference occurs and a peak in intensity appears. A detector records and processes the signal of the X-ray and converts it to a count rate, which is then output to a device such as a computer monitor or printer [95].

In the present work, the samples were prepared as a colloidal, centrifugation, dehydration then measures the obtained powder.

3.8.5 Experimental Aspects of Fourier Transform Infrared Spectroscopy (FTIR)

Fourier-transform infrared spectroscopy model (IRAffinity-1S) is used to obtain an infrared spectrum of absorption or emission of a solid, liquid, or gas. The instrument is shown in Figure 3.34



Figure 3. 34: FT-IR instrument.

Spectrometers are generally comprised of a light source, which is a system for selecting the light frequency and a detector. (Figure 3.35) [85].

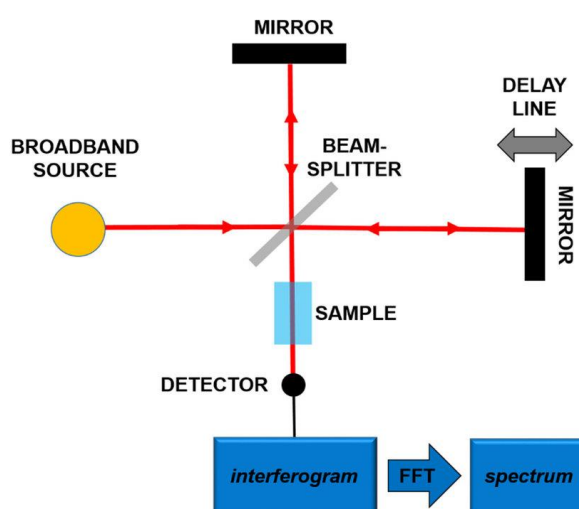


Figure 3. 35: Principle of the Fourier transform spectrometer.

The more sophisticated Fourier Transform Infrared (FTIR) instruments record an infrared interference pattern generated by a moving mirror, and a computer transforms this into an infrared spectrum [73].

The Fourier transform spectrometer (FTIR) is based on the Michelson interferometer [85]. Besides, the fast Fourier transform algorithm can calculate the discrete Fourier transform and its inverse, so the raw signal is converted quickly into a recognizable absorbance spectrum. FT-IR systems are made up of three components: the radiation source, the interferometer, and the detector. Figure 3.36 shows the basic components of an FT-IR spectrometer, including the light source, the detector and a Michelson interferometer (which consists of a fixed mirror, moving mirror, and a beam splitter) [87]. The light source is aimed at a beam splitter which sends 50% of the light to a fixed mirror M1, and the rest strikes to the movable mirror M2, which can move along the axis. When the reflected beams bounce back and are recombined, an interference pattern results. Mirrors converge on the sample reflect the two beams, passing through the beam splitter, before reaching the detector [85]. **IR radiation** is obtained from the thermal emission of a suitable source, the most common radiation source being an inert solid heated electrically in the range from 1,000°C to 1,800°C. There are several types of sources, such as the Nernst glower, the Globar source, the Nichrome coil, the high-pressure mercury arc, and the carbon dioxide laser. They all produce continuous radiation but have different radiation energy profiles and consequently, different applications [87].

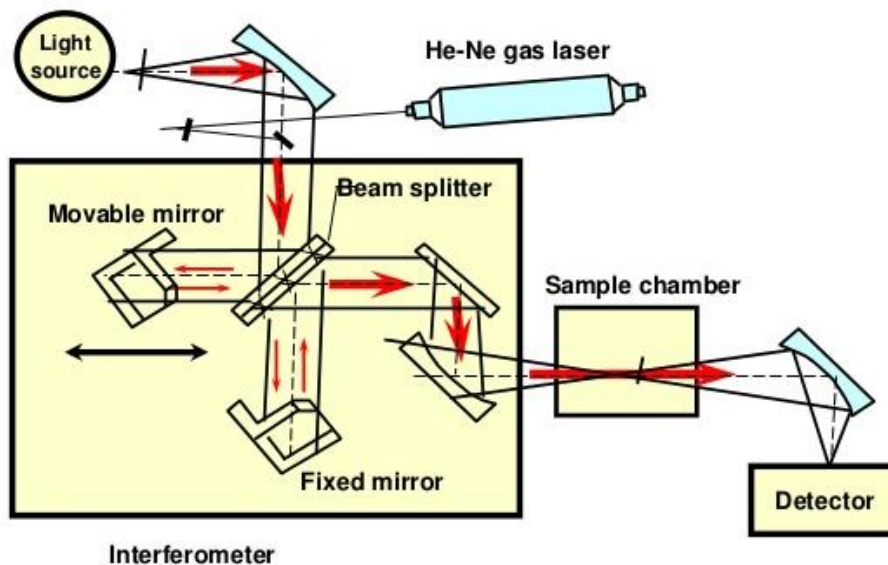


Figure 3. 36: Basic component of an FT-IR spectrometer, including the light source, the detector, and a Michelson interferometer consisting of a beam splitter, a fixed mirror, and a moving mirror.

The **interferometer** produces interference signals, which contain IR spectral information generated after a beam has passed through a sample. A **detector** produced repetitive interference signals and measured as a function of the optical path difference.

Instead of examining each wavenumber in succession, all frequencies are examined simultaneously. After the beam has passed through the sample or has been reflected, the measured signal is the resulting interferogram, which contains information from the entire IR region. Finally, the beam passes to the detector, and the measured signal is digitalized and sent to the computer. This Fourier transformation of the signal can be viewed as a mathematical method of converting the individual frequencies from the interferogram, by using a mathematical procedure able to transform a function from the time domain to the frequency domain.

Many spectroscopic techniques have been used to obtain IR spectra for the characterization of the molecular composition (Figure 3.37). In FT-IR transmittance techniques, the sample is placed in the path of the IR beam and scanned (Figure 3.37a). In diffuse reflectance FT-IR (DRIFT) spectroscopy, the IR beam is projected into the sample, where it is reflected by, scattered by, and transmitted through the sample. The part of the IR light that is diffusely scattered within a sample and returned to the detector optics is considered to be a diffuse reflection (Figure 3.37b). High-scattering samples, such as freeze-dried biological samples can be analyzed. In attenuated total reflectance (ATR) spectroscopy, the sample is placed onto an optically dense crystal of relatively high-refractive index, needing little or no sample preparation (Figure 3.37c). The IR beam is reflected from the internal surface of the crystal and creates an evanescent wave, which extends beyond the surface of the crystal and projects into the sample in close contact with the ATR crystal. Some of the energy of the evanescent wave is absorbed by the sample, and the reflected radiation is passed to the detector in the spectrometer as it exits the crystal.

For powders, potassium bromide (KBr) is applied to a sample in the range from 0.2% to 1%, and then the mixture is finely ground into a fine powder and subsequently compressed into a small, thin, quasi-transparent disc as shown in Figure 3.38 [7, 87]. KBr and NaCl are chosen as neither compound show an IR active stretch in the region typically observed for organic and some inorganic molecules. They are transparent over the whole of the IR range. Acquired IR spectra are subtracted from a background spectrum to remove unwanted signals, particularly, any water present in the atmosphere [7, 73].

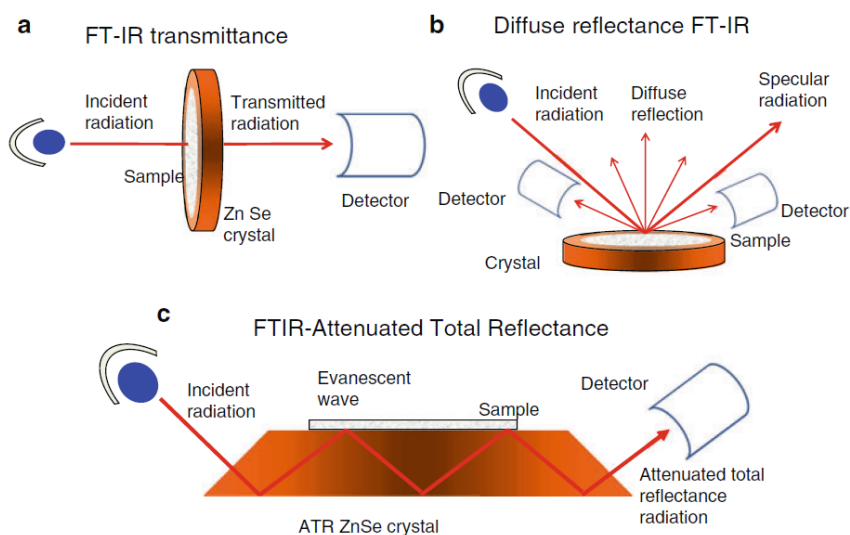


Figure 3. 37: The main spectroscopic methods used to characterize the molecular composition and stress response by FT-IR spectroscopy: (**a**) transmittance FT-IR; (**b**) diffuse reflectance FT-IR; (**c**) attenuated total reflectance (ATR) FT-IR [97]. IR measurement samples can be prepared in several ways. For liquids, a drop of sample sandwiched between two salt plates, Such as NaCl and stove-dried before being measured [7, 87].



Figure 3. 38: The preparation of a KBr for IR spectroscopy.

In the present work, the samples were prepared as colloidal, centrifugation, dehydration then the obtained powder mixed with KBr and measure in FT-IR.

3.9 Measurements of the Current-Voltage

The current-voltage of the solar cell samples was measured by using the LED Solar Simulator device (VeraSol-2), as shown in Figure 3.39. Also, efficiency and fill factor were obtained.

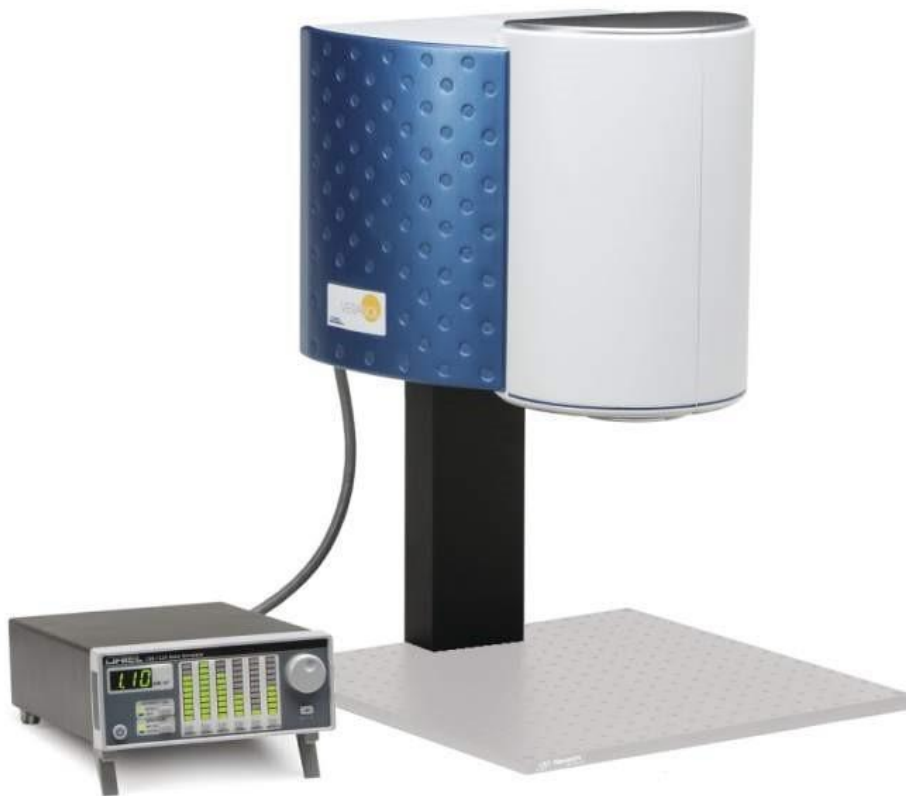


Figure 3. 39: I-V curve instrument.

CHAPTER IV

Results and Discussion

CHAPTER IV

RESULTS AND DISCUSSION

4.1 Results of Ultraviolet-Visible Spectroscopy

The absorptions of UV-Vis spectra are associated with electronic transitions from the ground state to an excited state [98]. In the present work, the UV-Vis spectroscopy technique used to study the surface plasmon resonance (SPR) of AuNPs, AgNPs, and ZnSNPs. Also, the absorption spectra of Ag/ZnS core-shell nanoparticles.

4.1.1 UV-Vis for Gold Nanoparticle Prepared at Different Concentrations of Sodium Borohydride

Figure 4.1 shows the absorption spectra of AuNPs that prepared using cetyltrimethylammonium bromide (CTAB) as a capping agent and at different concentrations of sodium borohydride (NaBH_4), according to Table 3.1. From the absorption spectra Figure 4.1, we noted that the maximum absorption band was seen at 527 nm, 526 nm, 526 nm, and 526 nm for the samples AuNPs(S1), AuNPs(S2), AuNPs(S3), and AuNPs(S4), respectively. The positions of these bands are relatively stable, with the change of the NaBH_4 concentrations. This points out to the fact that the majority of NaBH_4 concentrated as a reducing agent is not important for controlling the particle size, but it is essential and helps in the formation of AuNPs. The full width at half maximum (FWHM) has increased with increasing the NaBH_4 concentrations. All these bands are known as the surface plasmon resonance (SPR) of the AuNPs. Surface plasmon resonance (SPR) is an optical phenomenon originates from coupled oscillations of the electromagnetic field and density of electron plasma on a metal surface [99]. This phenomenon generated by light when it interacts

with conductive nanoparticles that are smaller than the incident wavelength [100].

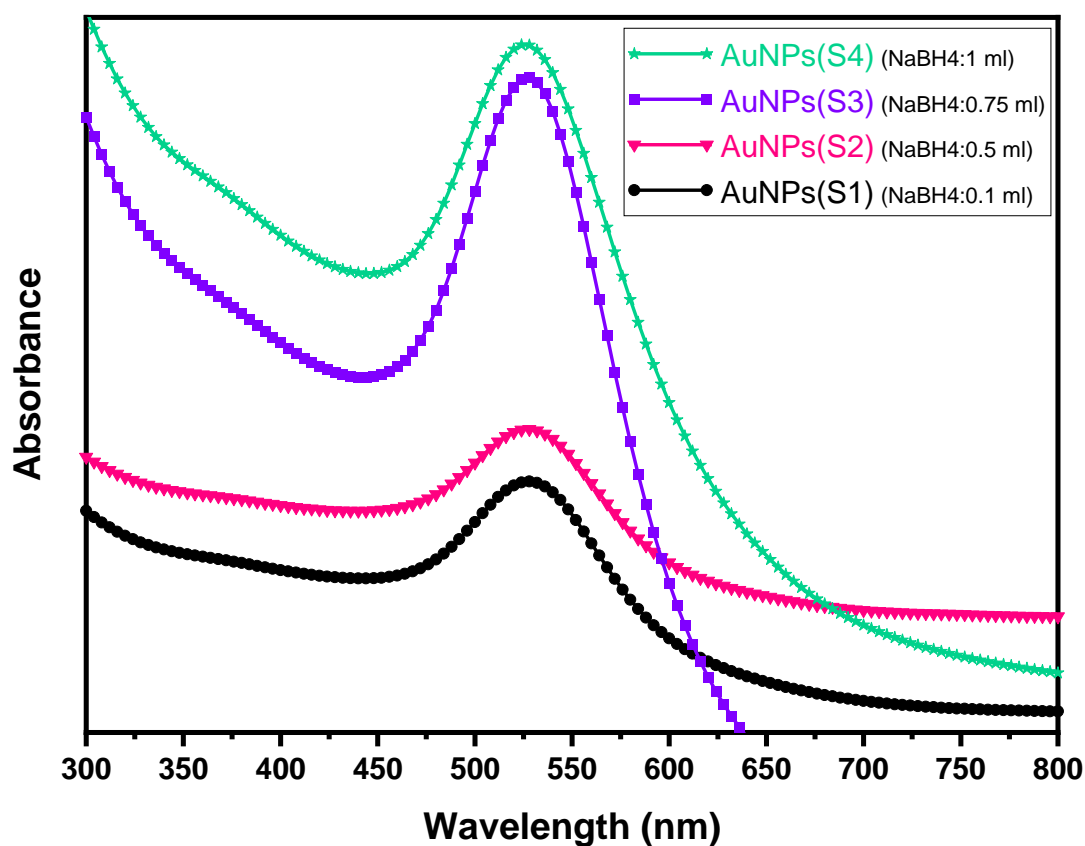


Figure 4. 1: UV-Vis absorbance spectra of AuNPs using CTAB as a stabilizing agent and at different concentration of NaBH₄ as a reducing agent.

When light irradiates a small spherical metallic nanoparticle, the oscillating electric field causes the conduction electrons to oscillate coherently. This is schematically pictured in Figure 4.2. When the cloud of the electrons is displaced relative to the nuclei, a restoring force arises from Coulomb attraction between nuclei and electrons that result in the oscillation of the electron cloud relative to the nuclear framework. The frequency of the oscillation is determined by four factors: the shape and size of the charge distribution, the effective electron mass, and the density of electrons. The

collective oscillation of the electrons is termed the dipole plasmon resonance of the particle [101].

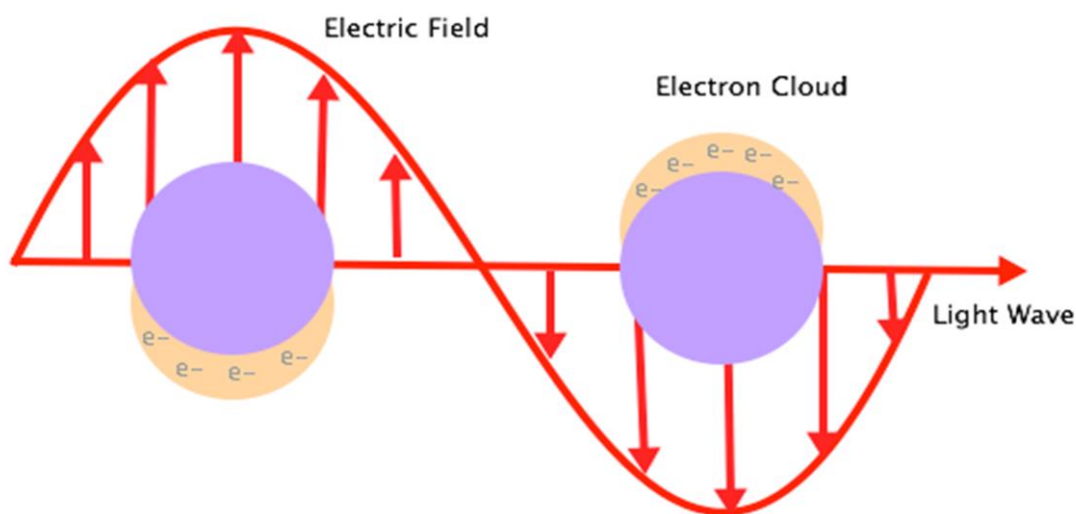


Figure 4. 2: Surface plasmon resonance of metal nanoparticle.

4.1.2 UV-Vis for Gold Nanoparticle Prepared at Different CTAB Concentrations

The absorption spectra of gold nanoparticles prepared using sodium borohydride (NaBH_4) as a reducing agent and at different concentrations of cetyltrimethylammonium bromide (CTAB) as a capping agent, according to Table 3.2, are shown in Figure 4.3. From this Figure, it has been seen that sharp peaks appeared at a wavelength of 528 nm for all the samples [AuNPs(S5) to AuNPs(S8)] which were synthesized at 0.2 gm, 0.3 gm, 0.4 gm, and 0.5 gm of CTAB concentrations added to 50 ml of distilled water, respectively. These bands are assigned to the surface plasmon resonance bands of AuNPs. The full width at half maximum (FWHM) has clearly increased with increasing CTAB concentrations. Also, as the CTAB concentrations increased, the bands became sharper. This may be due to the increase in the uniformity of AuNPs.

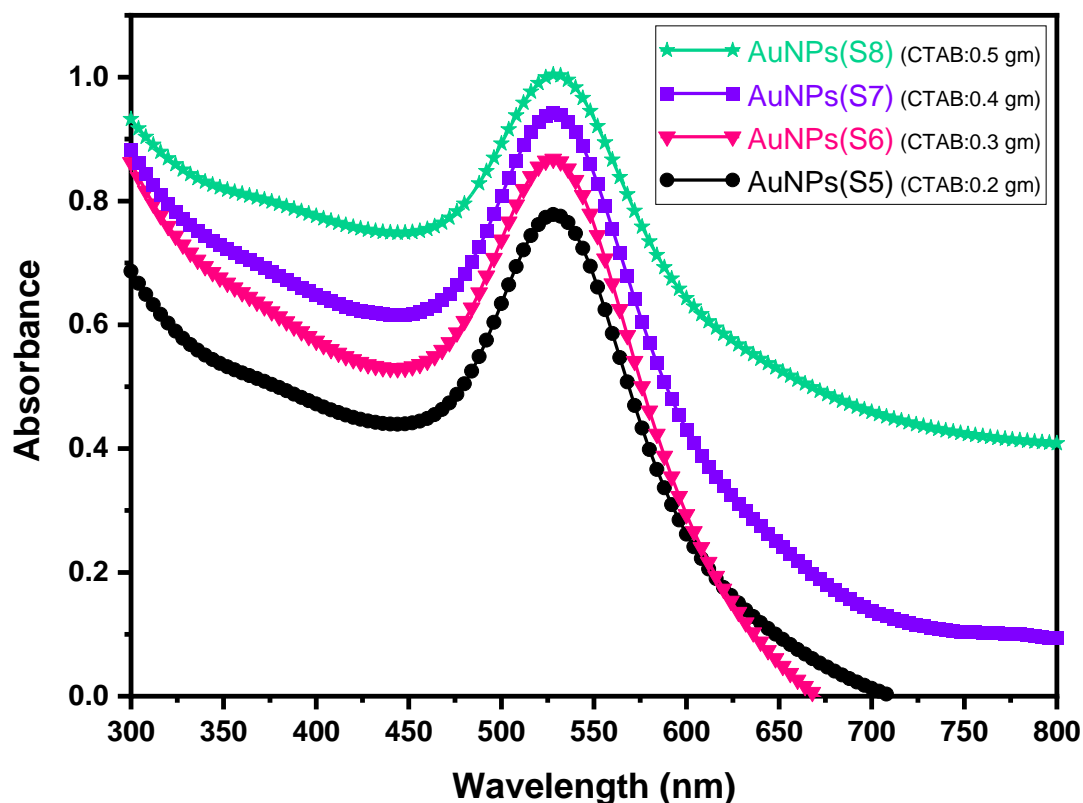


Figure 4. 3: UV-Vis absorption spectrums of gold nanoparticles synthesized by reduction $\text{HAuCl}_4 \cdot 3\text{H}_2\text{O}$ using NaBH_4 and stabilize it by different concentrations of CTAB [AuNPs(S5) 0.2gm, AuNPs(S6) 0.3gm, AuNPs(S7) 0.4gm, AuNPs(S8) 0.5gm].

4.1.3 UV-Vis for Silver Nanoparticle Prepared at Different Concentrations of Silver Nitrate

Figure 4.4 shows the absorption spectra of AgNPs prepared using NaBH_4 as a reducing agent, cetyltrimethylammonium bromide (CTAB) in chloroform as a surfactant, and polyvinylpyrrolidone (PVP) as a stabilizing agent at various concentrations of silver nitrate according to Table 3.3. It was seen that the maximum absorption band observed at 414 nm, 413 nm, 415 nm, 417 nm, and 425 nm for AgNPs(S9), AgNPs(S10), AgNPs(S11), AgNPs(S12), and AgNPs(S13), respectively. These bands could account for the surface plasmon resonance (SPR) of AgNPs. We noted that these bands were shifted to a higher wavelength (redshift) with increasing AgNO_3 concentration during the reaction process.

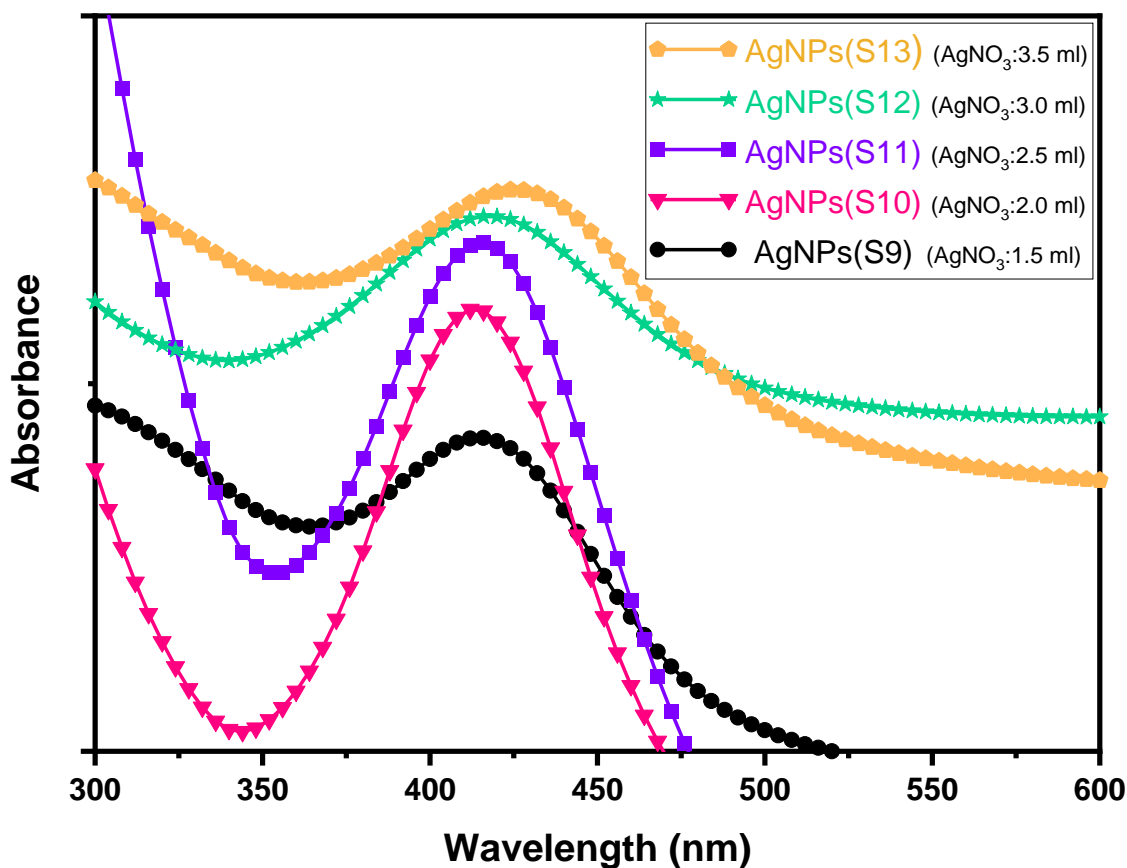


Figure 4. 4: UV-Vis spectra of the silver nanoparticle samples prepared by diluted a different silver nitrate AgNO_3 (1M) concentrations [AgNP(S9):1.5ml, AgNP(S10):2ml, AgNP(S11):2.5ml, AgNP(S12):3ml, AgNP(S13):3.5ml] in (0.1M) chloroform (first solution), and diluted a 0.8ml of (1M) NaBH_4 in (0.1M) chloroform (second solution). Mixed these two solutions and add 0.4 ml of (0.5%) PVP during the ultrasonication.

The change of the SPR band position may confirm that the particle size increase with increasing the concentration of silver nitrate as general behavior Figure 4.5. The broadening of the plasmon band increased as the silver nitrate concentrations increased. Moreover, the full width at half maximum (FWHM) increased with increasing in AgNO_3 concentrations. The increase of the particle size with increasing the silver nitrate concentration is perhaps related to the increase in Ag^0 ions. So far, none

of the ions gather in a place to each other, leading to an increase in the size and a decrease in the number of nanoparticles in the solution.

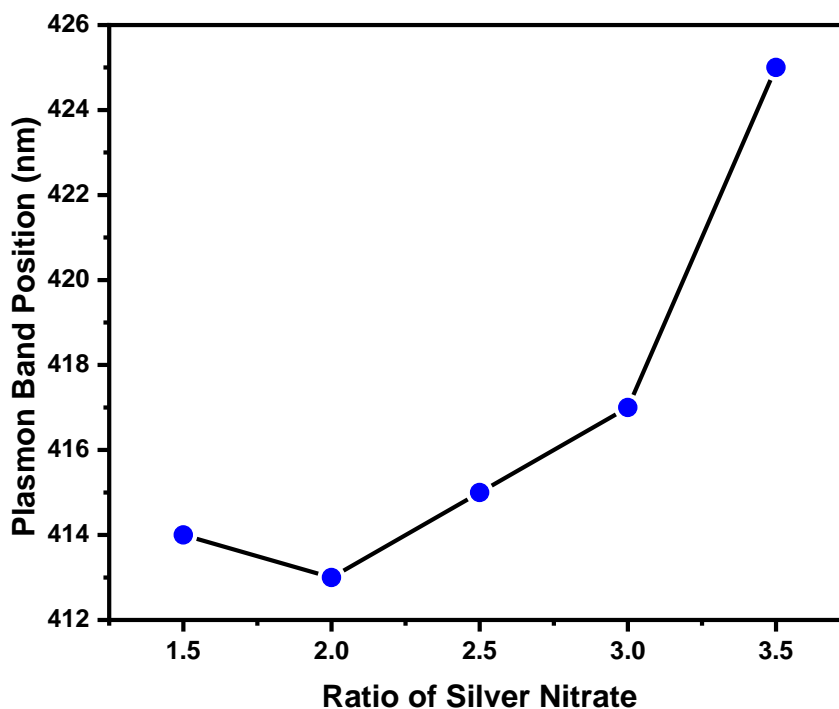


Figure 4. 5: Change of surface plasmon band position with silver nitrate concentrations.

4.1.4 UV-Vis for Zinc Sulfide Nanoparticle Prepared at Different Concentrations of Zinc Acetate Dihydrate

Figure 4.6 shows the absorption spectra of the ZnSNPs that synthesized using a fixed molar ratio of sodium sulfide (0.2M) and various molar ratios of zinc acetate dihydrate, according to Table 3.4. It has been found that ZnSNPs show absorption band at around 305 nm, 289 nm, 287 nm, 284 nm, and 283 nm for the zinc sulfide samples at (0.2M) of sodium sulfide and different zinc acetate dihydrate molar ratio ZnSNPs(S14) 0.1M, ZnSNPs(S15) 0.2M, ZnSNPs(S16) 0.3M, ZnSNPs(S17) 0.4M, and ZnSNPs(S18) 0.5M, respectively. These bands were indicating for the formation of ZnSNPs. We noted from Figure that as the zinc acetate dihydrate molar ratio increased, the absorption band decreased. As demonstrated in Figure 4.7, it can be shown that with increasing the zinc

acetate dihydrate molar ratio, the band position shifted toward lower wavelengths (blue shift). According to the quantum size effect, when the absorption peak shift toward lower wavelengths (blue shift), the particle size decreases, and the energy gap increased, which mean that when the zinc acetate dihydrate molar ratio increased the particle size decreased. Generally, the optical absorption related to electrons excitation from the valence band to the conduction band, and it is used to calculate the optical band energies of the prepared nanoparticles. Tauc's plot method was used to estimate the band gap of our samples. Tauc's classical relation of optical absorption in semiconductor shown in following eq.,

$$(\alpha hv) = A (hv - E_g)^n \quad (4.1)$$

Where α is the absorption coefficient, h is the plank's constant, ν is the frequency of incident light, A is empirical value, E_g is the band gap of the samples (i.e., a separation between the bottom of the conduction band and top of the valence band), and n is constant which depends on the type of transition. i.e, $n= 1/2$ for allowed direct transition (e.g., ZnS), $n=2$ for allowed indirect transition [102-105]. In this study, the transitions are direct, so we consider $n=1/2$. Extrapolation of the straight-line portion of $(\alpha hv)^2$ vs. hv graph (shown in Figure 4.8) to hv axis at $(\alpha = 0)$ gives energy band gap values. The estimated band gap values for samples ZnSNPs(S14), ZnSNPs(S15), ZnSNPs(S16), ZnSNPs(S17), and ZnSNPs(S18) were found to be 4.66 eV, 4.78 eV, 4.92 eV, 4.93 eV, and 4.94 eV, respectively. These band gap values are in accordance with that reported in the literature [106]. The band gap values of ZnSNPs are red-shifted from the bulk band gap of ZnS ($E_g = 3.54$ eV).

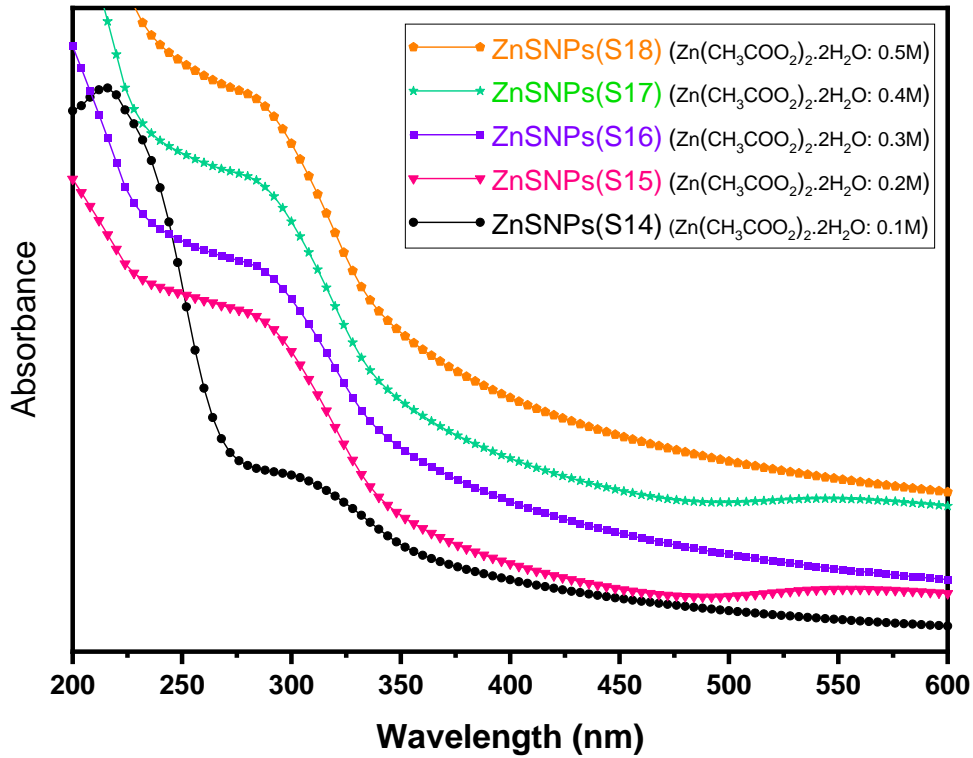


Figure 4. 6: UV-Vis absorbance spectra of the zinc sulfide nanoparticle prepared by adding 50 ml of sodium sulfide (0.2M) and 50 ml of zinc acetate dihydrate at different concentrations [ZnSNPs(S14) 0.1M, ZnSNPs(S15) 0.2M, ZnSNPs(S16) 0.3M, ZnSNPs(S17) 0.4M, ZnSNPs(S18) 0.5M].

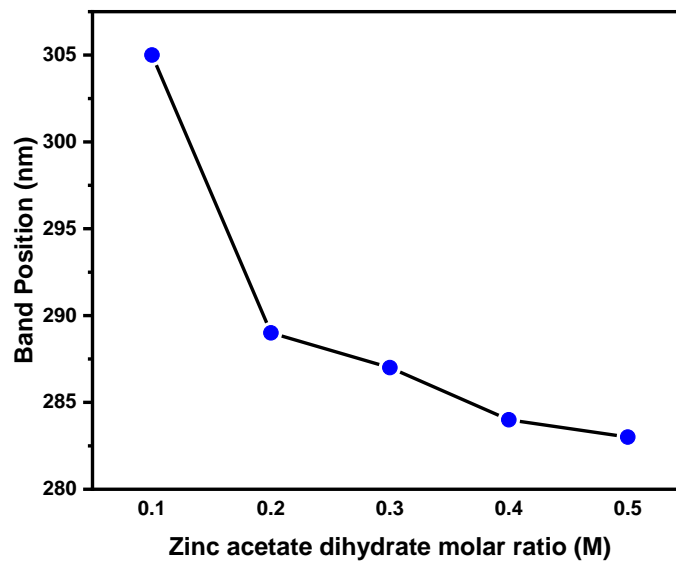


Figure 4. 7: Plasmon band position of ZnSNPs as a function of zinc acetate dihydrate molar ratio.

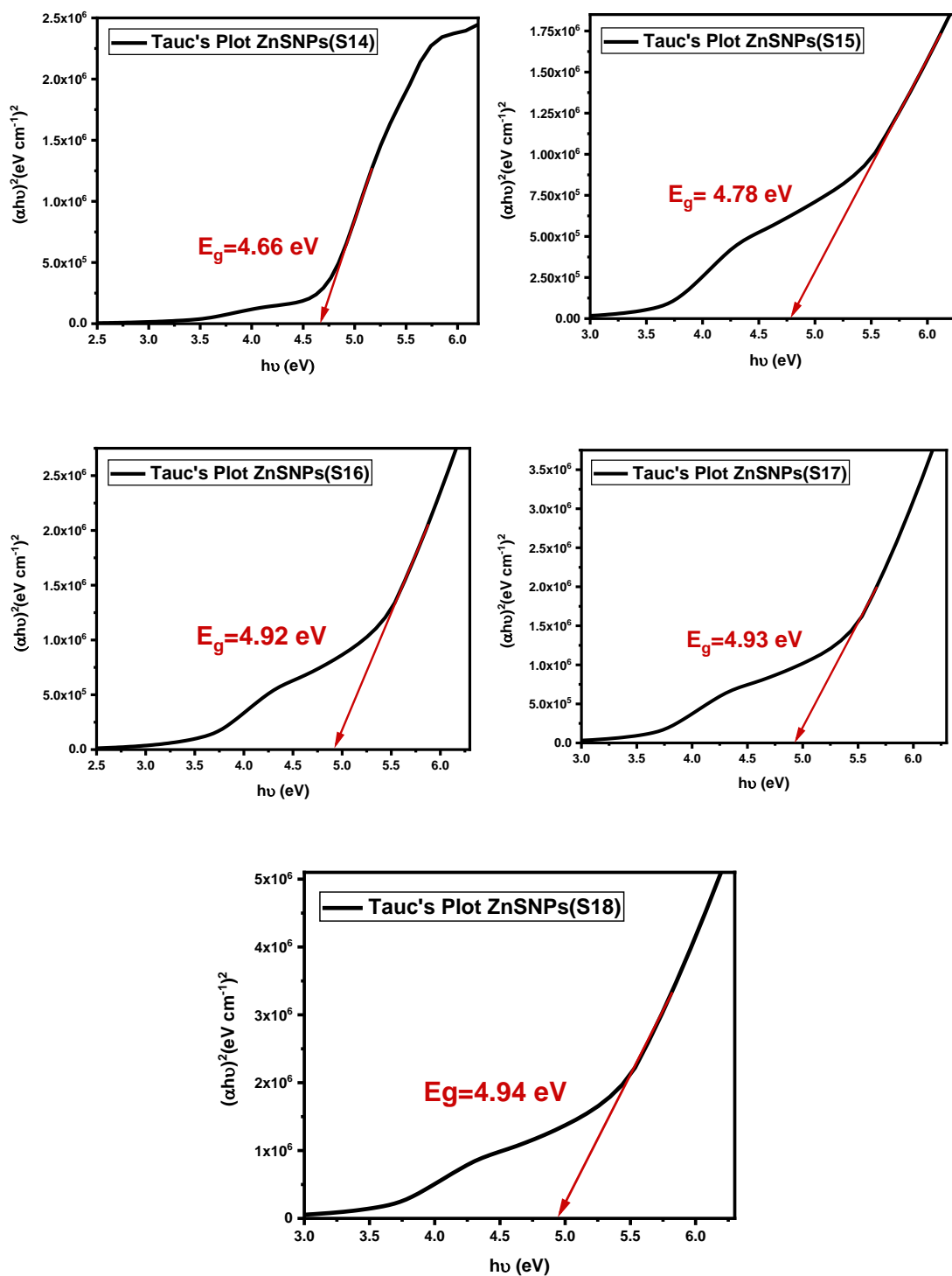


Figure 4. 8: Tauc's Plot of ZnSNPs prepared at a different molar ratio of zinc acetate dihydrate [(ZnSNPs(S14)-ZnSNPs(S18))].

4.1.5 UV-Vis for Zinc Sulfide Nanoparticle Prepared at Different Temperatures

Figure 4.9 shows the absorption spectra of ZnSNPs prepared using sodium sulfide (0.2M) and zinc acetate dihydrate (0.1M) at different temperatures, according to Table 3.5. The maximum absorption bands were seen at 308 nm, 307 nm, 304 nm, 303 nm, 302 nm, and 300 nm for the samples ZnSNPs(S19) ($T=50^\circ$), ZnSNPs(S20) ($T=60^\circ$), ZnSNPs(S21) ($T=70^\circ$), ZnSNPs(S22) ($T=80^\circ$), ZnSNPs(S23) ($T=90^\circ$), and ZnSNPs(S24) ($T=100^\circ$), respectively. These bands are implying the formation of ZnSNPs.

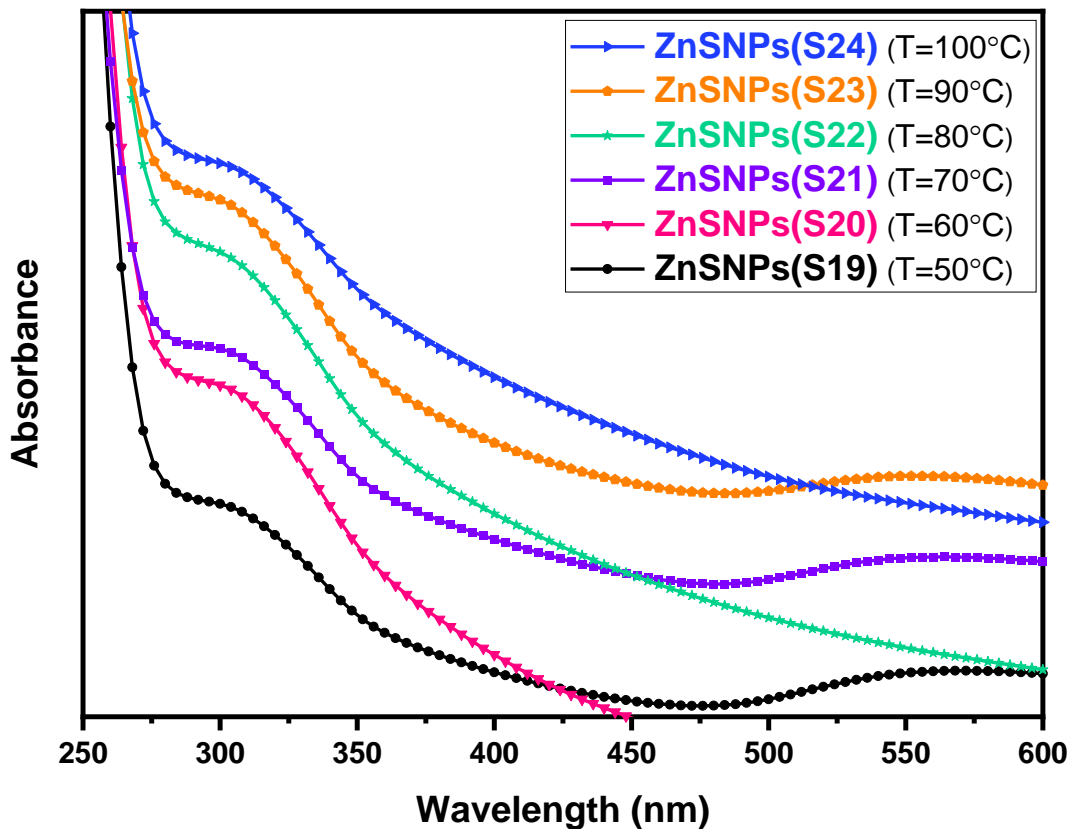


Figure 4. 9: UV-Vis absorbance spectra of the zinc sulfide nanoparticle prepared by adding an equivalent quantity of sodium sulfide (0.2M) and zinc acetate dihydrate (0.1M) at different temperatures [ZnSNPs(S19) 50°C , ZnSNPs(S20) 60°C , ZnSNPs(S21) 70°C , ZnSNPs(S22) 80°C , ZnSNPs(S23) 90°C , ZnSNPs(S24) 100°C].

The band position was decreased (blueshift) with increased temperatures. This is due to the decrease of the particle size discussed by the quantum size effect. The particle size decrease with increasing the temperature (Figure 4.10) is probably due to the acceleration of Zn^{+2} and breaks the bonds of the surface of the nanoparticles and thus reduces the size of ZnSNPs as a result of the increases in thermal energy. Further optical data has been analyzed by using Tauc's relation, as earlier discussed. The resultant values for the approximated energy band gap were deduced as 4.77 eV, 4.74 eV, 4.75 eV, 4.74 eV, 4.73 eV, 4.66 eV. The energy band gap in this range is larger than the bulk zinc sulfide that is equal to = 3.54 eV, which confirming the formation of zinc sulfide nanoparticles. The energy band gap in this range is also shown by another research [107].

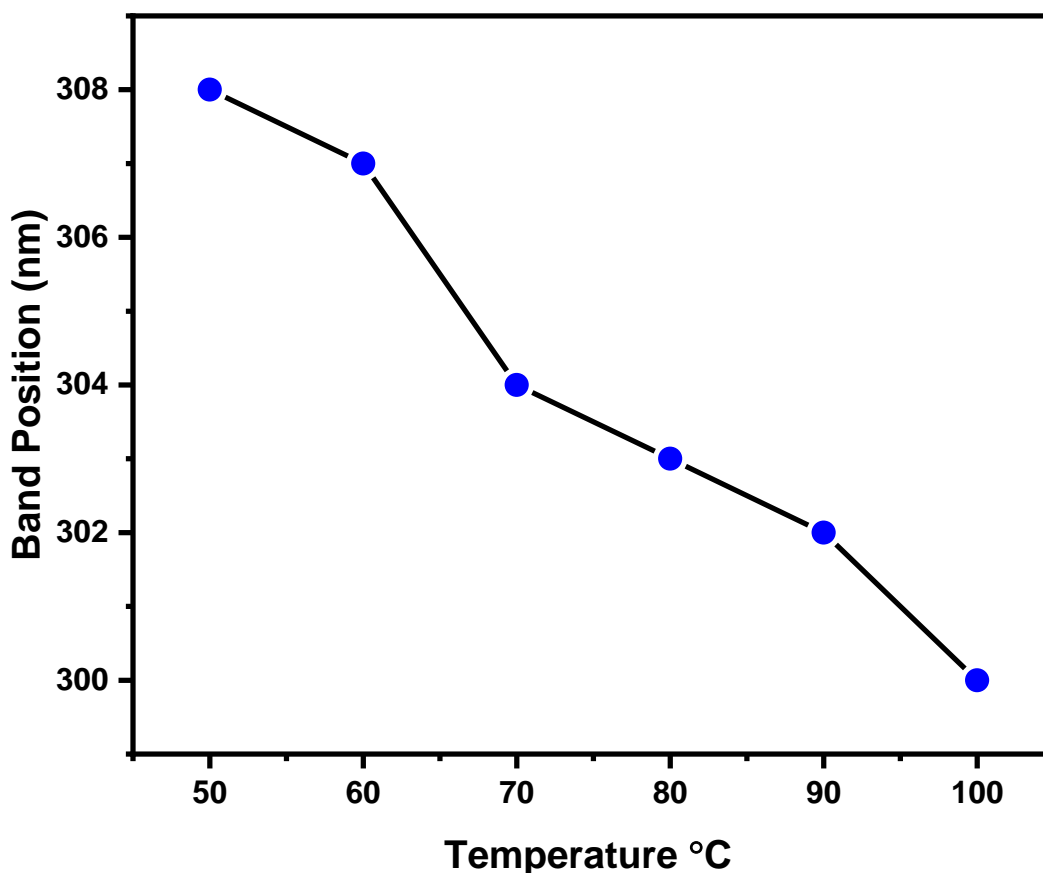


Figure 4. 10: Band position of ZnSNPs as a function of temperature.

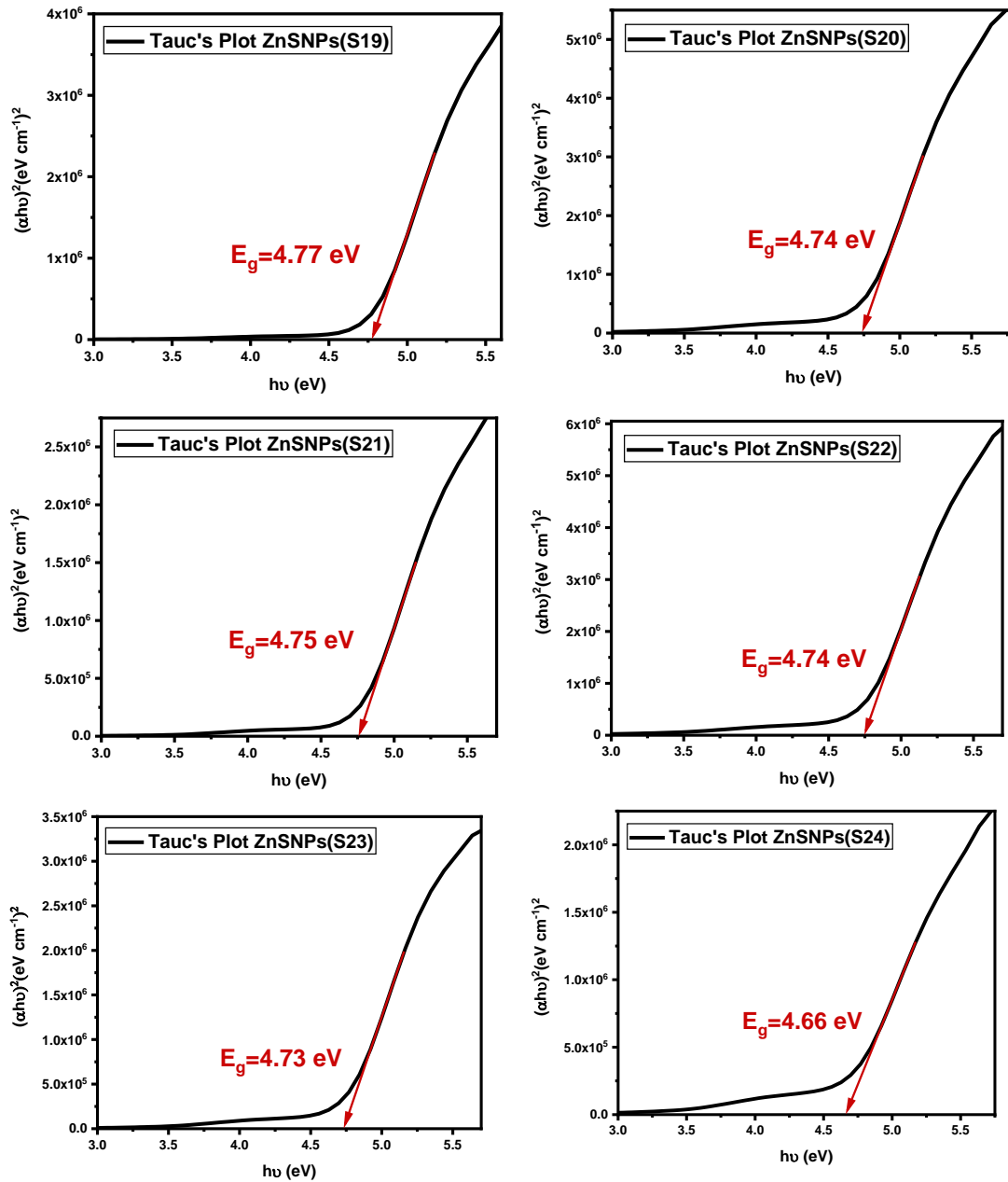


Figure 4. 11: Tauc's Plot of ZnSNPs prepared at different temperatures [ZnSNPs(S19)-ZnSNPs(S24)].

4.1.6 UV-Vis for Silver \ Zinc Sulfide Core-Shell Nanoparticles

Figure 4.12 shows the UV-Vis absorption spectra of the as-prepared AgNPs(S25) and the silver/zinc sulfide core-shell nanoparticles. The AgNPs were synthesized by using ascorbic acid as a reducer and PVP as a stabilizer. The Ag/ZnS CSNPs were prepared by using several amounts of as-prepared AgNPs(S25), according to Table 3.6. From the spectra, it can be noticed that the plasmon absorption band of silver sample AgNPs(S25) has appeared at 408 nm, which indicates to the formation of AgNPs. The small bands that appeared at about 290 nm are interpreted to the zinc sulfide nanoparticles. The broad bands were seen at 450 nm for Ag/ZnS(S26) CSNPs, 469 nm for Ag/ZnS(S27) CSNPs, and 498 nm Ag/ZnS(S28) CSNPs are depicted by the surface plasmon resonance of silver/zinc sulfide core-shell nanoparticles. The surface plasmon resonance is discussed before in (4.1.1). The surface plasmon resonance shifted to a higher wavelength (redshift) as demonstrated in Figure 4.13, due to increasing of AgNPs(S25). Moreover, the bands become broader with increasing in AgNPs(S25) molar ratio owing to the lower distribution of the core-shell nanoparticle. The change of the surface plasmon resonance absorption can be mostly ascribed to the formation of ZnS on the surface of AgNPs, implying the successful production of the Ag/ZnS core-shell structure of the composite nanoparticles. The surface plasmon resonance of the Ag core became broader as compared to AgNPs(S25), which might be due to the nucleation layer on the surface of Ag nanocore. With further increase in the core concentration, the absorption of the Ag core becomes wide, which may vary due to the aggregation of Ag/ZnS CSNPs.

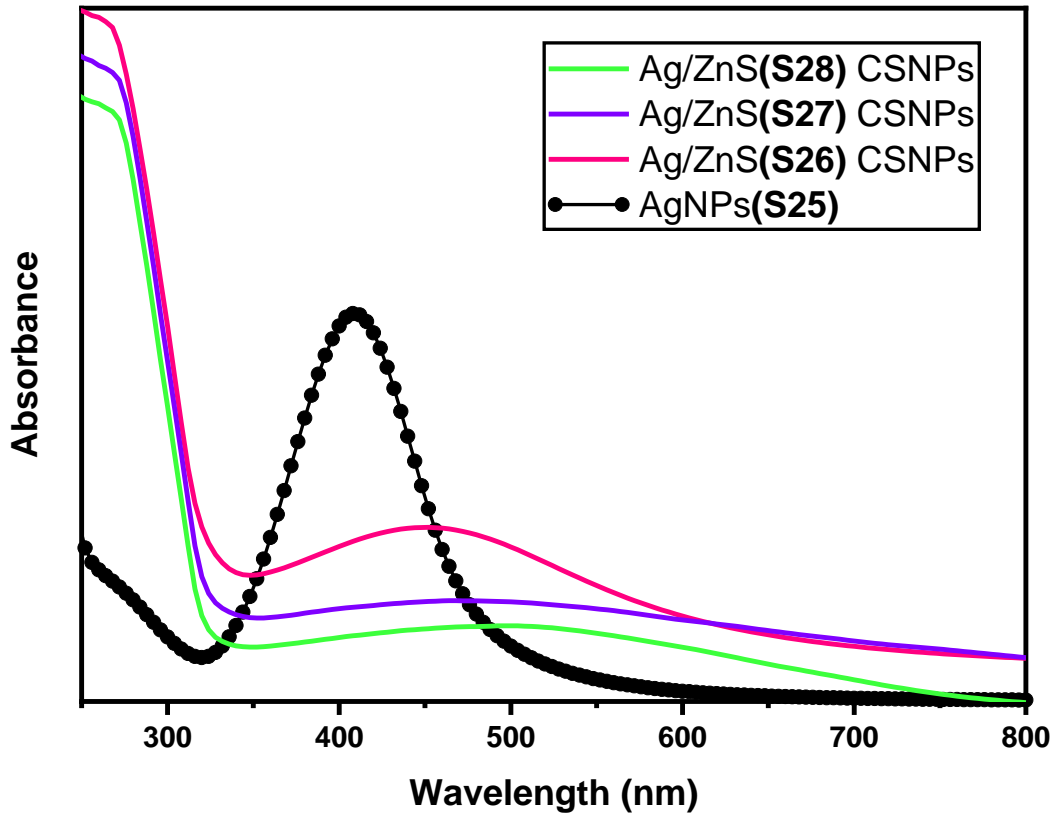


Figure 4. 12: UV-Vis absorbance spectra of Ag/ZnS (CSNPs) prepared at a different molar ratio of AgNPs(S25). Ag/ZnS(S26) [70 ml], Ag/ZnS(S27) [80 ml], and Ag/ZnS(S28) [90 ml].

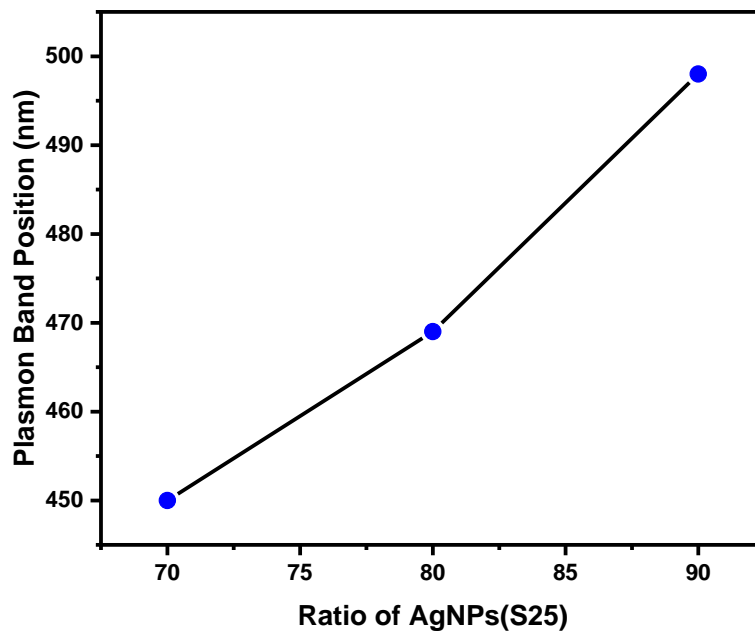


Figure 4. 13: Plasmon band position of Ag/ZnS (CSNPs) as a function of the Ag colloid ratio.

4.2 Results of Transmission Electron Microscopy (TEM)

Transmission electron microscopy is one of the most powerful and valuable technique for the characterization of nanoparticles. Its high resolution of structural details is considered essential, for example, to obtain information regarding the crystal structure and granularity of nanoparticles [108]. It is used to study the sizes, shapes, and morphology of our prepared nanoparticles samples.

4.2.1 Transmission Electron Microscopy (TEM) Images of Gold Nanoparticle Synthesized at Different Concentrations of NaBH_4 .

Figure 4.14 (a,c) displays the TEM image of AuNPs synthesized by adding 2 ml of $\text{HauCl}_4 \cdot 3\text{H}_2\text{O}$ (25 mM), 0.25 gm of CTAB to 50 ml distilled water at different concentrations of NaBH_4 (0.35M), according to Table 3.1. We used 0.75 ml and 1 ml of (0.35M) NaBH_4 for AuNPs(S3) and AuNPs(S4), respectively. From these two images for AuNPs(S3) and AuNPs(S4), it can be noted that the gold nanoparticles were formed with spherical in shape. Particle sizes have been determined by measuring the diameter of all-spherical nanoparticles on TEM images by using ImageJ software. Figure 4.14 (b,d) demonstrates the histogram of the Gaussian size distribution. The average size of both nanoparticle samples was estimated from the histogram at about 7 nm, with a few higher and lower size distribution.

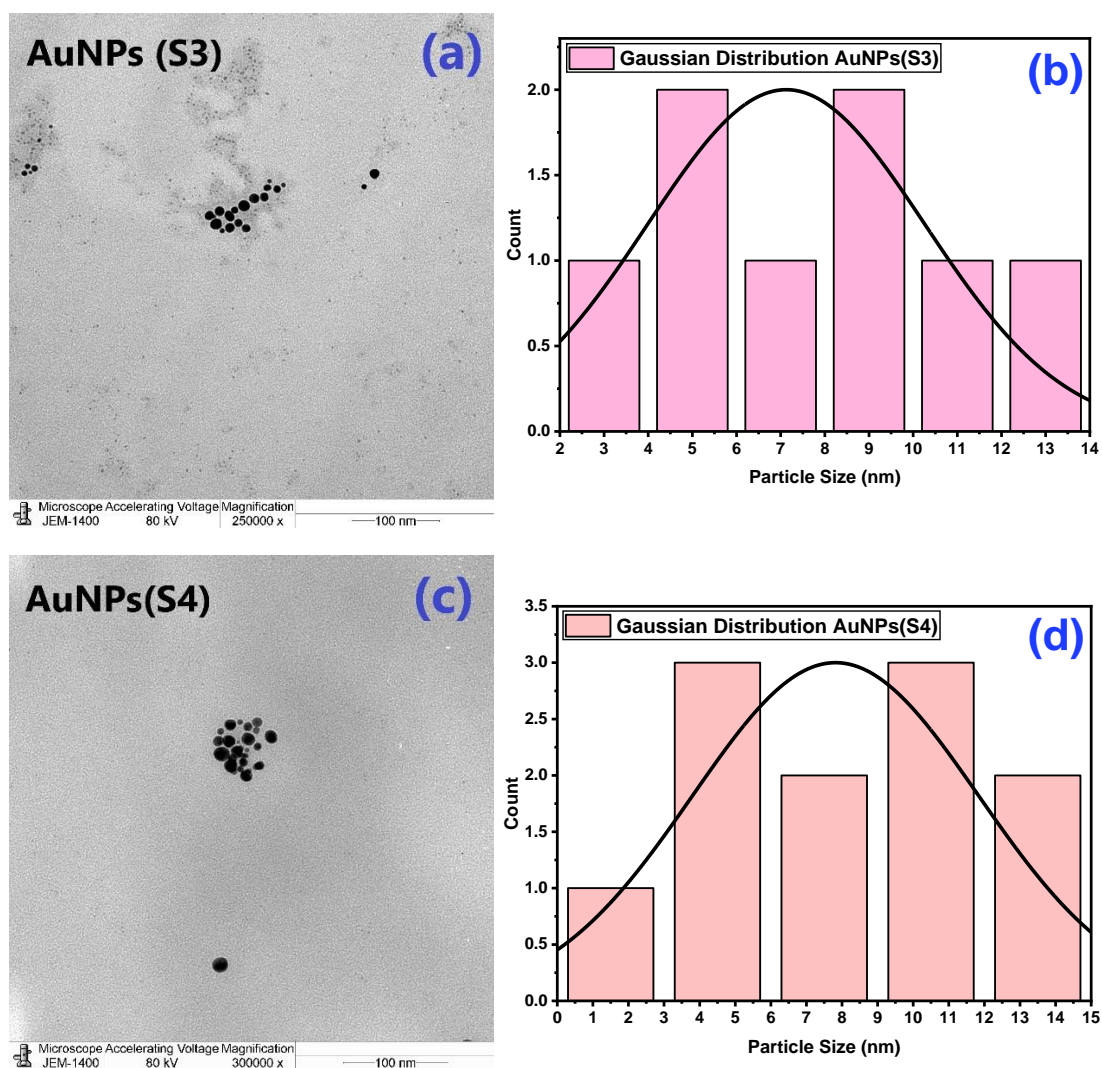


Figure 4. 14: (a,c) TEM images of AuNPs(S3) and AuNPs(S4) that prepared at different concentrations of NaBH_4 and (b,d) histogram of the Gaussian size distribution.

4.2.2 Transmission Electron Microscopy (TEM) Image of Gold Nanoparticle Synthesized Using CTAB as a Surfactant.

Figure 4.15 (a,b) shows the TEM image and the average particle size of AuNPs(S7) prepared using (0.40119 gm) of CTAB as a surfactant according to Table 3.2. From Figure, it notes that AuNPs was synthesized as a spherical form without regular morphology distribution. Besides, a few numbers of other forms like triangle, and hexagon shapes were seen. The appearance of these different shapes is due to the extent of CTAB. CTAB is a cationic surfactant that has a shape-directing property that responds to

the non-specific growth [109, 110]. The particle sizes have been determined by measuring the diameter of all-spherical nanoparticles on TEM images using ImagJ software, and the average size was obtained from the gaussian distribution as 10 nm.

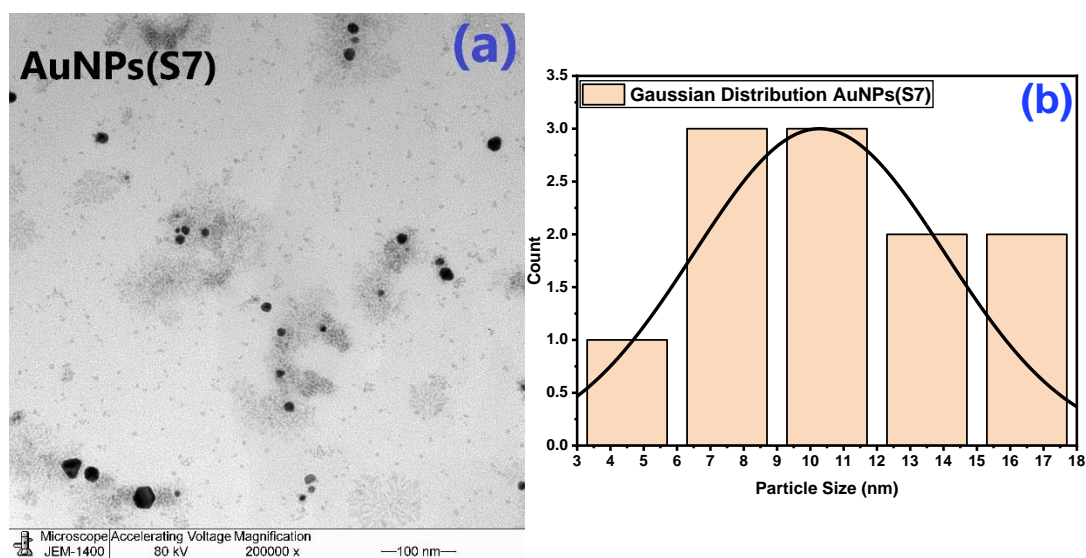


Figure 4. 15: (a) TEM image of AuNPs(S7) synthesized using CTAB and (b) the count of particles as a function of different particle sizes.

4.2.3 Transmission Electron Microscopy (TEM) Images of Silver Nanoparticle Synthesized at Different Concentrations of AgNO_3 .

Figure 4.16 (a,c) display The TEM images of silver nanoparticles synthesized by reverse micelle method at different concentrations of (1M) AgNO_3 (2 ml and 2.5 ml for AgNPs(S10) and AgNPs(S11), respectively), according to Table 3.3. The TEM image of AgNPs(S10) appears as a dark point with a spherical shape. Where one can see a rather good particle-size distribution with an average size of 2 nm. The particle size smaller than the Bohr's radius, thus, can be considered to be quantum dots. Most of the silver nanoparticles in AgNPs(S11) are spherical with random distribution. The average particle size was estimated at 4 nm. In conclusion, the size of the silver nanoparticle increases with increasing the AgNO_3 ratio. This is

due to the Ag^0 may be increased with increasing AgNO_3 that leads to an increase in the particle size. These results are in agreement with the UV-Vis data.

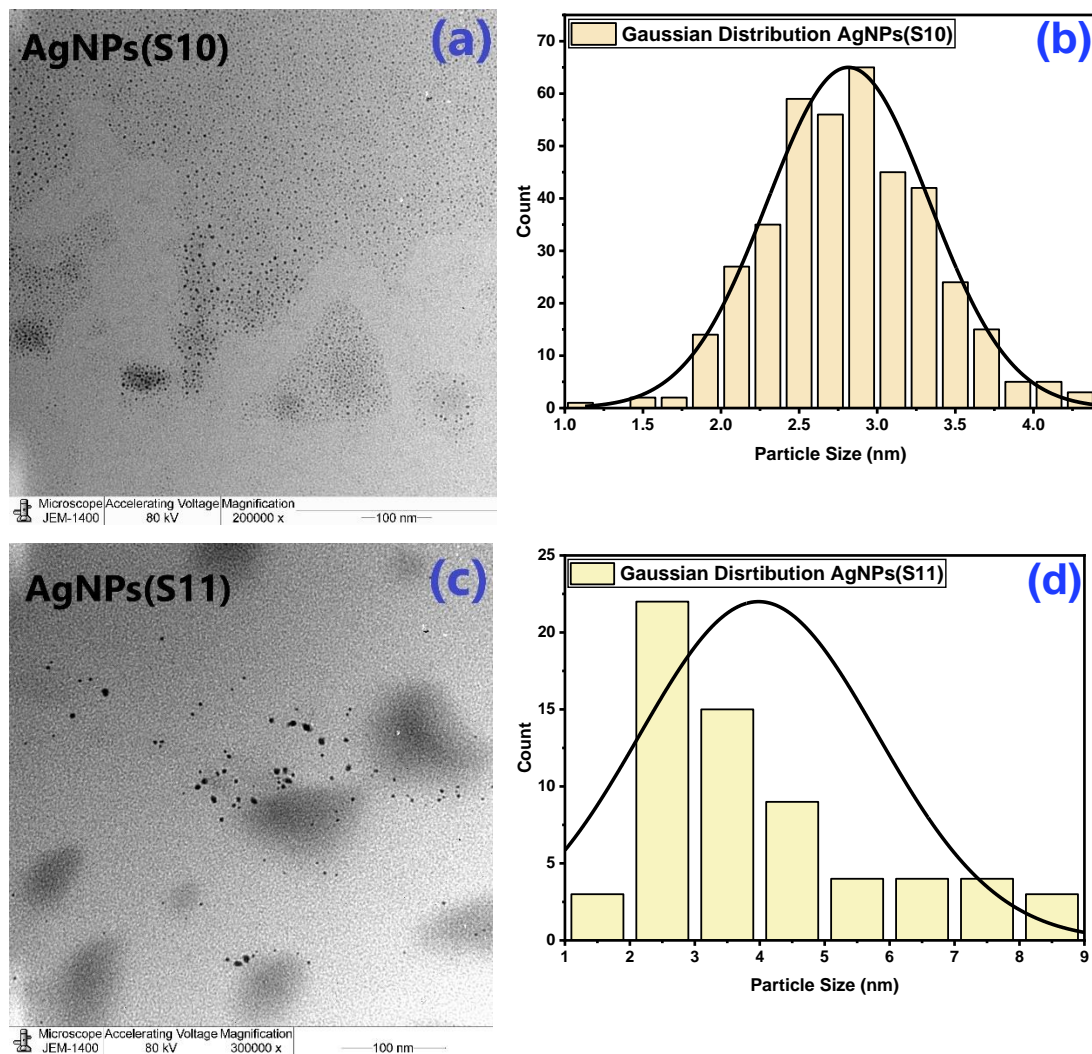


Figure 4. 16: (a,c) TEM images of AgNPs(S10), and AgNPs(S11) prepared by reverse micelle method at different concentrations of AgNO_3 and (b,d) the Gaussian size distribution.

4.2.4 Transmission Electron Microscopy (TEM) Images of Zinc Sulfide Nanoparticle Synthesized at Different Concentrations of Zinc Acetate Dihydrate.

Figure 4.17 (a,c) shows the TEM images of ZnSNPs that prepared at different concentrations of zinc acetate dihydrate, according to Table 3.4. Where ZnSNPs(S14) were synthesized using 0.1M of zinc acetate dihydrate and ZnSNPs(S18) at 0.5M of zinc acetate dihydrate. From these images, it is shown that the ZnS nanoparticles were formed with a nearly spherical shape. The mean particle size of both samples was calculated using ImageJ software. The average particle sizes were estimated through the Gaussian distribution in Figure 4.17 (b,d) of ZnSNPs(S14) and ZnSNPs(S18) at 5 nm, and 3 nm, respectively. From the measurements, it can note that as the zinc acetate dihydrate increased, the particle size decreased. These results are aligning with the UV-Vis data.

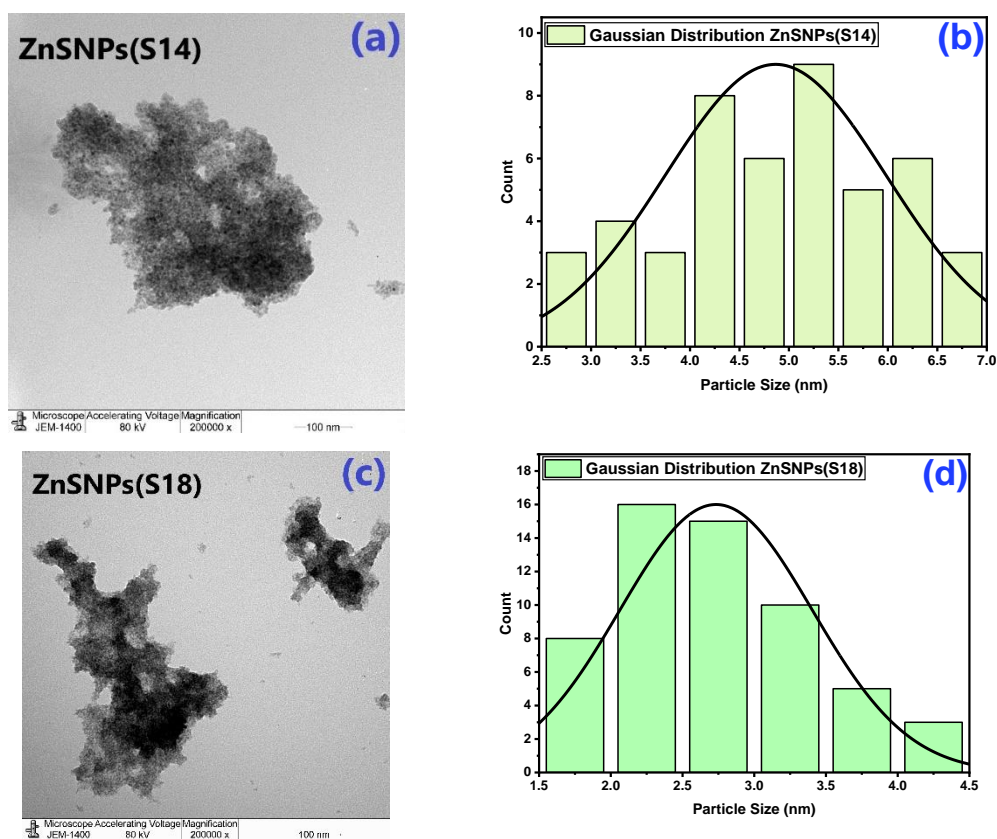


Figure 4. 17: (a,c) TEM images of Zinc Sulfide Nanoparticle ZnSNPs(S14), ZnSNPs(S18), and (b,d) their gaussian distribution.

4.2.5 Transmission Electron Microscopy (TEM) Images of Zinc Sulfide Nanoparticle Synthesized at Different Temperatures.

Figure 4.18 (a,c) shows TEM images of zinc sulfide nanoparticle synthesized at different temperatures. ZnSNPs(S19) is prepared at ($T=50^{\circ}$) and ZnSNPs(S22) synthesized at ($T=80^{\circ}$), according to Table 3.5. From these images, it shows that two regions were seen one is high spherical distribution, and the other is low distribution. The average diameter of the spherical shape was calculated for two samples via Gaussian distribution Figure 4.18 (b,d) at about 3 nm.

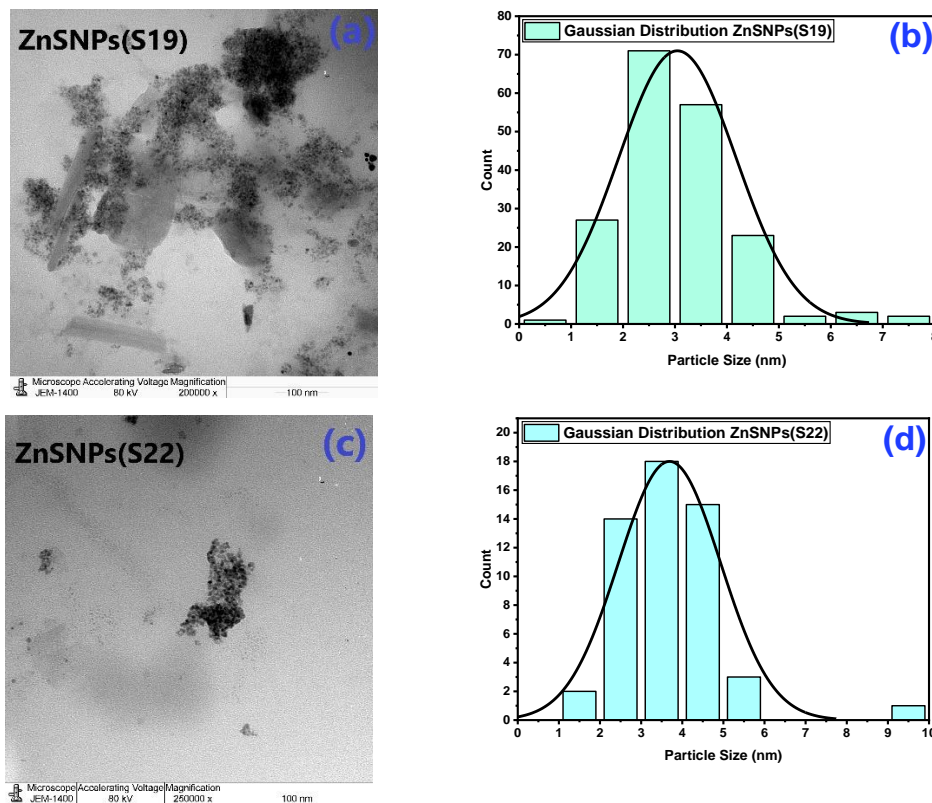


Figure 4. 18: (a,c) TEM images of zinc sulfide nanoparticle synthesized at different temperature ZnSNPs(S19) at ($T=50^{\circ}$) and ZnSNPs(S22) at ($T=80^{\circ}$), and (b,d) Gaussian distribution of each sample.

4.2.6 Transmission Electron Microscopy (TEM) Images of Silver/Zinc Sulfide Core-Shell Nanoparticle Synthesized at Different Quantities of Ag Nanoparticles.

Figure 4.19 shows silver/zinc sulfide core-shell nanoparticle synthesized at a different quantity of Ag nanoparticles (Ag/ZnS(S26):70 ml,

Ag/ZnS(S27):80 ml, and Ag/ZnS(S28):90 ml), according to Table 3.6. From Ag/ZnS(S26) it shows that the Ag/ZnS CSNPs formed in a spherical shape. Also, the results reveal that the particle appears as a spherical nanoparticle (core) with dark color and a (shell) surrounding the core with shiny color. The dark color represents the silver nanoparticle, and the shiny part (shell) represents the zinc sulfide nanoparticle. The count of core-shell nanoparticles size was calculated from ImageJ software, as shown on the right side of each sample. The average particle size of ZnSNPs(S26) is approximately 27 nm. The TEM image in Figure 4.19 (c) clearly indicates the formation of Ag/ZnS CSNPs with different sizes. The composition of the core and shell in each nanoparticle exhibit different image contrast, implying the core and shell are composed of different materials. Besides that, the well-distribution of core-shell Ag/ZnS CSNPs could also be recognized. The average thickness of the nanoparticles shells is about 18 nm, and the average core diameter of the nanoparticle is about 46 nm. All particle size (core and shell) of ZnSNPs(S27) were estimated by using ImageJ software at 81 nm. Figure 4.19 (e) shows the TEM image of Ag/ZnS(S28) NPs core-shell structure. This image demonstrates that the as-synthesized particle has a core-shell structure with dark contrast zinc sulfide shells and light contrast core of silver nanoparticles, implying that a zinc sulfide shell successfully and uniformly coated the surface of the silver nanoparticles. The mean shell thickness of the nanoparticle estimated at 33 nm. The average core diameter is 98 nm. The average particle size is 177 nm. By comparison of these samples, the particle size was increased with increasing the AgNPs(S25) quantity. These results are consistent with UV-Vis data.

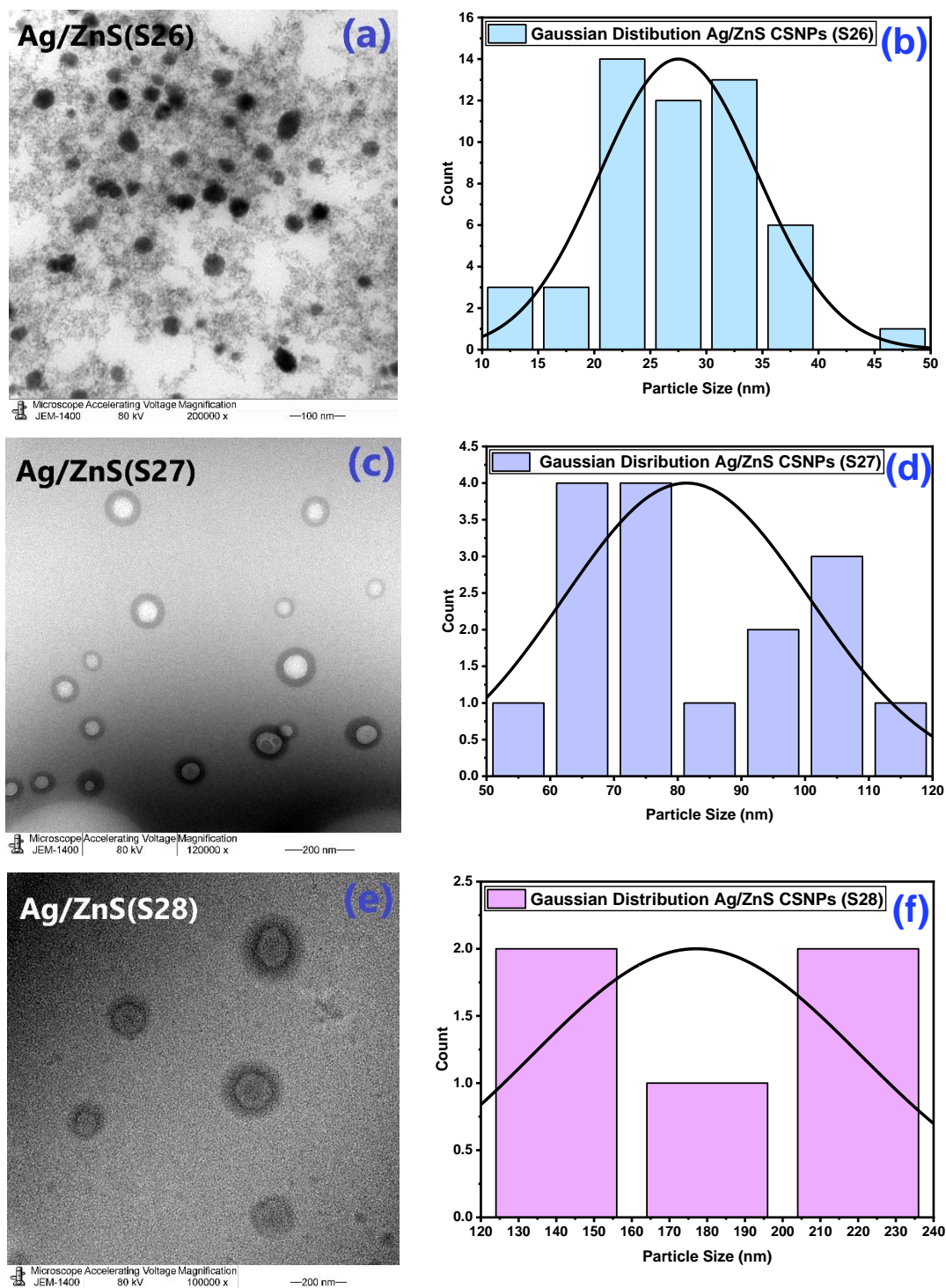
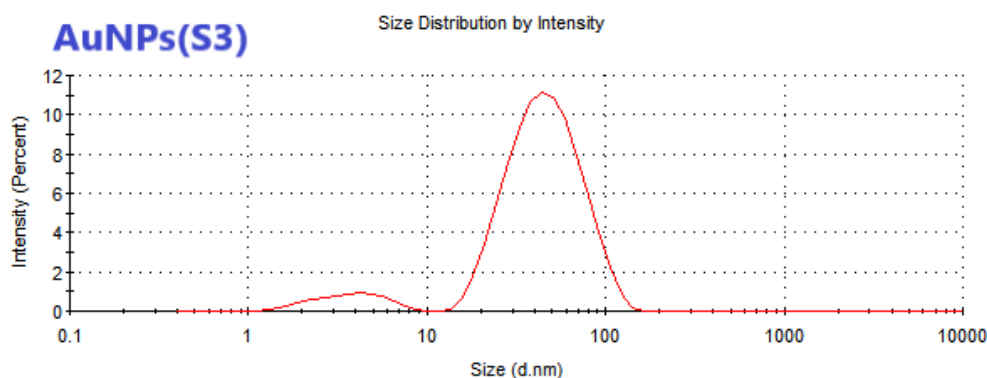


Figure 4. 19: TEM images of silver/zinc sulfide core-shell nanoparticle ZnSNPs(S26), ZnSNPs(S27), and ZnSNPs(S28) synthesized at a different quantity of AgNPs, and their Gaussian distribution.

4.3 Results of Dynamic Light Scattering (DLS)

Dynamic light scattering (DLS) is a common technique that depends on the interaction of light with particles. DLS use for determining particle size that undergoes random Brownian motion in colloidal suspension [111, 112]. DLS measures the scattered light from the laser that passes through a sample. The modulation of the scattered light intensity then analyzed as a function of time, and the hydrodynamic size of particles can be obtained [98].

Figure 4.20 shows the results of DLS for gold nanoparticles. DLS measurements confirmed the presence of gold nanoparticles in all tested solutions. The average hydrodynamic diameters of AuNPs(S3) and AuNPs(S4) obtained as 33.03 nm, and 23.46 nm. As expected, the hydrodynamic diameters in exposure medium were substantially larger than those estimated by TEM. The large variation in particle sizes reported by DLS and TEM could be due to the capping agent that surrounds the nanoparticle. Further, TEM measure the inorganic core of the particle, since the organic shell is less electron-dense in comparison to the inorganic core and thus transparent in TEM. This may account for the variation in measurements made using these techniques [111].



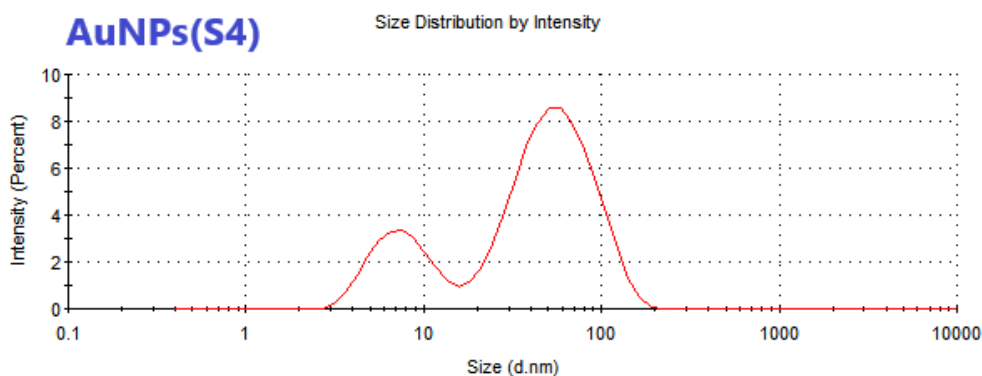


Figure 4. 20: Hydrodynamic size distributions of AuNPs(S3) and AuNPs(S4) that synthesized at different concentrations of NaBH_4 .

Figure 4.21 presents the average hydrodynamic particle size for sample AuNPs(S7). The average size was obtained at about 30.26 nm. It was observed that the hydrodynamic size obtained from DLS was always larger than the mean diameter of TEM indicating the presence of an adsorbed layer, and the variability was very sensitive to the presence of non-spherical particles [113].

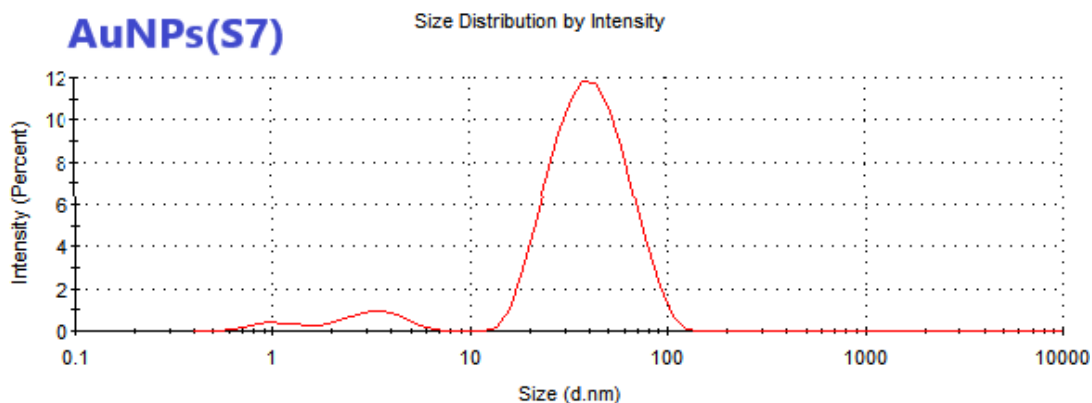
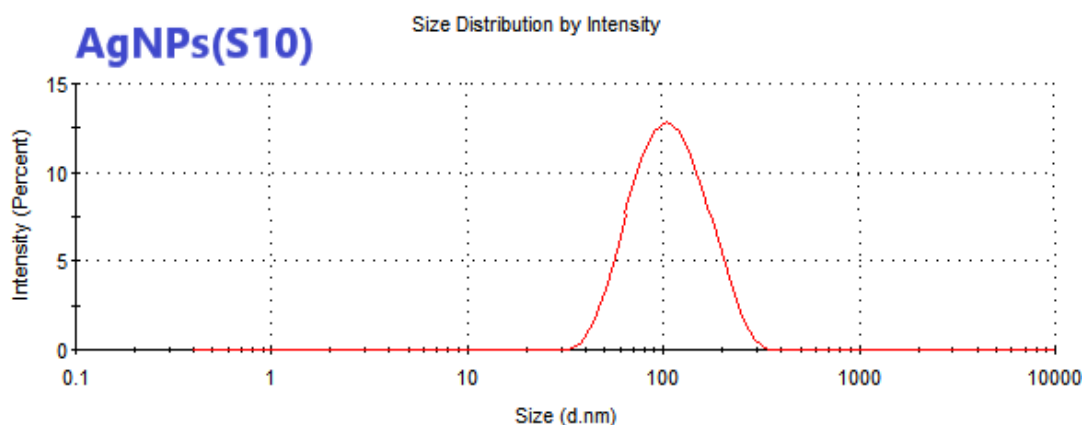


Figure 4. 21: Hydrodynamic size distributions of AuNPs(S7) synthesized using CTAB as a surfactant.

Figure 4.22 determines the hydrodynamic diameter of the silver nanoparticles using DLS for the aqueous preparation of AgNPs(S10) and AgNPs(S11) and was found to be 87 nm, 77.68 nm, respectively. As discussed before, the average particle size calculated from TEM was smaller compare to hydrodynamic particle size, which is logical because usually, hydrodynamic particle size is greater than TEM particle size.



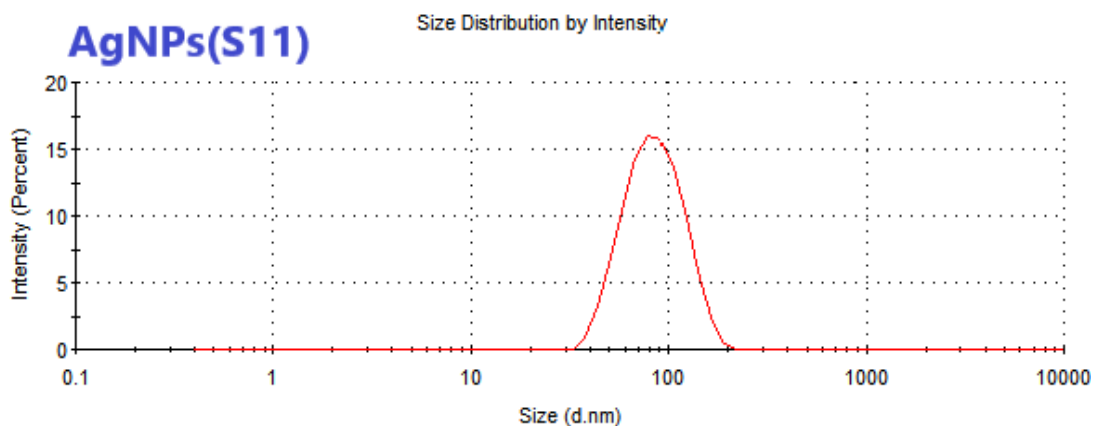


Figure 4. 22: Hydrodynamic size distributions of AgNPs(S10) and AgNPs(S11) that synthesized at different concentrations of AgNO_3 .

Figure 4.23 shows the hydrodynamic diameter of ZnSNPs(S14) that obtained at 11.74 nm.

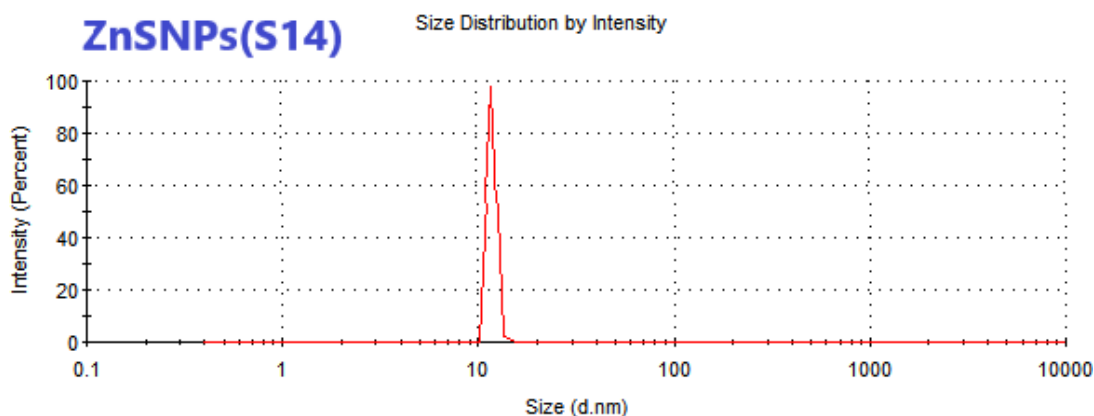


Figure 4. 23: Hydrodynamic size distributions of ZnSNPs(S14) that synthesized at (0.1M) of zinc acetate dihydrate.

Figure 4.24 shows the average size of the ZnSNPs prepared at different temperatures. The particle size distribution of the synthesized NPs was taken from the samples in a liquid state by DLS analysis. Here the incident laser beam induces the Brownian movement of synthesized nanoparticles. From the Figure, it is observed that a small variation comes from the particle size distribution compared to TEM analysis. The average size of ZnSNPs(S19) and ZnSNPs(S22) were found to be 132.9 nm, and 315.9 nm, respectively.

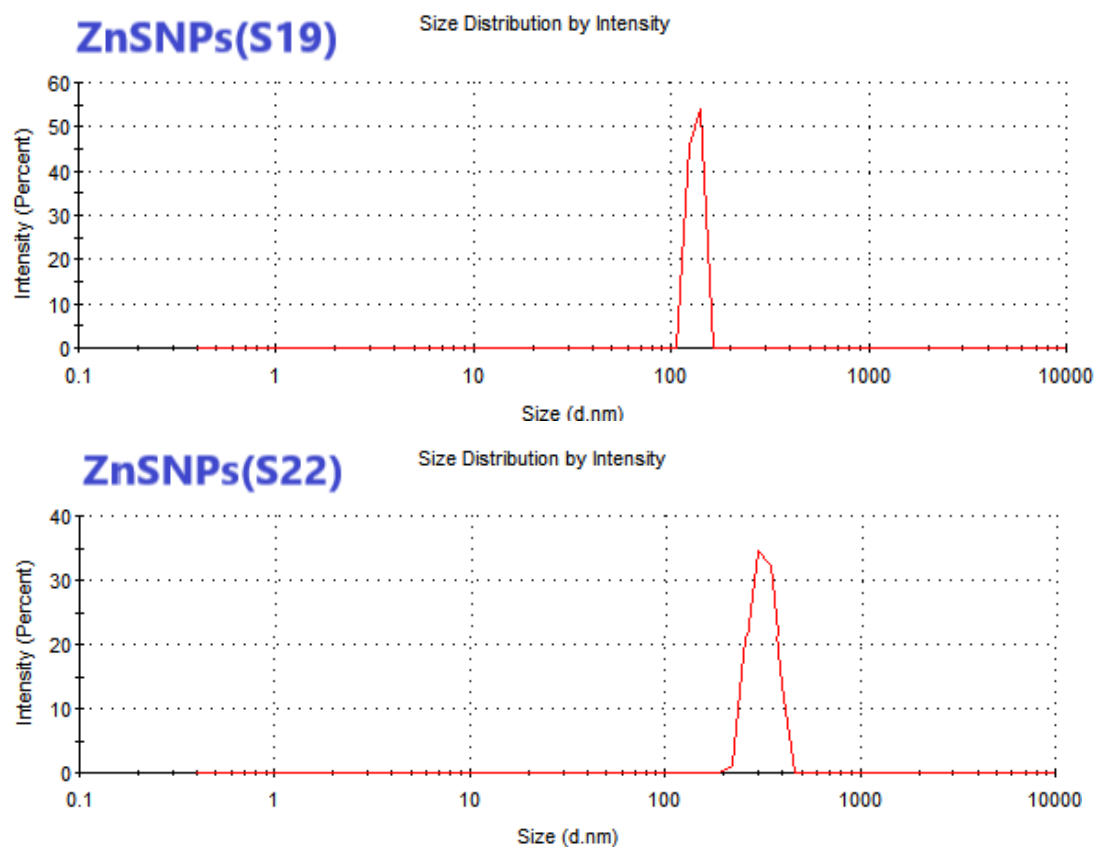


Figure 4. 24: Hydrodynamic size distributions of ZnSNPs(S19) and ZnSNPs(S22) that synthesized at different temperatures.

Figure 4.25 shows the hydrodynamic diameter of the silver/ Zinc sulfide core-shell nanoparticles that prepared at different quantities of AgNPs(S25). The hydrodynamic diameter for the samples Ag/ZnS(S26), Ag/ZnS(S27), and Ag/ZnS(S28) are 39.04 nm, 127.8 nm, and 48.39 nm, respectively.

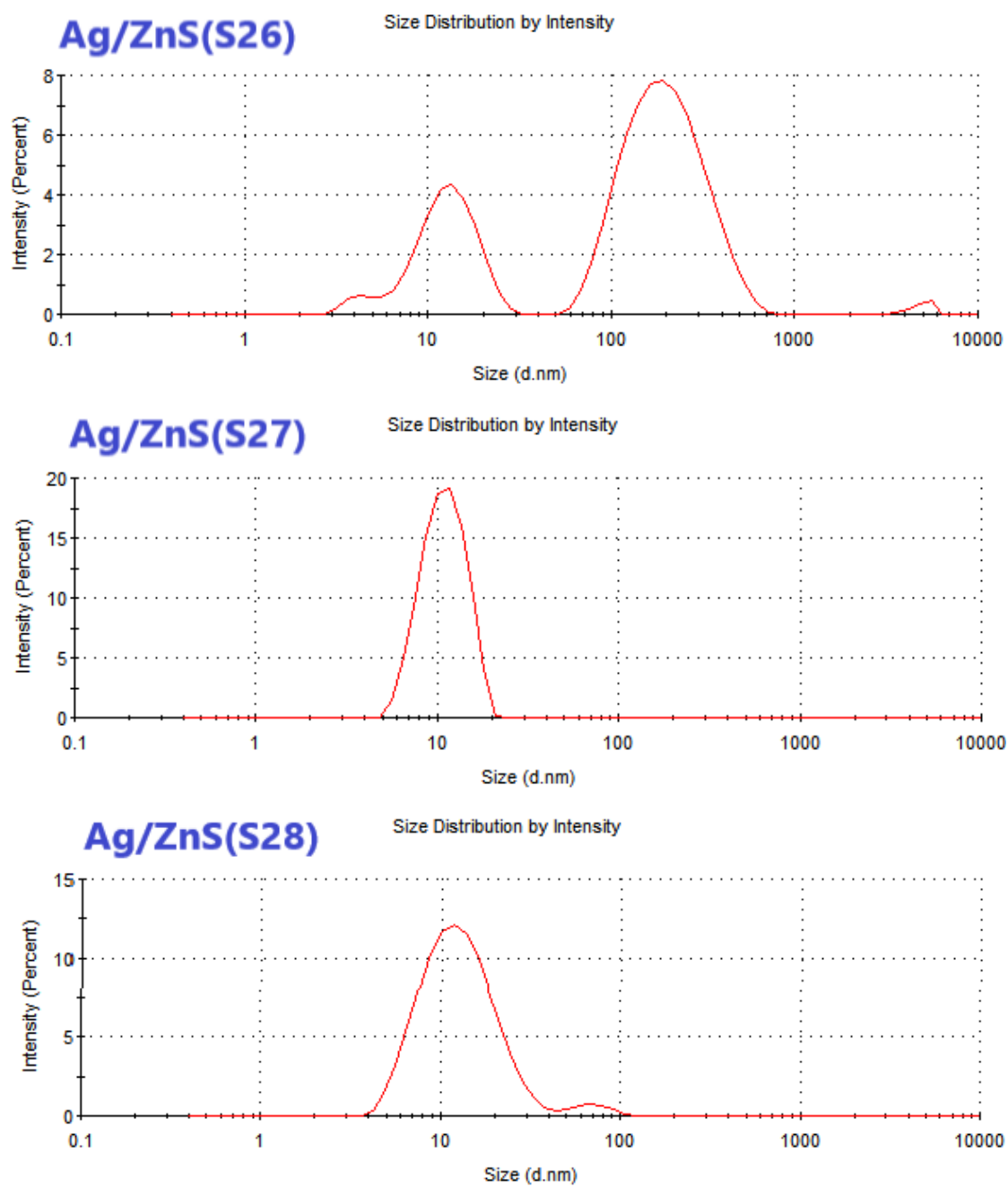


Figure 4. 25: Hydrodynamic size distributions of Ag/ZnS(S26), Ag/ZnS(S27), and Ag/ZnS(S28) that synthesized at different quantities of AgNPs(S25).

4.4 Results of X-Ray Diffraction (XRD)

X-ray diffraction (XRD) is the most common technique for quantitative analysis that used to identify the crystalline nature of our prepared samples [114].

4.4.1 X-Ray Diffraction (XRD) for Gold Nanoparticle Prepared at Different Concentrations of Sodium Borohydride

Figure 4.26 shows the XRD patterns of synthesized AuNPs that prepared using cetyltrimethylammonium bromide (CTAB) as a capping agent and at different sodium borohydride (NaBH_4) concentrations, according to Table 3.1. From this Figure, it can see that the diffraction peaks appeared at $2\theta^\circ$ (38° , 45° , 62.6° , and 74.38°) have different intensities and matched with the planes (111), (200), (202), and (311), respectively. All the peaks in the obtained patterns are well-matched with the card number (JCPDS no. 96-901-1614) of the standard cubic AuNPs [115]. It can conclude that the NaBH_4 does not affect the AuNPs crystalline structure. The crystallites size was calculated at each peak that appeared in the range of $2\theta^\circ$ ($30^\circ - 80^\circ$) using Scherrer's formula.

$$D = \frac{K\lambda}{\beta \cos \theta} \quad (4.2)$$

Where λ is a wavelength of the X-Ray beam ($=0.1540562$ nm), θ is diffraction angle, D is crystallite size, K is a shape factor ($=0.9$), and β is Full-Width Half Maximum (FWHM) of the peak [116].

The crystal sizes were estimated at $2\theta^\circ$ (38.23°) is 21.48 nm for AuNPs(S1), at $2\theta^\circ$ (38.19°) is 33.57 nm for AuNPs(S2), at $2\theta^\circ$ (38.58°) is 30.74 nm for AuNPs(S3). Mean particle sizes correspond to the plane (111). The particle sizes were summarized in Table 4.1.

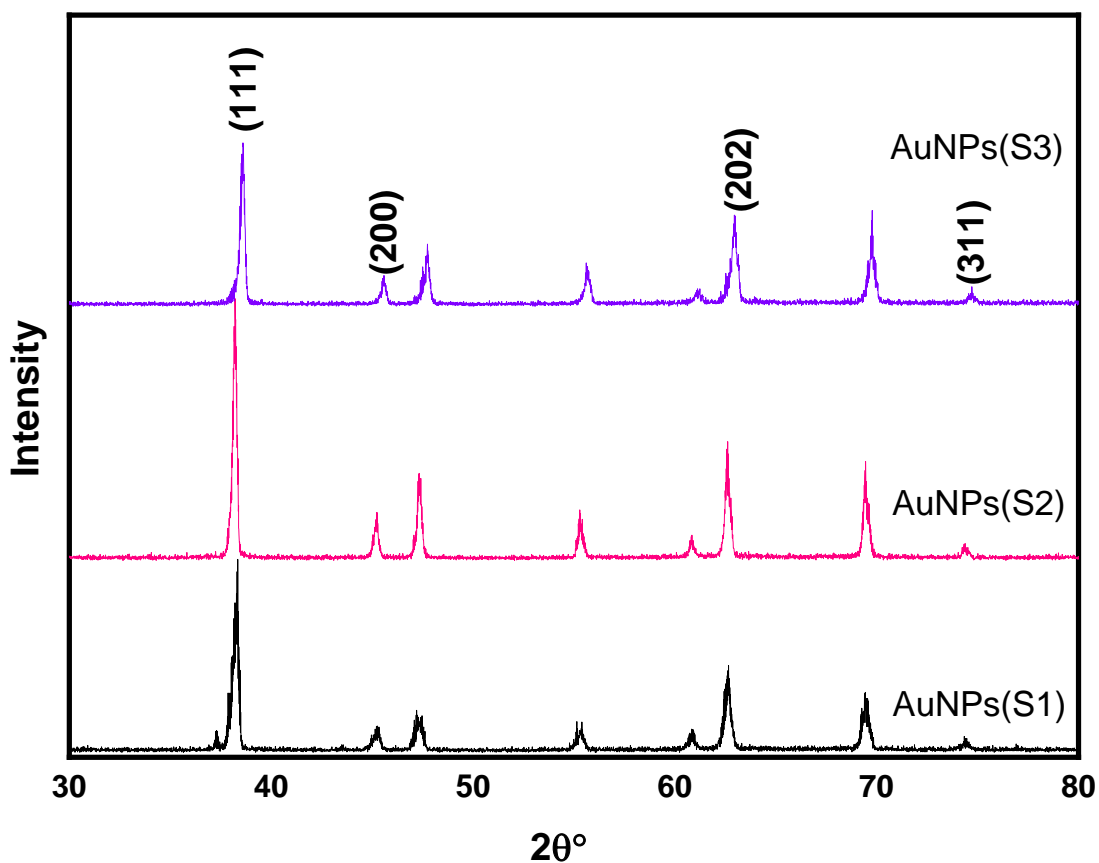


Figure 4. 26: XRD pattern of gold nanoparticle prepared at different concentrations of sodium borohydride AuNPs(S1): 0.1 ml NaBH₄, AuNPs(S2): 0.5 ml NaBH₄, and AuNPs(S3): 0.75 ml NaBH₄.

Table 4. 1 Peaks position, full width at half maximum (FWHM), and crystallite size of gold nanoparticle prepared at different concentrations of sodium borohydride.

Samples Name	Peaks Position (2θ °)	HFWM	Crystallite Size (nm)
AuNPs(S1)	38.23705°	0.39133	21.48583381
AuNPs(S2)	38.19836°	0.25039	33.57589311
AuNPs(S3)	38.58150°	0.27374	30.7476419

4.4.2 X-Ray Diffraction (XRD) for Gold Nanoparticle Prepared at Different CTAB Concentrations

Figure 4.27 presents the XRD patterns of AuNPs prepared using sodium borohydride as a reducing agent and different CTAB concentrations, according to Table 3.2. From this Figure, it is seen that the peaks values in the range of $2\theta^\circ$ ($30^\circ - 80^\circ$) positioned at about (37.7° , 43.9° , 64.2° , 77.1°) for all the samples. These diffraction peaks correspond to the planes (111), (200), (220), and (311), respectively. These results are consistent with the results in the card number (JCPDS no. 004-0783) of the face-centered-cubic (fcc) phase of gold [117]. The crystal sizes were calculated by using the Scherer equation, as earlier mentioned $2\theta^\circ$ (38.25°) and obtained at (9.94 nm, 8.25 nm, 8.59 nm) for the samples AuNPs(S5), AuNPs(S6), AuNPs(S7), respectively. All these data summarized in Table 4.2.

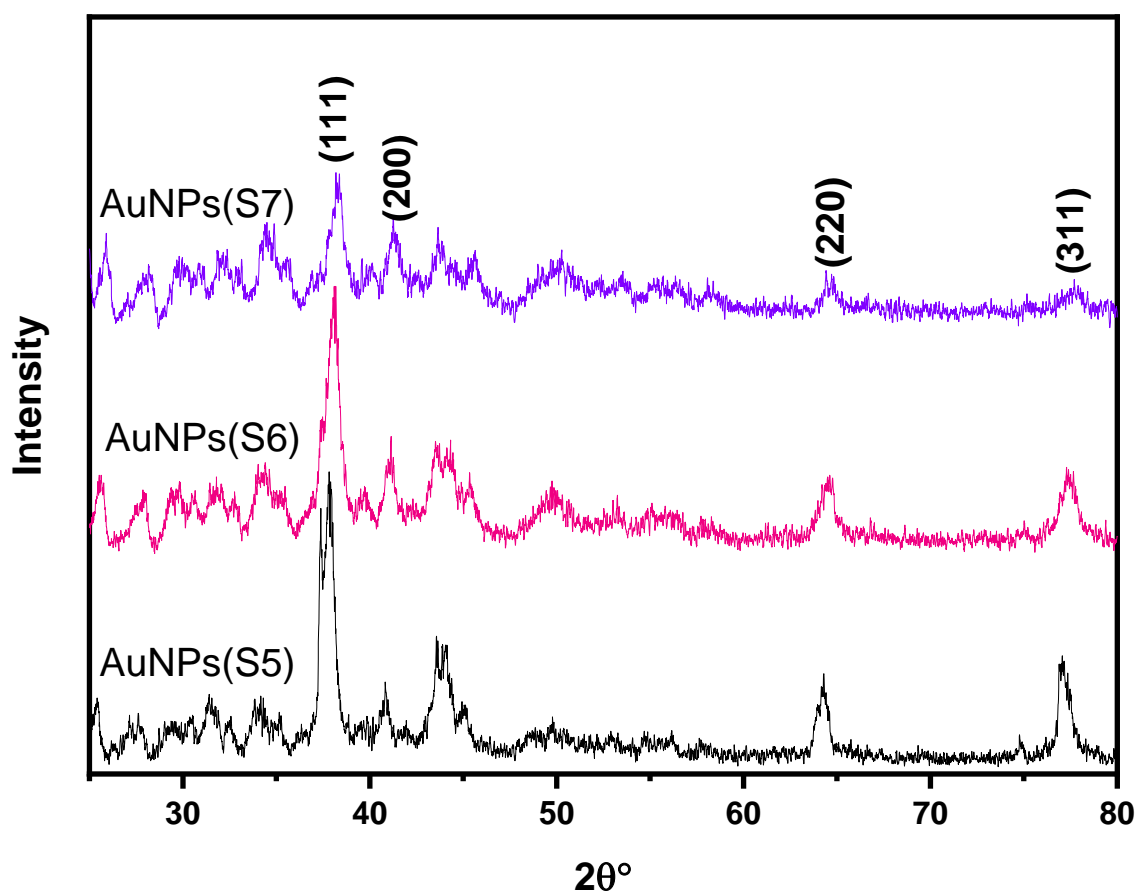


Figure 4. 27: XRD pattern gold nanoparticle prepared at different CTAB concentrations.

Table 4. 2 Peaks position, full width at half maximum (FWHM), and crystallite size of gold nanoparticle prepared at different CTAB concentrations.

Samples Name	Peaks Position (2θ)	FWHM	Crystallite Size (nm)
AuNPs(S5)	37.75649°	0.843950	9.948361848
AuNPs(S6)	38.05441°	1.0179747	8.255037333
AuNPs(S7)	38.25162°	0.9777779	8.599521451

4.4.3 X-Ray Diffraction (XRD) for Silver Nanoparticle Prepared at Different Concentrations of Silver Nitrate

Figure 4.28 displays typical XRD patterns of the silver nanoparticles samples obtained using NaBH_4 as a reducing agent, CTAB in chloroform as a surfactant, PVP as a stabilizing agent at different AgNO_3 concentrations, according to Table 3.3. As seen in Figure the diffraction peaks that have different intensities for all the samples were appeared in the range of 2θ ° (30°- 80°) at 2θ ° (37.79°, 45.27°, 64.09°, 77.02°) and matched with the planes (111), (200), (220), and (311), respectively. These results are matched with the data in card number (JCPDS no. 01-087-0717) and can be indexed to the cubic phase [118]. These diffraction patterns are confirming the extinct of silver nanoparticles. The crystal sizes for the mean peak were measured using Scherrer's equation, and the value were estimated for AgNPs(S9) is 8.08 nm for the peak at 2θ ° (37.7°), for AgNPs(S10) at 2θ ° (37.68°) is 7.89 nm, AgNPs(S11) at 2θ ° (38.08°) is 8.12 nm, AgNPs(S12) at 2θ ° (37.92°) is 12.42 nm, AgNPs(S13) at 2θ ° (37.93°) is 8.23 nm, as summarized in Table 4.3. The crystal size was measured for all samples at the same peak indexed to (111).

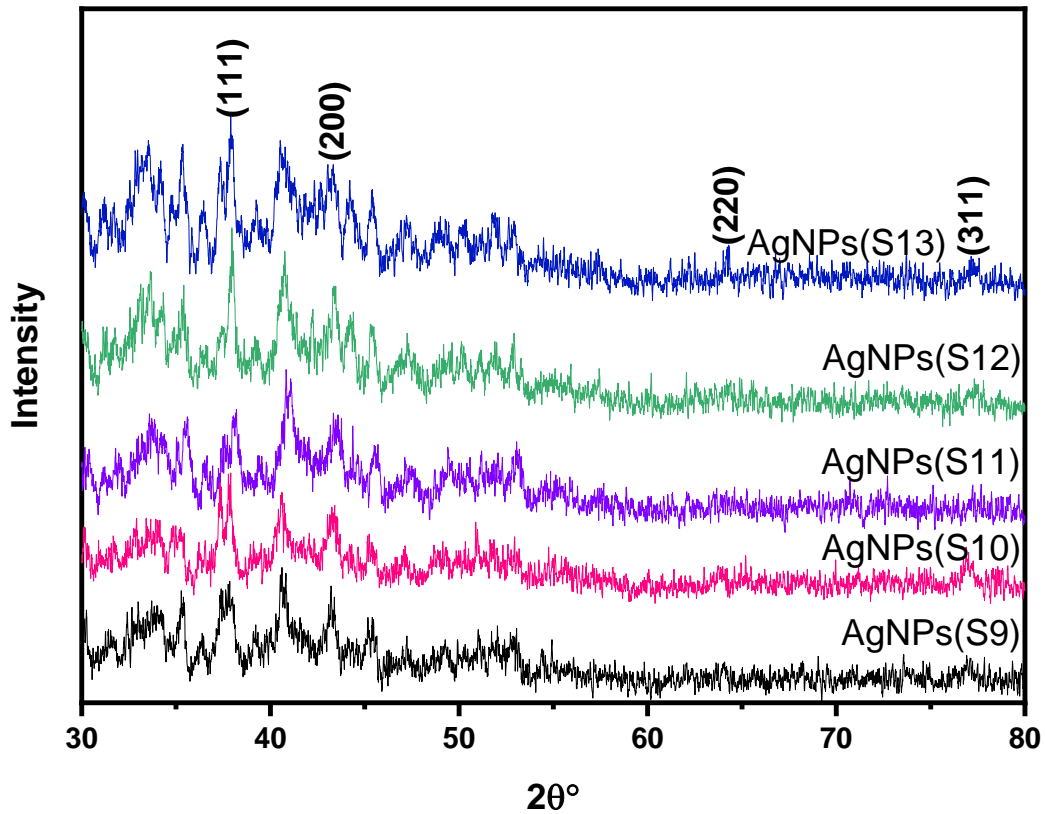


Figure 4. 28: XRD pattern of silver nanoparticles prepared at different concentrations of silver nitrate.

Table 4. 3 Peaks position, full width at half maximum (FWHM), and crystallite size of silver nanoparticle prepared at different concentrations of silver nitrate.

Samples Name	Peaks Position (2θ)	HFWM	Crystallite Size (nm)
AgNPs(S9)	37.7000000 °	1.038215	8.085520197
AgNPs(S10)	37.6832954 °	1.062713	7.898734154
AgNPs(S11)	38.0878791 °	1.034952	8.120438867
AgNPs(S12)	37.9299117 °	0.676139	12.42388669
AgNPs(S13)	37.9338077 °	1.020065	8.235133703

4.4.4 X-Ray Diffraction (XRD) for Zinc Sulfide Nanoparticle Prepared at Different Concentrations of Zinc Acetate Dihydrate

Figure 4.29 depicts the variation in the XRD pattern intensity with the angle (2θ) in the range ($20^\circ - 80^\circ$) of ZnSNPs that synthesized using a fixed molar ratio of sodium sulfide (0.2M) and different molar ratios of zinc acetate dihydrate, according to Table 3.4. The diffraction peaks for ZnSNPs(S14)-ZnSNPs(S18) that appeared at 2θ (28° , 47° , and 55.9°) were consistent with the plans (111), (220), and (311), respectively. The product was found to exhibit the characteristic features attributed to the FCC structure of cubic ZnS. This pattern has corresponded with the data in (JSPDS no. 651691) [111]. The crystal sizes for the mean peak among the range ($20^\circ - 80^\circ$) were measured via Scherrer formula. As shown in Table 4.4 mean peaks particle sizes were obtained at about 2θ (28°) is 3.83 nm, 2.18 nm, 2.19 nm, 2.15 nm, and 2.14 nm for ZnSNPs(S14), ZnSNPs(S15), ZnSNPs(S16), ZnSNPs(S17), and ZnSNPs(S18), respectively.

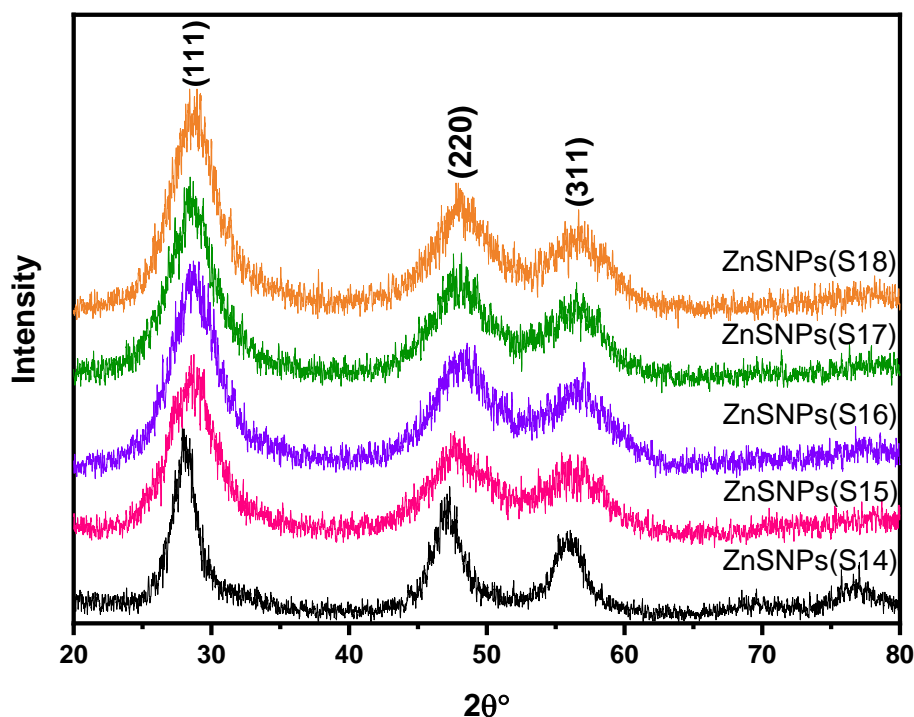


Figure 4. 29: XRD pattern of zinc sulfide nanoparticle prepared at different concentrations of zinc acetate dihydrate.

Table 4. 4 Peaks position, full width at half maximum (FWHM), and crystallite size of zinc sulfide nanoparticle prepared at different concentrations of zinc acetate dihydrate.

Samples Name	Peaks Position (2θ)	HFWM	Crystallite Size (nm)
ZnSNPs(S14)	28.06834°	2.13549	3.834582040
ZnSNPs(S15)	28.61764°	3.74559	2.188875284
ZnSNPs(S16)	28.78746°	3.73748	2.194456840
ZnSNPs (S17)	28.58753°	3.81256	2.150282284
ZnSNPs(S18)	28.75329°	3.83065	2.140918984

4.4.5 X-Ray Diffraction (XRD) for Zinc Sulfide Nanoparticle Prepared at Different Temperatures

Figure 4.30 shows the XRD pattern of ZnSNPs prepared using sodium sulfide (0.2M) and zinc acetate dihydrate (0.1M) at different temperatures, according to Table 3.5. Peak positions in Figure at 2θ ° in the range (20° – 80°) is 28° , 47° , and 56° give the clear evidence for the formation of cubic zinc blend crystal structure of ZnS nanoparticles with three crystallographic plans (111), (220), and (311). These results distinct to the ZnSNPs according to the data in (JCPDS no. 77-2100) [106]. The peaks are relatively broad, which is expected for a small size nanoparticle [119]. The crystallite sizes for the mean peak were obtained using Scherrer equation at about 2θ ° (28.3°) is 3.83 nm, 4.04 nm, 3.97 nm, 3.92 nm, 3.76 nm, and 4.17 nm for the samples ZnNPs(S19), ZnNPs(S20), ZnNPs(S21), ZnNPs(S22), ZnNPs(S23), and ZnNPs(S24), respectively, as summarized in Table 4.5.

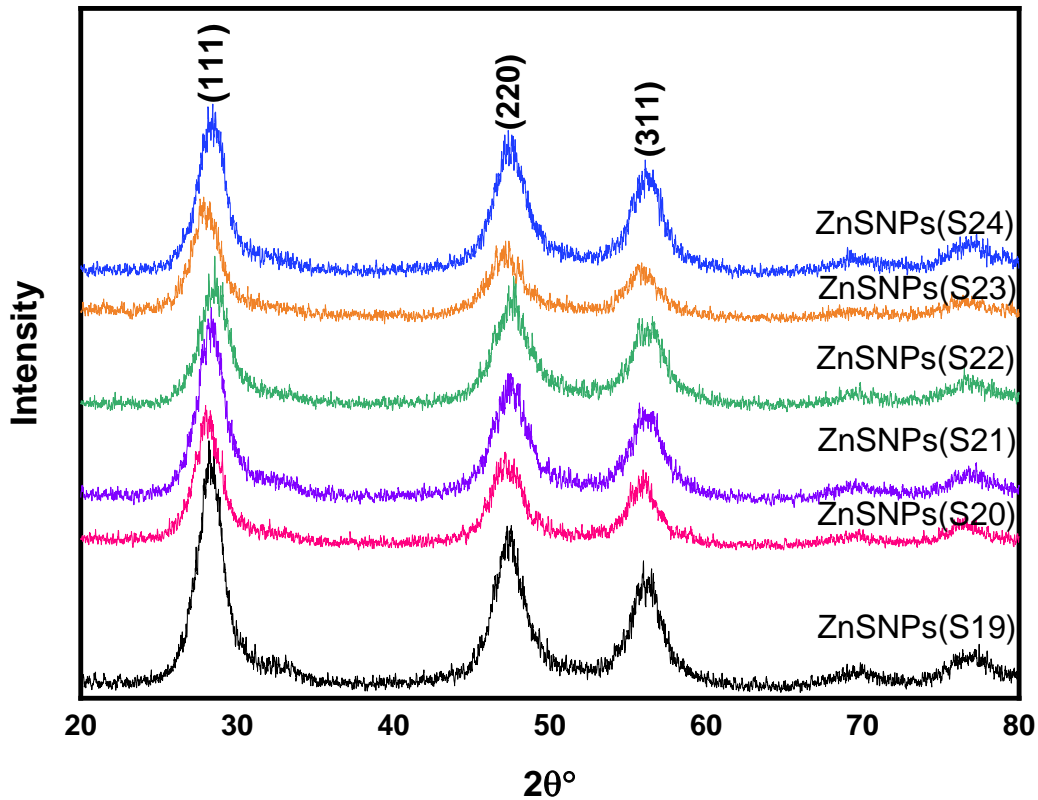


Figure 4. 30: XRD pattern of zinc sulfide nanoparticle prepared at different temperatures.

Table 4. 5 Peaks position, full width at half maximum (FWHM), and crystallite size of zinc sulfide nanoparticle prepared at different temperatures.

Samples Name	Peaks Position (2θ)	HFWM	Crystallite Size (nm)
ZnSNPs(S19)	28.30002°	2.1384	3.831307879
ZnSNPs(S20)	28.11862 °	2.02644	4.041378280
ZnSNPs(S21)	28.34324 °	2.06282	3.972061772
ZnSNPs(S22)	28.55736 °	2.08649	3.928861688
ZnSNPs(S23)	28.00474 °	2.17352	3.766966478
ZnSNPs(S24)	28.38753 °	1.96444	4.171391760

4.5 Results of Fourier Transform Infrared Spectroscopy (FT-IR)

Fourier transform infrared (FT-IR) spectroscopy is a Physico-chemical method based on vibration measurement of a molecule excited by FT-IR radiation at a specific wavenumber range [120]. FT-IR is used to obtain a transmission or absorption spectrum of organic, metalorganic in a solid, liquid, or gas form.

4.5.1 Fourier Transform Infrared Spectroscopy (FT-IR) for Gold Nanoparticle Prepared at Different Concentrations of Sodium Borohydride or Different Concentrations of CTAB

Figure 4.31 (a) displays the FTIR spectra of AuNPs(S1)-AuNPs(S4) prepared using cetyltrimethylammonium bromide (CTAB) as a capping agent and at different sodium borohydride (NaBH_4) concentrations, according to Table 3.1. From these spectra, it can show that a broad transmittance band at 3419 cm^{-1} corresponds to OH vibration due to the absorption of the water molecules in the sample [121]. The band at 3017 cm^{-1} is attributed to N–H group in CTAB. Strong transmittance band appeared at 2917 cm^{-1} , and 2847 cm^{-1} are attributed to asymmetric and symmetric CH vibration band of the $-\text{CH}_2$ group in CTAB. The transmittance band occurred at 1635 cm^{-1} may be attributed to the CH bending. In addition, the transmittance band seen at 1481 cm^{-1} is the stretching vibration of $\text{C} - \text{N}^+$. This band observed at 1467 cm^{-1} of FT-IR of CTAB, according to the previous work by Elfeky et al. [121]. In our opinion, the shift of this band to higher frequency may be owing to the AuNPs coordinate with the nitrogen atom in $\text{C} - \text{N}^+$. Additionally, the transmittance bands at 958 cm^{-1} and 904 cm^{-1} correspond to the out-of-plane and in-plane $-\text{CH}$ vibration of CH_3 , respectively. The transmittance band that could be assigned to $\text{C} - \text{Br}^-$ is shifted to 722 cm^{-1} . The summarized transmittance bands of the samples are shown in Table 4.6.

Figure 4.31 (b) depicts the FT-IR spectra of AuNPs(S5)-AuNPs(S8) synthesized using NaBH_4 as a reducing agent and different CTAB concentrations according to Table 3.2. By comparing the bands of AuNPs with CTAB transmittance bands in literature [121]. The transmittance band of OH vibration mode shifted to 3414 cm^{-1} , the band at 3017 cm^{-1} is assigned to the N–H group in CTAB, where the intense transmittance peak observed at 2917 cm^{-1} , and 2841 cm^{-1} was due to CH_2 asymmetric stretching vibration and symmetric stretching vibration of CH_2 , respectively. The transmittance peak at 1622 cm^{-1} assigned to the C – H bending vibration. The transmittance band around at 1476 cm^{-1} could be allocated to the asymmetric stretching vibration of $\text{C} – \text{N}^+$. The transmittance peaks found at 962 cm^{-1} and 909 cm^{-1} are due to the out-of-plane and in-plane -CH bond of $–\text{CH}_3$ group. The transmittance band that could be attributed to $\text{C} – \text{Br}^-$ is observed at 722 cm^{-1} . The summarized of transmittance bands are shown in Table 4.7. As a conclusion, it notes that the IR spectra of AuNPs prepared at different concentration of NaBH_4 (Figure 4.31(a)) and AuNPs synthesized at different concentrations of CTAB (Figure 4.31(b)) are nearly the same except that some small shifted of the band of $\text{C} – \text{N}^+$ to higher wavenumber in Table 4.7 this is may be due to the change of AuNPs size which can affect the electronegativity of AuNPs with $\text{C} – \text{N}^+$.

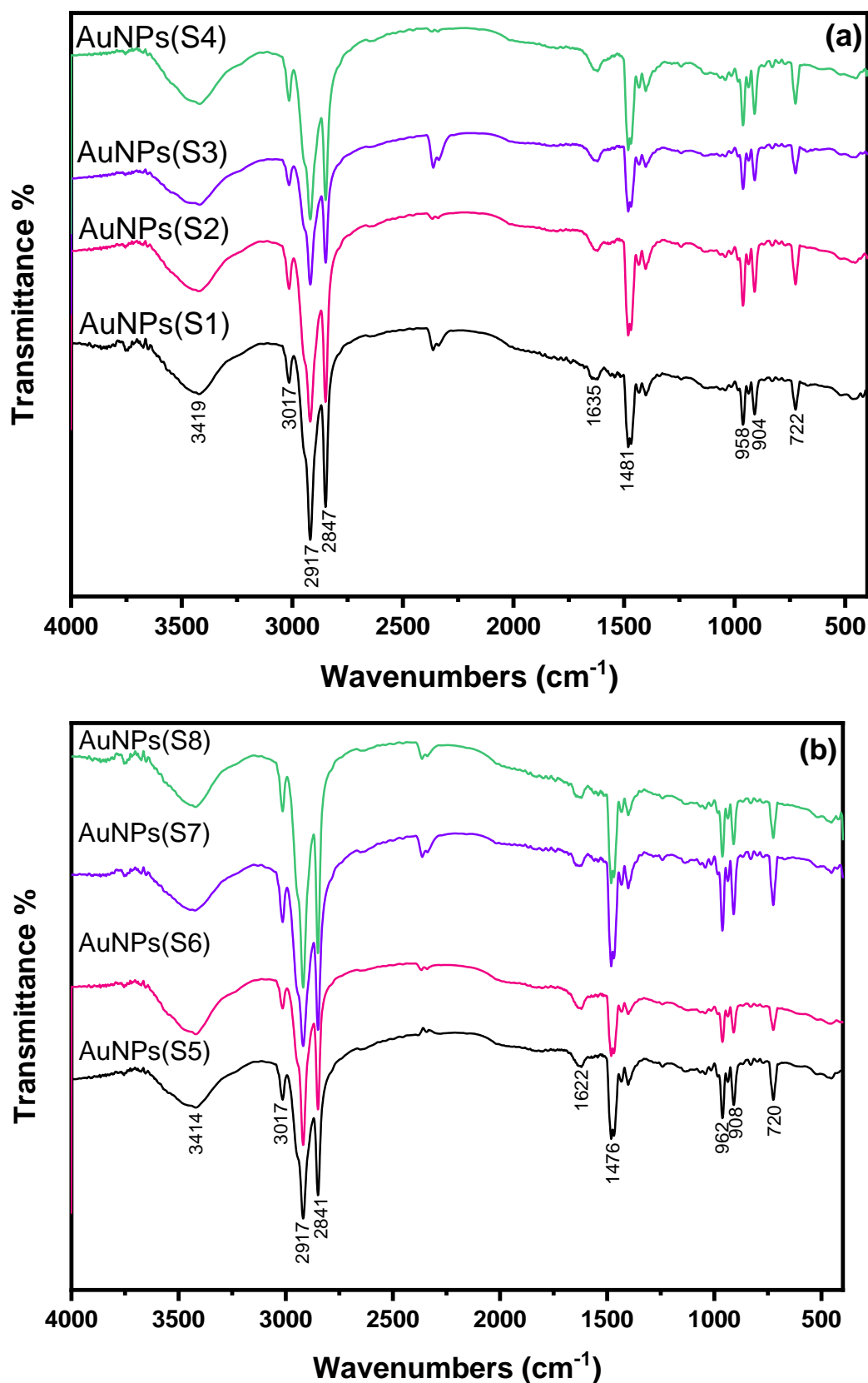


Figure 4. 31: FT-IR spectra of (a) gold nanoparticle prepared at different concentrations of sodium borohydride and (b) gold nanoparticle prepared at different CTAB concentrations.

Table 4. 6 FT-IR bands and their assignments of AuNPs prepared at different concentrations of NaBH₄.

Wavenumbers (cm ⁻¹)				Assignments
AuNPs (S1)	AuNPs (S2)	AuNPs (S3)	AuNPs (S4)	
3419	3423	3419	3419	OH stretching vibration of water
3017	3012	3017	3017	N–H S.V in CTAB
2917	2917	2917	2917	asymmetric CH vibration band of the –CH ₂ group
2847	2847	2847	2847	symmetric CH vibration band of the –CH ₂ group
1635	1626	1626	1626	C – H bending vibration
1481	1481	1481	1481	Coordinate of AuNPs with C – N ⁺
958	958	962	962	out-of-plane -CH bond
904	908	908	908	in-plane -CH bond
722	722	726	726	C – Br ⁻

Table 4. 7 FT-IR band positions of AuNPs capped by different concentrations of CTAB.

Wavenumbers (cm ⁻¹)				Assignments
AuNPs (S5)	AuNPs (S6)	AuNPs (S7)	AuNPs (S8)	
3414	3419	3423	3419	OH stretching vibration of water
3017	3012	3017	3017	N–H S.V in CTAB
2917	2917	2917	2917	asymmetric CH vibration band of the –CH ₂ group
2841	2850	2850	2850	symmetric CH vibration band of the –CH ₂
1622	1622	1626	1626	C – H bending vibration
1476 ¹	1477	1481	1481	Coordinate of AuNPs with C – N ⁺
962	962	962	962	out-of-plane -CH bond
908	908	908	908	in-plane -CH bond
720	726	726	726	C – Br ⁻

4.5.2 Fourier Transform Infrared Spectroscopy (FT-IR) for Silver Nanoparticle Prepared at Different Concentrations of Silver Nitrate

Figure 4.33 measures the FT-IR spectra of AgNPs prepared using NaBH_4 as a reducing agent, CTAB in chloroform as a surfactant, and PVP as a stabilizing agent at different AgNO_3 concentrations, according to Table 3.3. It has been found that a transmittance band appeared at 3432 cm^{-1} attributed to -OH group of H_2O . The transmittance band seen at 3017 cm^{-1} may be assigned to C – H in the ring of PVP. Other observed transmittance bands at 2917 cm^{-1} and 2850 cm^{-1} are assigned to the asymmetric and symmetric stretching vibrations of C-H bond in PVP. The transmittance peak appeared at 2361 cm^{-1} is belonged to carbon in CO_2 in air. Also, the transmittance band appeared at 1626 cm^{-1} is assigned to C = O in PVP. The low intensity and broad of this band may be due to the coordinate of silver nanoparticles with oxygen atom during C = O stretching vibration. The two transmittance bands occurred at 1485 cm^{-1} , and 1469 cm^{-1} may be attributed to C – C stretching vibration or C – H bending vibration of heterocyclic in PVP. Moreover, the bands of C – N were appeared at 1342 cm^{-1} , 1344 cm^{-1} , 1342 cm^{-1} , 1341 cm^{-1} , and 1341 cm^{-1} , for the samples AgNPs(S9), AgNPs(S10), AgNPs(S11), AgNPs(S12), and AgNPs(S13), respectively. The shift of this band position indicates that the nitrogen atom in pyrrolidinyl is involved in the formation of silver nanoparticles by the donation of electrons from N to Ag or coordination between these atoms. The transmittance bands appeared in the range ($1000\text{ cm}^{-1} - 700\text{ cm}^{-1}$) are assigned to the wagging, rocking, bending vibration, and out-of-plane C – H and C – N in the PVP skeleton. Finally, the low peaks observed at 530 cm^{-1} and 452 cm^{-1} may correspond to the Ag – O or Ag – N bending vibration. The slightly visible differentiating shifts in the spectra of pure

PVP and silver nanoparticles capped by PVP indicate that the electrostatic coordination between Ag and C = O, C – N group, and suggest coordination between silver nanoparticles and stabilizers [122].

Generally, the possible formation process was shown in Figure 4.32. The reduction between silver ions and PVP proceeded through a solid-liquid (S–L) mechanism since silver immiscible with water. PVP may adsorb on the surface of solid Ag due to the heterocyclic ring in the PVP structure. The reducing ability of PVP may be attributed to the nitrogen and oxygen atom heterocyclic ring. Under conditions, the reaction took place at sites where Ag was adsorbed on the nitrogen and oxygen atoms. The main reason for PVP protecting AgNPs was N and O in PVP coordinated with silver and formed the protective layer around the silver nanoparticle. Polyvinylpyrrolidone (PVP) reduction has a weak effect on free complex ionic metals, Ag^+ in $AgNO_3$. This explanation is based on the coordinative field of a polar group in PVP molecules [123]. All band and their assignment are expressed in Table 4.8.

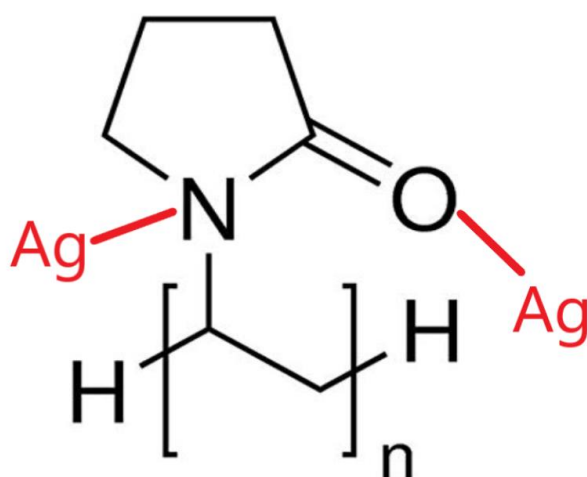


Figure 4. 32: AgNPs coordinated with nitrogen and oxygen atom.

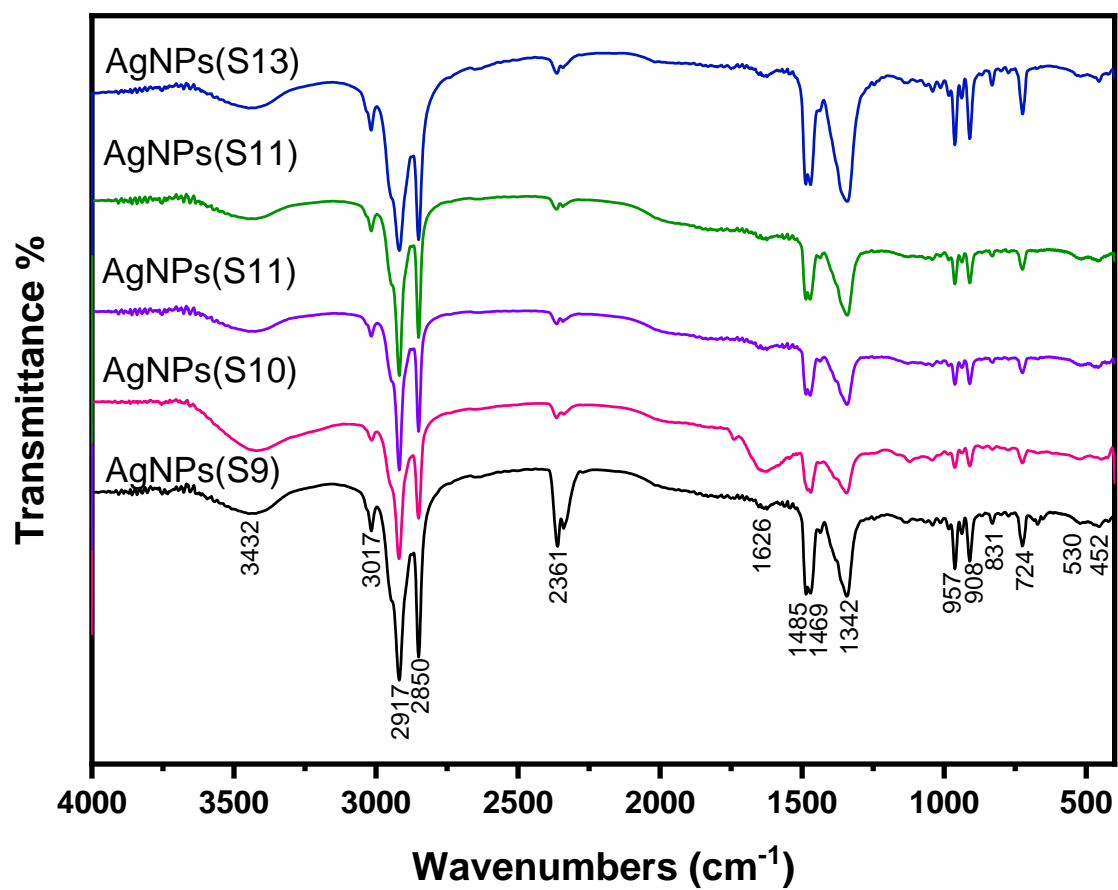


Figure 4. 33: FT-IR spectra of silver nanoparticle prepared at different concentrations of silver nitrate.

Table 4. 8 FT-IR band positions of AgNPs prepared at different concentrations of AgNO₃.

Wavenumbers (cm ⁻¹)					Assignments
AgNPs (S9)	AgNPs (S10)	AgNPs (S11)	AgNPs (S12)	AgNPs (S13)	
3432	3419	3430	3436	3436	OH of water
3017	3012	3012	3017	3017	C – H in the ring of PVP
2917	2917	2917	2917	2917	asymmetric stretching vibrations of C-H in –CH ₂
2850	2850	2850	2850	2850	symmetric stretching vibrations of C-H in –CH ₂
2361	2363	2365	2363	2363	Carbon of CO ₂ in air
1626	1630	1622	1626	1630	C = O stretching vibration
1485	1485	1485	1489	1485	C – C vibration or C – H bending of heterocyclic in PVP
1469	1469	1469	1473	1469	
1346	1340	1340	1340	1340	C-N
957	962	962	962	962	wagging, rocking, bending vibration and out-of-plane C – H and C – N in the PVP skeleton
908	908	912	912	912	
831	829	829	834	834	
724 ¹	726	726	726	726	
530	523	523	518	518	Ag – O or Ag – N vibration
452	448	456	452	452	

4.5.3 Fourier Transform Infrared Spectroscopy (FT-IR) of Zinc Sulfide Nanoparticle Prepared at Different Concentrations of Zinc Acetate Dihydrate

Figure 4.34 displays the FT-IR spectra in the range of 400 cm⁻¹ - 4000 cm⁻¹ at T= 70° of ZnSNPs synthesized at (0.2M) of sodium sulfide and different molar ratios of zinc acetate dihydrate (0.1M), (0.2M), (0.3M), (0.4M), and (0.5M). Transmittance bands rising from OH stretching vibration are merged with the very broad envelope between 3000 cm⁻¹ and

3600 cm^{-1} representing OH stretching vibrations, which indicating the absorption of water molecules on the surface of the samples [124]. The CH vibration peak from zinc acetate dihydrate disappeared in the spectra, suggesting its involvement in reduction during the nanoparticle synthesis [125]. Transmittance bands appeared at 1411 cm^{-1} , and 1346 cm^{-1} belong to asymmetric and symmetric stretching vibrations of Zn–O in zinc acetate dihydrate [119]. The transmittance bands occurred at 1004 cm^{-1} , and 929 cm^{-1} are the characteristics bands for ZnS and corresponding to asymmetric and symmetric Zn-S vibrations (metal-sulfur vibration modes). The sharp transmittance peaks at 664 cm^{-1} , 591 cm^{-1} , and 473 cm^{-1} are attributed to out-of-plane, in-plane, and rocking ZnS bending mode. As conclusion, the characteristic ZnS vibration peaks can be observed at 1004 cm^{-1} , 664 cm^{-1} , and 473 cm^{-1} [126]. It can be noted that this characterized bands of Zn-S, as shown in Table 4.9 was small shifted to higher or lower wavenumber might be due to the change of the particle size for ZnS nanoparticles. The value of the stretching vibration frequency of bond can be obtained theoretically by using Hooke's law. Hooke's law state that the vibrational frequency of a bond is directly proportional to the bond strength and inversely proportional to the mass at the ends of the bonds.

$$\bar{\nu} = \frac{1}{2\pi c} \sqrt{\frac{k}{\mu}} \quad (4.3)$$

Where c is the velocity of light 3×10^8 , k is the force constant, μ is the reduced mass. The stretching vibration bond of Zn-S was calculated at 628 cm^{-1} .

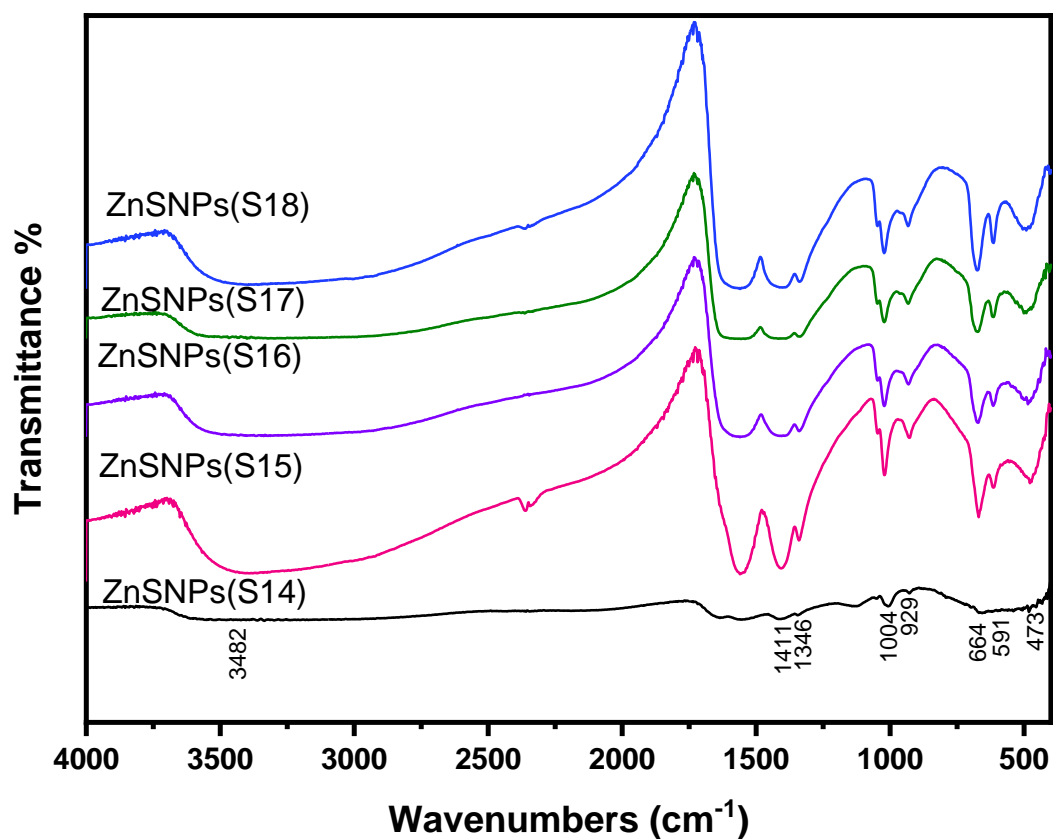


Figure 4. 34: FT-IR spectra of zinc sulfide nanoparticle prepared at different concentrations of zinc acetate dihydrate.

Table 4. 9 FT-IR band positions of ZnSNPs prepared at different concentrations of zinc acetate dihydrate.

Wavenumbers (cm ⁻¹)					Assignments
ZnSNPs (S14)	ZnSNPs (S15)	ZnSNPs (S16)	ZnSNPs (S17)	ZnSNPs (S18)	
3482	3394	3464	3524	3437	OH stretching
1411	1406	1402	1411	1398	C – H Bending
1346	1340	1340	1340	1336	
1004	1020	1020	1020	1020	Asymmetric Zn-S vibration
929	929	933	929	933	Symmetric Zn-S vibration
664	672	676	672	676	Out-of-plane, in-plane, and rocking of ZnS bending vibration
591	614	614	614	614	
473	473	481	494	489	

4.5.4 Fourier Transform Infrared Spectroscopy (FT-IR) For Zinc Sulfide Nanoparticle Prepared at Different Temperatures

Figure 4.35 displays the FT-IR spectra of ZnSNPs prepared using sodium sulfide (0.2M) and zinc acetate dihydrate (0.1M) at different temperatures, according to Table 3.5. The broad transmittance peak appeared at 3511 cm^{-1} corresponded to -OH group, and it is indicating to the existence of water absorbed in the sample [126]. The transmittance band at 1630 cm^{-1} corresponds to the O-H bending vibration of water [127]. Transmittance bands were seen at 1560 cm^{-1} , and 1411 cm^{-1} may represent the vibration of ZnS crystal structure vibration. The transmittance bands occurred at 1004 cm^{-1} , and 925 cm^{-1} are the characteristics of asymmetric and symmetric Zn-S vibrations modes (metal-sulfur vibration modes). Finally, the transmittance peaks at 655 cm^{-1} , 614 cm^{-1} , and 468 cm^{-1} are attributed to out-of-plane, in-plane, and rocking ZnS bending mode. These modes indicate the presence of resonance interaction between vibrational modes of sulfide ions in the crystal [128].

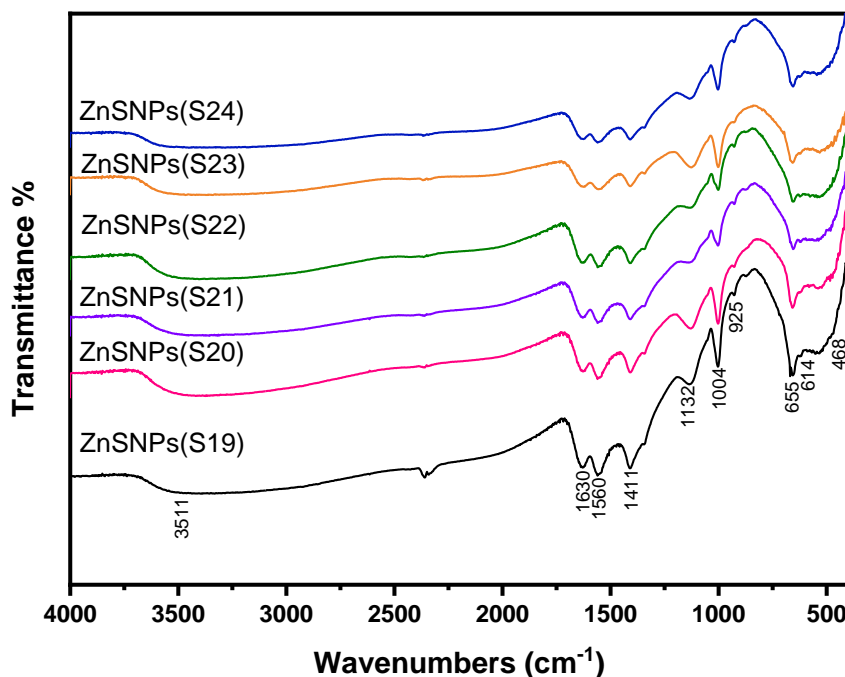


Figure 4. 35: FT-IR spectra of zinc sulfide nanoparticle prepared at different temperatures.

Table 4. 10 FT-IR band positions of ZnSNPs prepared at different temperatures and their assignments.

Wavenumbers (cm ⁻¹)						Assignments
ZnSNPs (S19)	ZnSNPs (S20)	ZnSNPs (S21)	ZnSNPs (S22)	ZnSNPs (S23)	ZnSNPs (S24)	
3511	3469	3494	3484	3548	3519	–OH
1630	1626	1630	1630	1630	1630	OH Bending vibration
1560	1555	1555	1561	1555	1555	C – H Bending vibration
1411	1406	1406	1406	1406	1406	Lattice vibration
1004	1000	1000	1000	1000	1000	Asymmetric Zn-S vibration
925	929	925	925	925	925	Symmetric Zn-S vibration
655	655	655	655	655	655	Out-of-plane, in- plane, and rocking of Zn-S bending vibration
614	618	622	618	618	618	
468	485	497	473	458	481	

4.5.5 Fourier Transform Infrared Spectroscopy (FT-IR) for Silver \ Zinc Sulfide Core-Shell Nanoparticles

Figure 4.36 shows the FT-IR spectra of Ag/ZnS CSNPs synthesized using different quantities of AgNPs(S25), according to Table 3.6. To indicate the presence of ZnSNPs as a shell around AgNPs as a core, the FTIR spectra of Ag/ZnS samples were recorded in the range 4000 cm⁻¹- 400 cm⁻¹. Patel et al., [129] present the FT-IR spectra data of pure PVP. By comparing the bands of PVP spectra with our observed Ag/ZnS(S28) absorbance bands, it was observed that for the Ag/ZnS nanoparticles, there were shifts in

peaks from 3434 cm^{-1} - 3432 cm^{-1} , 2955 cm^{-1} - 2926 cm^{-1} , 1661 cm^{-1} - 1630 cm^{-1} , 1424 cm^{-1} - 1377 cm^{-1} , 1291 cm^{-1} - 1116 cm^{-1} , and 1018 cm^{-1} - 1008 cm^{-1} . The observed absorbance band at 651 cm^{-1} is assigned to Zn–S vibrations that the peak due to Zn and S interaction. This variation in band position occurred due to the surrounding of AgNPs (capped by PVP) by ZnS and confirmed the strong interaction of PVP with ZnS nanoparticles. The main assignments of Ag/ZnS core-shell nanoparticles are summarized in Table 4.11.

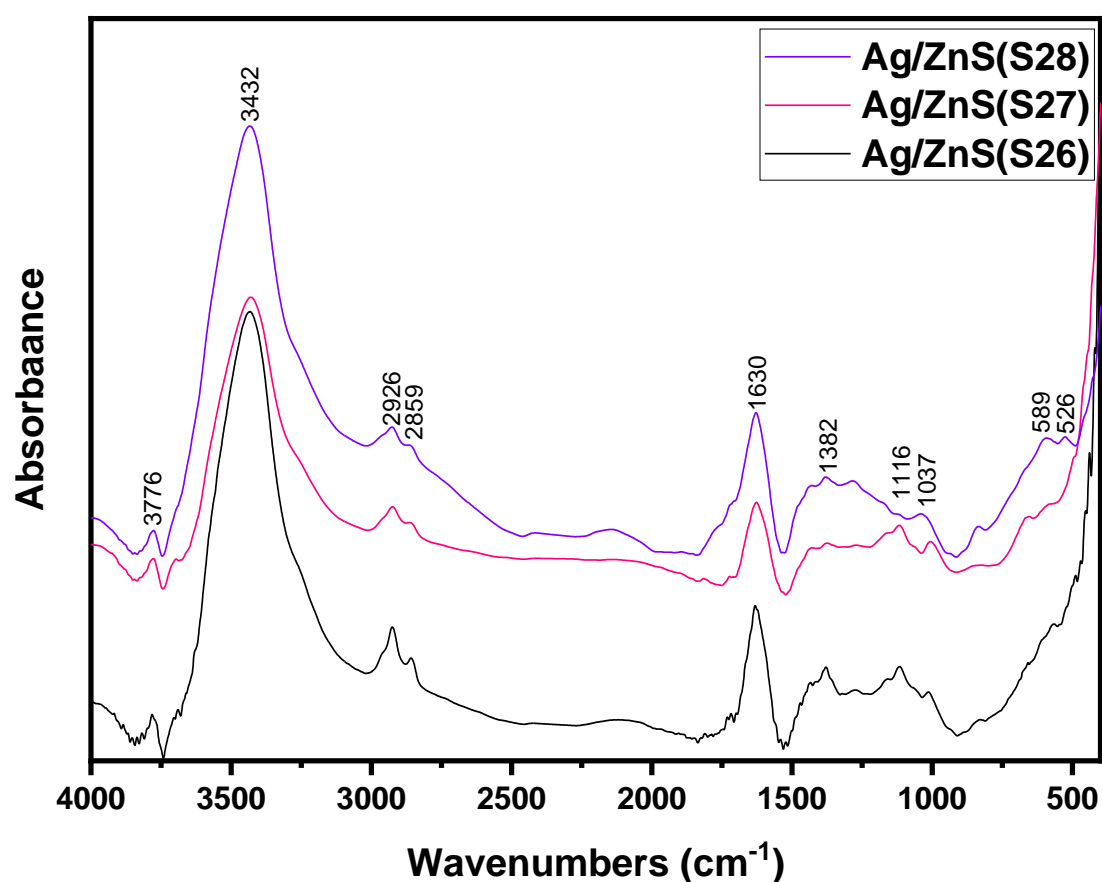


Figure 4. 36: FT-IR spectra of silver nanoparticle \ zinc sulfide core-shell nanoparticles.

Table 4. 11 FT-IR bands and their assignments of PVP and Ag/ZnS capped by PVP.

Wavenumbers (cm ⁻¹)			Assignments
Ag/ZnS(S26)	Ag/ZnS(S27)	Ag/ZnS(S28)	
3432	3432	3432	O – H stretching vibration
2926	2926	2926	C – H asymmetric stretching vibration
2855	2855	2859	C – H symmetric stretching vibration
1630	1626	1630	C = O stretching vibration
1382	1373	1382	CH bending vibration in PVP
1116	1116	1116	C – N vibration or ZnS bending
1016	1004	1037	C – N vibration
568	581	589	Rocking and out-of-plane Zn-S
495	497	526	

4.6 Application of Nanoparticles in Solar Cells

Based on the promising chemical and optical properties results of nanomaterials. Gold, silver, zinc sulfide, silver/zinc sulfide core-shell nanoparticles were selected for further solar cell performance tests. In order to demonstrate the effect of incorporated nanoparticles and polycrystalline silicon solar cell we studied this part.

4.6.1 I-V Characteristic Curve of Polycrystalline Silicon Solar Cell Coated by Gold Nanoparticles

Figure 4.37 illustrates I-V characteristic curves for polycrystalline silicon solar cells with an active area (52mmx52mm) covered by a layer of AuNPs(7 nm) and AuNPs(10 nm) using a spin coater. The curves were recorded under simulated sunlight at AM-1.5 (100mW/cm²). It was clear from Figure that the current increased with increasing the applied voltage for samples under investigations. This behavior is acceptable because when the applied voltage increases, the charge carriers, and the mobility

increased. Carrier mobility is proportional to the current. Therefore, ohm's law can be explained in terms of drift velocity as:

$$V_d = \mu E \quad (4.3)$$

Where μ is the mobility of the charge carrier that measures how easily charge carriers move under the influence of the applied electric field E .

The solar cell parameters such as V_{OC} (open-circuit voltage), I_{SC} (short-circuit current), FF (fill factor), and η (light-to-electricity conversion efficiency) were calculated and summarized in Table 4.12. Short-circuit current (I_{SC}) was extrapolated from the I-V curve, which represents the y-axis(current) intercept. Open-circuit voltage (V_{OC}) stands for the intercept where the curve crosses the horizontal axis (voltage) at $y=0$. Maximum current (I_m) and maximum voltage (V_m) were obtained by drawing two tangents a line with the curve, the point of intersection of these two tangents represents the maximum current and voltage. The fill factor was calculated using

$$FF = \frac{I_m \times V_m}{I_{SC} \times V_{OC}} \quad (4.4)$$

Where I_{SC} is short-circuit current, V_{OC} is open-circuit voltage, I_m is the maximum current, and V_m is the maximum voltage [130].

Also, the efficiency (η) of the solar cell is measured using

$$\eta = \frac{I_{SC} \times V_{OC} \times FF}{P_{in}} \quad (4.5)$$

Where P_{in} is the power of incident light, which is equal to light intensity/area [131].

In general, metal nanoparticles are well known to increase the efficiency of the solar cell by reducing the reflection and increasing light trapping. Our experimental results indicated that depositing gold nanoparticles into

solar cells nearly not affected their efficiency. This may be attributed to the silicon solar cell is not completely covered by gold nanoparticles using a spin coater, which decreases light scattering. Low surface coverage by metal nanoparticles yields a weak shadowing effect, but also reduce weak light scattering [65]. In detail, the cell that is deposited by AuNPs(10 nm) show a slight increase in short-circuit current (I_{SC}). The increase of I_{SC} may be assigned to the enhanced light absorption resulting from the SPR of AuNPs [117]. By comparing the efficiencies according to the nanoparticle size, as the particle size increase, the efficiency increased.

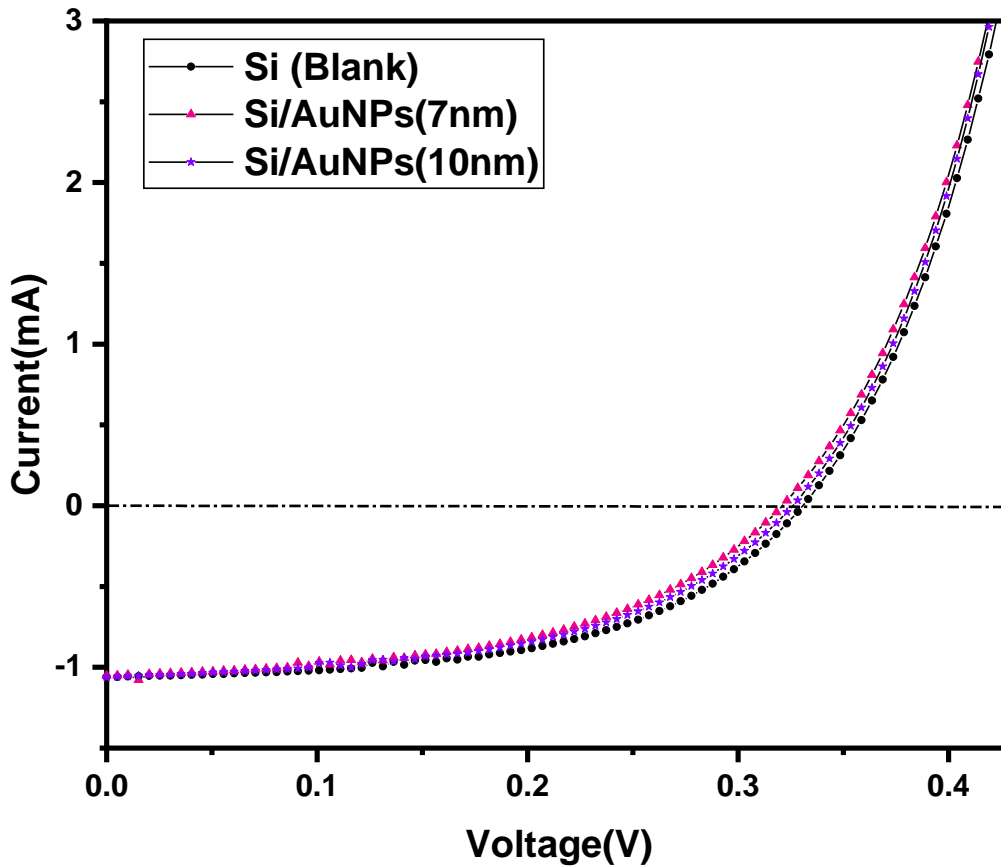


Figure 4. 37: I-V of characteristics curves of the polycrystalline silicon solar cell and polycrystalline silicon solar cell deposited by AuNPs(7 nm) and AuNPs(10 nm) under illumination.

Table 4. 12 Performance parameters of polycrystalline silicon solar cell and polycrystalline silicon solar cell deposited by AuNPs(7 nm) and AuNPs(10 nm).

Samples	V _{OC} (V)	I _{SC} (mA)	V _M (V)	I _M (mA)	FF	η %
Si (Blank)	0.33	1.05	0.26	0.88	0.66	14.29
AuNPs(7nm)	0.32	1.05	0.24	0.91	0.65	13.65
AuNPs(10nm)	0.32	1.06	0.25	0.85	0.62	13.14

4.6.2 I-V Characteristic Curve of Polycrystalline Silicon Solar Cell Coated by Zinc Sulfide Nanoparticles

Figure 4.38 presents the I-V characteristic curves of polycrystalline silicon solar cell and polycrystalline silicon solar cells deposited by ZnSNPs(2.15 nm) and ZnSNPs(3.97 nm) with an active area (52mmx52mm) via spin coater. As discussed before, it was noticed that the current increased with increasing voltage. The characteristics parameters of the solar cells, including open-circuit voltage (V_{OC}), short-circuit current (I_{SC}), fill factor (FF), and overall photoconversion efficiency (η (%)) were calculated from the I-V curve as discussed in the previous section and presented in Table 4.13. Like those with gold nanoparticles, the efficiencies of the cells after deposition do not cause apparent change, and no clear improvement was observed. Even though the efficiency does not show an enhancement, the layer of the nanoparticles prevents the effect of the environment on the cells. Also, this performance may be resulting from the random distribution of the nanoparticles on the surface of the solar cell that does not completely cover the entire cell. Moreover, the samples may require annealing at high temperatures before measurements to evaporate the water from the surface of the samples. For bare solar cells, the η value is about 14.29%. By deposited the zinc sulfide nanoparticle, the efficiency obtained at 12.57% and 11.74% for ZnSNPs(2.15 nm) and ZnSNPs(3.97 nm), respectively. In

addition, The V_{OC} values of the cell that are deposited by the ZnS nanoparticles are low compared with the bare cell, which is attributed to higher charge recombination. The decrease in the efficiencies is acceptable according to the bandgap values. The bandgap values were found to be at 3.58 eV and 3.39 eV for the samples ZnSNPs(2.15 nm) and ZnSNPs(3.97 nm), respectively. As the particle size increased, the energy gap decreased. Therefore, the number of exciting photons from the valence band to the conduction band increased, leading to the enhancement in the efficiency.

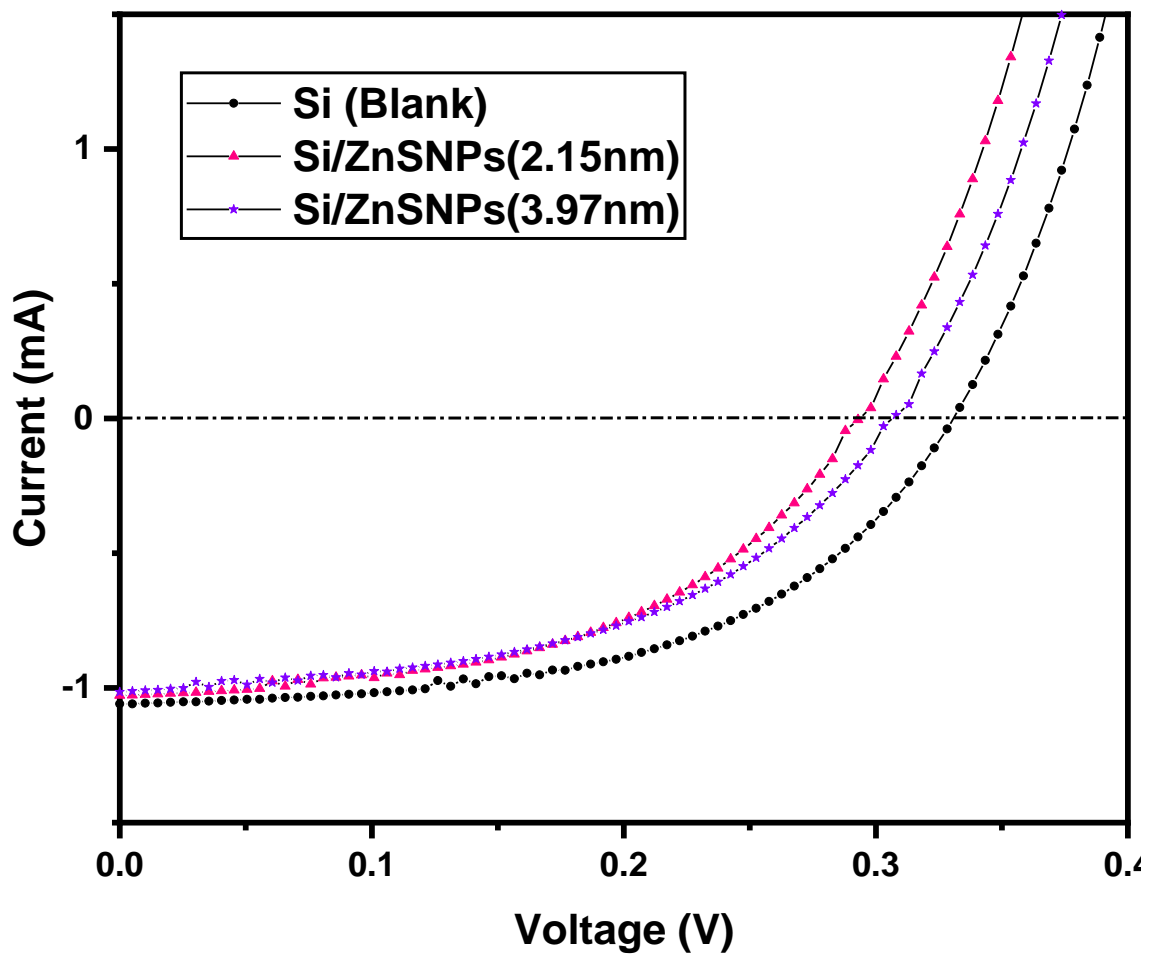


Figure 4. 38: I-V of characteristics curves of the polycrystalline silicon solar cell, and it is covered by ZnSNPs(2.15 nm) and ZnSNPs(3.97 nm) under illumination.

In comparison with the other kinds of literature, the I_{SC} values in the present work are small. This is mainly due to the smaller particle size of the synthesized materials, which does not support for charge space region (no electric field that can assist the separation of the electrons in the semiconductor), leading to the photogenerated charge carrier's recombination. To enhancing efficiency, we can improve the crystallinity of the prepared nanoparticles by annealing and increasing the particle size to an optimum level can improve I_{SC} values.

Table 4. 13 Performance parameters of polycrystalline silicon solar cell and polycrystalline silicon solar cell deposited by ZnSNPs(2.15 nm) and ZnSNPs(3.97 nm).

Samples	V_{OC} (V)	I_{SC} (mA)	V_M (V)	I_M (mA)	FF	η %
Si (Blank)	0.33	1.05	0.26	0.88	0.66	14.29
ZnSNPs(2.15nm)	0.29	1.02	0.22	0.92	0.68	12.57
ZnSNPs(3.97nm)	0.30	1.01	0.23	0.82	0.62	11.74

4.6.3 I-V Characteristic Curve of Polycrystalline Solar Cell Deposited by Silver/Zinc Sulfide Core-Shell Nanoparticles

The relation between I-V characteristic curve of polycrystalline silicon solar cell and polycrystalline silicon solar cell deposited by Ag/ZnS(177 nm) with an active area (52mmx52mm) using a spin coater are depicted in Figure 4.39. As a general behavior of matter, the current increased with an increase in voltage. The solar cell parameters, such as open-circuit voltage (V_{OC}), short-circuit current (I_{SC}), fill factor (FF), and efficiency (η (%)) were estimated from the I-V curve and summarized in Table 4.14. The performance parameters did not make a significant change after Ag/ZnS CSNPs deposition on the finished solar cell. Precisely, the preparation of

core material (silver nanoparticles) coated by shell layer (zinc sulfide nanoparticles) over an energy barrier at the electrode interface providing a pathway for interfacial recombination. This could be further improved when the core (silver nanoparticles) pre-deposited on the silicon solar cell before the shell layer (zinc sulfide nanoparticles) was coated on its surface. This technique may reduce the interfacial recombination that takes place between individual core nanoparticles and provides a direct pathway for electron transport.

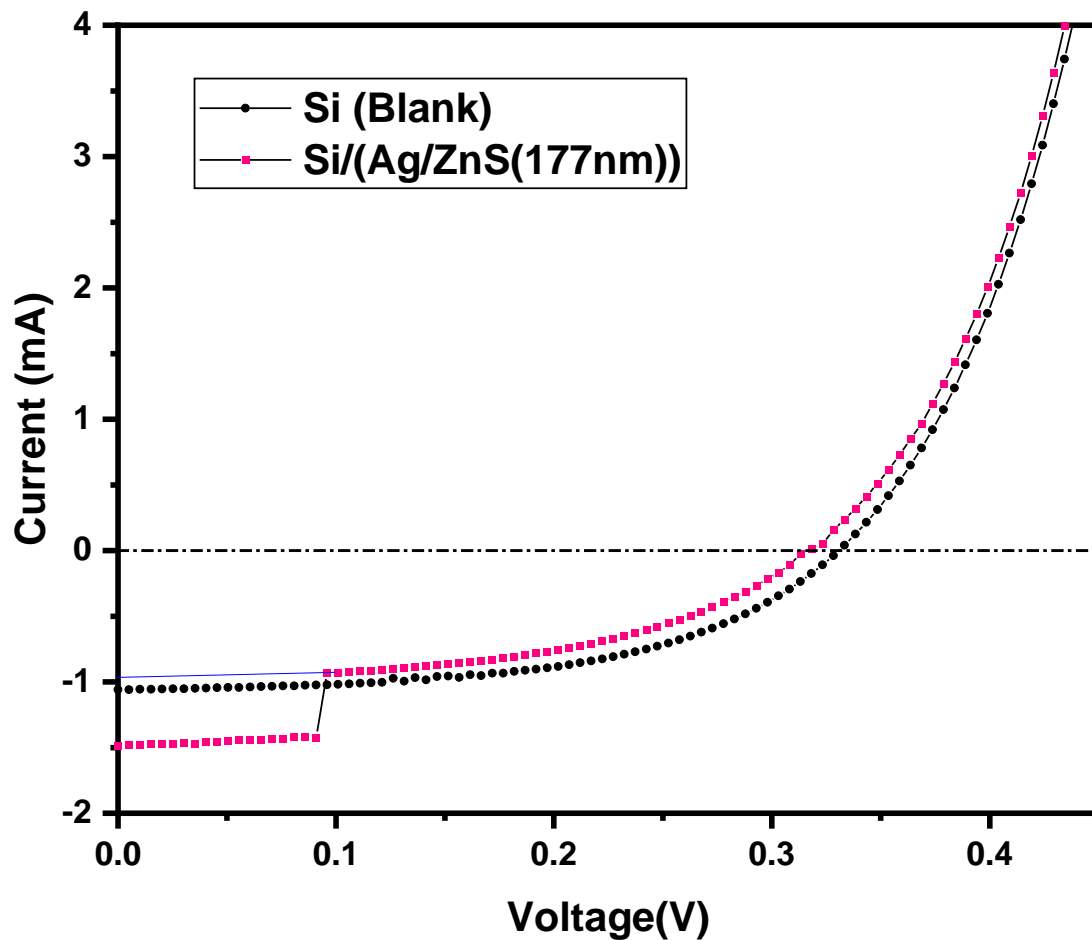


Figure 4. 39: I-V of characteristics curves of the polycrystalline silicon solar cell and polycrystalline silicon solar cell deposited by Ag/ZnS(177 nm) under illumination.

Table 4. 14 Performance parameters of polycrystalline silicon solar cell and polycrystalline silicon solar cell deposited by Ag/ZnS(177 nm).

Samples	V _{OC} (V)	I _{SC} (mA)	V _M (V)	I _M (mA)	FF	η %
Si (Blank)	0.33	1.05	0.26	0.88	0.66	14.29
Ag/ZnS(177nm)	0.31	0.96	0.25	0.84	0.70	13.02

4.6.4 Photocurrent Measurements

The photocurrent values were measured for the samples under investigation and summarized in Table 4.15. From the Table, it notes that a remarkable enhancement in photocurrent of silicon solar cell after using our prepared sample. Such that, AuNPs(S7) shows an improvement in photocurrent related to the presence of the plasmonic materials. The results obtained in AgNPs(S11) present that impeding metallic nanoparticles within the active layer can also improve photocurrent. Furthermore, cells that are deposited by zinc sulfide nanoparticles showed an enhancement in photocurrent. In contrast with the I-V curve data, silver/zinc sulfide nanoparticles exhibit the highest photocurrent compared to the bare silicon solar cell.

By comparing the values of the photocurrent and the efficiency of the solar cell, it can be noted that the photocurrent increased after nanoparticle deposition. On the other side, our I-V results above show that the efficiency of the solar cell was slightly decreased after covering by the prepared nanoparticles. This variation may be due to the fact that the photocurrent was measured after a long time of I-V characteristic curve measuring. This

long period caused the sample to dry, which confirmed our opinion on the effect of annealing on the samples and how it can increase efficiency.

Table 4. 15 Photocurrent Values.

Samples	Photocurrent (mA)
Blank (Si)	58.5
AuNPs (S7)	72
AgNPs (S11)	75.7
ZnSNPs (S17)	78.4
ZnSNPs (S21)	76.3
Ag/ZnS (S26)	76.5
Ag/ZnS (S28)	79.4

Conclusion

Conclusion

Gold, silver, zinc sulfide, and silver/zinc sulfide core-shell nanoparticles were prepared via variable parameters. These samples have been applied in solar cells after it were characterized using different techniques such as UV-Vis, TEM, DLS, XRD, and FT-IR.

UV-Vis spectra show absorption bands in the range (526nm - 528 nm) and (414 nm- 425 nm) for AuNPs and AgNPs, respectively. These bands were known by a surface plasmon resonance (SPR). Band positions of zinc sulfide nanoparticles were seen in the range (283nm-305nm), and optical band gaps were calculated using Tauc's Plot and found to be (4.66 eV-4.93 eV). In contrast, the silver/zinc sulfide core-shell nanoparticle absorption bands were observed in the range (450 nm-498nm).

Gold nanoparticles were visualized by TEM and had spherical in shapes with a small triangle, and hexagon. Particle sizes were estimated using ImageJ software via Gaussian distribution in the range (7nm-10nm). TEM images show a spherical form and a random distribution for silver nanoparticles with average size (2nm-4nm). Zinc sulfide images have confirmed the formation of ZnSNPs with a nearly spherical shape in two regions (high and low spherical distribution), and average particle sizes were estimated in the range (3nm-5nm). Silver/zinc sulfide core-shell nanoparticle images reveal a zinc sulfide shell successfully coated the surface of the silver nanoparticles. The average particle sizes were (27nm-177nm).

Dynamic light scattering (DLS) had also used to estimate the average particle size of our samples using Brownian motion. The average particle sizes were calculated in the range (23.46nm-33.03nm) for AuNPs, (77.68nm, 87nm) for AgNPs, (11nm-315nm) for ZnSNPs, and (39nm-127nm) Ag/ZnS CSNPs. The large variation in particle size obtained by

dynamic light scattering and transmission electron microscopy is logical because dynamic light scattering measures the average particle size of huge quantity comparable with the transmission electron microscopy.

XRD results showed that the crystalline sizes of gold, silver, zinc sulfide nanoparticles were dependent on the preparation conditions. The Scherrer equation was used to determine the crystal size. Mean crystal sizes were calculated at 2θ (38.45°) in the range (8.25nm-33.57nm) of AuNPs samples. The crystal size of silver nanoparticles was estimated at 2θ (37.7°) in the range (7.89nm-12.42nm). Zinc sulfide crystal size at 2θ (28°) was in the range (2.14-4.17nm).

The chemical coordination between our nanoparticle samples and the chemical groups in stabilizing materials was discussed from FT-IR spectroscopy results. The band appeared at about 1481 cm^{-1} in gold nanoparticles spectra indicating the coordination of gold nanoparticles with $C - N^+$ group in CTAB molecules. Spectra of silver nanoparticles clarified a shift in the band appeared at 1346 cm^{-1} , and this resulted from the coordination of silver nanoparticles with pyrrolidinyl. The bands appeared at 530 cm^{-1} , and 452 cm^{-1} indicate the coordination between silver atom and oxygen or nitrogen atom. Furthermore, the spectra of zinc sulfide nanoparticles reveal a band at about 1004 cm^{-1} and 925 cm^{-1} due to the asymmetric and symmetric $Zn - S$ vibration. Moreover, silver/zinc sulfide core-shell nanoparticles show a new band that confirmed the presence of the zinc sulfide nanoparticles and silver nanoparticles core-shell.

The power conversion efficiency achieved for polycrystalline silicon solar cell ($\eta = 14.29\%$) and after deposition by AuNPs (7 nm), AuNPs (10 nm), ZnSNPs (2.15 nm), ZnSNPs(3.97 nm), and Ag/ZnS(177 nm) were 13.65 % , 13.14%, 12.57 % , 11.74%, 13.02 % respectively. The change was in the range of Experimental, and this was the opposite of what we expected.

Maybe the samples were needed more drying processes before the measurements. This viewpoint is confirmed by measuring the photocurrent after drying, which increases for the samples deposited by our prepared nanomaterials.

References

References

- [1] BS Murty, P Shankar, Baldev Raj, , BB Rath, and James Murday,” Textbook of nanoscience and nanotechnology”, Springer Science & Business Media, (2013).
- [2] Alexei Nabok, “Organic And Inorganic Nanostructures (Artech House Mems and Sensors Library)”, Artech House Publishers Hardcover, (2005).
- [3] Fatma Hadeif, “An Introduction to Nanomaterials”, Springer, (2018) 1-58.
- [4] Ketaki Deshmukh, “Nanotechnology in Ancient Era”, Springer, (2019) 3-14.
- [5] Ian Freestone, Nigel Meeks, Margaret Sax, and Catherine Higgitt, “The Lycurgus cup—a roman nanotechnology” Gold bulletin, 40 (2007) 270-277.
- [6] Sujoy K Das and Enrico Marsili, “Bioinspired metal nanoparticle: synthesis, properties and application”, Nanomaterials, (2011) 253-274.
- [7] Kouros Kalantar-zadeh and Benjamin Fry, “Nanotechnology-enabled sensors”, Springer Science & Business Media, (2007).
- [8] Richard P Feynman, “There’s plenty of room at the bottom: An invitation to enter a new field of physics, Handbook of Nanoscience, Engineering, and Technology”, CRC Press, (2018) 26-35.
- [9] Dr P Gouthami Avula, atchuta abhinav, and suryakanth malgikar, “Nanotechnology in periodontics: current concepts & challenges faced in its application”, (2019).
- [10] Daniel Rugar, and Paul Hansma, “Atomic force microscopy”, Physics today, 43 (1990) 23-30.

- [11] Bertram Schwarzschild, “Search and discovery: Nobel chemistry prize goes to Curl, Kroto and Smalley for discovering fullerenes”, *Physics Today*, 49 (1996) 19-21.
- [12] Christoph Gerber, “Heinrich Rohrer (1933–2013)”, Nature Publishing Group, (2013).
- [13] Chris Toumey, “Does scale matter at the nanoscale?”, *Nature nanotechnology*, 9 (2014) 6.
- [14] JE Hulla, SC Sahu, and AW Hayes, “Nanotechnology: History and future”, 34 (2015) 1318-132.
- [15] Yuhan Yao, He Liu, Yifei Wang, , Yuanrui Li, Boxiang Song, Alexandre Bratkovsk, Shih-Yuan Wang, and Wei Wu, “Nanoimprint lithography: an enabling technology for nanophotonics”, *Applied Physics*, 121 (2015) 327-333.
- [16] Glen R Boyd, Mary Ellen Tuccillo, Anne Sandvig, Miguel Pelaez, Changseok Han, and Dionysios D Dionysiou, “Nanomaterials: Removal processes and beneficial applications in treatment”, *Journal-American Water Works Association*, 105 (2013) 699-708.
- [17] David Carlander, “Defining nano”, SOC chemical industry, (2012).
- [18] Tawfik Abdo Saleh, and Vinod Kumar Gupta, “Nanomaterial and polymer membranes: synthesis, characterization, and applications”, Elsevier, (2016).
- [19] Cristina Buzea, and Ivan Pacheco, “Nanomaterials and their Classification”, Springer, (2017) 3-45.
- [20] Vijaykumar B Sutariya, and Yashwant Pathak, “Biointeractions of nanomaterials”, CRC Press, (2014).

- [21] Patricia I Dolez, “Nanoengineering: global approaches to health and safety issues”, Elsevier, (2015).
- [22] Guo Min Lin, Miao Shang, and Wen Guang Zhang, “Research on nanomaterials and its latest application”, Trans Tech Publ, 912 (2014) 305-308.
- [23] Narendra Kumar, and Sunita Kumbhat, “Essentials in nanoscience and nanotechnology”, Wiley, (2016).
- [24] Shawn Y Stevens, LeeAnn M Sutherland, and Joseph S Krajcik, “The big ideas of nanoscale science and engineering”, NSTA press, (2009).
- [25] Mahmoud Goodarz Naseri, and Elias B Saion, “Crystalization in spinel ferrite nanoparticles”, inAdvances in Crystallization Processes, (2012) 349-380.
- [26] HR Rezaie, A Shokuhfar, and F Arianpour, “Nanocomposite materials from theory to application”, Springer, (2012) 171-232.
- [27] Ramakrishna Podila and Jared M Brown, “Toxicity of engineered nanomaterials: a physicochemical perspective”, Journal of biochemical and molecular toxicology, 27 (2013) 50-55.
- [28] Emil Roduner, “Size matters: why nanomaterials are different”, Chemical Society Reviews, 35 (2006) 583-592.
- [29] Yashwant Vishnupant Pathak, and Jayant N Lokhande, “Handbook of metallonutraceuticals”, CRC Press, (2014).
- [30] Wesley V Prescott, and Arnold I Schwartz, “Nanorods, nanotubes, and nanomaterials research progress”, Nova Publishers, (2008).
- [31] Nada M Čitaković, “Physical properties of nanomaterials”, Vojnotehnički glasnik, 67 (2019) 159-171.

- [32] Catherine Bréchnignac, Philippe Houdy, and Marcel Lahmani, “Nanomaterials and nanochemistry”, Springer Science & Business Media, (2008).
- [33] Andrew G Mark, John G Gibbs, Tung-Chun Lee, and Peer Fischer, “Hybrid nanocolloids with programmed three-dimensional shape and material composition”, *Nature materials*, 12 (2013) 802.
- [34] Kevin Robbie, Gisia Beydaghyan, Tim Brown, Cory Dean, Jonathan Adams, and Cristina Buzea, “Ultrahigh vacuum glancing angle deposition system for thin films with controlled three-dimensional nanoscale structure”, *Review of Scientific Instruments*, 75 (2004) 1089-1097.
- [35] Costas A Charitidis, Pantelitsa Georgiou, Malamatenia A Koklioti, Aikaterini-Flora Trompeta, and Vasileios Markakis, “Manufacturing nanomaterials: from research to industry”, *Manufacturing Review*, 1 (2014) 11.
- [36] Federico Rosei, “Nanostructured surfaces: challenges and frontiers in nanotechnology”, *Journal of Physics: Condensed Matter*, 16 (2004) 1373.
- [37] Richard W Siegel, and Evelyn Hu, “Nanostructure science and technology: R & D status and trends in nanoparticles, nanostructured materials and nanodevices”, Springer Science & Business Media, (1999).
- [38] Thomas AJ Kuhlbusch, Christof Asbach, Heinz Fissan, Daniel Göhler, and Michael Stintz, “Nanoparticle exposure at nanotechnology workplaces: a review”, *Particle and fibre toxicology*, 8 (2011) 22.
- [39] KT Ramesh, “Nanomaterials: Mechanics and Mechanisms”, Springer, (2009).

- [40] XH Wang, K Eguchi, C Iwamoto, and T Yoshida, “Ultrafast thermal plasma physical vapor deposition of thick SiC films”, *Science and Technology of Advanced Materials*, 4 (2003) 159.
- [41] Sagar E Shirsath, Danyang Wang, Santosh S Jadhav, ML Mane, and Sean Li, “Ferrites obtained by sol-gel method”, *Handbook of Sol-Gel Science and Technology: Processing, Characterization and Applications*, (2018) 695-735.
- [42] Xiaohua Huang, Prashant K Jain, Ivan H El-Sayed, and Mostafa A El-Sayed, “Gold nanoparticles: interesting optical properties and recent applications in cancer diagnostics and therapy”, (2007).
- [43] Michael Faraday, “X. The Bakerian Lecture. Experimental relations of gold (and other metals) to light”, *Philosophical Transactions of the Royal Society of London*, (1857) 145-181.
- [44] O Petravic, X Chen, S Bedanta, W Kleemann, S Sahoo, S Cardoso, and PP Freitas, “Collective states of interacting ferromagnetic nanoparticles”, *Journal of Magnetism and Magnetic Materials*, 300 (2006) 192-197.
- [45] C Djéga-Mariadassou, “FePt-based heterocomposites: Magnetic properties and nanostructure”, Springer, (2015) 211-296.
- [46] Zhympargul Abdullaeva, “Nanomaterials in Daily Life”, Springer, (2017).
- [47] James S Murday, “Workshop Report International Benchmark Workshop on K-12”, *Nanoscale Science and Engineering Education (NSEE)*, (2010), Washington, 6-7.
- [48] Thomas Ihn, “Semiconductor Nanostructures: Quantum states and electronic transport”, Oxford University Press, (2010).

- [49] Ferric Christian, Dendy Adityawarman, and Antonius Indarto, “Application of nanotechnologies in the energy sector: A brief and short review”, *Frontiers in Energy*, 7 (2013) 6-18.
- [50] OECD, “Nanotechnology for Green Innovation”, *Technology and Industry Policy Papers*, 5 (2013).
- [51] Peter Lund, “Nanoscience and technology for energy applications”, *International Journal of Energy Research*, 33 (2009) 1099-1100.
- [52] Ahmed Kadhim Hussein, “Applications of nanotechnology in renewable energies-A comprehensive overview and understanding”, *Renewable and Sustainable Energy Reviews*, 42 (2015) 460-476.
- [53] C Jeffrey Brinker, and David Ginger, “Nanotechnology for sustainability: energy conversion, storage, and conservation”, Springer, (2011) 261-303.
- [54] Suresh Sagadevan, “Recent trends on nanostructures based solar energy applications: a review”, *Reviews on advanced materials science*, 34 (2013) 44-61.
- [55] Navid Mohammad Sadeghi Jahed, “Heterojunction Quantum Dot Solar Cells”, PhD Thesis. University of Waterloo, (2016).
- [56] Simon M Sze and Kwok K Ng, “Physics of semiconductor devices”, John wiley & sons, (2006).
- [57] KM Gupta and Nishu Gupta, “Advanced semiconducting materials and devices”, Springer, (2016).
- [58] Jeffery Steevens and Igor Linkov, “Nanomaterials: Risks and Benefits”, Springer, (2009).

- [59] David G Capco and Yongsheng Chen, “Nanomaterial”, Springer, (2014).
- [60] Amretashis Sengupta and Chandan Kumar Sarkar, “Introduction to nano: basics to nanoscience and nanotechnology”, Springer, (2015).
- [61] Takuya Tsuzuki, “Commercial scale production of inorganic nanoparticles”, *International journal of nanotechnology*, 6 (2009) 567-578.
- [62] Hyun-Young Kim, Ho-Sub Kim, Jung Sang Suh, Bong-Hyun Jun, and Won-Yeop Rho, “Preparation of plasmonic monolayer with Ag and Au nanoparticles for dye-sensitized solar cells”, 687 (2017) 152-157.
- [63] Yehoshua Aguilar Molina, Víctor Rentería Tapia, and Enrique Barrera Calva, “Silver nanoparticles in epoxy resin deposited on silicon substrates for light trapping”, *Plasmonics*, 11 (2016) 971-979.
- [64] Mrinmoy Misra, Raju Kumar Gupta, AK Paul, and Madanlal Singla, “Influence of gold core concentration on visible photocatalytic activity of gold–zinc sulfide core–shell nanoparticle”, *Journal of Power Sources*, 294 (2015) 580-587.
- [65] Ming-Jer Jeng, Zih-Yang Chen, Yu-Ling Xiao, Liann-Be Chang, Jianping Ao, Yun Sun, Ewa Popko, Witold Jacak, and Lee Chow, “Improving efficiency of multicrystalline silicon and CIGS solar cells by incorporating metal nanoparticles”, *Materials*, 8 (2015) 6761-6771.
- [66] Matheus Costa de Oliveira, André Luis Silveira Fraga, Anderson Thesing, Rocelito Lopes de Andrade, Jacqueline Ferreira Leite Santos, and Marco José Leite Santos, “Interface dependent plasmon induced enhancement in dye-sensitized solar cells using gold nanoparticles”, *Journal of Nanomaterials*, 2015 (2015).

- [67] Sanjay K Sardana, Venkata SN Chava, Eshwar Thouti, Nikhil Chander, Sanjai Kumar, SR Reddy, and Vamsi K Komarala, “Influence of surface plasmon resonances of silver nanoparticles on optical and electrical properties of textured silicon solar cell”, *Applied Physics Letters*, 104 (2014) 073903.
- [68] Kazi Islam, Aasha Alnuaimi, Enes Battal, Ali Kemal Okyay, and Ammar Nayfeh, “Effect of gold nanoparticles size on light scattering for thin film amorphous-silicon solar cells”, *Solar Energy*, 103 (2014) 263-268.
- [69] Teen-Hang Meen, Jenn-Kai Tsai, Shi-Mian Chao, Yu-Chien Lin, Tien-Chuan Wu, Tang-Yun Chang, Liang-Wen Ji, Walter Water, Wen-Ray Chen, and I-Tseng Tang, “Nanoscale research letters”, 8 (2013) 1-6.
- [70] Marco Notarianni, Kristy Vernon, Alison Chou, Muhsen Aljada, Jinzhang Liu, and Nunzio Motta, “Plasmonic effect of gold nanoparticles in organic solar cells”, *Solar Energy*, 106 (2014) 23-37.
- [71] MG Raymer, and Brian J Smith, “The Maxwell wave function of the photon”, *International Society for Optics and Photonics*, 5866 (2005) 293-297.
- [72] A Mark Pollard, Catherine M Batt, Ben Stern, Suzanne MM Young, and SMM Young, “Analytical chemistry in archaeology”, Cambridge University Press, (2007).
- [73] Leslie D Field, Sev Sternhell, and John R Kalman, “Organic structures from spectra”, John Wiley & Sons, (2012).
- [74] T Owen, “Fundamentals of UV-visible Spectroscopy, Hewlett-Packard Company”, preparation, (1996).

- [75] Heinz-Helmut Perkampus, “UV-VIS Spectroscopy and its Applications “, Springer Science & Business Media, (2013).
- [76] Bernard Valeur, and Mário Nuno Berberan-Santos, “Molecular Fluorescence: Principles and Applications”, John Wiley & Sons, (2012).
- [77] Brent Fultz, and James M Howe, “Transmission electron microscopy and diffractometry of materials”, Springer Science & Business Media, (2012).
- [78] Alf Mews, “Nanomaterials Handbook. Edited by Yury Gogotsi”, Angewandte Chemie International Edition, 46 (2007) 2143-2143.
- [79] Ray F Egerton, “Physical principles of electron microscopy”, Springer, (2005).
- [80] Helmut Kohl, and Ludwig Reimer, “Transmission electron microscopy: physics of image formation”, Springer, (2008).
- [81] Uwe Kätzel, “Dynamic light scattering for the characterization of polydisperse fractal systems by the example of pyrogenic silica”, PhD dissertation Dresden university, (2007).
- [82] Walther Tscharnuter,” Photon correlation spectroscopy in particle sizing”, Encyclopedia of analytical chemistry: applications, theory and instrumentation, (2006).
- [83] Malvern Instruments, “Dynamic light scattering: an introduction in 30 minutes”, Technical Note Malvern, 1 (2012).
- [84] John Faber and Tim Fawcett, “The powder diffraction file: present and future”, Acta Crystallographica Section B: Structural Science, 58 (2012) 325-332.

- [85] Sebastian Volz, “Thermal nanosystems and nanomaterials”, Springer Science & Business Media, 118 (2009).
- [86] Kathryn Lawson-Wood, Ian Robertson, and UK Seer Green, “Comparison of Near-and Mid-Infrared Spectroscopy for Herb and Spice Authenticity Analysis”, (2017).
- [87] Avelino Alvarez-Ordóñez, and Miguel Prieto, “Fourier transform infrared spectroscopy in food microbiology”, Springer, (2012).
- [88] Christoph Richter, Daniel Lincot, and Christian A. Gueymard, “Solar Energy”, Springer, (2012).
- [89] Martin A Green, “Third generation photovoltaics: advanced solar energy conversion”, *Physics Today*, 57 (2004) 71-72.
- [90] Rick Docksai, “Outlook Is Sunny for Solar Energy: An Interview with Aalto University Physicist Peter Lund”, *World Future Review*, 5 (2013) 266-268.
- [91] Arthur J Nozik, “Quantum dot solar cells”, *Physica E: Low-dimensional Systems and Nanostructures*, 14 (2002) 115-120.
- [92] C Barry Carter, and David B Williams, “Transmission electron microscopy: Diffraction, imaging, and spectrometry”, Springer, (2016).
- [93] Jeanne Ayache, Luc Beaunier, Jacqueline Boumendil, Gabrielle Ehret, and Danièle Laub, “Sample preparation handbook for transmission electron microscopy: techniques”, Springer Science & Business Media, 2 (2010).
- [94] Zetasizer Nano Series User Manual, “Size Theory”, Chapter, (2013).
- [95] Andrei A Bunaciu, Elena Gabriela UdriȘTioiu, and Hassan Y

Aboul-Enein, "X-ray diffraction: instrumentation and applications", *Critical reviews in analytical chemistry*, 45 (2015) 289-299.

[96] Ruggero Frison, Antonio Cervellino, Giuseppe Cernuto, Antonietta Guagliardi, and Norberto Masciocchi, "Testing the Debye Function Approach on a Laboratory X-ray Powder Diffraction Equipment. A Critical Study", *Powder Diffraction*, 28 (2013) 11-21.

[97] Sander De Bruyne, Marijn M Speeckaert, and Joris R Delanghe, "Applications of mid-infrared spectroscopy in the clinical laboratory setting", *Critical reviews in clinical laboratory sciences*, 55 (2018) 1-20.

[98] Michael Grätzel, "Photoelectrochemical cells", *Nature*, 414 (2001) 338-344.

[99] Ahmet Sarı, Cemil Alkan, Derya Kahraman Döğüşcü, and Alper Biçer, "Micro/nano-encapsulated n-heptadecane with polystyrene shell for latent heat thermal energy storage", *Solar energy materials and solar cells*, 126 (2014) 42-50.

[100] Eleonora Petryayeva, and Ulrich J Krull, "Localized surface plasmon resonance: Nanostructures, bioassays and biosensing-A review", *Analytica chimica acta*, 706 (2011) 8-24.

[101] K Lance Kelly, Eduardo Coronado, Lin Lin Zhao, and George C Schatz, "The optical properties of metal nanoparticles: the influence of size, shape, and dielectric environment", ACS Publications, (2003).

[102] Nanasaheb P Huse, Avinash S Dive, Sandip V Mahajan, and Ramphal Sharma, "Facile, one step synthesis of non-toxic kesterite $\text{Cu}_2\text{ZnSnS}_4$ nanoflakes thin film by chemical bath deposition for solar cell application", *Journal of Materials Science: Materials in Electronics*, 29 (2018) 5649-5658.

[103] Ch Venkata Reddy, Jaesool Shim, and Migyung Cho, “Synthesis, structural, optical and photocatalytic properties of CdS/ZnS core/shell nanoparticles”, *Journal of Physics and Chemistry of Solids*, 103 (2017) 209-217.

[104] IB Vashistha, , MC Sharma, and SK Sharma, “Post annealing treatment of zinc sulphide thin film as a buffer layer for solar cell application”, *Surface Engineering*, 33 (2017) 299-304.

[105] Young In Choi, Seungwon Lee, Seog K Kim, Young-II Kim, Dae Won Cho, Mohammad Mansoob Khan, and Youngku Sohn, “Fabrication of ZnO, ZnS, Ag-ZnS, and Au-ZnS microspheres for photocatalytic activities, CO oxidation and 2-hydroxyterephthalic acid synthesis”, 675 (2016) 46-56.

[106] Dhruvajyoti Samanta, Parita Basnet, T Inakhunbi Chanu, Somenath Chatterjee, Shyamasree Gupta Chatterjee, and Jaya Mukherjee, “Photocatalytic activity of green synthesized pure ZnS and Ag-ZnS nanocomposite under sunlight”, AIP Publishing LLC, 2115 (2019) 030203.

[107] F de A La Porta, AE Nogueira, Lourdes Gracia, WS Pereira, Gleice Botelho, Tatiana A Mulinari, Juan Andrés, and Elson Longo, “An experimental and theoretical investigation on the optical and photocatalytic properties of ZnS nanoparticles”, *Journal of Physics and Chemistry of Solids*, 103 (2017) 179-189.

[108] Marija Petrushevska, Kristina Pavlovska, Jovanka Laskova, Pance Zdravkovski, and Marija Glavas Dodov, “Transmission Electron Microscopy: Novel Application of Established Technique in Characterization of Nanoparticles as Drug Delivery Systems”, *Prilozi*, 40 (2019) 67-72.

[109] B Samiey, C-H Cheng, and J Wu, "Effects of surfactants on the rate of chemical reactions", *Journal of chemistry*, 2014 (2014).

[110] Zaheer Khan, Shaeel Ahmed AL-Thabaiti, Abdullah Yousif Obaid, Ziya Ahmad Khan, and Abdulrahman AO Al-Youbi, "Shape-directing role of cetyltrimethylammonium bromide in the preparation of silver nanoparticles", 367 (2012) 101-108.

[111] M Divya Rao, and Gautam Pennathur, "Facile bio-inspired synthesis of zinc sulfide nanoparticles using *Chlamydomonas reinhardtii* cell free extract: optimization, characterization and optical properties", *Green Processing and Synthesis*, 5 (2016) 379-388.

[112] Christopher M Hoo, Natasha Starostin, Paul West, and Martha L Mecartney, "A comparison of atomic force microscopy (AFM) and dynamic light scattering (DLS) methods to characterize nanoparticle size distributions", *Journal: Journal of Nanoparticle Research*, 10 (2008) 89-96.

[113] Sankar K Sivaraman, Sanjeev Kumar, and Venugopal Santhanam, "Room-temperature synthesis of gold nanoparticles-Size-control by slow addition", *Gold Bulletin*, 43 (2010) 275-286.

[114] Atul Sharma, Takashi Kyotani, and Akira Tomita, "Comparison of structural parameters of PF carbon from XRD and HRTEM techniques", *Carbon*, 38 (2000) 1977-1984.

[115] Sireesh babu Maddinedi, Badal Kumar Mandal, Shivendu Ranjan, and Nandita Dasgupta, "Diastase assisted green synthesis of size-controllable gold nanoparticles", *RSC Advances*, 5 (2015) 26727-26733.

[116] N Senthil Kumar, M Ganapathy, S Sharmila, M Shankar, M Vimalan, and I Vetha Potheher, "ZnO/Ni (OH) 2 core-shell nanoparticles:

synthesis, optical, electrical and photoacoustic property analysis”, *Journal of Alloys and Compounds*, 703 (2017) 624-632.

[117] T Solaiyammal, and P Murugakoothan, “Green synthesis of Au and Au@ TiO₂ core-shell structure formation by hydrothermal method for dye sensitized solar cell applications”, *Journal of Materials Science: Materials in Electronics*, 29 (2018) 491-499.

[118] V Gopinath, D MubarakAli, S Priyadarshini, N Priyadharsshini, Meera, N Thajuddin, and P Velusamy, “Biosynthesis of silver nanoparticles from *Tribulus terrestris* and its antimicrobial activity: a novel biological approach”, *Colloids and Surfaces B: Biointerfaces*, 96 (2012) 69-74.

[119] SHA Allehyani, R Seoudi, DA Said, AR Lashin, and A Abouelsayed, “Synthesis, characterization, and size control of zinc sulfide nanoparticles capped by poly (ethylene glycol)”, 44 (2015) 4227-4235.

[120] R Davis and LJ Mauer, “Fourier transform infrared (FT-IR) spectroscopy: a rapid tool for detection and analysis of foodborne pathogenic bacteria”, *Current research, technology and education topics in applied microbiology and microbial biotechnology*, 2 (2010) 1582-1594.

[121] Souad A Elfeky, Shymaa Ebrahim Mahmoud, and Ahmed Fahmy Youssef, “Applications of CTAB modified magnetic nanoparticles for removal of chromium (VI) from contaminated water”, *Journal of advanced research*, 8 (2017) 435-443.

[122] Dagmara Malina, Agnieszka Sobczak-Kupiec, Zbigniew Wzorek, and Zygmunt Kowalski, “Silver nanoparticles synthesis with different concentrations of polyvinylpyrrolidone”, *Digest Journal of Nanomaterials & Biostructures (DJNB)*, 7 (2012).

- [123] R Seoudi, AA Fouda, and DA Elmenshawy, “Synthesis, characterization and vibrational spectroscopic studies of different particle size of gold nanoparticle capped with polyvinylpyrrolidone”, *Physica B: Condensed Matter*, 405 (2010) 906-911.
- [124] Shahina Riaz, Zulfiqar Ali Raza, Muhammad Irfan Majeed, and Tariq Jan, “Synthesis of zinc sulfide nanoparticles and their incorporation into poly (hydroxybutyrate) matrix in the formation of a novel nanocomposite”, *Materials Research Express*, 5 (2018) 055027.
- [125] OF Obidi, AO Nejo, RA Ayeni, and N Revaprasadu, “Insights into Comparative Antimicrobial Efficacies of Synthetic and Organic Agents: The Case of ZnS Nanoparticles and *Zingiber officinale* Rosc”, *JOM*, 70 (2018) 982-987.
- [126] S Ummartyotin, N Bunnak, J Juntaro, M Sain, and H Manuspiya, “Synthesis and luminescence properties of ZnS and metal (Mn, Cu)-doped-ZnS ceramic powder”, *Solid State Sciences*, 14 (2012) 299-304.
- [127] Rita John, and Sasi Florence, “Optical, structural and morphological studies of bean-like zns nanostructures by aqueous chemical method”, *Chalcogenide letters*, 7 (2010).
- [128] U Baishya, and D Sarkar, “Structural and optical properties of zinc sulphide-polyvinyl alcohol (ZnS-PVA) nanocomposite thin films: effect of Zn source concentration”, *Bulletin of Materials Science*, 34 (2011) 1285-1288.
- [129] Kamakshi Patel, MP Deshpande, and SH Chaki, “Effect of Ag on structural, optical and luminescence properties of ZnS nanoparticles synthesized by microwave-assisted chemical route”, *Applied Physics A*, 123 (2017) 367.

[130] Mohammed A Al-Azawi, Noriah Bidin, M Bououdina, and Sabah M Mohammad, “Preparation of gold and gold–silver alloy nanoparticles for enhancement of plasmonic dye-sensitized solar cells performance”, *Solar Energy*, 126 (2016) 93-104.

[131] Wuletaw Andargie Ayalew, and Delele Worku Ayele, “Dye-sensitized solar cells using natural dye as light-harvesting materials extracted from *Acanthus sennii* chiovenda flower and *Euphorbia cotinifolia* leaf”, *Journal of science: Advanced materials and devices*, 1 (2016) 488-494.

الملخص العربي

تهتم هذه الرسالة بدراسة تحضير وتوصيف جسيمات الذهب والفضة وكبريتيد الزنك ومركب مكون من الفضة وكبريتيد الزنك في صورة (لب-قشرة) في الصورة النانوية. تم تحضير هذه المواد بأحجام وأشكال مختلفة ودراسة خصائصها وتأثيرها على الخلايا الشمسية.

اقتضت طبيعة البحث إلى تقسيم الرسالة لأربعة فصول على النحو الآتي:

الفصل الأول:

احتوى هذا الفصل على جزئين رئيسيين وهما مقدمة عامة حول المواد النانوية وعدد من الدراسات السابقة المتعلقة بالبحث. ابتداءً هذا الفصل بنبذة مختصرة لتاريخ المواد النانوية وبعدها عرض مقدمة للمواد النانوية ثم انتقل لطرح بعض المصطلحات الهامة ثم توصيف المواد النانوية بحسب المنشأ والابعاد والشكل الخارجي والتركيب. أيضاً تم ذكر أهم العوامل التي تؤثر في المواد النانوية كتأثير الكم الحصري ونسبة مساحة السطح إلى الحجم. كذلك تم استعراض طرق تصنيع المواد النانوية وتحضيرها بحسب الهيكل البنائي والمواد الأولية. كما تمت الإشارة إلى بعض تطبيقات المواد النانوية. بالإضافة إلى ذلك تم سرد مجموعة من الدراسات السابقة فيما يخص تحضير الذهب والفضة وكبريتيد الزنك ومركبات (الفضة/كبريتيد الزنك) في صورة (لب-قشرة) في مدى النانو وتطبيقاتها في الخلايا الشمسية. اختتم هذا الفصل بإيجاز خطة العمل بشكل مختصر.

الفصل الثاني:

في هذا الفصل تم مناقشة وشرح الأسس النظرية التي بني عليها عمل الأجهزة المستخدمة لتوصيف المواد النانوية، مثل: التحليل الطيفي للأشعة المرئية وال فوق بنفسجية، والمجهر الإلكتروني النافذ، وتشتت الضوء الديناميكي، وحيود الأشعة السينية، والتحليل الطيفي للأشعة تحت الحمراء، وفي

ختام هذا الفصل تم ايجاز مبدأ عمل الخلية الشمسية وذكر أجيالها والعوامل التي تؤثر في كفاءتها.

الفصل الثالث:

في هذا الفصل تم ذكر المواد الكيميائية وتوضيح الطرق المعملية المستخدمة لتحضير جسيمات الذهب والفضة وكبريتيد الزنك النانوية ومركب الفضة/كبريتيد الزنك (لب-قشرة) النانوي.

أولاً: جسيمات الذهب النانوية تم تحضيرها بطريقتين مختلفتين، الطريقة الأولى: تم استخدام نسب ثابتة من هيدرات كلوريد الذهب ($\text{HAuCl}_4 \cdot 3\text{H}_2\text{O}$) وسيتيل بروميد الأمونيوم (CTAB) مع تغيير نسبة بوروهيدريد الصوديوم (NaBH_4). الطريقة الثانية: تم استخدام نسب ثابتة من هيدرات كلوريد الذهب ($\text{HAuCl}_4 \cdot 3\text{H}_2\text{O}$) وبوروهيدريد الصوديوم (NaBH_4) مع تغيير نسبة سيتيل بروميد الأمونيوم (CTAB).

كما تم تحضير جسيمات الفضة النانوية عن طريق تحضير محلولين، المحلول الأول: 60 مل من سيتيل بروميد الأمونيوم (CTAB) بتركيز (0.1M) في الكلوروفورم مع إضافة نسب مختلفة من نترات الفضة (AgNO_3) المحضرة بتركيز (1M) في محلول مائي. المحلول الثاني: 60 مل من سيتيل بروميد الأمونيوم (CTAB) بتركيز (0.1M) في الكلوروفورم مع إضافة نسبة ثابتة من بوروهيدريد الصوديوم (NaBH_4) المحضرة بتركيز (1M) في محلول مائي. بعد ذلك يتم خلط المحلولين بالتحريك المغناطيسي واستخدام الصوتنة الفائقة وخلال ذلك تم إضافة 0.4 مل من محلول بولي فاينيل بيرليدون (PVP) بنسبة (0.5%).

كذلك تم تحضير كبريتيد الزنك بطريقتين مختلفتين، الطريقة الأولى: باستخدام نسب مولية ثابتة من كبريتيد الصوديوم (Na_2S) مع تغيير النسبة المولية لخلات الزنك ($\text{ZnC}_4\text{H}_6\text{O}_4$) عند درجة

حرارة ثابتة. الطريقة الثانية: باستخدام نسب مولية ثابتة لكل من كبريتيد الصوديوم (Na_2S) وخلات الزنك ($\text{ZnC}_4\text{H}_6\text{O}_4$) عند درجات حرارة مختلفة [50-100].

أما بالنسبة لمركب الفضة/كبريتيد الزنك (لب-قشرة) النانوي، فقد تم تحضيره على مرحلتين، المرحلة الأولى: تحضير جسيمات الفضة النانوية عن طريق استخدام 240 مل من حمض الأسكوربيك ($\text{C}_6\text{H}_8\text{O}_6$) بتركيز ($5 \times 10^{-4}\text{M}$) وإضافة 2.4 جرام من بولي فاينيل بيرليدون (PVP) والتحريك المغناطيسي لمدة 15 دقيقة ثم إضافة 4.2 مل من هيدروكسيد الصوديوم (NaOH) بتركيز (0.1M) والتحريك المغناطيسي لمدة 5 دقائق، ثم إضافة 2.4 مل من نترات الفضة (AgNO_3) بتركيز (0.1M) والتحريك لمدة 15 دقيقة في حمام مائي عند درجة حرارة 30° درجة مئوية ثم عند درجة حرارة 80° درجة مئوية. المرحلة الثانية: تحضير المركب عن طريق استخدام نسب ثابتة من خلات الزنك ($\text{ZnC}_4\text{H}_6\text{O}_4$) ونترات الأمونيوم (NH_4NO_3) وبولي فاينيل بيرليدون (PVP) وكبريتيد الصوديوم (Na_2S) وحمض الأسكوربيك ($\text{C}_6\text{H}_8\text{O}_6$) مع تغيير كمية محلول جسيمات الفضة النانوية المعدة مسبقاً في المرحلة الأولى.

إضافة إلى ما سبق، تم شرح طرق تحضير العينات لتوصيفها. كذلك تم استعراض مكونات أجهزة التوصيف مثل: التحليل الطيفي للأشعة المرئية وفوق البنفسجية، والمجهر الإلكتروني النافذ، وتشتت الضوء الديناميكي، وحيود الأشعة السينية، والتحليل الطيفي للأشعة تحت الحمراء، ومنحنى (التيار-الجهد) وطريقة طلاء الخلايا الشمسية.

الفصل الرابع:

خلال هذا الفصل تم عرض وتفسير النتائج التي تم الحصول عليها من العينات النانوية التي تم تحضيرها سابقاً، حيث تمت دراسة أطراف الأشعة المرئية وفوق البنفسجية لجسيمات الذهب النانوية عند قياس قمم طيف الامتصاص لها ظهرت شرائط مميزة لرنين السطح البلازموني (SPR)

عند الأطوال الموجية (527 nm, 526 nm, 526 nm, and 526 nm) لعينات الذهب التي تم تحضيرها بالطريقة الأولى (AuNPs(S1-S4) ، كما ظهرت عند (528 nm) لجميع عينات الذهب المحضرة بالطريقة الثانية (AuNPs(S5-S8) استنتجنا من ذلك أن زيادة تركيز بوروهيدريد الصوديوم (NaBH_4) وسيتيل بروميد الأمونيوم (CTAB) لا تؤثر في تغيير حجم الجسيمات لكن تأثيرها واضح في زيادة كامل عرض النطاق عند منتصف الارتفاع (FWHM). أما بالنسبة لعينات الفضة النانوية فالشرائط المميزة لرنين السطح البلازموني (SPR) ظهرت عند (414 nm, 413 nm, 415 nm, 417 nm, and 425 nm) للعينات (AgNPs (S9-S13) يظهر لنا من النتائج أنه كلما انزاحت الأطوال الموجية لقيم أعلى يزداد حجم الجسيمات، نستدل من ذلك أنه كلما زاد تركيز نترات الفضة (AgNO_3) أثناء عملية التحضير يزداد حجم الجسيمات وذلك نتيجة لزيادة عدد أيونات الفضة مما يؤدي إلى انخفاض عدد الجسيمات المتكونة مع زيادة حجمها. كذلك، جسيمات كبريتيد الزنك النانوية أظهرت قمم امتصاص عند (305 nm, 289 nm, 287 nm, 284 nm, and 283 nm) وعند (308 nm, 307 nm, 304 nm, 303 nm, and 300 nm)، أيضاً تم حساب فجوة الطاقة الطيفية عن طريق (Tauc's plot) حيث كانت عند (4.66 eV, 4.78 eV, 4.92 eV, and 4.93 eV) وعند (4.77 eV, 4.74 eV, 4.75 eV, 4.74 eV, 4.73 eV, and 4.66 eV) للعينات المحضرة عند تراكيز مختلفة لخلات الزنك (ZnS(S14-S18) و للعينات المحضرة عند درجات حرارة مختلفة ZnS(S19-S23) ، على التوالي. يظهر من النتائج ان هناك تناقص في قيم الطول الموجي وهذا يعني تضائل في حجم الجسيمات لذلك من المفترض أن قيم فجوات الطاقة تتزايد مع تناقص حجم الجسيمات وهذا يظهر بشكل جلي في نتائج الطريقة الأولى لتحضير جسيمات الزنك النانوية. نتائج عينات المركب المكون من الفضة /كبريتيد الزنك (لب-قشرة) النانوي تظهر شريط امتصاص مميز لرنين السطح البلازموني (SPR) للفضة المعدة في المرحلة الأولى عند (408 nm) للعينة AgNPs(S25) و قمم امتصاص المركب ظهرت عند (450 nm, 469 nm, and 498 nm) للعينات

المحضرة باستخدام كميات مختلفة من محلول الذهب النانوي ZnS (S26-S28) هناك تزايد في الطول الموجي مع ازدياد تركيز محلول الفضة النانوي مما يعني أنه مع زيادة تركيز الفضة يزداد حجم الجسيمات، أيضاً اتساع نطاق المنحنى يؤكد تكون المركب في صورة (لب-قشرة) في مدى النانو.

تم فحص بعض العينات باستخدام المجهر الإلكتروني النافذ من خلال هذا الفحص تم التعرف على أشكال وأحجام وتوزيع الجسيمات النانوية. جميع جسيمات الذهب النانوية ظهرت في شكل كروي ماعدا عدد قليل ظهر على هيئة مثلثات وسداسي الزوايا والتي ظهرت في عينة الذهب AuNPs(S7). تم حساب حجم الجسيمات بواسطة برنامج (Image) وكانت متوسط الاحجام التي حصلنا عليها من خلال توزيع جاوسيان كالتالي (7 nm, 7 nm, and 10 nm) لعينات الذهب النانوية [AuNPs(S3), AuNPs(S4), and AuNPs(S7)]. جسيمات الفضة النانوية للعينة AgNPs(10) كانت في صورة نقط غامقة مع متوسط حجم (2nm)، أما بالنسبة للعينة رقم AgNPs(S11) يغلب على جسيماتها الشكل الكروي ولها توزيع عشوائي مع متوسط حجم (4nm). كذلك، عينات كبريتيد الزنك النانوية أكدت النتائج تكون الجسيمات في شكل كروي وانقسمت الصور إلى جزئين توزيع منخفض وتوزيع مرتفع ومتوسط الحجم كالتالي (5 nm, 3 nm, 3 nm, and 3 nm) للعينات [ZnSNPs(S14), ZnSNPs(S18), ZnSNPs(S19), and ZnSNPs(S22)]. ظهر لنا في عينات الفضة/كبريتيد الزنك النانوية تكون الجسيمات في صورة كروية مع ظهور اختلاف في لون اللب (core) والقشرة (shell) مما يؤكد احتواء المركب على مواد مختلفة، متوسط حجم الجسيمات (27 nm, 81 nm, and 177 nm) للعينات [Ag/ZnS(S26-S28)] على التوالي.

كما بينت نتائج تشتت الضوء الديناميكي نتائج لحجم العينات أيضاً، متوسط حجم العينات كان (33.03 nm, 23.46 nm, and 30.26 nm) لعينات الذهب النانوية [AuNPs(S3), AuNPs(S4),

AgNPs(S10) and [عينات الفضة النانوية (87 nm and 77.68 nm) و AuNPs(S7)]
[AgNPs(S11)]، و (11.74 nm, 132.9 nm, and 315.9 nm) لعينات كبريتيد الزنك النانوية
[ZnSNPs(S14), ZnSNPs(S19), and ZnSNPs(S22)]، و (39.04 nm, 127.8 nm, and 48.39 nm)
Ag/ZnS(S26), Ag/ZnS(S27), and [عينات الفضة/كبريتيد الزنك (لب-قشرة) النانوية]
[Ag/ZnS(S28)] على التوالي. التغير الكبير بين قياسات الحجم في المجهر الالكتروني النافذ وتشتت
الضوء الديناميكي منطقي، لأسباب عدة منها أن الكمية المقاسة في تشتت الضوء أكثر بكثير مما
تم قياسه بواسطة المجهر الالكتروني النافذ أيضاً شدة حساسية تشتت الضوء للأشكال غير
الكروية كذلك، المجهر الالكتروني يقيس المواد المعدنية (الغير عضوية) في الجسيمات فقط بعكس
تشتت الضوء الديناميكي الذي يقيس المواد العضوية والغير عضوية للجسيمات.

تم تطبيق حيود الأشعة السينية على جسيمات الذهب والفضة وكبريتيد الزنك. تم حساب الحجم
البلوري بواسطة معادلة شيرير. احجام بلورات جسيمات الذهب النانوية عند زاوية الحيود (38)
كانت (21.48 nm, 33.57 nm, and 30.74 nm) للعينات [AuNPs(S1-S3)]، وكانت عند (9.94
nm, 8.25 nm, and 8.59 nm) للعينات [AuNPs(S5-S7)] على التوالي. أما بالنسبة للحجم البلوري
لجسيمات الفضة النانوية عند زاوية الحيود (37) كانت (8.08 nm, 7.89 nm, 8.12 nm, 12.42 nm)
(nm, and 8.23 nm) للعينات [AgNPs(S9-S13)] على التوالي. كبريتيد الزنك النانوي عند زاوية
الحيود (28) ظهرت الاحجام (2.83 nm, 2.18 nm, 2.19 nm, 2.15 nm, and 2.14 nm) للعينات
[ZnSNPs(S14-S18)] وكانت (2.83 nm, 4.04 nm, 3.97 nm, 3.92 nm, 3.76 nm, and 4.17 nm)
للعينات [ZnSNPs(S19-S23), and ZnSNPs(S24)] على التوالي.

نتائج تحليل الطيف للأشعة تحت الحمراء بينت الترابط الكيميائي بين المواد النانوية المحضرة
والمجموعات الوظيفية للمواد المثبتة (capping materials). عينات الذهب النانوية أظهرت شريط

نفاذي مميز عند العدد الموجي 1481 cm^{-1} نتيجة ارتباط جسيمات الذهب مع مجموعة $C - N^+$ (CTAB). الموجودة في جزيئات سييتيل بروميد الأمونيوم. كذلك، الازاحة التي ظهرت للشريط النفاذي عند العدد الموجي 1346 cm^{-1} نتيجة مشاركة ذرة النيتروجين الموجودة في بولي فاينيل يرليدون (PVP) في تكوين جسيمات الفضة النانوية. كذلك ظهور أشرطة نفاذية عند القيم 1004 cm^{-1} و 925 cm^{-1} لعينات كبريتيد الزنك تدل على ارتباط الزنك بالكبريتيد $Zn - S$. أما بالنسبة لمركب الفضة/كبريتيد الزنك (لب-قشرة) النانوي ظهرت عدة شرائط نفاذية تؤكد وجود جسيمات الفضة وكبريتيد الزنك مما يثبت تكون المركب.

وفي الختام تم استعراض نتائج دراسة منحني (التيار-الجهد) للخلايا الشمسية متعددة البلورات. حيث تم طلاء الخلايا الشمسية بمادة الذهب والفضة وكبريتيد الزنك ومركب الفضة/كبريتيد الزنك (لب-قشرة) النانوي بواسطة جهاز الدوران السريع تحت الضغط (vacuum spin coater) وقياس العوامل المتغيرة فيها كجهد الدائرة المفتوحة (V_{oc}) والتيار دائرة الموصله (I_{sc}) والجهد الأقصى للدائرة (V_m) والتيار الأقصى للدائرة (I_m) ومعامل الامتلاء (FF) والكفاءة (η). تم مقارنة الخلايا التي تم طلاؤها بالخلية الأصل (قبل الطلاء) وكانت النتائج كالتالي كفاءة الخلية قبل الطلاء ($\eta = 14.29\%$) وبعد إضافة جسيمات الذهب النانوية كانت الكفاءة عند ($\eta = 13.65\%$ and 13.14%) للعينات [AuNPs(7 nm) and AuNPs(10 nm)]، وجسيمات كبريتيد الزنك عند ($\eta = 12.57\%$ and 11.74%) للعينات [ZnSNPs(2.15 nm) and ZnSNPs(3.97 nm)]، ومركب الفضة/كبريتيد الزنك (لب-قشرة) النانوي عند ($\eta = 13.02\%$) للعينة (Ag/ZnS(177 nm)، كما يظهر لنا من النتائج السابقة أن المواد النانوية لم تؤثر التأثير المنشود وهذا من الممكن أن يعزى لعدة أسباب أولها عدم انتظام توزيع الطلاء على الخلية مما سبب في انخفاض تشتت الضوء أيضاً ربما العينات كانت تحتاج إلى تسخين عند درجات حرارة مرتفعة لتبخير المياه الموجودة على سطح

العينة. مما يثبت فرضيتنا، أنه عند قياس التيار الضوئي بعد فترة طويلة من قياس منحني (التيار- الجهد) ظهر لنا تحسن ملحوظ في القيم وذلك بسبب جفاف العينة خلال هذه المدة. قيم التيار الضوئي كانت عند 58.5, 72, 75.7, 78.4, 76.3, 76.5, and 79.4 للعينات [blank (silicon solar cell), Si/AuNPs (S7), Si/AgNPs (S11), Si/ZnSNPs (S17), Si/ZnSNPs (S21), Si/Ag / ZnS (S26), and Si/Ag / ZnS (S28), على التوالي.

المخلص العربي

اهداء

إلى نور عيني، صاحبة القلب النقي، رمز الحنان والتضحية من بدعواتها قلبي
اطمأن وبعلمها عقلي استضاء..

إليك أمي الحبيبة.

إلى قدوتي ومصدر فخري، رمز الأمان والحب من بحمته اهتدي، وعلى ثقته
اعتمد..

إليك أبي الغالي.

إلى سندي عند الشدائد اخواني الأعزاء.

إلى اليد اليمنى، رفيقات السعادة والحزن أخواتي اللطيفات.

إليكم يا من غرستم بذرة العلم الأولى .. الثمرة الأولى.



المملكة العربية السعودية
وزارة التعليم
جامعة أم القرى
كلية العلوم التطبيقية
قسم الفيزياء

تحضير وتوصيف ودراسة الخصائص الضوئية للجسيمات النانوية في صورة (لب-قشرة) وتطبيقاتها في الخلايا الضوئية

رسالة مقدمة إلى

قسم الفيزياء – كلية العلوم التطبيقية – جامعة أم القرى

كجزء مكمل للحصول على درجة الماجستير في العلوم-فيزياء

الطالبة

سامية عبد الرحمن عثمان الغامدي

(بكالوريوس فيزياء 2017)

الرقم الجامعي: 43880212

إشراف

أ.د رشدي سعودي محمد عوض

أستاذ الأطياف والنانوتكنولوجيا

قسم الفيزياء – كلية العلوم التطبيقية – جامعة أم القرى

المشرف المساعد

أ.د سعود حميد اللحاني

أستاذ الفيزياء الطبية

قسم الفيزياء – كلية العلوم التطبيقية – قسم الفيزياء

1441-2020